TAŞKIN YATAK
NÜKLEER YAKIT KAPLAYICI İÇİN HESAPLAMALI AKIŞKANLAR DİNAMİĞİ ÇALIŞMALARI

COMPUTATIONAL FLUID DYNAMICS STUDIES FOR A SPOUTED BED NUCLEAR FUEL COATER

SENEM ŞENTÜRK LÜLE

A dissertation submitted in partial satisfaction of the

requirements for the degree of

DOCTOR of PHILOSOPHY

in

NUCLEAR ENGINEERING

According to the Regulations of

The Institute for Graduate Studies in Pure and Applied Sciences

HACETTEPE UNIVERSITY

2012

To The Institute for Graduate Studies in Pure and Applied Sciences,

This study has been approved by The Graduate Committee as a partial fulfillment of the requirements for the degree of **DOCTOR of PHILOSOPHY** in the field of **NUCLEAR ENGINEERING**.

Graduate Committee

Head : Prof. Dr. Okan ZABUNOĞLU

Member (Advisor) : Prof. Dr. Üner ÇOLAK

Member : Assoc. Prof. Dr. Niyazi SÖKMEN

Member : Assoc. Prof. Dr. Murat KÖKSAL

Member : Assoc. Prof. Dr. Görkem KÜLAH

APPROVED

This dissertation has been approved on / /2012 by the Graduate Committee established by the Board of the Institute.

/ /2012

Prof. Dr. Fatma SEVİN DÜZ
HEAD OF THE INSTITUTE FOR GRADUATE
STUDIES IN PURE AND APPLIED SCIENCES

To my husband

and

my sons

COMPUTATIONAL FLUID DYNAMICS STUDIES FOR A SPOUTED BED NUCLEAR FUEL COATER

Senem Şentürk Lüle

ABSTRACT

The inherent safety features of high temperature reactors may be attributed to their fuel characteristics. TRISO coated particles, the essential part of the fuel, are produced by coating fuel kernels using chemical vapor deposition technique in conical cylindrical spouted bed coating reactors operated at high temperatures. The knowledge about flow patterns and concentration distributions in spouted beds as well as the effect of geometric parameters on hydrodynamics of spouted beds is of great interest for the design of such equipment. Computational fluid dynamics simulations can be instrumental for design as well as possible improvements.

In this study, basics of nuclear fuel coating, fluidization, and multiphase flow modeling are discussed. Then, computational fluid dynamics simulations of two existing experimental studies containing high density (6050 kg/m^3) and low density (2500 kg/m^3) particles are performed using Eulerian-Eulerian approach to investigate hydrodynamics of conical cylindrical spouted beds and to understand the effects of simulation parameters on particle velocity and voidage distributions as well as bed pressure drop. Furthermore, effects of geometric and operation factors such as conic angle, particle size, and static bed height on hydrodynamics of heavy particle filled conical cylindrical spouted beds are investigated.

It was found that magnitude of drag coefficient therefore drag model and maximum packing limit have vital importance for computational fluid dynamics simulations of conical cylindrical spouted beds. Both can cause unrealistic simulation results when used inappropriately. Other parameters such as restitution coefficient and inclusion of frictional stress into simulations have secondary effect on simulations. If they are not properly assigned, they may cause discrepancies between the simulation and experimental results but they do not change the gas-solid flow characteristics of the system.

It was also found that as static bed height increases, particle velocity and voidage in spout and annulus regions increase as well as bed pressure drop. As particle size increases, particle velocity and voidage decrease in spout and annulus regions similar to bed pressure drop. As conic angle increases, particle velocity and voidage increase in spout and annulus regions but bed pressure drop decreases.

Overall, it was concluded that Eulerian-Eulerian approach is capable of simulating complex flow patterns observed in conical cylindrical spouted beds with both high and low density particles. Therefore, it can be used in the design of CVD fuel coaters.

Keywords: spouted beds, multiphase flow, computational fluid dynamics

Advisor: Prof. Dr. Üner ÇOLAK, Hacettepe University, Department of Nuclear Engineering.

TAŞKIN YATAK NÜKLEER YAKIT KAPLAYICI İÇİN HESAPLAMALI AKIŞKANLAR DİNAMİĞİ ÇALIŞMALARI

Senem Şentürk Lüle

ÖZ

Yüksek sıcaklıklı reaktörlerin güvenliğinin temeli yakıt karakteristiğine dayandırılabilir. Yakıtın temel kısmı olan TRISO yakıt çekirdeği yüksek sıcaklıkta, konik silindirik taşkın yataklarda kimyasal buhar depolama yöntemi ile kaplanarak üretilir. Taşkın yataklarda katı parçacıkların akış düzeni ve konsantrasyonunun ayrıca geometrik parametrelerin akış hidrodinamiği üzerindeki etkilerinin bilinmesi, bu ekipmanın tasarımı için çok önemlidir. Hesaplamalı akış dinamiği simülasyonları konik silindirik taşkın yatakların tasarımı ve geliştirilmesi amacıyla kullanılabilen araçlardır.

Bu çalışmada, ilk olarak nükleer yakıt kaplaması, akışkanlaşma ve çok fazlı akış modellemesi konularına değinilmiştir. Daha sonra, yüksek yoğunluklu (6050 kg/m^3) ve düşük yoğunluklu (2500 kg/m^3) parçacıklar içeren iki farklı deney düzeneği için Euler-Euler yaklaşımı kullanılarak konik silindirik taşkın yatakların akış dinamiğini incelemek ve simülasyon parametrelerinin parçacık hızı ve konsantrasyonu ile yatak basınç düşümü üzerindeki etkilerini belirlemek için hesaplamalı akış dinamiği simülasyonları gerçekleştirilmiştir. Aynı zamanda, ağır parçacıklar içeren konik silindirik taşkın yataklarda konik açı, parçacık boyutu ve yatak yüksekliği gibi geometrik ve çalışma faktörlerinin akış hidrodinamiği üzerindeki etkileri araştırılmıştır.

Çalışma sonucunda Euler-Euler yaklaşımının hem ağır hem hafif parçacıklarla yüklü konik silindirik yataklarda gerçekleşen karmaşık akışı modellemede yeterli olduğu sonucuna varılmıştır.

Çalışma sonucunda ayrıca maksimum sürükleme katsayısı değeri dolayısıyla sürükleme modelinin ve sıkıştırma limitinin akış hidrodinamiği üzerinde birinci derece etkisi olduğu görülmüştür. Yanlış kullanıldıklarında her ikisi de gerçek dışı simülasyon sonuçlarına neden olabilmektedir. Restitüsyon katsayısı ve katı sürtünme gerilmesinin simülasyonlara eklenmesi gibi diğer parametrelerin simülasyonlar üzerinde ikinci derecede etkili olduğu gözlenmiştir. Uygun

kullanılmadıkları durumlarda sonuçlarda sapmaya neden olabilmektedirler. Ancak sistemin fiziğini değiştirmemektedirler.

Yatak yüksekliliğinin arttırılması ile taşkın ve halka bölgelerinde parçacık hızı artmakta, parçacık konsantrasyonu azalmaktadır. Yatak basınç düşümünün de yatak yüksekliğinin arttırılması ile arttığı bulunmuştur. Parçacık boyutunun arttırılması ile parçacık hızının taşkın ve halka bölgelerinde azaldığı diğer taraftan parçacık konsantrasyonunun arttığı fakat yatak basınç düşümünün azaldığı gözlenmiştir. Konik açının arttırılması ile taşkın ve halka bölgelerinde parçacık hızının arttığı, parçacık konsantrasyonunun ve yatak basınç düşümünüm azaldığı sonucuna varılmıştır.

Anahtar Kelimeler: taşkın yataklar, çok fazlı akış, hesaplamalı akışkanlar dinamiği

Danışman: Prof. Dr. Üner ÇOLAK, Hacettepe Üniversitesi, Nükleer Enerji Mühendisliği Bölümü.

ACKNOWLEDGEMENTS

This thesis would have not been possible unless my advisor Prof. Dr. Üner ÇOLAK provided the encouragement, supervision, and support from the preliminary to the concluding level of this thesis. I am not only grateful for his support throughout this thesis but also grateful for his guidance throughout my entire carrier.

I owe my deepest gratitude to Assoc. Prof. Dr. Murat KÖKSAL for his support in number of ways. His valuable comments shaped my thesis and his efforts on the experiments made this thesis possible.

It is a pleasure to thank Assoc. Prof. Dr. Görkem KÜLAH also for her efforts and expertise on the experiments and her valuable contributions to my thesis.

I would also like to thank Prof. Dr. Okan ZABUNOĞLU and Assoc. Prof. Dr. Niyazi SÖKMEN, who kindly agreed to be members of my committee, for their insightful comments and suggestions on my thesis.

Last but not least I would like to express my deepest appreciation to my husband Sezgin LÜLE for his unlimited support and unceasing love throughout our marriage and for taking care of our son Yavuz and me therefore our baby in my tummy while I was writing this thesis. Without him this thesis would not have been possible.

CONTENTS

Page

ABSTRACT i

ÖZ iii

ACKNOWLEDGEMENTS v

LIST OF FIGURES viii

LIST OF TABLES xv

1 INTRODUCTION 1

2 THE HIGH TEMPERATURE REACTOR FUEL 4

2.1 The HTR History 4

2.2 The Coated Particles 6

3 THE FLUIDIZATION 10

3.1 The Spouted Bed 16

4 THE MULTIPHASE FLOW MODELING 22

4.1 The Eulerian-Eulerian Approach 24

4.1.1 Conservation equations 25

4.1.1.1 Conservation of mass 25

4.1.1.2 Conservation of momentum 26

4.1.2 The closure equations 26

4.1.2.1 The solid-gas momentum exchange coefficient 26

4.1.3 Kinetic theory of granular flow 28

4.1.3.1 The dissipation of granular energy 31

4.1.3.2 The solid phase stress tensor 31

4.1.3.3 The solid phase pressure 33

5 LITERATURE REVIEW 34

6 CFD STUDIES ON LIGHT PARTICLE FILLED EXPERIMENTAL SETUP 40

6.1 The Literature Review 40

6.2 The Experimental Setup 43
6.3 The CFD Simulations 44
6.3.1 The influence of maximum packing limit 48
6.3.2 The influence of restitution coefficient 59
6.3.3 The influence of drag model 60
6.3.4 The influence of solid frictional viscosity 61
6.3.5 The influence of drag coefficient 67
6.4 Results and Discussions 74
7 CFD STUDIES ON HEAVY PARTICLE FILLED EXPERIMENTAL SETUP 81
7.1 The Experimental Setup 81
7.2 The Preparations for CFD Simulations 85
7.3 Findings from CFD Simulations 89
7.3.1 The Experimental Set 1 90
7.3.2 The Experimental Set 2 100
7.3.3 The Experimental Set 3 109
7.3.4 The Experimental Set 4 124
7.3.5 The Experimental Set 5 133
7.3.6 The Experimental Set 6 142
7.3.7 The Experimental Set 7 149
7.4 Results and Discussions 153
7.5 Comparison of Effects of CFD Model Parameters on Light and Heavy Particle Simulations 173
7.6 The Findings about Hydrodynamics of Spouted Beds 176
8 CONCLUSION 187
BIBLIOGRAPHY 193
APPENDIX A SUMMARY OF A SAMPLE FLUENT INPUT 199

LIST OF FIGURES

Page

Figure 2.1 The reference design for fuel particles and fuel elements (a) Germany (b) USA (c) Japan (IAEA-TECDOC-987, 1997). 6
Figure 2.2 A schematic of TRISO particle (Pannala et al., 2007). 7
Figure 2.3 The U-based kernels after drying (left) and after sintering (right) (Charollais, 2004). 8
Figure 3.1 Various forms of contacting of a batch of solids by fluid (Kunii et al., 1991). 11
Figure 3.2 Examples of fluid like behavior of fluidized bed relative to fixed bed (Gupta et al., 1999). 13
Figure 3.3 The Geldart classification of particles from air at ambient conditions (Gidaspow, 1994). 14
Figure 3.4 Pressure drop versus gas velocity diagram of a fluidized bed (Gupta et al., 1999). 16
Figure 3.5 Three configurations of spouted beds: (a) cylindrical, (b) conical-cylindrical, and (c) conical. 17
Figure 3.6 Regime transitions in spouted beds with increasing gas flow (Epstein et al., 2011). 17
Figure 3.7 The evaluation of spouting process (a) formation of small cavity, (b) development of internal spout, (c) onset of external spout. 18
Figure 3.8 Schematic view of spouted beds. (a) (Kunii et al., 1991), (b) (Olazar et al., 2004). 19
Figure 3.9 The geometric parameters of the spouted beds. 19
Figure 4.1 Modeling approaches for multiphase flows; (a) Volume of fluid approach, (b) Eulerian-Lagrangian approach (c) Eulerian-Eulerian approach (Ranade, 2002). 23
Figure 6.1 A schematic of He's experimental set up. 43
Figure 6.2 The computational domain generated for the spouted bed. 44
Figure 6.3 Comparison of particle velocity and voidage profiles of different mesh sizes. 46
Figure 6.4 Speed-up factor versus number of cores from parallel computing of FLUENT on 8 HP ProLiant BL680C G5 system. 47

Figure 6.5 Instantaneous (t=15s) solid volume fraction distributions of Gidaspow drag model for different e_{ss} and $\alpha_{s,max}$ values. 51
Figure 6.6 Instantaneous (t=15s) solid volume fraction distributions of Syamlal-O'Brien drag model for different e_{ss} and $\alpha_{s,max}$ values. 52
Figure 6.7 Comparison of Gidaspow drag model voidage and particle velocity profiles of $\alpha_{s,max}$=0.63 a) e_{ss} =0.95, b) e_{ss} =0.90, c) e_{ss} =0.80 case with experimental results (open pointers). 53
Figure 6.8 Comparison of Gidaspow drag model voidage and particle velocity profiles of $\alpha_{s,max}$=0.61 d) e_{ss} =0.95, e) e_{ss} =0.90, f) e_{ss} =0.80 case with experimental results (open pointers). 54
Figure 6.9 Comparison of Gidaspow drag model voidage and particle velocity profiles of $\alpha_{s,max}$=0.59 g) e_{ss} =0.95, h) e_{ss} =0.90, i) e_{ss} =0.80 case with experimental results (open pointers). 55
Figure 6.10 Comparison of Syamlal-O'Brien drag model voidage and particle velocity profiles of $\alpha_{s,max}$=0.63 a) e_{ss} =0.95, b) e_{ss} =0.90, c) e_{ss} =0.80 case with experimental results (open pointers). 56
Figure 6.11 Comparison of Syamlal-O'Brien drag model voidage and particle velocity profiles of $\alpha_{s,max}$=0.61 d) e_{ss} =0.95, e) e_{ss} =0.90, f) e_{ss} =0.80 case with experimental results (open pointers). 57
Figure 6.12 Comparison of Syamlal-O'Brien drag model voidage and particle velocity profiles of $\alpha_{s,max}$=0.59 d) e_{ss} =0.95, e) e_{ss} =0.90, f) e_{ss} =0.80 case with experimental results (open pointers). 58
Figure 6.13 Comparison of gas-solid momentum exchange coefficient for z=0.053 m of Gidaspow and Syamlal-O'Brien drag models (t=15.0 s, e_{ss} =0.80, $\alpha_{s,max}$=0.63)..... 61
Figure 6.14 Instantaneous (t=15s) particle concentration distributions of Gidaspow drag model with and without solid frictional stress term. 64
Figure 6.15 Instantaneous (t=15s) particle concentration distributions of Syamlal-O'Brien drag model with and without solid frictional stress term..... 64
Figure 6.16 Comparison of results of Gidaspow drag model voidage and particle velocity profiles of a) without b) with solid frictional stress term with experimental results (open pointers)..... 65

Figure 6.17 Comparison of results of Syamlal-O'Brien drag model voidage and particle velocity profiles of a) without b) with solid frictional stress term with experimental results (open pointers). 66
Figure 6.18 Instantaneous (t=15s) solid volume fraction of 2, 3, and 4 times of the Syamlal-O'Brien drag coefficient model without $\mu_{s,fric}$. 68
Figure 6.19 Comparison of voidage and particle velocity profiles of e_{ss} =0.90, $\alpha_{s,max}$=0.63, 1 times Syamlal-O'Brien drag model without $\mu_{s,fric}$ case with experiment (open pointers)..... 70
Figure 6.20 Comparison of voidage and particle velocity profiles of e_{ss} =0.90, $\alpha_{s,max}$=0.63, 2 times Syamlal-O'Brien drag model without $\mu_{s,fric}$ case with experiment (open pointers)..... 71
Figure 6.21 Comparison of voidage and particle velocity profiles of e_{ss} =0.90, $\alpha_{s,max}$=0.63, 3 times Syamlal-O'Brien drag model without $\mu_{s,fric}$ case with experiment (open pointers)..... 72
Figure 6.22 Comparison of voidage and particle velocity profiles of e_{ss} =0.90, $\alpha_{s,max}$=0.63, 4 times Syamlal-O'Brien drag model without $\mu_{s,fric}$ case with experiment (open pointers)..... 73
Figure 6.23 Comparison between the experimental and simulation results of particle velocity. 78
Figure 6.24 Comparison between the adjusted experimental and simulation results of particle velocity. 78
Figure 6.25 The particle velocity distribution comparison between the experimental results and simulation results of Wang (2004)..... 79
Figure 7.1 A schematic view of Sari's experimental setup (Sari et al., 2011). 82
Figure 7.2 The geometry of the experimental conical cylindrical spouted bed. 83
Figure 7.3 The schematic view of measurement holes (Sari et al., 2011). 83
Figure 7.4 The picture of measurement with fiber optic probe..... 84
Figure 7.5 A sample computational mesh generated for calculations. 86
Figure 7.6 The scaled schematic view of each bed. 86
Figure 7.7 Comparison of particle velocity and solid volume fraction profiles of three mesh sizes. 88
Figure 7.8 The speed-up graph of FLUENT on 8 HP ProLiant BL680C G5 system. 89

Figure 7.9 The effect of drag model on particle velocity distribution for experimental set 1, measurement height 100 mm. 93
Figure 7.10 The effect of drag model on solid volume fraction distribution for experimental set 1, measurement height 100 mm. 94
Figure 7.11 The effect of restitution coefficient on particle velocity distribution for experimental set 1, measurement height 100 mm. 95
Figure 7.12 The effect of restitution coefficient on solid volume fraction distribution for experimental set 1, measurement height 100 mm. 96
Figure 7.13 The effect of solid frictional stress on particle velocity distribution for experimental set 1, measurement height 100 mm. 97
Figure 7.14 The effect of solid frictional stress on solid volume fraction distribution for experimental set 1, measurement height 100 mm. 98
Figure 7.15 Contours of solid volume fraction at t= 15 s for experimental set 1. .. 99
Figure 7.16 The effect of drag model on particle velocity distribution for experimental set 2, measurement height 42 mm. 102
Figure 7.17 The effect of drag model on solid volume fraction distribution for experimental set 2, measurement height 42 mm. 103
Figure 7.18 The effect of restitution coefficient on particle velocity distribution for experimental set 2, measurement height 42 mm. 104
Figure 7.19 The effect of restitution coefficient on solid volume fraction distribution for experimental set 2, measurement height 42 mm. 105
Figure 7.20 The effect of solid frictional stress on particle velocity distribution for experimental set 2, measurement height 42 mm. 106
Figure 7.21 The effect of solid frictional stress on solid volume fraction distribution for experimental set 2, measurement height 42 mm. 107
Figure 7.22 Contours of solid volume fraction at t= 15 s for experimental set 2. 108
Figure 7.23 The effect of drag model on particle velocity distribution for experimental set 3, measurement height 42 mm. 111
Figure 7.24 The effect of drag model on solid volume fraction distribution for experimental set 3, measurement height 42 mm. 112
Figure 7.25 The effect of drag model on particle velocity distribution for experimental set 3, measurement height 80 mm. 113
Figure 7.26 The effect of drag model on solid volume fraction distribution for experimental set 3, measurement height 80 mm. 114

Figure 7.27 The effect of restitution coefficient on particle velocity distribution for experimental set 3, measurement height 42 mm. 115
Figure 7.28 The effect of restitution coefficient on solid volume fraction distribution for experimental set 3, measurement height 42 mm. 116
Figure 7.29 The effect of restitution coefficient on particle velocity distribution for experimental set 3, measurement height 80 mm. 117
Figure 7.30 The effect of restitution coefficient on solid volume fraction distribution for experimental set 3, measurement height 80 mm. 118
Figure 7.31 The effect of solid frictional stress on particle velocity distribution for experimental set 3, measurement height 42 mm. 119
Figure 7.32 The effect of solid frictional stress on solid volume fraction distribution for experimental set 3, measurement height 42 mm. 120
Figure 7.33 The effect of solid frictional stress on particle velocity distribution for experimental set 3, measurement height 80 mm. 121
Figure 7.34 The effect of solid frictional stress on solid volume fraction distribution for experimental set 3, measurement height 80 mm. 122
Figure 7.35 Contours of solid volume fraction at t=15 s for experimental set 3. . 123
Figure 7.36 The effect of restitution coefficient on particle velocity distribution for experimental set 4, measurement height 42 mm, 82 mm, and 120 mm. 127
Figure 7.37 The effect of restitution coefficient on solid volume fraction distribution for experimental set 4, measurement height 42 mm, 82 mm, and 120 mm. 128
Figure 7.38 The effect of frictional stress on particle velocity and solid volume fraction distributions for experimental set 4, measurement height 42 mm. 129
Figure 7.39 The effect of frictional stress on particle velocity and solid volume fraction distributions for experimental set 4, measurement height 82 mm. 130
Figure 7.40 The effect of frictional stress on particle velocity and solid volume fraction distributions for experimental set 4, measurement height 120 mm. 131
Figure 7.41 Contours of solid volume fraction at t=15 s for experimental set 4. . 132
Figure 7.42 The effect of drag model on particle velocity distribution for experimental set 5, measurement height 50 mm. 135
Figure 7.43 The effect of drag model on solid volume fraction distribution for experimental set 5, measurement height 50 mm. 136
Figure 7.44 The effect of restitution coefficient on particle velocity distribution for experimental set 5, measurement height 50 mm. 137

Figure 7.45 The effect of restitution coefficient on solid volume fraction distribution for experimental set 5, measurement height 50 mm. 138
Figure 7.46 The effect of solid frictional stress on particle velocity distribution for experimental set 5, measurement height 50 mm. 139
Figure 7.47 The effect of solid frictional stress on solid volume fraction distribution for experimental set 5, measurement height 50 mm. 140
Figure 7.48 Contours of solid volume fraction at t=15 s for experimental set 5. . 141
Figure 7.49 The effect of restitution coefficient on particle velocity distribution for experimental set 6, measurement height 50 mm, 93 mm. 144
Figure 7.50 The effect of restitution coefficient on solid volume fraction distribution for experimental set 6, measurement height 50 mm, 93 mm. 145
Figure 7.51 The effect of frictional stress on particle velocity and solid volume fraction distributions for experimental set 6, measurement height 50 mm. 146
Figure 7.52 The effect of frictional stress on particle velocity and solid volume fraction distributions for experimental set 6, measurement height 93 mm. 147
Figure 7.53 Contours of solid volume fraction at t=15 s for experimental set 6. . 148
Figure 7.54 The effect of magnitude of drag coefficient on particle velocity and solid volume fraction distributions for experimental set 7, measurement height 50 mm. 151
Figure 7.55 The effect of magnitude of drag coefficient on particle velocity and solid volume fraction distributions for experimental set 7, measurement height 93 mm. 152
Figure 7.56 Contours of solid volume fraction at t=15 s for experimental set 7. . 153
Figure 7.57 The gas-solid exchange coefficient comparison between Syamlal-O'Brien and Gidaspow drag models. 154
Figure 7.58 The effect of restitution coefficient on granular temperature. 155
Figure 7.59 Comparison of CFD results with experimental results for experimental set 1, measurement height 50 mm- left: Gidaspow drag model, right: Syamlal-O'Brien drag model. 158
Figure 7.60 Comparison of CFD results with experimental results for experimental set 2, measurement height 42 mm- left: Gidaspow drag model, right: Syamlal-O'Brien drag model. 160

Figure 7.61 Comparison of CFD results with experimental results for experimental set 3, measurement height 42 mm- left: Gidaspow drag model, right: Syamlal-O'Brien drag model. 161
Figure 7.62 Comparison of CFD results with experimental results for experimental set 3, measurement height 80 mm - left: Gidaspow drag model, right: Syamlal-O'Brien drag model. 162
Figure 7.63 Comparison of CFD results with experimental results for experimental set 4, measurement height 42 mm - Gidaspow drag model. 164
Figure 7.64 Comparison of CFD results with experimental results for experimental set 4, measurement height 82 mm - Gidaspow drag model. 165
Figure 7.65 Comparison of CFD results with experimental results for experimental set 4, measurement height 120 mm - Gidaspow drag model. 166
Figure 7.66 Comparison of CFD results with experimental results for experimental set 5, measurement height 50 mm - left: Gidaspow drag model, right: Syamlal-O'Brien drag model. 167
Figure 7.67 Comparison of CFD results with experimental results for experimental set 6, measurement height 50 mm - Gidaspow drag model. 169
Figure 7.68 Comparison of CFD results with experimental results for experimental set 6, measurement height 93 mm - Gidaspow drag model. 170
Figure 7.69 Comparison of CFD results with experimental results for experimental set 7, measurement height 50 mm - Gidaspow drag model. 171
Figure 7.70 Comparison of CFD results with experimental results for experimental set 7, measurement height 93 mm - Gidaspow drag model. 172
Figure 7.71 The effect of static bed height on solid volume fraction distribution. 179
Figure 7.72 The effect of static bed height on particle velocity distribution. 180
Figure 7.73 The effect of particle size on solid volume fraction distribution. 181
Figure 7.74 The effect of particle size on particle velocity distribution. 182
Figure 7.75 The effect of conic angle on solid volume fraction distribution. 183
Figure 7.76 The effect of conic angle on particle velocity distribution. 184
Figure 7.77 Change in solid volume fraction distribution with measurement height. 185
Figure 7.78 Change in particle velocity distribution with measurement height. .. 186

LIST OF TABLES

Page

Table 2.1 Specifications of first experimental HTR reactors (Nickel et al., 2002). .. 5
Table 2.2 Specifications of two HTR prototypes operated in Germany and USA. .. 5
Table 2.3 Coating parameters of TRISO particles (Hockey, 2004)..... 8
Table 2.4 Specifications of TRISO particles (Phelip, 2004). 9
Table 3.1 List of minimum fluidization velocity correlations in the literature. 20
Table 6.1 Summary of CFD simulation studies on He et al. experimental setup. . 42
Table 6.2 The experimental conditions used in He's experiments..... 44
Table 6.3 Pressure drop and computational time comparison of three mesh sizes. 45
Table 6.4 The bed pressure drop results from simulations. 48
Table 6.5 Values of radial distribution function from Equation (6.1) for different maximum packing limit values. 50
Table 6.6 Area weighted average kinetic parameters of solid phase for Gidaspow drag model (t=15.0 s). 50
Table 6.7 Area weighted average kinetic parameters of solid phase for Syamlal-O'Brien drag model (t=15.0 s). 59
Table 6.8 Simulated total pressure drop values with and without solid frictional stress for sample case e_{ss} =0.90, $\alpha_{s,max}$=0.63. 63
Table 6.9 Area weighted average kinetic parameters of solid phase for Gidaspow drag model (t=15.0 s, e_{ss} =0.90, $\alpha_{s,max}$=0.63). 63
Table 6.10 Area weighted average kinetic parameters of solid phase for Syamlal-O'Brien drag model (t=15.0 s, e_{ss} =0.90, $\alpha_{s,max}$=0.63) 63
Table 6.11 Calculated pressure drops of cases 1, 2, 3, and 4 times of the Syamlal-O'Brien drag coefficient. 69
Table 6.12 Literature review about existence of denser particle zone. 80
Table 7.1 The geometric parameters of the Sari's experimental setup. 83
Table 7.2 The definition of experimental sets. 84
Table 7.3 The description of parameters of measurements. 85
Table 7.4 Pressure drop and computational time comparison of three mesh sizes. 87

Table 7.5 The grid size values and total number of computational elements for each bed..... 87
Table 7.6 The parameters of cases used for CFD simulations..... 90
Table 7.7 Calculated bed pressure drops for experimental set 1. 91
Table 7.8 Calculated bed pressure drops for experimental set 2. 100
Table 7.9 Calculated bed pressure drops for experimental set 3. 109
Table 7.10 The percent reduction in mass of solid particles due to outflow from the bed for experimental set 4..... 124
Table 7.11 Calculated bed pressure drops for experimental set 4. 125
Table 7.12 Calculated bed pressure drops for experimental set 5. 133
Table 7.13 The percent reduction in mass of solid particles due to outflow from the bed for experimental set 6..... 142
Table 7.14 Calculated bed pressure drops for experimental set 6. 143
Table 7.15 The percent reduction in mass of solid particles due to outflow from the bed for experimental set 7..... 149
Table 7.16 The effect of magnitude of drag coefficient on bed pressure drop results for experimental set 7. 150
Table 7.17 Percent error in bed pressure drop calculations for each case..... 157
Table 7.18 The comparison of effects of model parameters on particle velocity and bed pressure drop for light and heavy particle simulations..... 176
Table 7.19 The experimental and CFD results for bed pressure drop..... 177

1 INTRODUCTION

The most distinct design feature of High Temperature Reactor fuel is multilayer functional coating. These coating layers provide barrier against fission products, act as pressure boundary, and keep the stress distributions in layers as desired. The common method to produce coating layers on top of the fuel kernels is chemical vapor deposition in vertical high temperature conical cylindrical spouted beds.

The knowledge of flow patterns and concentration distribution in spouted beds is of great interest for the design of such processing equipment since solid trajectories should fit the requirements of the coating process. In the high temperature coaters, it is nearly impossible to visually observe and monitor the coater due to opaque carbon wall of the bed and dense carbon soot inside the bed. In addition, it is also very expensive to set up and run a high-temperature surrogate coater. Given these constraints, experimental studies are generally carried out at ambient temperature.

Recognition of the lack of fundamental understanding of hydrodynamics of nuclear fuel coaters has led to an increasing interest in the utilization of computational fluid dynamics modeling. The objective of this thesis is to develop a methodology for the analysis for CFD simulations with sufficient detail necessary for spouted bed design and operating parameters.

In this thesis, basics of nuclear fuel coating, fluidization, and multiphase flow modeling are discussed. Then, computational fluid dynamics simulations of two experimental setups are performed in order to investigate hydrodynamics of conical cylindrical spouted beds and to make comparison with experimental observations. At the same time, effects of simulation and operation parameters are investigated.

Several researchers (He et al. (1994a; 1994b), San Jose et al. (1998), Wang et al. (2004), Goldschmidt et al. (2004)) performed experimental and theoretical studies on conical cylindrical spouted beds with particles of density around 2500 kg/m^3 which is less than the average density of 6000 kg/m^3 in nuclear fuel coaters. Most of these experimental works were focused on minimum spouting velocity and total

bed pressure drop and a few were interested in local solid velocity and solid concentration. In addition, very few of them investigated the effect of bed geometry (conic angle) and experimental conditions (static bed height, particle size) on hydrodynamics of conical cylindrical spouted beds (Olazar et al. (1992), He et al. (2004)). A few researchers investigated the effects of CFD simulation parameters such as maximum packing limit, restitution coefficient, drag model, and magnitude of drag coefficient on local solid velocity and concentration in conical cylindrical spouted beds (Du et al. (2006a; 2006b), Lu et al. (2004)). There is a gap in the literature, not only experimentally but also computationally, about hydrodynamics of conical cylindrical spouted beds filled with particles having higher densities.

First experimental setup used in this study is referred as He et al. experiments in the literature. It is established with collaboration of the Department of Chemical Engineering in University of British Colombia, Vancouver and the Institute of Chemical Metallurgy in Chinese Academy of Science, Beijing. He's experiments contain glass beads of 1.41 mm diameter and 2500 kg/m^3 density. There is only one bed geometry which has 60^o conic angle and the experiments are focused on the effect of inlet velocity on hydrodynamics of conical cylindrical spouted beds. Its results have been used for verification of computational fluid dynamics simulations in the literature.

The second experimental setup used in this study is referred as Sari et al. It is established in Multiphase Laboratory of Department of Mechanical Engineering in Hacettepe University, Ankara and the project was completed in 2011. Sari's experiments were performed to fill the gap in the literature about conical cylindrical spouted bed containing high density particles. Sari's experimental setup is more detailed than He's experimental setup since it contains three different bed geometries having 60, 45, and 30^o conic angles and two different particle sizes of 1.0 and 0.5 mm in diameter. The most important of all it has Zirconia particles with 6050 kg/m^3 density which is close to average density of particles in nuclear fuel coaters. Sari's experimental study is the first comprehensive experimental study measuring minimum fluidization velocity, bed pressure drop, particle velocity and concentration as well as gas mixing for conical cylindrical spouted beds filled with high density particles.

The first part of this study contains the theoretical background of multiphase flow modeling. Methods which can be used for simulations are discussed and reasons of selecting Eulerian-Eulerian model are given. Methods and parameters used for the solution of the conservation of mass and momentum equations in Eulerian-Eulerian modeling are given in Chapter 4. The effects of some of these parameters such as maximum packing limit, restitution coefficient, drag model, and magnitude of drag coefficient on flow hydrodynamics are also investigated.

Then, the details of computational fluid dynamics simulations for low and high density particle filled conical cylindrical spouted beds are discussed in Chapter 6 and 7. The effect of parallel computing for computational time reduction is also discussed.

Finally, CFD simulation results, their comparison with experimental results, comparison between low and high density particle simulations, and conclusions of this study are presented. This study is the first comprehensive CFD study in the literature about the effects of simulation and operation parameters on hydrodynamics of conical cylindrical spouted beds containing high density particles.

2 THE HIGH TEMPERATURE REACTOR FUEL

The commercial experience with gas cooled power reactors (GCRs) began in 1956, with the generation of electricity from the Calder Hall plant in United Kingdom.

The high temperature reactor (HTR) studies had started in the 1950s to improve GCR performance. HTRs utilize ceramic fuel particles surrounded by coating and dispersed in a graphite matrix, along with graphite moderator. Either prismatic type graphite moderator blocks (block type reactor), or spherical fuel elements (pebble bed reactor) are employed. Helium is used as the coolant to permit an increase in the operating temperature, and flows through coolant holes in the block type elements or through the interstices present in the pebble bed core. HTRs can operate at very high temperatures because of the absence of metal in the core and the inertness of the helium coolant. The high temperature operation improves thermodynamic efficiency and allows advanced applications such as closed-cycle gas turbine or high temperature process heat for industry. The combination of graphite core structure, ceramic fuel, and inert helium coolant increase the inherent safety of the system.

Today, Very High Temperature Reactors, as successors of the HTRs, are among the prospective designs of Generation IV Reactors selected by Generation IV International Forum (GIF) (Goethem, 2008).

2.1 The HTR History

Through the years, three experimental HTRs have been developed and successfully operated in United Kingdom, USA, and Germany as summarized in Table 2.1. Following the successful operation of these experimental reactors, two HTR prototypes were constructed in Germany (Thorium High Temperature Reactor-THTR) and USA (Fort St. Vrain). Their parameters are summarized in Table 2.2.

The HTR development programs are still under way in different countries especially in USA, Japan, Germany, South Africa, and China. Recently, Japan and China constructed and operated two experimental test reactors in 1998 and 2000.

Table 2.1 Specifications of first experimental HTR reactors (Nickel et al., 2002).

	Dragon	**Peach Bottom 1**	**AVR Pebble Bed**
Country	UK	USA	Germany
Power (MW_{th}/MW_e)	20/-	115/40	46/15
Fuel Material (coated particle)	U/Th carbide	U/Th carbide	U/Th oxide /carbide
Fuel Element Geometry	Prismatic	Cylindrical	Spherical
Coolant	Helium	Helium	Helium
Operating Pressure (MPa)	1.0	2.4	1.0
Inlet/Outlet Temperature (^oC)	350/750	345/745	270/950
Active Core Diameter/Height (m)	1.07/1.6	2.8/2.3	3.0/3.5
Operation Time	1968-1975	1967-1974	1967-1988

Table 2.2 Specifications of two HTR prototypes operated in Germany and USA.

	THTR	**Fort St. Vrain**
Country	Germany	USA
Power (MW_{th})	750/300	842/330
Fuel Material (coated particle)	U/Th carbide	U/Th carbide
Fuel Elements	spherical	Hexagonal
Coolant	Helium	Helium
Operating Pressure (MPa)	3.9	4.5
Inlet/Outlet Temperature (^oC)	270/750	405/784
Active Core Diameter/Height (m)	5.6/6.0	5.9/4.75
Operation Time	1986-1989	1976-1989

High Temperature Engineering Test Reactor (HTTR) in Japan with a thermal power of 30 MW is a research facility constructed for the development of HTR technology and nuclear heat utilization (hydrogen production system was connected to the HTTR in 2008). 4.0 MPa pressure Helium coolant has 395 ^oC inlet and 850^oC outlet temperatures (950 ^oC for high temperature test operation). It contains prismatic block type uranium dioxide fuel.

HTR-10 in China is 10 MW_{th} prototype pebble bed reactor. 3.0 MPa pressure Helium coolant has 250 ^oC inlet and 700 ^oC outlet temperatures. It is a representative of features of modular HTR design.

It is seen from the history of HTRs that even though the fuel elements of HTRs are being developed in various countries and have various shapes as seen in Figure

2.1 they have the same generic coated particles for the retention of fission products.

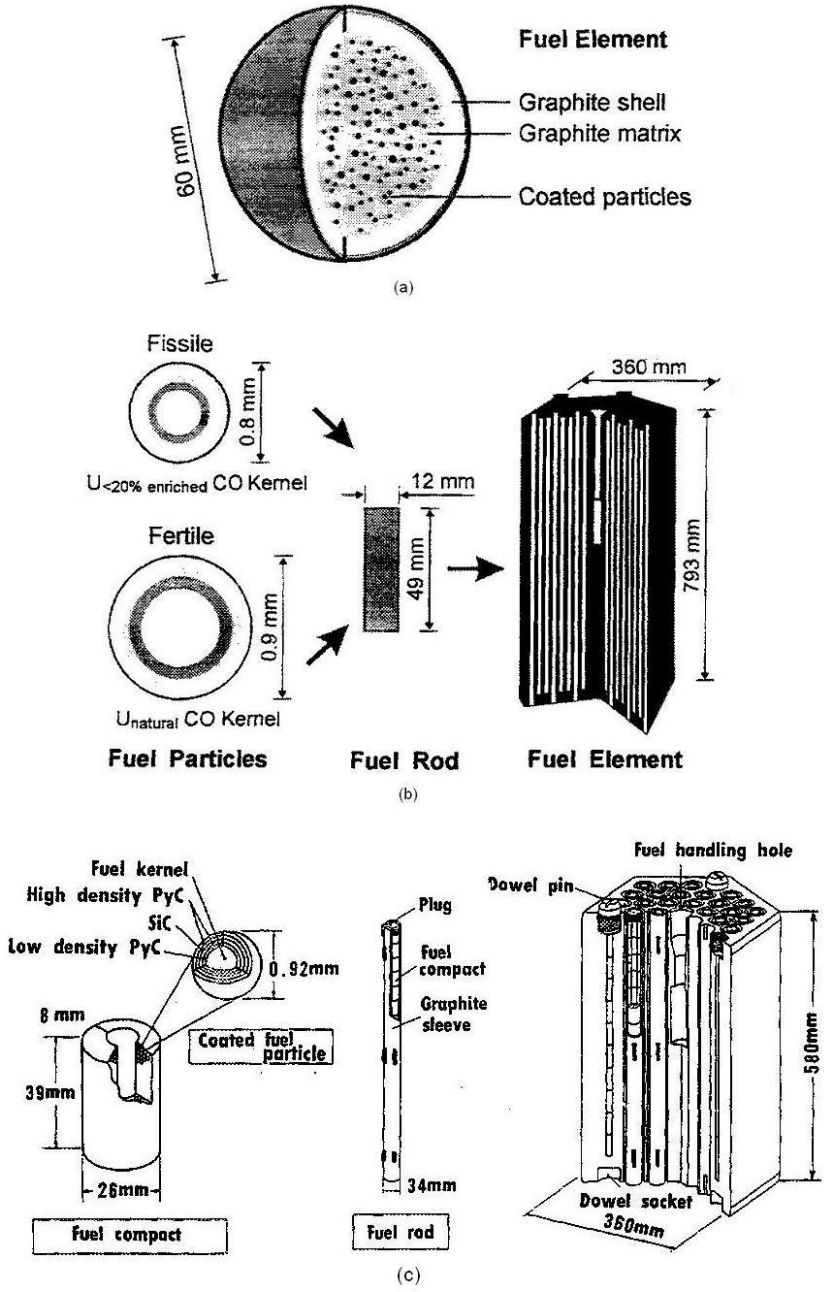

Figure 2.1 The reference design for fuel particles and fuel elements (a) Germany (b) USA (c) Japan (IAEA-TECDOC-987, 1997).

2.2 The Coated Particles

The coated particle design consists of a fuel kernel (fuel oxide, carbide or a mixture of oxide and carbide) which is surrounded by a low density pyrocarbon

layer (Buffer), a high density and isotropic inner pyrocarbon layer (IPyC), a dense silicon carbide layer (SiC), and a high density and isotropic outer pyrocarbon (OPyC) layer. This design of coated particles is called TRISO particles and is shown in Figure 2.2.

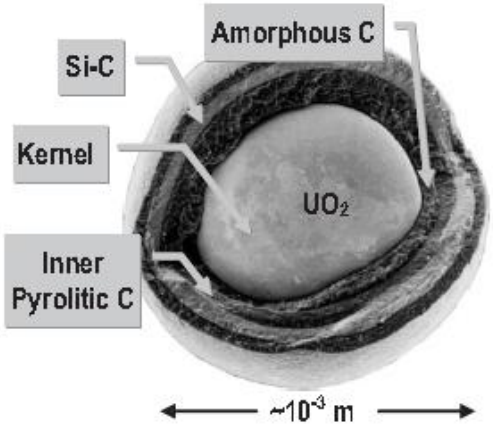

Figure 2.2 A schematic of TRISO particle (Pannala et al., 2007).

The kernels are made via traditional sol-gel processes. The process is based on the precipitation of uranyl nitrate by ammonia into ammonium diuranate (ADU). The feed solution is dispersed into droplets through a vibrating nozzle. The spherical droplets are formed in air from the effect of surface tension which is hardening the bead surface into the final shape. Then, spherical particles are aged, washed, dried, calcined, reduced, and sintered into UO_2 kernels. The picture of uranium based fuel kernels after drying and sintering is shown in Figure 2.3.

The Buffer layer, IPyC, SiC, and OPyC coatings are applied using the Chemical Vapor Deposition (CVD) in a vertical high temperature conical cylindrical fluidized bed. The CVD is a synthesis process in which the chemical constituents react in the vapor phase near or on a heated substrate to form a solid deposit.

The pyrolytic carbon layers are obtained by the cracking of hydrocarbon gases. The silicon carbide is deposited by decomposition of methyltrichlorosilane (MTS) in hydrogen. The fluidization of the kernels is ensured by inert argon flow for pyrocarbon coatings and hydrogen for silicon carbide coating. The parameters of coating process are summarized in Table 2.3.

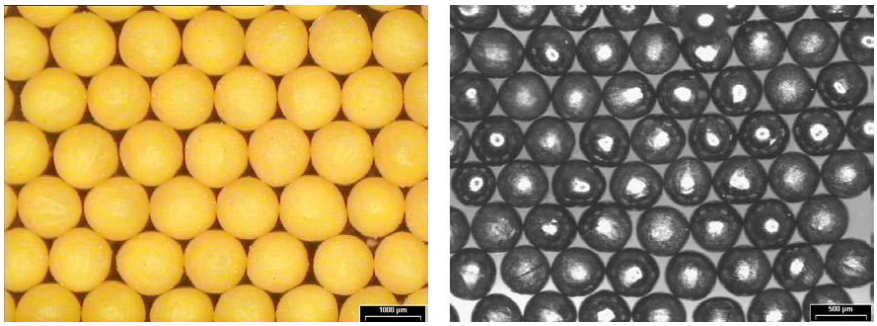

Figure 2.3 The U-based kernels after drying (left) and after sintering (right) (Charollais, 2004).

Table 2.3 Coating parameters of TRISO particles (Hockey, 2004).

Coating Layer	Diluent and Levitation Gas	Active Coating Gas	Mean Coating Rate[(a)] (μm/min)	Active Coating Gas Fraction[(b)] C/(C+L+D)	Nominal Coating Temperature[(c)]
Buffer	Ar/ Ar & He	C_2H_2	(d)	(d)	1250
IPyC	Ar	C_2H_2 & C_3H_6	≥ 3.0	0.25 - 0.35	1300
SiC	H_2	CH_3SiCl_3	≤ 0.33	0.012-0.021	1500
OPyC	Ar	C_2H_2 & C_3H_6	≥ 3.0	0.25 - 0.35	1300

[(a)] Mean coating thickness divided by coating deposition time.
[(b)] C=active coating gas flow rate to coating zone (C_2H_2 + C_3H_6 for PyC coating only), (CH_3SiCl_3 for SiC coating only).
L=levitation gas flow rate to coating zone (Ar for PyC coatings only), (H_2 for SiC coating only).
D=diluent gas flow to coating zone (Ar for PyC coatings only), (H_2 for SiC coating only).
[(c)] Normal temperature in the active coating zone of the particle bed.
[(d)] Not defined.

The low density PyC buffer layer is obtained by decomposition of acetylene (C_2H_2) at 1250^{o}C. It produces free volume for accumulation of gases from the kernel and provides accommodation for fuel swelling. The IPyC layer is obtained by decomposition of a mixture of propylene (C_3H_6) and acetylene (C_2H_2) at 1300 ^{o}C. It acts as diffusion barrier for solid fission products and protects kernel from chlorine resulted from SiC layer production. The SiC coating is obtained by decomposition of methyltrichlorosilane (MTS, CH_3SiCl_3) in a hydrogen flow at a fixed pressure at 1500 ^{o}C. It serves as the main mechanical barrier for the retention of fission products. The OPyC layer is obtained by decomposition of a mixture of propylene (C_3H_6) and acetylene (C_2H_2) at 1300 ^{o}C. It provides bonding for matrix material,

acts as barrier for gaseous fission products, and reduces the tensile stress on SiC layer. The typical parameters of TRISO particles are summarized in Table 2.4.

Table 2.4 Specifications of TRISO particles (Phelip, 2004).

Part	Parameter	Value
UO_2 Kernel	**Diameter (μm)**	500 ± 40
	Density (kg/m^3)	10,400
	Sphericity	<1.1
Coated Fuel Particle	**Buffer layer thickness (μm)**	95 ± 20
	IPyC layer thickness (μm)	40 ± 10
	SiC layer thickness (μm)	35 ± 7
	OPyC layer thickness (μm)	40 ± 10
	Buffer layer density (kg/m^3)	≤ 1050
	IPyC layer density (kg/m^3)	1850 ≤ x ≤ 2000
	SiC layer density (kg/m^3)	≥ 3180
	OPyC layer density (kg/m^3)	1850 ≤ x ≤ 2000

3 THE FLUIDIZATION

Fluidization is a process whereby a bed of solid particles is transformed into something closely resembling a fluid. This is achieved by pumping a fluid, either a gas or a liquid, upwards through the bed at a rate that is sufficient to exert a force on the particles that exactly counteracts their weight. In this way, instead of a rigid structure held in place by means of gravity derived contact forces, the bed acquires fluid like properties, free to flow and deform, with the particles able to move relatively freely with respect to one another (Gibliaro, 2001).

If a fluid is pumped upward through a bed of fine particles as shown in Figure 3.1 (a), at a low velocity, the fluid percolates through the void spaces between the stationary particles without disturbing the bed. This is a fixed bed process. In the fixed bed, the particles are in direct contact with each other therefore supporting each other's weight. The fluid flow through a bed will exert a drag force upon the particles resulting in a pressure drop across the bed.

When the fluid velocity increases, the drag force will cause particles to move apart and a few vibrate and move in restricted regions. This is an expanded bed. Due to this expansion, the particles are less resistant to the fluid flow. At the same time, the increase in the fluid's superficial velocity magnifies the pressure drop.

With the further increase in fluid velocity, a point is reached where the upward drag force exerted by the fluid on the particles is equal to the apparent weight of particles in the bed. At this point the particles are lifted by the fluid, the separation of the particles increases, and the bed becomes fluidized. This is a fluidized bed or a bed at minimum fluidization (Figure 3.1 (b)). The fluid velocity at this state of the bed is called as minimum fluidization velocity (U_{mf}).

The response of fluidized bed to further increase in fluid velocity depends on type of the fluid. In liquid fluidized beds, increase of fluid velocity beyond minimum fluidization results in smooth, progressive expansion of the bed. Due to this expansion, the bed can become much higher than its initial height. This is called a particularly fluidized bed, a homogeneously fluidized bed, or a smoothly fluidized bed (Figure 3.1(c)).

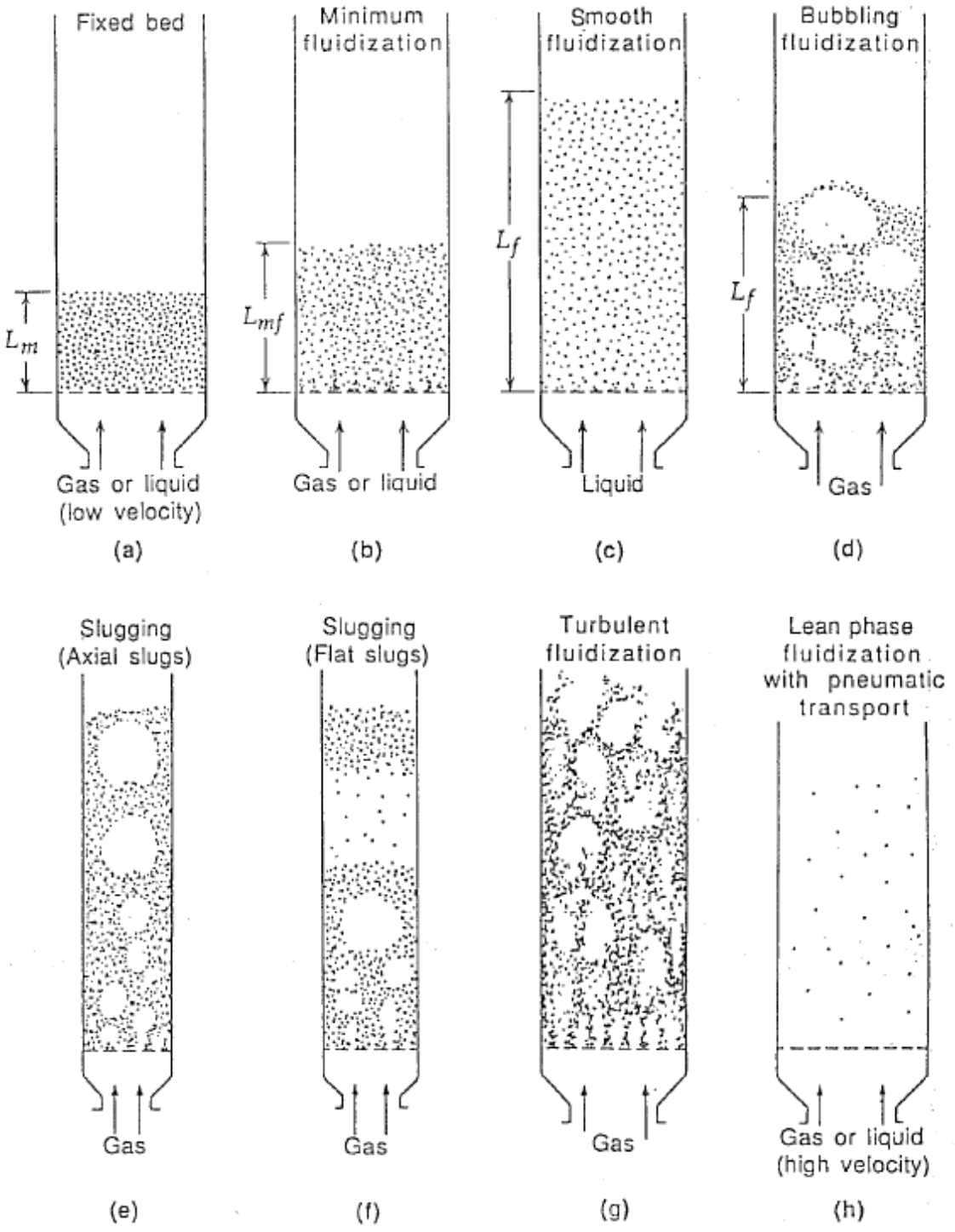

Figure 3.1 Various forms of contacting of a batch of solids by fluid (Kunii et al., 1991).

In contrast, a gas fluidized bed is heterogeneous or aggregative or bubbling in nature and its expansion is limited, unlike in a liquid fluidized bed. This is called an aggregative fluidized bed, a heterogeneous fluidized bed, or a bubbling fluidized

bed (Figure 3.1(d)). In the bubbling fluidized bed, when gas bubbles coalescence and grow as they rise, slugs occur especially in a deep and/or narrow column. In the case of fine particles, they flow smoothly down by the wall around the rising void of gas. This is called slugging with axial slugs as shown in Figure 3.1(e). For coarse particles, solids move above the gas slug like a piston, and they rain through the rising slugs as shown in Figure 3.1(f). This is called a flat slug. Here the gas–solid contact is poor. At sufficiently high gas velocity, the upper surface of the bed disappears, turbulent motion of solid clusters is observed, and voids of gas of various size and shapes occur. This is termed as turbulent fluidized bed (Figure 3.1(g)).

At very high fluid; gas or liquid; velocities (beyond the particle terminal velocity), solid particles are carried out of the bed. This is a disperse-, dilute-, or lean- phase fluidized bed with pneumatic transport of solids as seen in Figure 3.1(h).

Both gas and liquid fluidized beds are considered as dense-phase fluidized beds as long as there is a fairly clearly defined upper limit or surface of the bed. A dense-phase gas fluidized beds looks very much like a boiling liquid in many ways exhibits liquid like behavior. An example of such is shown in Figure 3.2. With fluidization, a bed that maintains an uneven surface in a fixed bed now has an even or horizontal surface. It stays horizontal even the bed tiles. A heavy object that would rest on the top of a static bed would now sink; likewise, a light object would now float. The pressure would now vary proportional to the height, like a liquid column, and any hole made on the vessel or column would allow the solid to flow like a liquid.

When gas is passed through a bed of solid particles, various types of flow regime, ranging from fixed bed to pneumatic conveying, are observed as explained above. The prevailing flow regime and quality of fluidization depend on several factors. Operating conditions, solids flow rate, gas flow rate, and system configuration affect the prevailing flow regime. In addition, the properties of solid particles (size distribution, shape, density, cohesiveness, etc.) significantly affect the quality of fluidization.

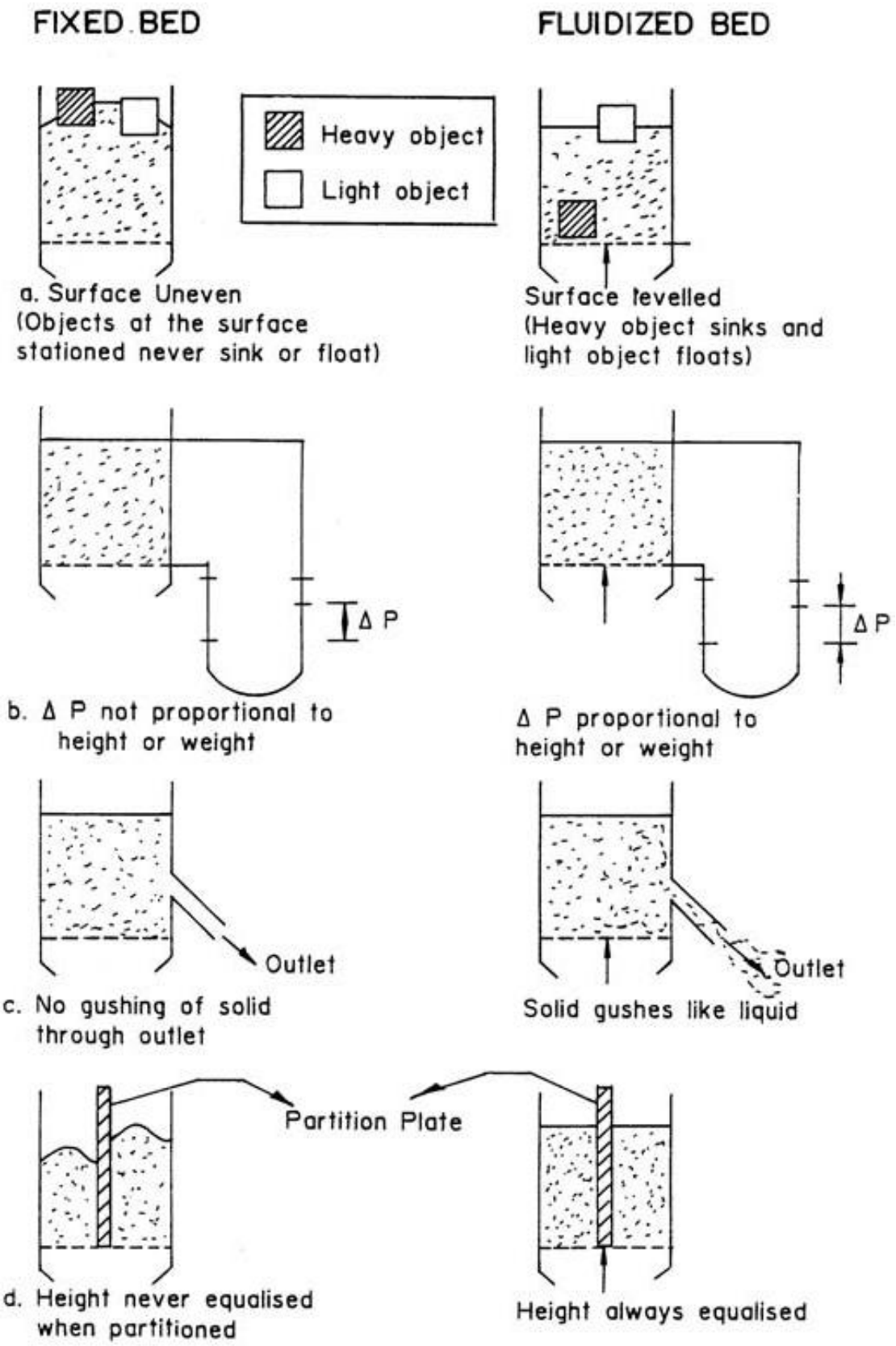

Figure 3.2 Examples of fluid like behavior of fluidized bed relative to fixed bed (Gupta et al., 1999).

Geldart, by carefully observing the fluidization of all sorts and size of solids at ambient conditions, suggested a simple, four-group classification of solids within which the range of bed behavior can be categorized based on particle density and particle size (Kunii et al., 1991). A mapping of these groups for air as fluidization fluid is shown in Figure 3.3. For any solid of known density, ρ_s, and mean particle diameter, d_p, this graph shows the type of the fluidization to be expected. The classification of Geldart groups has been well recognized and is often referred to in the literature, even though several other criteria based on similar conceptual premises (Molerus groups, Clart et.al. groups, etc.) were proposed later.

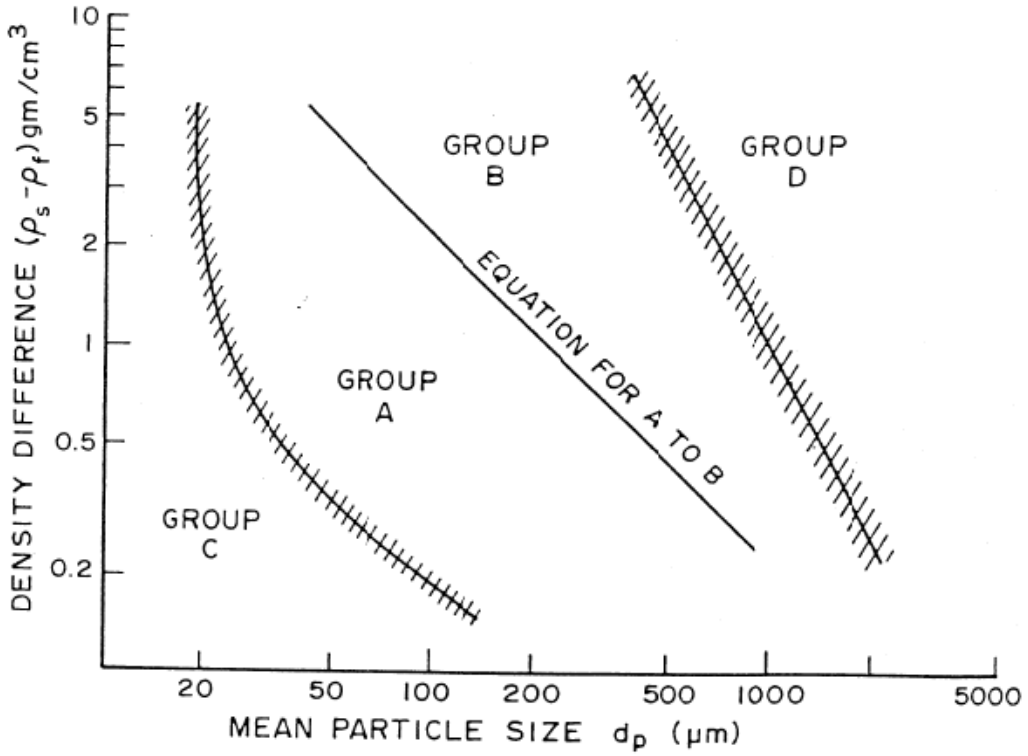

Figure 3.3 The Geldart classification of particles from air at ambient conditions (Gidaspow, 1994).

Group A: Solid particles having a small mean particle size or low particle density (<~1500 kg/m^3). Typical examples of this class are catalysts used for fluid catalytic cracking (FCC) processes. These solids fluidize easily, with smooth fluidization at low gas velocity and bubbling/turbulent fluidization at higher velocity.

Group B: Solids having particle size 40 μm < d_p< 500 μm and density in the range 1400 < ρ_s < 4000 kg/m^3. These solids fluidize vigorously with formation of bubbles, which grow in size; e.g. sand particles.

Group C: This class of solids includes very fine and cohesive powders, e.g. cement, flour, starch etc. With this class, normal fluidization is extremely difficult and channeling takes place when fluidized.

Group D: These solid particles are large and/or dense and are spoutable. Deep beds of these solids are difficult to fluidize. They behave erratically, giving large exploding bubbles, severe channeling or spouting.

Although, Geldart's classification chart often provides a useful starting point to examine fluidization quality of a specific gas–solid system, the minimum fluidization velocity is an important parameter controlling the quality of fluidization. There are experimental and theoretical methods for determining the minimum fluidization velocity. The experimental methods include pressure drop method, voidage method, and heat transfer method. The most commonly used method is pressure drop method. The voidage method is not simpler than the bed pressure drop method because the bed expansion cannot be accurately determined by any simple (i.e., visual) means and the heat transfer method is more expensive than the two aforementioned methods.

In pressure drop method, known quantity of particles is charged into the bed and the variation in bed pressure drop across a bed with fluid velocity is measured. This can be done either increasing or decreasing the fluid velocity. Resulting graph is called characteristic curve of the bed pressure drop against superficial gas velocity and a sample of it is shown in Figure 3.4. The minimum fluidizing velocity corresponds to the velocity at the point of intersection between the rising and flat portions of the characteristic curve.

The theoretical predictions can be broadly classified into four groups: dimensional analysis (Direct Correlation), drag force method, pressure drop method, and terminal velocity method. Details of these methods can be seen in (Gupta et al., 1999).

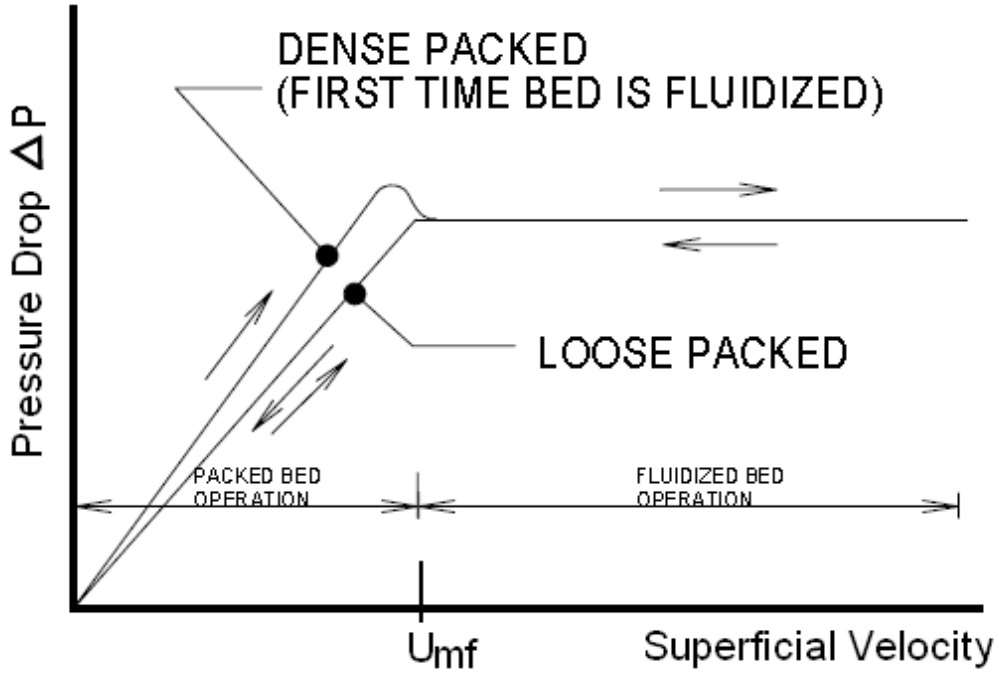

Figure 3.4 Pressure drop versus gas velocity diagram of a fluidized bed (Gupta et al., 1999).

3.1 The Spouted Bed

The spouted beds are introduced in Canada by Mathur et al. (1955) as an alternative to fluidized beds for handling coarse particles and are now widely applied in various physical operations such as treatments of wood residues including the sawdust and industrial by-products, agro-forest residues by combustion, gasification or pyrolysis, drying vegetables of different degrees of humidity and of pharmaceutical products, catalytic polymerization, burning low heating value fuels, such as liquid wastes that cannot be burned without the use of auxiliary fuels, and coating of nuclear fuel particles. In addition to their ability to handle coarse particles, the spouted beds also possess certain structural and flow characteristics that are very desirable for some chemical reaction systems. In spouted beds, the solids turnover is very high due to a high circulation rate of solids. In a spout fluid bed, particulate solids with a wide range in size from fine (micrometer) to coarse (millimeter) can be successfully brought into intimate contact with the fluidizing fluid. Geometrically, spouted beds can be cylindrical, conical, or conical-cylindrical (Figure 3.5).

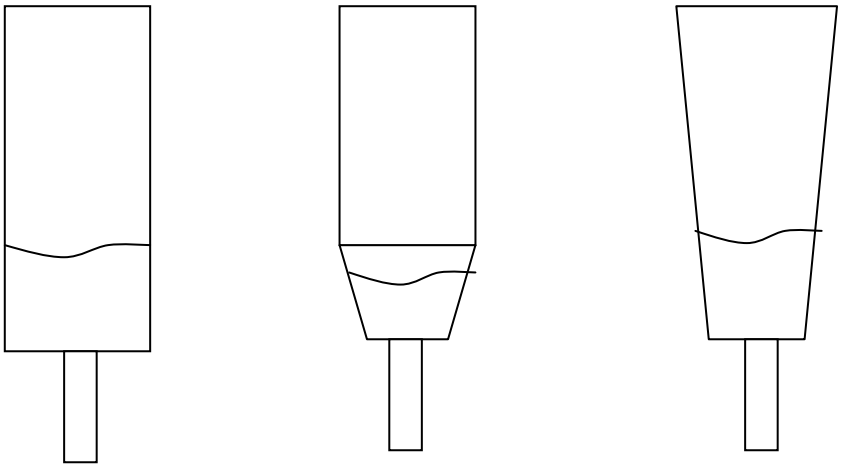

Figure 3.5 Three configurations of spouted beds: (a) cylindrical, (b) conical-cylindrical, and (c) conical.

Spouting occurs over a definite range of gas velocity for a given combination of gases, solids, and vessel geometry. Figure 3.6 illustrates schematically the transition from a fixed bed to a spouted bed, and hence often to a bubbling and a slugging bed, as gas velocity is increased.

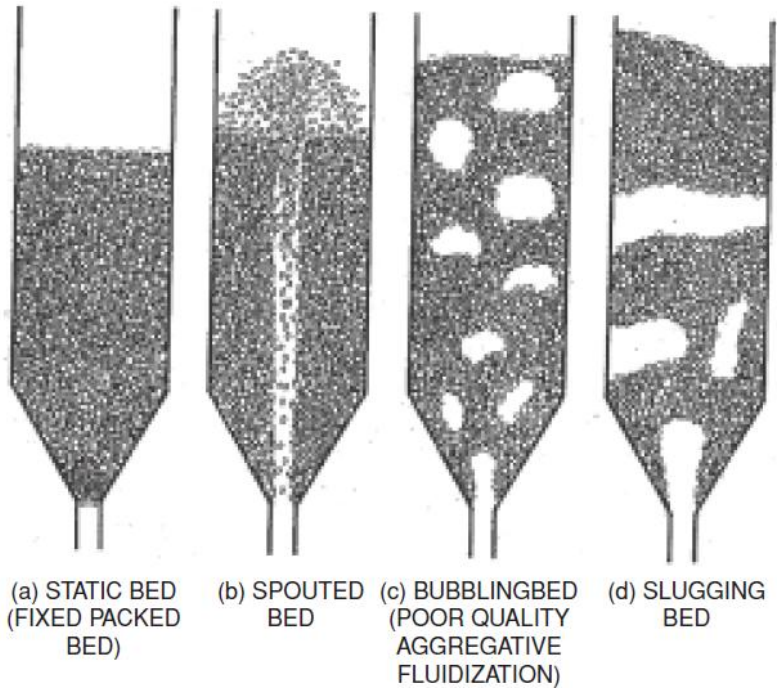

Figure 3.6 Regime transitions in spouted beds with increasing gas flow (Epstein et al., 2011).

The evaluation of spouting process is presented in Figure 3.7. When a gas is pumped up through a static bed, a cavity is formed if the fluid velocity is high enough to push the particles aside as shown in Figure 3.7 (a). The cavity expands as gas velocity increases and internal spout establishes as seen in Figure 3.7 (b). With further increase in gas velocity, the cavity reaches the upper surface of the bed and breaks as a result external spout is formed as illustrated in Figure 3.7 (c).

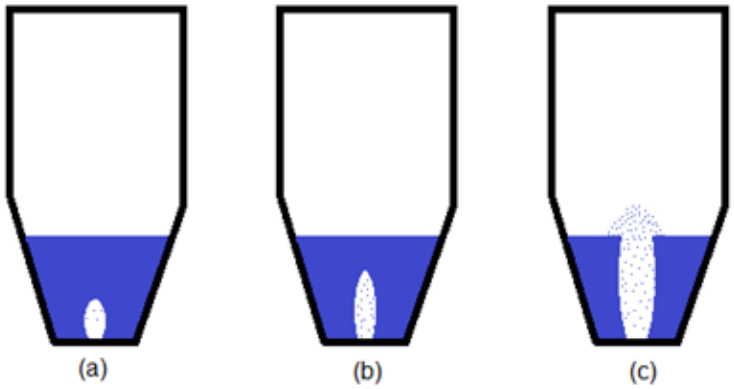

Figure 3.7 The evaluation of spouting process (a) formation of small cavity, (b) development of internal spout, (c) onset of external spout.

The solid and fluid movement in the spouted beds is seen in Figure 3.8 (a). A high-velocity spout of gas punches through bed of solids, thereby transporting particles to the top of the bed. The rest of the solids move downward slowly around the spout through gently upward percolating gas.

The experiments showed that there are well defined spout, annulus, and fountain zones in the spouted beds. When the jet flow penetrates the bed of particles, it creates a central spout zone, a fountain above the spout, and an annulus surrounding the spout as seen in Figure 3.8 (b).

The velocity corresponding to the minimum total flow required to create a fountain above the static bed at the minimum condition is called as minimum spouting velocity, U_{ms}, and the knowledge of it has a fundamental importance in the design and operation of spouted beds. The minimum spouting velocity can be determined experimentally like minimum fluidization velocity. Same experimental pressure drop technique can be used for the measurement of the minimum spouting velocity. Several correlations in the literature that are derived from experiments for

minimum spouting velocity are given in Table 3.1. The geometric parameters in these correlations are shown in Figure 3.9. The Re_{ms} is the minimum spouting Reynolds number defined according to gas inlet diameter D_o and *Ar* is the Archimedes number ($Ar = g\rho_g(\rho_s - \rho_g)d_s^3/\mu_g^2$). It should be noted that the applicability of each correlation depends on the bed geometry, particle size, particle density, and other geometrical factors.

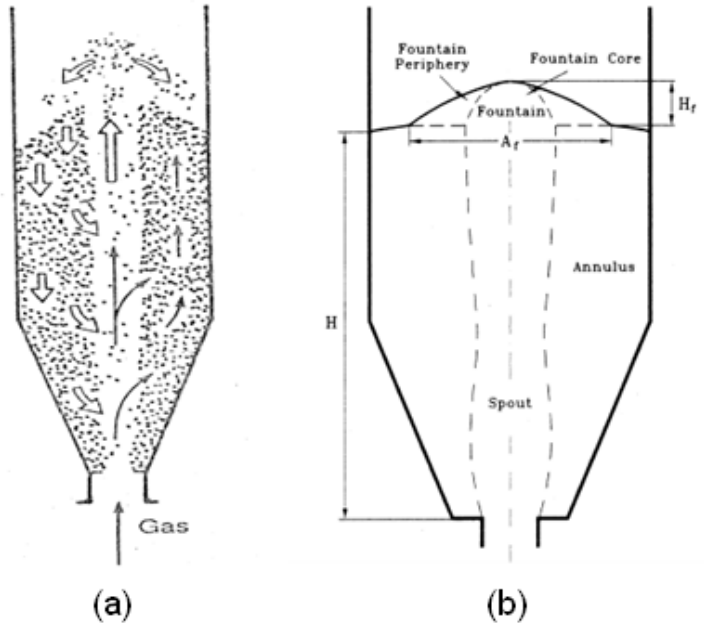

Figure 3.8 Schematic view of spouted beds. (a) (Kunii et al., 1991), (b) (Olazar et al., 2004).

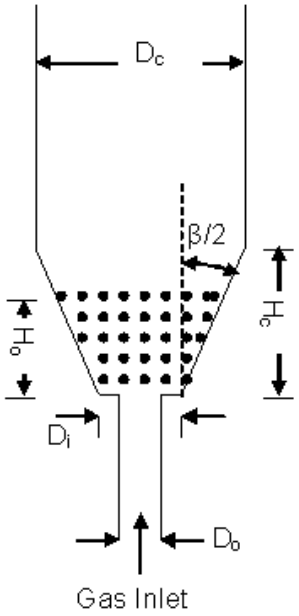

Figure 3.9 The geometric parameters of the spouted beds.

Table 3.1 List of minimum fluidization velocity correlations in the literature.

Researcher	Correlation	
Mathur and Gishler (San Jose et al., 2001)	$U_{ms} = \left(\frac{d_s}{D_c}\right)\left(\frac{D_o}{D_c}\right)^{1/3}\left[\frac{2gH_o(\rho_s-\rho_g)}{\rho_g}\right]^{0.5}$	(3.1)
Bi et al. (Jing et al., 2000)	$Re_{ms} = 0.202\left[Ar\left(\frac{D_b}{D_i}\right)\left(\frac{(D_b/D_i)^2+(D_b/D_i)+1}{3}\right)\right]^{0.5} for\ \frac{D_b}{D_o} < 1.66$	(3.2)
Bi et al. (Bi et al., 1997)	$Re_{ms} = \left[0.30 - 0.27\left(\frac{D_i}{D_b}\right)^2\right]\left[Ar\left(\frac{D_b}{D_i}\right)\left(\frac{(D_b/D_i)^2+(D_b/D_i)+1}{3}\right)\right]^{0.5} for\ \frac{D_b}{D_o} \geq 1.66$	(3.3)
Olazar et al. (Duarte et al., 2009)	$Re_{ms} = \left(\frac{D_o}{D_c}\right)^2\left[0.126Ar^{0.5}\left(\frac{D_c}{D_o}\right)^{1.68} tan\left(\frac{\beta}{2}\right)\right] + \left(\frac{d_s}{D_c}\right)\left(\frac{D_o}{D_c}\right)\left[\frac{2g(H-H_c)(\rho_s-\rho_g)}{\rho_g}\right]^{0.5}$	(3.4)
Ogino et al. (Duarte et al., 2009)	$U_{ms} = 0.0151\left(\frac{\alpha_g^4}{2(1-\alpha_g)}\right)^{0.5}(1-\alpha_g)^{0.25}Ar^{0.25}\left(\frac{d_s}{D_c}\right)\left(\frac{D_c}{D_o}\right)^{1/3}\left(\frac{2gH_o(\rho_s-\rho_g)}{\rho_g}\right)^{0.5}$	(3.5)
Nikolaev and Golubev (Olazar et al., 1992)	$Re_{ms} = 0.051Ar^{0.59}\left(\frac{\mathrm{D_o}}{\mathrm{D_c}}\right)^{0.1}\left(\frac{\mathrm{H_o}}{\mathrm{D_c}}\right)^{0.25}$	(3.6)
Gorshtein and Mukhlenov (Bi, 2004)	$Re_{ms} = 0.17Ar^{0.5}\left[1 + 2\tan\left(\frac{\beta}{2}\right)\left(\frac{\mathrm{H_o}}{\mathrm{D_o}}\right)\right]^{0.25}\left(\tan\left(\frac{\beta}{2}\right)\right)^{-1.25}$	(3.7)
Tsvik et al. (Olazar et al., 1992)	$Re_{ms} = 0.4Ar^{0.52}\left(\frac{\mathrm{H_o}}{\mathrm{D_o}}\right)^{1.24}\left(\tan\left(\frac{\beta}{2}\right)\right)^{0.42}$	(3.8)
Goltsiker (Olazar et al., 1992)	$Re_{ms} = 73Ar^{0.14}\left(\frac{\mathrm{H_o}}{\mathrm{D_o}}\right)^{0.9}\left(\frac{\rho_s}{\rho_g}\right)^{0.47}$	(3.9)
Markowski and Kaminski (Olazar et al., 1992)	$Re_{ms} = 0.028Ar^{0.57}\left(\frac{\mathrm{H_o}}{\mathrm{D_o}}\right)^{0.48}\left(\frac{\mathrm{D_c}}{\mathrm{D_o}}\right)^{1.27}$	(3.10)
Choi and Meisen (Salam et al., 2006)	$U_{ms} = 18.5(2gH_o)^{0.5}\left(\frac{d_s}{D_c}\right)^{1.19}\left(\frac{D_o}{D_c}\right)^{0.373}\left(\frac{H_o}{D_c}\right)^{-0.193}\left[\frac{(\rho_s-\rho_g)}{\rho_g}\right]^{0.263}$	(3.11)

Table 3.1 cont.

Researcher	Correlation	
Wu et al. (Salam et al., 2006)	$U_{ms} = 10.6(2gH_o)^{0.5}\left(\frac{d_s}{D_c}\right)^{1.05}\left(\frac{D_o}{D_c}\right)^{0.266}\left(\frac{H_o}{D_c}\right)^{-0.095}\left[\frac{(\rho_s-\rho_g)}{\rho_g}\right]^{0.256}$	(3.12)
Uemaki et al. (Salam et al., 2006)	$U_{ms} = 0.977\left(\frac{d_s}{D_c}\right)^{0.615}\left(\frac{D_o}{D_c}\right)^{0.274}\left[\frac{2gH_o(\rho_s-\rho_g)}{\rho_g}\right]^{0.324}$	(3.13)
Smith and Reddy (Venkatachalam et al., 2009)	$U_{ms} = \left[\frac{d_s(0.95-152{D_o}^2)}{(2H_o)^{3.52D_o}}\right]\left[\frac{2gH_o(\rho_s-\rho_g)}{\rho_g}\right]^{0.5}$	(3.14)
Brunello et al. (Venkatachalam et al., 2009)	$U_{ms} = 0.0143{D_o}^{0.741}{H_o}^{0.592}\left[\frac{2gH_o(\rho_s-\rho_g)}{\rho_g}\right]^{0.5}$	(3.15)
Murthy and Singh (Venkatachalam et al., 2009)	$U_{ms} = 1.4\left(\frac{d_s}{D_c}\right)\left(\frac{D_o}{D_c}\right)^{0.125}\left[\frac{2g(\rho_s-\rho_g)}{\rho_g}\right]^{0.5}$	(3.16)
Anabtawi (Venkatachalam et al., 2009)	$U_{ms} = 0.25\left(\frac{d_s}{D_c}\right)^{0.65}\left(\frac{D_o}{D_c}\right)^{0.312}\left(\frac{H_o}{D_c}\right)^{0.254}\left[\frac{2gH_o(\rho_s-\rho_g)}{\rho_g}\right]^{0.5}$	(3.17)
Mukhlenov and Gorsthein (Bi, 2004)	$Re_{ms} = 3.32Ar^{0.33}\left(\frac{\mathrm{H_o}}{\mathrm{D_o}}\right)\left(\tan\left(\frac{\beta}{2}\right)\right)^{0.5}$	(3.18)
Fane and Mitchell (Bi, 2004)	$U_{ms} = 2.0D_c^{1-exp(-7D_c^2)}\left(\frac{d_s}{D_c}\right)\left(\frac{D_o}{D_c}\right)^{1/3}\left[\frac{2gH_o(\rho_s-\rho_g)}{\rho_g}\right]^{0.5}$	(3.19)

4 THE MULTIPHASE FLOW MODELING

Multiphase flow occurs in many operations in the chemical, petroleum, and power generation industries. These industries cover a wide range, from very large-scale operations such as fluid catalytic cracking operations, to specialized operations to produce high value, low volume specialty chemicals.

There are three main approaches for modeling multiphase flows:

(a) Eulerian framework for both phases with reformulation of interface forces on volumetric basis- Volume of Fluid Approach (Figure 4.1 (a)).

(b) Eulerian framework for continuous phase and Lagrangian framework for all the dispersed phases- Eulerian-Lagrangian Approach (Figure 4.1 (b)).

(c) Eulerian framework for all phases- Eulerian-Eulerian Approach (Figure 4.1 (c)).

In the volume of fluid (VOF) approach, the motion of all phases is modeled by formulating local, instantaneous conservation equations for mass, momentum, and energy. Such local instantaneous conservation equations can be solved using appropriate jump boundary conditions at the interface. The VOF approach tracks motion of all the phases, from which motion of the interface is inferred indirectly. All the interfacial forces, therefore, have to be replaced by smoothly varying volumetric forces. If the shape and flow processes occurring near the interface are of interest, the VOF approach should be used. This approach is, however, naturally limited to modeling the motion of only a few dispersed phase particles. For simulations of dispersed multiphase flows containing a large number of dispersed phase particles in large equipment, this approach is not suitable, as it requires huge computational resources to resolve flow processes around each dispersed phase particle.

In the Eulerian–Lagrangian approach, explicit motion of the interface is not modeled. This means small-scale fluid motions around individual dispersed phase particles are not considered. Their influence is modeled indirectly while considering the motion of dispersed phase particles. In this approach, motion of the continuous phase is modeled using an Eulerian framework and the motions of dispersed phase particles (trajectories) are explicitly simulated in a Lagrangian

framework. Trajectories of dispersed phase particles are simulated by solving the Newton's equation of motion for each dispersed phase particle.

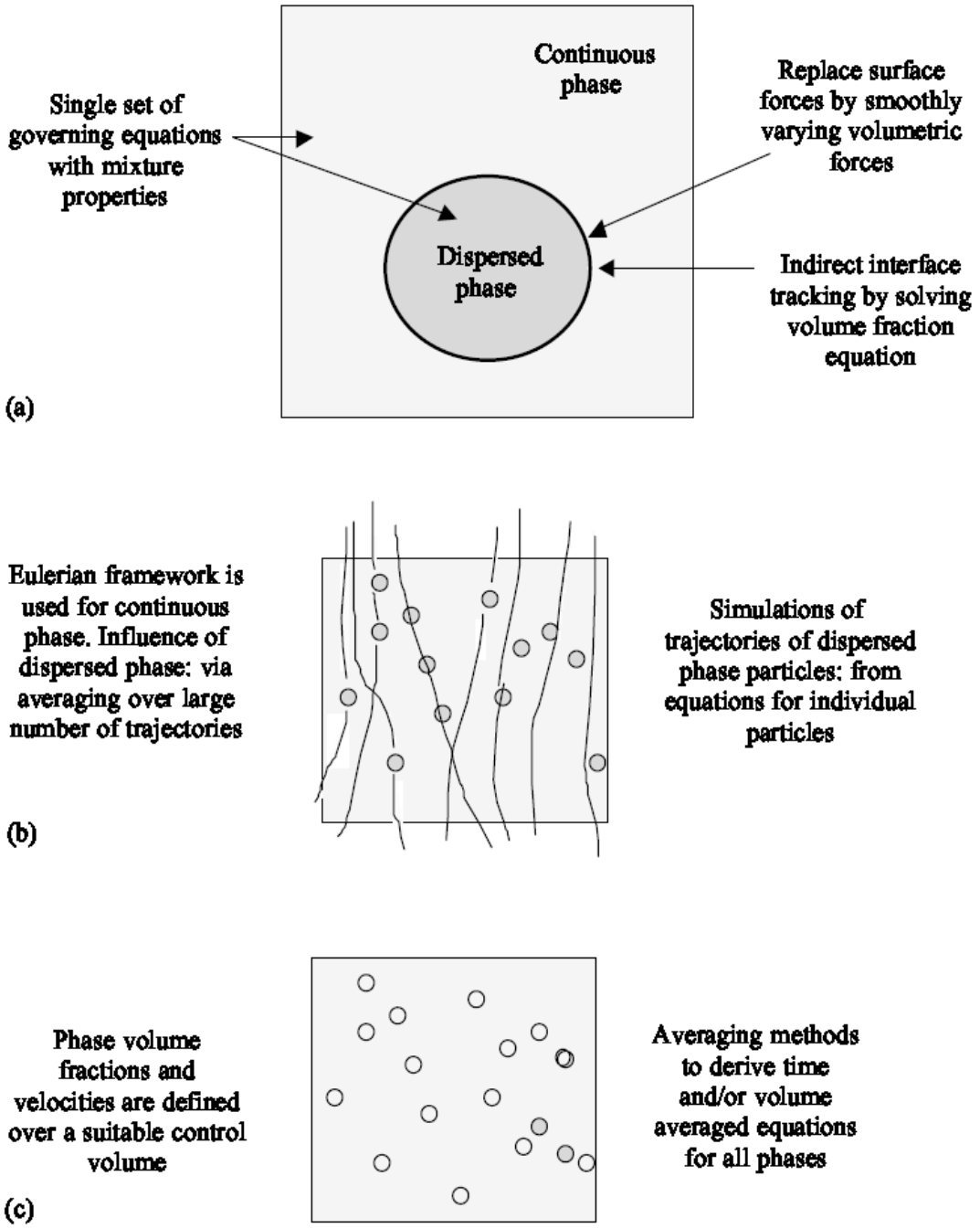

Figure 4.1 Modeling approaches for multiphase flows; (a) Volume of fluid approach, (b) Eulerian-Lagrangian approach (c) Eulerian-Eulerian approach (Ranade, 2002).

Averaging over a large number of trajectories is then carried out to derive the required information for the modeling of the continuous phase. In this approach, particle-level processes such as reactions, heat and mass transfer etc. can be simulated in adequate detail. In the case of turbulent flows, it is necessary to simulate a very large number of particle trajectories to obtain meaningful averages. Therefore, even with this approach, when the number of particles to be simulated increases, the computational resources becomes stretched. This approach is, therefore, suitable for simulating dispersed multiphase flows containing a low (<10%) volume fraction of the dispersed phases (Ferziger et al., 2002). Several attempts have been made to simulate a large number of dispersed phase particles simultaneously by using hard sphere approach, soft sphere approach or Monte Carlo techniques.

The Eulerian–Eulerian approach models the flow of all phases in an Eulerian framework based on the interpenetrating continuum assumption. In this approach, trajectory simulations and averaging are not carried out at a computational level but are implicitly achieved at a conceptual level. The discrete character of the underlying process is, therefore, averaged out to provide a model involving a continuum associated with the dispersed phase particles. Various averaging issues will have to be addressed while formulating the governing equations in this approach. If modeled successfully, this approach can be applied to multiphase flow processes containing large volume fractions of dispersed phase (Goldschmidt et al., 2004). It may, therefore, be extended to modeling and simulation of complex industrial multiphase reactors consisting of a large number of dispersed particles.

4.1 The Eulerian-Eulerian Approach

In the Eulerian-Eulerian approach, the two phases are mathematically treated as interpenetrating continua. This continuum representation of the solid phase requires additional closure laws to describe the rheology of the fluidized particles. These closure laws are based on kinetic theory for granular flows. A model to predict the granular viscosity and stress is developed and the concept of granular temperature as a measure of the agitation of particles is introduced. Granular temperature provides a link between kinetic theory and traditional fluid mechanics. A full derivation of the theory equations can be found in Gidaspow (1994).

The derivation of Eulerian-Eulerian model is based on a time-averaging procedure applied to the balance of a quantity (mass, momentum, energy) in a unit volume of a continuum for each phase.

Each phase is represented by a phasic volume fraction since the volume of a phase cannot be occupied by other phases. These volume fractions are assumed to be continuous function of space and time and their sum is equal to 1 as shown in Equation (4.1).

$$\sum_{k=1}^{n} \alpha_k = 1.0 \tag{4.1}$$

where α_k is volume fraction of phase k (k=g for gas, s for solid phase).

4.1.1 Conservation equations

Since the subject of this thesis is about gas-solid multiphase flow, the fluid phase is referred as gas phase throughout the equations given in this section. In the formulations, the mass and heat generation due to chemical reactions and radiative heat transfer phenomena are neglected. Energy conservation equations of phases are not given here because energy transfer is not the subject of this study.

4.1.1.1 Conservation of mass

Gas Phase:

$$\frac{\partial}{\partial t}\left(\alpha_g \rho_g\right) + \nabla \cdot \left(\alpha_g \rho_g \vec{u}_g\right) = 0 \tag{4.2}$$

Solid Phase:

$$\frac{\partial}{\partial t}(\alpha_s \rho_s) + \nabla \cdot (\alpha_s \rho_s \vec{u}_s) = 0 \tag{4.3}$$

where α , ρ , and $\vec{u}$ represents volume fraction, density, and velocity.

The first term on the left-hand side of Equations (4.2) and (4.3) accounts for the rate of mass accumulation per unit volume and the second term is the net rate of convective mass flux.

4.1.1.2 Conservation of momentum

Gas Phase:

$$\frac{\partial}{\partial t}\left(\alpha_g \rho_g \vec{u}_g\right) + \nabla \cdot \left(\alpha_g \rho_g \vec{u}_g \vec{u}_g\right) = -\alpha_g \nabla p + \nabla \cdot \bar{\bar{\tau}}_g + \alpha_g \rho_g \vec{g} + K_{gs}\left(\vec{u}_g - \vec{u}_s\right) \tag{4.4}$$

Solid Phase:

$$\frac{\partial}{\partial t}\left(\alpha_s \rho_s \vec{u}_s\right) + \nabla \cdot \left(\alpha_s \rho_s \vec{u}_s \vec{u}_s\right) = -\alpha_s \nabla p + \nabla \cdot \bar{\bar{\tau}}_s + \alpha_s \rho_s \vec{g} + K_{gs}\left(\vec{u}_s - \vec{u}_g\right) - \nabla p_s \tag{4.5}$$

where p is pressure shared by all phases, $\bar{\bar{\tau}}_g$ and $\bar{\bar{\tau}}_s$ are the gas and solid phase stress tensors, $\vec{g}$ is the gravitational acceleration, K_{gs} is gas-solid momentum exchange coefficient, and p_s is the solid phase pressure.

The first term on the left hand side of Equations (4.4) and (4.5) represents the rate of increase in momentum per unit volume. The second term represents change in momentum per unit volume due to convection. The first term on the right hand side represents the phase pressure force per unit volume, the second term is the viscous force per unit volume, the third term is the gravitational force per unit volume, and the fourth term represents the gas-solid interaction force per unit volume. There is an additional solid phase pressure force per unit volume term in Equation (4.5).

4.1.2 The closure equations

The fundamental conversation equations of mass and momentum cannot be solved directly in the Eulerian-Eulerian approach. Supplementary equations are needed for several of the terms. These supplementary equations are known as closure equations. Some of these equations are defined by empirical correlations and some are defined by using kinetic theory of granular flow.

4.1.2.1 The solid-gas momentum exchange coefficient

The momentum transfer between the fluid and the solid phases is usually obtained experimentally from pressure drop measurements. Hence, there are several correlations available in the literature. A review of some of these empirical correlations and their applicability can be found in (Gryczka et al., 2009,

Benyahnia et al., 2005, Du et al. 2006a). Only the ones used in this study are summarized here.

Ergun (Hoef et al., 2004) suggested Equation (4.6) based on experimental data for the pressure drop over fixed dense beds of mono-disperse particles.

$$K_{gs} = 150\frac{\alpha_s(1-\alpha_g)\mu_g}{\alpha_g {d_s}^2} + 1.75\frac{\rho_g \alpha_s |\vec{u}_s - \vec{u}_g|}{d_s}, \qquad \alpha_g < 0.8 \tag{4.6}$$

where ρ_g, μ_g, and $\vec{u}_g$ are the density, viscosity, and velocity of the gas phase and d_s is diameter of solid particles.

However, as this equation is solely valid for voidage lower than 0.8. Wen and Yu (Chiesa et al., 2005) developed Equation (4.7) where voidage is in the range 0.37 to 0.9. It is recommended for dilute systems.

$$K_{gs} = \frac{3}{4} C_D \frac{\alpha_s \alpha_g \rho_g |\vec{u}_s - \vec{u}_g|}{d_s} \alpha_g^{-2.65}, \tag{4.7}$$

$$C_D = \begin{cases} \frac{24}{\alpha_g Re_s}\left[1 + 0.15(\alpha_g Re_s)^{0.687}\right], & Re_s < 1000 \\ 0.44, & Re_s \geq 1000 \end{cases} \tag{4.8}$$

$$Re_s = \frac{\rho_g d_s |\vec{u}_s - \vec{u}_g|}{\mu_g} \tag{4.9}$$

where Re_s is particle Reynolds number, and C_D is drag coefficient.

Syamlal and O'Brien proposed a new drag model given in Equation (4.10) based on measurements of terminal velocity of particles in fluidized beds (Wachem et al., 2000).

$$K_{gs} = \frac{3}{4} C_D \frac{\alpha_s \alpha_g \rho_g}{\vartheta_{r,s}^2 d_s}\left(\frac{Re_s}{\vartheta_{r,s}}\right)(\vec{u}_s - \vec{u}_g), \tag{4.10}$$

$$C_D = \left[0.63 + \frac{4.8}{\sqrt{Re_s/\vartheta_{r,s}}}\right]^2, \tag{4.11}$$

$$\vartheta_{r,s} = 0.5\left(A - 0.06Re_s + \sqrt{(0.06Re_s)^2 + 0.12Re_s(2B - A) + A^2}\right), \tag{4.12}$$

$$A = \alpha_g^{4.14},$$
$$B = \begin{cases} 0.8\alpha_g^{1.28}, & for\ \alpha_g \leq 0.85 \\ \alpha_g^{2.65}, & for\ \alpha_g > 0.85 \end{cases} \tag{4.13}$$

where $\upsilon_{r,s}$ is terminal velocity .

Although Wen and Yu used experimental data to correct the solid-gas momentum exchange coefficient for voidage larger than 0.8, Gidaspow (Cooper et al., 2005) suggested Equation (4.14) that uses the Ergun Equation for voidage smaller than 0.8, and Wen and Yu equation for voidage larger than 0.8. This model is preferred for densely packed fluidized beds.

$$for\ \alpha_g \geq 0.8, \qquad K_{gs} = \frac{3}{4} C_D \frac{\alpha_s \alpha_g \rho_g \left|\vec{u}_s - \vec{u}_g\right|}{d_s} \alpha_g^{-2.65}, \tag{4.14}$$

$$C_{D=} \frac{24}{\alpha_g Re_s}\left[1 + 0.15\left(\alpha_g Re_s\right)^{0.687}\right] \tag{4.15}$$

$$for\ \alpha_g\ < 0.8, \qquad K_{gs} = 150 \frac{\alpha_s(1-\alpha_g)\mu_g}{\alpha_g d_s^2} + 1.75 \frac{\rho_g \alpha_s \left|\vec{u}_s - \vec{u}_g\right|}{d_s} \tag{4.16}$$

The effect of Syamlal-O'Brien drag model and Gidaspow drag model on hydrodynamics of conical cylindrical spouted beds filled with low and high density particles is compared in this study.

4.1.3 Kinetic theory of granular flow

The kinetic theory of granular flow is based on similarities between the flow of a granular material, a population of particles with or without interstitial gas, and the molecules of gas. This treatment uses classical results from the kinetic theory of gases to predict the form of transport equations for a granular material.

According to this theory, the velocity of particles after the collision is decomposed into two components: a mean velocity - $\vec{u}_{s,mean}$ and a superimposed fluctuating random velocity - $\vec{u}_s'$ as shown in Equation (4.17).

This fluctuating velocity results in a kinetic energy which is quantified by granular temperature - θ_s. Granular temperature given in Equation (4.18) is a measure of the kinetic energy contained in the fluctuating velocity of particles. The solid phase stresses, hence the solid phase viscosity and pressure can be directly related to the granular temperature similar to the relation of molecular viscosity to thermodynamic temperature in kinetic theory of gases.

$$\vec{u}_s = \vec{u}_{s,mean} \pm \vec{u}'_s \tag{4.17}$$

$$\frac{2}{3}\theta_s = (\vec{u}'_s \cdot \vec{u}'_s) \tag{4.18}$$

$$\frac{3}{2}\left[\frac{\partial}{\partial t}(\alpha_s \rho_s \theta_s) + \nabla \cdot (\alpha_s \rho_s \vec{u}_s \theta_s)\right] = \left(-p_s \bar{\bar{I}} + \bar{\bar{\tau}}_s\right) : \nabla \vec{u}_s + \nabla \cdot \left(k_{\theta_s} \nabla \theta_s\right) - \gamma_{\theta_s} + \phi_{gs} \tag{4.19}$$

where k_{θ_s} is granular temperature conductivity, γ_{θ_s} is the dissipation of granular energy due to inelastic collisions, and ϕ_{gs} is the energy exchange between the solid and gas phases.

The first term on the left hand side of Equation (4.19) represents the rate of change of granular energy, the second term is the granular energy due to convection. The first term on the right hand side is the generation of granular energy by solid stress tensor, the second term expresses the diffusion of granular energy, the third term stands for collisional dissipation of energy, and the fourth term is the energy exchange between the solid and gas phases.

Rather than solving the complete granular energy balance equation given in Equation (4.19), it is often assumed that granular energy is in steady state and dissipates locally therefore it is possible to neglect convection and diffusion (Fluent, 2006). Retaining only the generation and dissipation terms, Equation (4.19) simplifies to an algebraic relation as seen in Equation (4.20).

$$0 = \left(-p_s \bar{\bar{I}} + \bar{\bar{\tau}}_s\right) : \nabla \vec{u}_s - \gamma_{\theta_s} \tag{4.20}$$

Wachem et al. (2001) concluded that simplifying the granular energy balance by neglecting convection and diffusion is a reasonable assumption for fluidized bed

modeling and reduces the computational effort by about 20%. Therefore, throughout this study, algebraic relation for granular energy is used.

There are number of unknown quantities like solid pressure, solid stress tensor, and energy flux that must be expressed in terms of the basic hydrodynamic variables e.g. density, velocity, and temperature in order to get a closed set of equations. Therefore, new parameters like restitution coefficient, radial distribution function, and maximum packing limit are introduced.

The restitution coefficient, e_{ss}, is a measure of the elasticity of the collision between two particle, and relates to how much of the kinetic energy of the colliding particles before the collision remains after the collision. A perfectly elastic collision has a coefficient of restitution of 1 which means particle does not lose its kinetic energy after the collision. A perfectly plastic, or inelastic, collision has a coefficient of restitution of 0 which means particles stick together. Different values of restitution coefficient (0.95, 0.90, and 0.80) are used in this study to examine the effect of it on hydrodynamics of conical cylindrical spouted beds.

The radial distribution function, g_0, can be interpreted as the probability of a particle touching another particle. It is a correction factor that modifies the probability of collisions between particles when the solid granular phase becomes dense. The Lun et al. (Fluent, 2006) expression given in Equation (4.21) is used in this study.

$$g_0 = \left[1 - \left(\frac{\alpha_s}{\alpha_{s,max}}\right)^{1/3}\right]^{-1} \tag{4.21}$$

The maximum packing limit, $\alpha_{s,max}$, is used for the control of solid volume fraction to check whether the granular flow is compressible or incompressible. When solids volume fraction is less than maximum packing limit, the granular flow is compressible where the spacing between the solid particles can continue to decrease. When solid volume fraction reaches the maximum packing limit value no further decrease in the spacing can occur therefore the flow is now incompressible. For mono-dispersed spheres, maximum packing limit is about 0.63. Different values of maximum packing limit (0.63, 0.61, and 0.59) are used in

this study to examine the effect of it on hydrodynamics of conical cylindrical spouted beds.

4.1.3.1 The dissipation of granular energy

Due to inelastic collisions of particles dissipation of granular temperature occurs. It is represented by Lun et al. (Fluent, 2006) expression given in Equation (4.22).

$$\gamma_{\theta_s} = \frac{12(1-e_{ss}^2)g_0}{d_s\sqrt{\pi}}\rho_s\alpha_s^2\theta_s^{3/2} \tag{4.22}$$

4.1.3.2 The solid phase stress tensor

In order to use momentum conservation equation to calculate the velocity field, it is necessary to express the viscous stress in terms of velocity field. The equations which relate the stress tensor to the motion of the continuous fluid are called constitutive equations or rheological equations of state. The gas and solid phase stresses are expressed as

$$\bar{\bar{\tau}}_g = \mu_g\left[\nabla\vec{u}_g + \left(\nabla\vec{u}_g\right)^{\mathrm{T}}\right] \tag{4.23}$$

$$\bar{\bar{\tau}}_s = \left(\lambda_s - \frac{2}{3}\mu_s\right)\nabla\cdot\vec{u}_s\bar{\bar{I}} + \mu_s[\nabla\vec{u}_s + (\nabla\vec{u}_s)^{\mathrm{T}}] \tag{4.24}$$

where μ_s and μ_g are shear viscosity of solid and gas phases, λ_s is bulk viscosity of solid phase, and $\bar{\bar{I}}$ is the unit tensor.

The shear viscosity represents the tangential force arising due to particle collisions. It is usually expressed as the combination of collisional, kinetic, and frictional viscosities as shown in Equation (4.25).

$$\mu_s = \mu_{s,col} + \mu_{s,kin} + \mu_{s,fric} \tag{4.25}$$

In this study, collisional and kinetic parts of shear viscosity are always included into simulations.

The collisional part of the shear viscosity is modeled as in Equation (4.26) (Taghipour et al., 2005).

$$\mu_{s,col} = \frac{4}{5}\alpha_s \rho_s d_s g_0 (1 + e_{ss}) \left(\frac{\theta_s}{\pi}\right)^{1/2} \quad (4.26)$$

For the kinetic part of the shear viscosity Gidaspow –Equation (4.27) and Syamlal O'Brien –Equation (4.28) developed different expressions (Wachem et al., 2000).

Gidaspow expression:

$$\mu_{s,kin} = \frac{10\rho_s d_s \sqrt{\theta_s \pi}}{96\alpha_s (1 + e_{ss}) g_0} \left[1 + \frac{4}{5} g_0 \alpha_s (1 + e_{ss})\right]^2 \quad (4.27)$$

Syamlal-O'Brien expression:

$$\mu_{s,kin} = \frac{\alpha_s \rho_s d_s \sqrt{\theta_s \pi}}{6(3 - e_{ss})} \left[1 + \frac{2}{5} g_0 \alpha_s (1 + e_{ss})(3e_{ss} - 1)\right]^2 \quad (4.28)$$

Both expressions are used during simulations performed in this study depending on other parameter settings.

Frictional part of the shear viscosity is important for dense flow at low shear in which the generation of stress is mainly due to friction between particles. Schaeffer (Fluent, 2006) model given in Equation (4.29) is used in this study.

$$\mu_{s,fric} = \frac{p_s sin(\phi)}{2\sqrt{I_{2D}}} \quad (4.29)$$

where p_s is the solid pressure, Φ is the angle of friction, and I_{2D} is the second invariant of the deviatoric stress tensor.

The effect of inclusion of kinetic part of shear viscosity into simulations on hydrodynamics of conical cylindrical spouted beds is investigated in this study.

The bulk viscosity correlation by Lun et al. (Du et al., 2006b) in Equation (4.20) accounts for the resistance of granular particles to compression and expansion.

$$\lambda_s = \frac{4}{3}\alpha_s \rho_s d_s g_0 (1 + e_{ss}) \left(\frac{\theta_s}{\pi}\right)^{1/2} \quad (4.30)$$

4.1.3.3 The solid phase pressure

The solid pressure, p_s, represents the solid-phase normal forces due to particle-particle interactions and can be divided into two parts, a kinetic contribution and a collisional contribution. The solid pressure given by Lun et al. (Du et al., 2006a) in Equation (4.31) is used in this study.

$$p_s = \alpha_s \rho_s \theta_s + 2\rho_s (1 + e_{ss}) \alpha_s^2 g_0 \theta_s \quad (4.31)$$

The kinetic part, the first term on the right hand side of Equation (4.31), is due to the momentum transferred by the shear stress caused by the flow of particles, and the second term, related to the collisional contribution, is due to the momentum transferred between particle collisions.

5 LITERATURE REVIEW

Hydrodynamic behavior of gas-solid motion in spouted beds has been experimentally and theoretically studied by many researches in the past. Early studies are focused on theoretical work. Sinclair et al. (1989) were the first to analyze fully developed riser flow using kinetic theory of granular flow. They developed a model for fully developed gas–solid flow in a vertical pipe based on the particle kinetic theory model in which the interaction of the particles and the gas was restricted to a mutual drag force. The analytical solution for granular temperature is a special case of that theory for elastic particles. Their computational results demonstrated that the interaction between individual particles produces lateral segregation of solids in the radial direction. The model yielded reasonable results when elastic particle-particle collisions were considered and revealed remarkable rich varieties of behavior in a vertical pipe over a wide range of flow conditions. The kinetic theory model was also modified by many other researchers such as Lun (1991), Grace et al. (1991), and Kim et al. (1995) to account for the slightly elastic and rough particles, non-uniformly sized particles and cohesive particles.

The dynamic behavior of gas and solid phase in the spout was predicted by Lefroy et al. (1969) using a one dimensional two-fluid model based on momentum balance equations. They indicated that the gas flow in the annular zone follows Darcy's law and the pressure distribution at the interface between spout and annulus follows a cosine function. Littman et al. (1985) used the vector form of the Ergun equation to predict gas and solid phase motion in the spouted bed. A modified model was employed by Day et al. (1987) to predict axial variations of radially averaged voidage and solid phase velocity in the spout at minimum spouting conditions. Krzywanski et al. (1992) developed a multi-dimensional model to describe the gas and solid dynamic behavior in spouted beds. Kawaguchi et al. (2000) predicted the velocity distributions of gas and solid phases in a conical spouted bed. Solid phase motions were traced discretely by solving Newton's equation of motion for individual particles.

Later, experimental studies are performed to investigate the hydrodynamics of spouted beds. One of the first experimental studies of spouted beds was

performed by Gorshtein et al. (1967). The vertical solid phase velocity was measured in the spout of a conical spouted bed by using the piezoelectric method. The solid phase velocities in a half conical spouted bed were measured by Boulos et al. (1986) using Laser-Doppler Anemometry. Waldie et al. (1986) measured average solid phase velocity at different heights in the spout by measuring the change of inductance of a search coil using a tracer particle with high electromagnetic permeability.

Several researchers used optical fibers for the determination of trajectories, velocity, and recirculation time of solid phase and several used the radioactive particle tracking (RPT) (non-intrusive technique) method. Olazar et al. (1993) used fiber optical probe to determine the stable operation conditions of conical-cylindrical spouted beds. Glass spheres of different sizes were used with conical contractors of different geometry (angle, inlet diameter) and under different operating conditions (stagnant bed height and inlet gas velocity). The air was used as spouting gas. They observed that the regime of stable spouting is achieved within certain limits of operation that are given by combination of geometric factors of the contractor inlet, properties of the solids, and gas velocity. Beyond these limits, no cycling and uniform movement of particles was attained. The design parameters such as $1/2<D_o/D_i<5/6$; $\beta/2<28^o$ and $2<D_o/d_s<60$ were suggested for stable operating conditions. He et al. (1994a) used a relatively large fiber optic probe system to measure the voidage profiles in the spout, annular and fountain regions of a full/half-column spouted bed filled with relatively large particles (diameter of 1.41×10^{-3} m). The air was used as spouting gas. It was found that the voidage in the annulus is higher than the loose-packed voidage and that it increases with increasing the gas velocity. Olazar et al. (1995) used optical fiber probe to study local properties of conical spouted beds. The solid phase trajectory map was achieved. San Jose et al. (1998) quantified the solid cross-flow into the spout and particle trajectories in conical spouted beds and determined the position of this cross-flow by measuring the solid flow rate with an optical fiber probe at different longitudinal positions along the spout. Wang et al. (2004) compared the pressure drop and minimum fluidization velocity results of the circular conical and semi-circular conical spouted beds by measuring the pressure drop in the bed. Glass beads of 2500 kg/m^3 and 1.16×10^{-3} m diameter with air as spouting gas

were used. The results indicated that for circular conical and semi-circular conical spouted bed, there is little difference on the pressure drop and the same minimum spouting velocity can be determined from absolute pressure measured at different axial locations along the bed height and the minimum spouting velocity is a strong function of the static bed height, cone angle, and much less sensitive to the inlet diameter.

The methods other than fibre optic probe were also used for experimental investigation of spouted beds. Roy et al. (1994) measured the solid phase velocity in a spouted bed using a γ-ray-emitting particle tracking technique. Djeridane et al. (1998) experimentally investigated the turbulent dynamic behavior of solid phase flow in a spouted bed using a non-invasive radioactive particle tracking technique. Liu et al. (2008) used particle image velocimetry technique that can non-intrusively measure instantaneous velocity fields within global flow domain, which is greatly distinct from both the single-point measurement techniques such as optical fiber system and radioactive particle tracking techniques for solid phase flow in spouted beds. The positron emission particle tracking method was used by Seiler et al. (2008) to determine particle trajectories, cycle times, and the size and voidage of the spout.

In the past decade, computational fluid dynamic simulation studies about conical cylindrical spouted beds were performed. Wachem et al. (2001) reviewed the different forms of governing equations and closure relations and compared the resulting hydrodynamics through CFD simulations by using CFD code CFX. The benchmark experimental data of Hilligardt et al. (1986), Kehoe et al. (1971), Darton et al. (1977), and Kuipers et al. (1990) were used (Wachem et al., 2001). The results showed that flow predictions were not sensitive to the use of different solid stress models or radial distribution functions but the application of different drag models significantly impacted the flow of the solids and simplifying granular temperature relation to algebraic form did not lead significantly different results.

Lu et al. (2004) incorporated the kinetic-frictional constitutive model for dense assemblies of solids in the simulations of spouted beds. This model treats the kinetic and frictional stresses additively. Particle concentration and velocity distributions revealed that the shape of spout, annulus, and fountain changed

appreciably when frictional stresses were dropped. Computed solid phase velocities and porosities showed good agreement with the measurements obtained by He et al. (1994a) and San Jose et al. (1998). However, an experimental setup by San Jose et al. (1998) used in this study was critiqued recently by Wu et al. (2009) based on their calculation on acceleration required for particles to reach measured velocities is 100 times higher than the gravitational acceleration.

He et al. (2004) aimed to numerically study the effect of geometric factors of the angle on vertical and horizontal component of solid velocity and solid phase volume fraction distribution. K-FIX program that employs a staggered finite difference mesh system was used. The CFD model was tested on He et al. (1994a; 1994b) first then parametric study on cone angle was performed with hypothetical particles of 1600 kg/m^3 density and 1.5 mm diameter. The results revealed that horizontal particle velocities predicted were much smaller than their vertical counterparts indicating that main solids motion is up or down. In addition, enlargement of spout diameter with decrease in inclined angle was spotted. It was concluded that for an inclined angle of 60^o and higher, a neck in the spout appears, thus limits the solids upward motion in the spout.

Du et al. (2006a) investigated the influence of the drag models on the CFD modeling of spouted beds and Du et al. (2006b) described the influences of the solid frictional stress, maximum packing limit, and restitution coefficient on CFD simulations of spouted beds, using experimental data of He et al. (1994a;1994b) with FLUENT commercial CFD package. The most commonly used drag models were selected for evaluation. The simulation results by different drag models showed that the Gidaspow model gives the best fit to the experimental results and the selection of drag model makes difference in CFD simulation (i.e. formation of fountain at lower gas velocity, over or under estimating of minimum spouting velocity). It was concluded that the frictional stress is important only for annulus region and has slight effect on hydrodynamics of the flow in spout region, higher values of maximum packing limit leads to the predictions of increased particle velocities and slightly increased bed voidage, and restitution coefficient makes difference in the simulated hydrodynamics of the spouted bed.

Pannala et al. (2007) constructed an approximate transition function to provide smooth transition between two granular regimes (rapidly moving granular particles in spout and slowly moving granular particles in annulus) in the void-fraction space. MFIX code was used as modeling tool. The experiments performed in Oak Ridge National Laboratory (ORNL) and University of Tennessee (UT). The UT experiments are primarily focused on ambient conditions with Zirconia particles and the ORNL experiments are typically conducted under high temperature conditions with Zirconia, Hafnia or natural uranium particles. The CFD simulations captured the main features of the solid circulation. It was observed that there are typically very regular pressure pulsations at the gas inlet. The qualitative agreement in pulsation frequency was achieved at low temperatures.

Bettega et al. (2009a) compared the experimental results from the semi-cylindrical spouted bed with CFD simulations of cylindrical spouted bed to understand the effect of flat wall in the solid phase behavior. The particles were glass beads of 2512 kg/m^3 density and 2.18 x 10^{-3} m diameter. The air flow was used for spouting. The experimental data of solid phase velocities were obtained from images captured by a high speed video camera. FLUENT commercial package was used for simulations. The study showed that even the friction between the flat wall and solid phase was neglected, the dynamic behavior tends to disturb the flow inside the bed. It was concluded that it is necessary to take care when using information collected from semi-cylindrical vessel to infer fluid dynamic behavior in full-column spouted bed.

Shuyan et al. (2009) simulated the spouted beds to investigate the effect of frictional solid stress on particle velocity and volume fraction. An inverse tangent function was used to provide smooth transition between plastic and viscous regimes. He et al. (1994a; 1994b) experimental data was use to compare the simulation results. MFIX code was used as modeling tool. It was observed that when solid frictional stress included into simulations, it results in lower solid volume fraction in spout region and higher solid volume fraction in annulus region.

Dan et al. (2010) used second-order moment method to model the kinetic interaction of particle collisions. MFIX code and He et al. (1994a; 1994b) experimental data were used. Simulations indicated that normal second-order

moments in the direction of flow are much larger than the lateral normal second-order moments and second order-moments are much higher in the spout region than that in the annulus region.

Liu et al. (2011) studied the different gas inlet types of gas distributors (single-nozzle and multi-nozzle) to reduce the aggregation of particles near the wall. The effects of gas velocity and temperature were also investigated. The simulations are carried out using glass beads of 2500 kg/m^3 density and 0.5 mm diameter. Commercial CFD software FLUENT was used to simulate the hydrodynamics of the spouted bed. It was concluded that maximum spout height was increased with increasing temperature and gas velocity. Gas was better dispersed, more particles were spouted up into the fountain region, and particles did not aggregate near the entrance of the gas inlet when multi-nozzle gas inlet was used.

Lan et al. (2012) investigated the influence of solid phase wall boundary condition in terms of specularity coefficient and particle-wall restitution coefficient on flow behavior of spouted beds. FLUENT CFD code and He et al. (1994a; 1994b) experimental data were used. The results showed that smaller specularity coefficient leads to higher particle velocities both in spout and annulus regions and higher bed pressure drop. The particle-wall restitution coefficient hardly influences the flow in the spout and annulus regions. The value of 0.05 for speculatrity coefficient provides the best agreement with experimental pressure drop results.

6 CFD STUDIES ON LIGHT PARTICLE FILLED EXPERIMENTAL SETUP

A set of well known experiments about the spouted beds were performed with collaboration of the Department of Chemical Engineering in University of British Colombia, Vancouver and the Institute of Chemical Metallurgy in Chinese Academy of Science, Beijing. The results of the measurements of void fraction profiles, particle velocity profiles, and solid flow patterns in spouted beds were presented in various papers (He et al., 1994a; 1994b).

The CFD simulation of He's experimental setup was performed with FLUENT commercial CFD package and the results are represented here. The effect of maximum packing limit, drag model, restitution coefficient, and solid frictional stress on flow hydrodynamics was investigated.

6.1 The Literature Review

Several researchers have analyzed the results of the experimental results of the He's experiment through years. Huilin et al. (2001) developed a hydrodynamic computer model of dense gas-solid flow and concluded that the model results agree well with the published experimental data by San Jose et al. (1998) and He et al. (1994a) and the frictional solid stress has an important effect on the results of the simulations. But experimental data of San Jose et al. (1998) used in this study for testing the computer model has recently been criticized by Wu et al. (2009) with a letter to the editor of Chemical Engineering Science journal titled "Comments on: "Solid cross-flow into the spout and particle trajectories in conical spouted beds" by San José Maria, J., et al., Chemical Engineering Science 53 (1998) 3561–3570". The letter implied that the experimental results from this particular setup cannot be correct. The argument is based on the fact that the calculated particle acceleration required to reach the measured particle velocity values is 100 times the gravitational acceleration.

Kawaguchi et al. (2000) used Discrete Element Method to model interaction between the particles. The simulation results were compared with He's experimental results. Due to large number of particles (approximately 2,000,000 particles) for a given static bed height, the calculations were performed with higher particle diameter of 3×10^{-3} m although the real particle diameter was 1.4×10^{-3} m.

It was mentioned in the paper that the discussion of results is limited to qualitative comparison.

Zhonghua et al. (2008) simulated the experimental results of He's experiment by using 2D axial symmetric Eulerian-Eulerian model (Gidaspow drag model, Lun et al. kinetic theory, and Schaffer's frictional shear viscosity were adopted) and pointed out that near the top of the spout and at the centre of the fountain there exists a somewhat denser zone surrounding the spout axis. They also pointed out that this phenomenon was also observed experimentally in the work of Grace et al. (1978). The conclusion was that the typical flow patterns of spouted beds were obtained in agreement with the reported experimental results.

Du et al. (2006b) investigated the effect of solid fractional solid stress, maximum packing limit, and the restitution coefficient by simulating the He's experimental setup. It was reported that the simulations with and without the frictional stress are almost identical for the lower part of the spout region where the particle volume fraction is low but the influence emerges for the upper part of the spout. The conclusion was that the inclusion of frictional stress into calculations did affect neither the spout shape nor the voidage nor particle velocity profile.

Bettega et al. (2009b) also studied the He et al. experiment for scale up calculations of spouted beds with FLUENT commercial CFD package. In order to get the same spouting height, they increased the gas inlet velocity for the simulations. It was shown that the results of the He et al. experiment were well represented by CFD simulations indicating the capacity of this tool.

The summary of the CFD simulations on He's experimental setup is given in Table 6.1. As seen in Table 6.1, different models, CFD packages, and simulation parameters are used for the simulations. Some authors changed the experimental conditions like particle size and superficial gas velocity due to either computational limitations or to achieve similar results with experiments. There is also difference in computational methods such as inclusion of solid frictional stress into simulations implying that it has significant effect on simulations although some authors say it does not have significant effect or using different combinations of drag models, restitution coefficient, and maximum packing limit values. This is a

good indication of the fact that CFD simulation results can vary with different settings of simulation parameters.

The effects of different modeling parameters for the Eulerian-Eulerian model implemented using FLUENT 6.3 commercial CFD package are going to be investigated in this chapter by using He's experimental setup and experimental results.

Table 6.1 Summary of CFD simulation studies on He et al. experimental setup.

Authors	CFD Methodology	Remarks
Huilin et al. (2001)	Simulation parameters same as experiments, K-FIX program is used	Time averaged particle velocity and concentration distributions agree well with simulations.
Kawaguchi et al. (2000)	Discrete element method, particle diameter is higher than the real value	Although the particles used in the calculations were larger than those in the experiments, the flow pattern agreed well with that observed in experiments.
Zhonghua et al. (2008)	Eulerian-Eulerian model, parameters same as experiments, FLUENT 6.2 commercial CFD package is used	Near the top of the spout and at the center of the fountain there exists a somewhat denser region surrounding the spout axis. The simulations underestimate average particle velocity distribution.
Du et al. (2006b)	Eulerian-Eulerian model, simulation parameters same as experiments, FLUENT 6.1 commercial CFD package is used	The frictional stress is important in the annulus and has a slight effect on the hydrodynamics of the flow in the spout region. Specifying a higher value of the maximum packing limit leads to the predictions of increased particle velocities and slightly increased bed voidage.
Bettega et al. (2009b)	Eulerian-Eulerian model, superficial gas velocity is increased to get the same fountain height with the experiment, FLUENT 6.3 commercial CFD package is used	The simulation results agree well with the experimental results.

6.2 The Experimental Setup

He's experiments were carried out in a fully cylindrical Plexiglas column of inside diameter 0.152 m, base diameter 0.0191 m with 1.4 m height. The inclined conical angle was 60^o as shown in Figure 6.1.

The measurements were taken from eighteen holes which were drilled at 0.05 m vertical intervals along the column wall. The fiber optic probe was inserted into the holes and moved radially to measure voidage and particle velocity profiles.

The particles used for the experiments were glass beads of mean diameter 1.41×10^{-3} m and density 2500 kg/m^3. The fluid was air at room temperature. The Plexiglas column was filled up to height of 0.325 m. The minimum spouting velocity (U_{ms}) reported for this static bed height was 0.54 m/s.

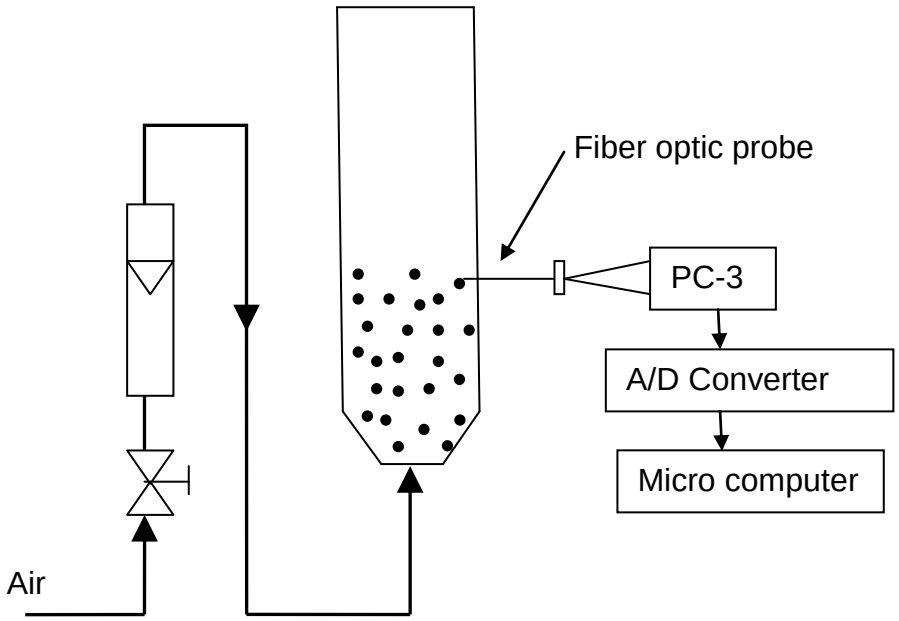

Figure 6.1 A schematic of He's experimental set up.

The radial profiles of voidage and particle velocity at different levels in the bed for three gas velocities U/U_{ms}=1.1, 1.2, and 1.3 were measured (U: Superficial gas velocity). More details about the experiments can be found in (He et al., 1994a; 1994b).

6.3 The CFD Simulations

By using U/U_{ms}=1.3 and the experimental conditions listed in Table 6.2, the CFD simulation was performed with commercial CFD simulation package FLUENT 6.3.

Table 6.2 The experimental conditions used in He's experiments.

Parameter	Value
Column Diameter (m)	0.152
Orifice Diameter (m)	0.0191
Static bed height (m)	0.325
Particle diameter (m)	1.41×10^{-3}
Particle density (kg/m^3)	2,500
Gas density (kg/m^3)	1.225
Gas viscosity (kg/m-s)	1.7894×10^{-5}

The 2D axially symmetric model of the experimental spouted bed was generated with GAMBIT 2.4. GAMBIT is a program for the generation of the geometry and grid system needed for the computations done by FLUENT. The 2D axial symmetric model was selected to reduce the computational load. The resulting computational domain is shown in Figure 6.2. It contains 40,000 quadrilateral cells where 5,000 of which in the conical section of the bed.

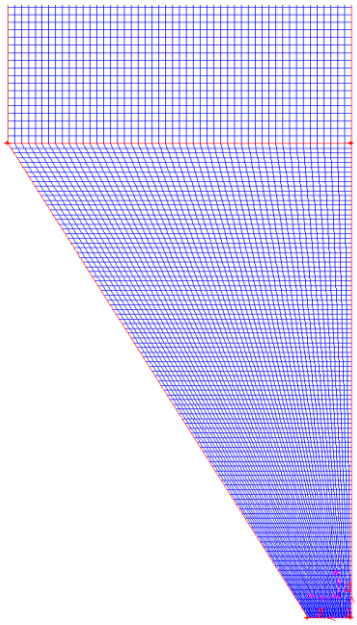

Figure 6.2 The computational domain generated for the spouted bed.

The gas inlet boundary is defined as velocity inlet such that the gas is injected only in axial direction and the solid inlet velocity is set to zero. At the outlet, the outflow boundary condition is applied which implies the velocity gradients for the two phases in the axial direction are zeros. For the walls of the bed, no slip boundary condition is used. The symmetry axis requires the velocity gradients for the two phases and the granular temperature gradient along the radial direction to be zeros. The set of governing equations of Eulerian-Eulerian multiphase model was solved by a finite volume method. General transport equations for mass and momentum were applied to each computational cell by using first order implicit node based, unsteady, and pressure based solver. The phase coupled SIMPLE algorithm was used to solve pressure-velocity coupling. The first order discretization scheme was set for momentum and volume fraction variables. Summary of models, boundary conditions, solver controls, and material properties are given in Appendix A. The detailed information about models, boundary conditions, and solver controls given in Appendix A can be found in Fluent (2006).

For 15 s of total simulation time, 30,000 time steps with 5×10^{-4} s time step size was used.

Grid independence study for the CFD simulations was performed by running a test case with three different mesh sizes- coarse mesh (17556 cells), fine mesh (40000 cells), and very-fine mesh (90000 cells). The resulting particle velocity and voidage profiles at measurement heights 53 and 118 mm were compared as seen in Figure 6.3. Figure 6.3 indicates that results of fine and very-fine meshes are very close to each other. In addition, bed pressure drop values and simulation times are compared as seen in Table 6.3. The bed pressure drop results of fine and very-fine meshes are exactly the same. Since results of fine and very-fine meshes are close to each other and computational time of fine mesh is half of the computational time of very-fine mesh, fine mesh is used in this study.

Table 6.3 Pressure drop and computational time comparison of three mesh sizes.

	Coarse	**Fine**	**Very-fine**
Computational Time (s)	47440	105855	244035
Pressure Drop (Pa)	3592	3565	3565

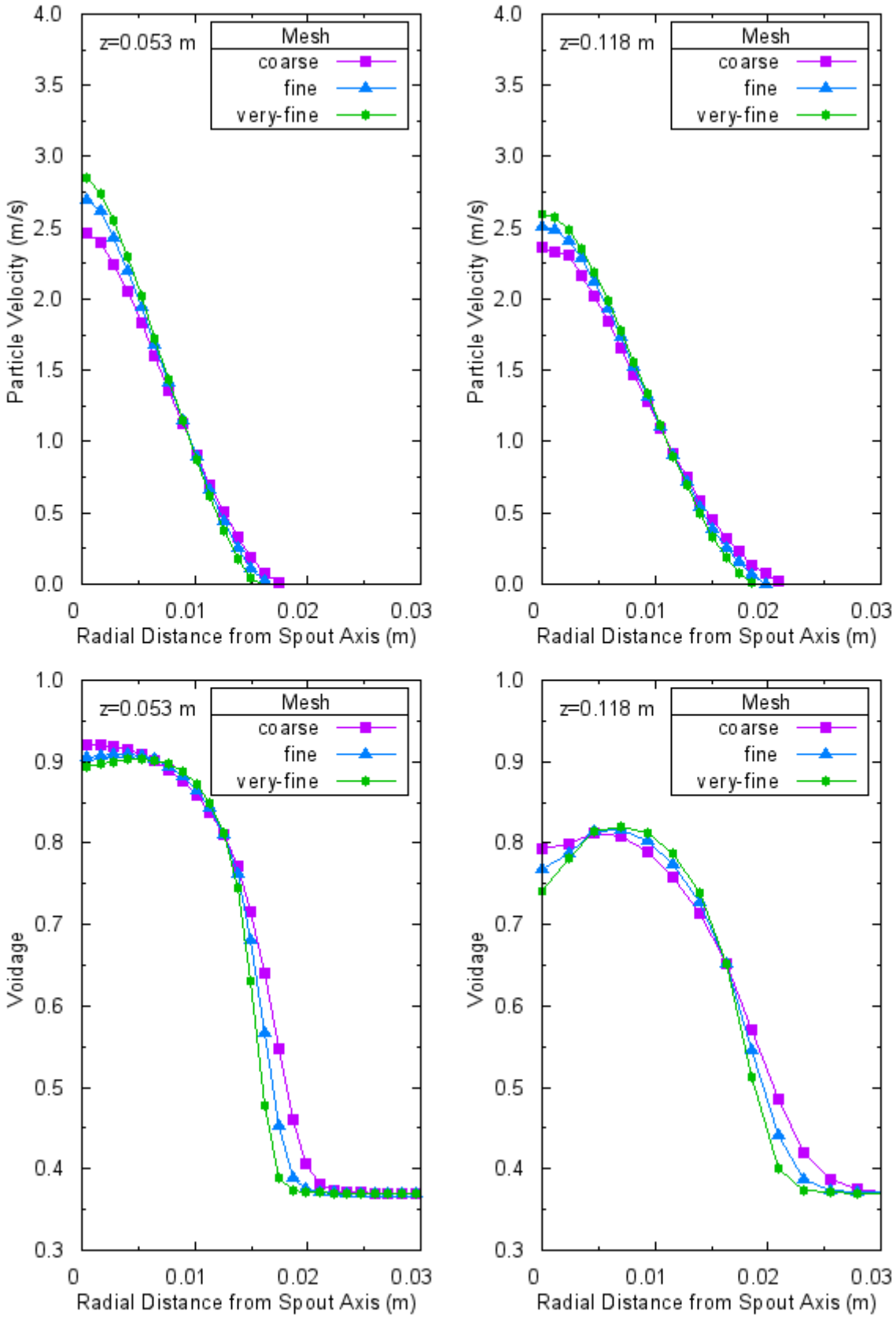

Figure 6.3 Comparison of particle velocity and voidage profiles of different mesh sizes.

Since the longer computation time is a major drawback of multiphase CFD simulations, parallel processing was performed on 8 HP ProLiant BL680C G5 systems with 4 quad-cores Intel Xeon E7300 CPU that contains 128 cores. In order to determine the optimum number of cores, a test case was created by using parameters in Table 6.2 and run on different number of cores. For each simulation different input files were generated by using METIS partitioning technique implemented in FLUENT. The number of cores versus speed-up factor graph in Figure 6.4 was generated. It is seen from Figure 6.4 that the speed-up factor reaches a maximum around 16 cores. Addition of extra cores clearly decreases the speed-up factor therefore increases the simulation time because the amount of messaging and data transfer between the cores increase. Since the addition of extra cores after 16 is not going to fasten the simulation, all the simulations in this study were performed by using 16 cores. With the speed-up factor around 16, the computation of 15 s simulation was completed approximately in 2 days.

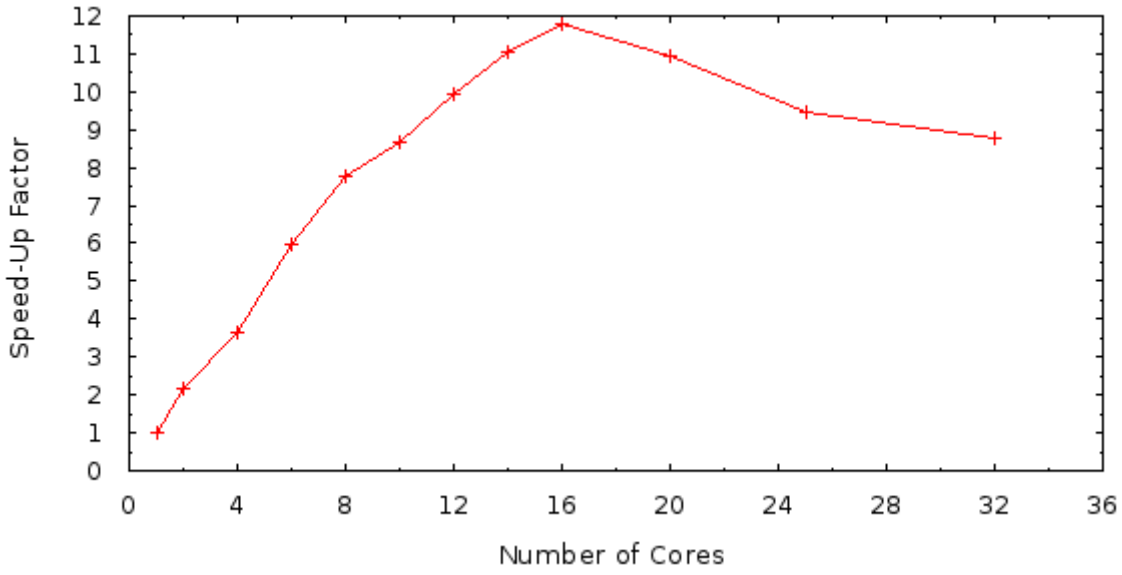

Figure 6.4 Speed-up factor versus number of cores from parallel computing of FLUENT on 8 HP ProLiant BL680C G5 system.

After determining the number of cores to be used, several CFD simulations with different values of maximum packing limit (0.63, 0.61 and 0.59) and restitution coefficient (0.80, 0.90, and 0.95) for different drag models (Gidaspow and Syamlal-O'Brien) were performed to observe their effects on hydrodynamic

simulations of spouted bed. The influence of solid frictional stress on the results of the simulations is also evaluated.

6.3.1 The influence of maximum packing limit

Figure 6.5 and Figure 6.6 show the instantaneous solid volume fraction distributions after 15 seconds of simulation for nine combinations of three different e_{ss} and $\alpha_{s,max}$ values for Gidaspow and Syamlal-O'Brien drag models. Figure 6.7 through Figure 6.12 represents the time averaged radial voidage and particle velocity distributions of the last 5 second of the simulation for different axial positions together with experimental results. The experimental results at heights 0.053 m, 0.118 m, 0.168 m, and 0.268 m are used. The solid lines with open pointers in the figures are the experimental data. Table 6.4 presents bed pressure drop results and their percent errors when compared with experimental results.

Table 6.4 The bed pressure drop results from simulations.

Drag Model	Maximum Packing Limit	Restitution Coefficient	Bed Pressure Drop (Pa)	% error
Gidaspow	0.63	0.95	3620	20.67
	0.63	0.90	3565	18.83
	0.63	0.80	3492	16.40
	0.61	0.95	3586	19.53
	0.61	0.90	3522	17.40
	0.61	0.80	3431	14.37
	0.59	0.95	3826	27.53
	0.59	0.90	3823	27.43
	0.59	0.80	3800	26.67
Syamlal-O'Brien	0.63	0.95	3605	20.17
	0.63	0.90	3538	17.93
	0.63	0.80	3424	14.13
	0.61	0.95	3580	19.33
	0.61	0.90	3521	17.37
	0.61	0.80	3410	13.67
	0.59	0.95	3605	20.17
	0.59	0.90	3492	16.40
	0.59	0.80	3414	13.80

It is seen from Figure 6.5 and Figure 6.6 that when 0.59 is used for maximum packing limit (cases g, h, and i in figures) there is only internal spouting regardless

of the value of the restitution coefficient and the dag model. This fact is very clear for Gidaspow drag model case seen in Figure 6.9 that the particle velocity profiles near the top of the bed is almost zero and voidage profile is at its initial value of 0.4 throughout the simulations. Although it is not as clear as in Gidaspow drag model case, Syamlal-O'Brien case also implies similar result as seen in Figure 6.12.

For maximum packing limit of 0.61 (cases d, e, and f in figures), either external spouting occurs or it almost occurs depending on restitution coefficient and drag model used. For all combinations of drag models and restitution coefficients, the voidage profile differs from the initial value as shown in Figure 1.7 and Figure 1.10 and indicates that there is an expansion in the bed at all levels.

External spouting occurs for all cases if the maximum packing limit is set to 0.63 (cases a, b, and c in figures).

There isn't any specific effect of maximum packing limit on pressure drop values as it first decreases then increases as maximum packing limit decreases.

In summary, decrease in maximum packing limit value results in decrease in particle velocity and voidage. This is observed for every combination of drag model and restitution coefficient and for all measurement heights. Similarly, fountain height decreases as maximum packing limit decreases. On the other hand, the effect on bed pressure drop cannot be determined.

Another observation from simulations is that as measurement height increases, particle velocity and voidage decrease.

The maximum packing limit is used to set the maximum solid volume fraction so that it does not exceed the set value. It is used in the formulation of radial distribution function as seen in Equation (6.1) which is a measure of probability of particles touching each other.

$$g_0 = \left[1 - \left(\frac{\alpha_s}{\alpha_{s,max}}\right)^{1/3}\right]^{-1} \tag{6.1}$$

For smaller values of maximum packing, the radial distribution function therefore probability of particle touching one another increases. The effect magnifies when the solid volume fraction gets close to maximum packing limit as seen in Table 6.5. As a result separation of particles from each other becomes difficult for a given amount of force.

Table 6.5 Values of radial distribution function from Equation (6.1) for different maximum packing limit values.

Maximum Packing Limit	**Solid Volume Fraction**						
	0.4	0.5	0.58	0.59	0.6	0.61	0.63
0.63	7.1	13.4	36.7	46.2	61.9	93.4	187.9
0.61	7.6	15.5	59.9	90.4	181.9		
0.59	8.2	18.6	175.9				

When instantaneous area weighted average values of kinetic parameters of the solid particles are analyzed, it is seen in Table 6.6 and Table 6.7 that with decrease of maximum packing limit results in decrease of granular temperature. It is because of the fact that particles touching each other increases as radial distribution function increases due to decrease in maximum packing limit therefore particles cannot fluctuate freely. This causes reduction in granular temperature. That is why spouting is retarded when maximum packing limit decreases.

Table 6.6 Area weighted average kinetic parameters of solid phase for Gidaspow drag model (t=15.0 s).

Maximum Packing Limit ($\alpha_{s,max}$)	**Restitution Coefficient (e_{ss})**	**Bulk Viscosity (kg/m-s)**	**Molecular Viscosity (kg/m-s)**	**Granular Pressure (Pa)**	**Granular Temperature**
0.63	0.95	4.78	2.26	48.80	0.0011450
	0.90	3.99	1.89	36.24	0.0011095
	0.80	3.28	1.55	27.42	0.0016092
0.61	0.95	4.84	2.22	47.72	0.0007186
	0.90	4.14	1.90	36.60	0.0006791
	0.80	3.52	1.62	28.88	0.0005509
0.59	0.95	5.76	2.57	52.36	0.0004322
	0.90	4.77	2.13	38.70	0.0003492
	0.80	3.76	1.67	26.62	0.0001924

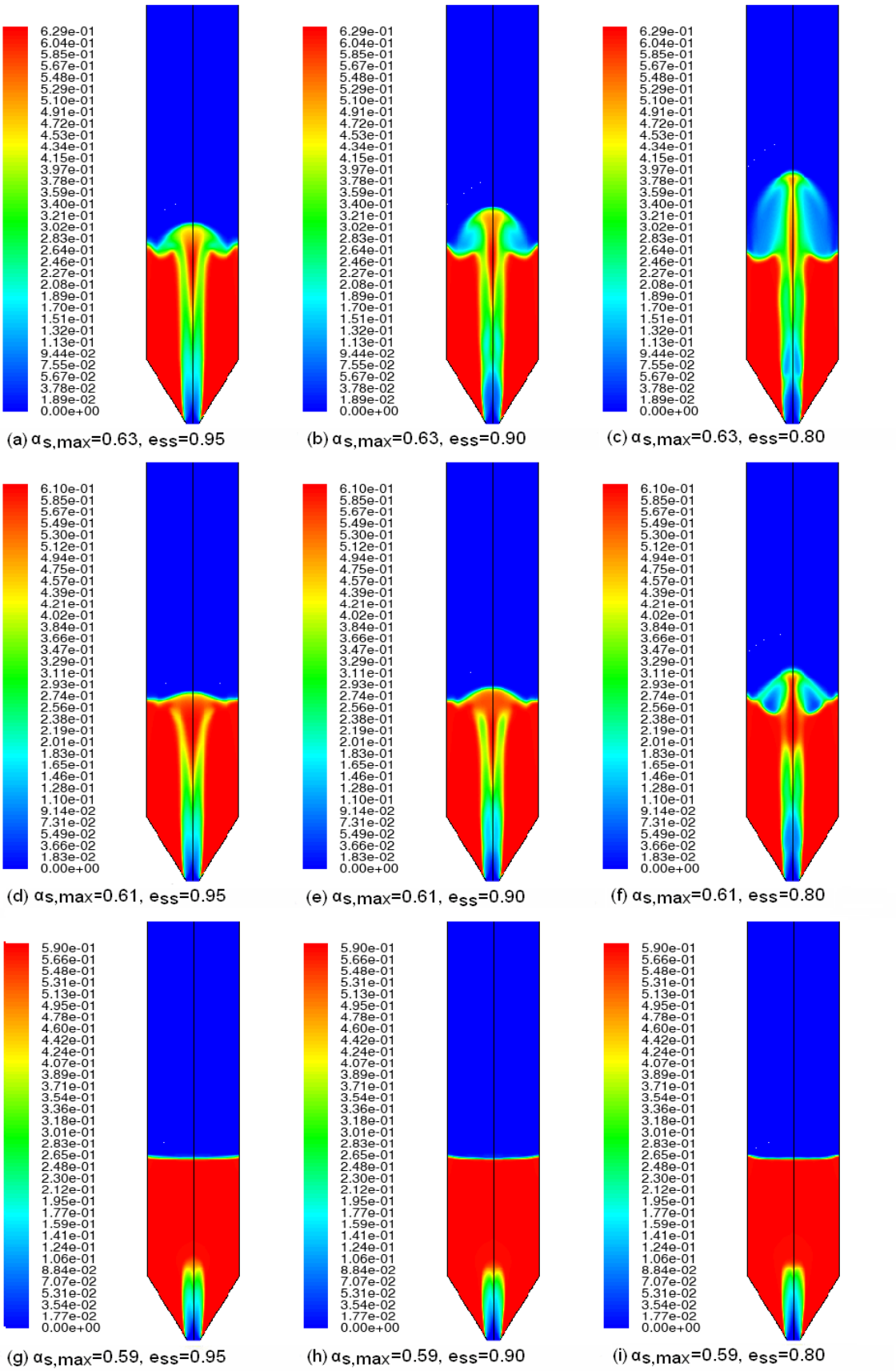

Figure 6.5 Instantaneous (t=15s) solid volume fraction distributions of Gidaspow drag model for different e_{ss} and $\alpha_{s,max}$ values.

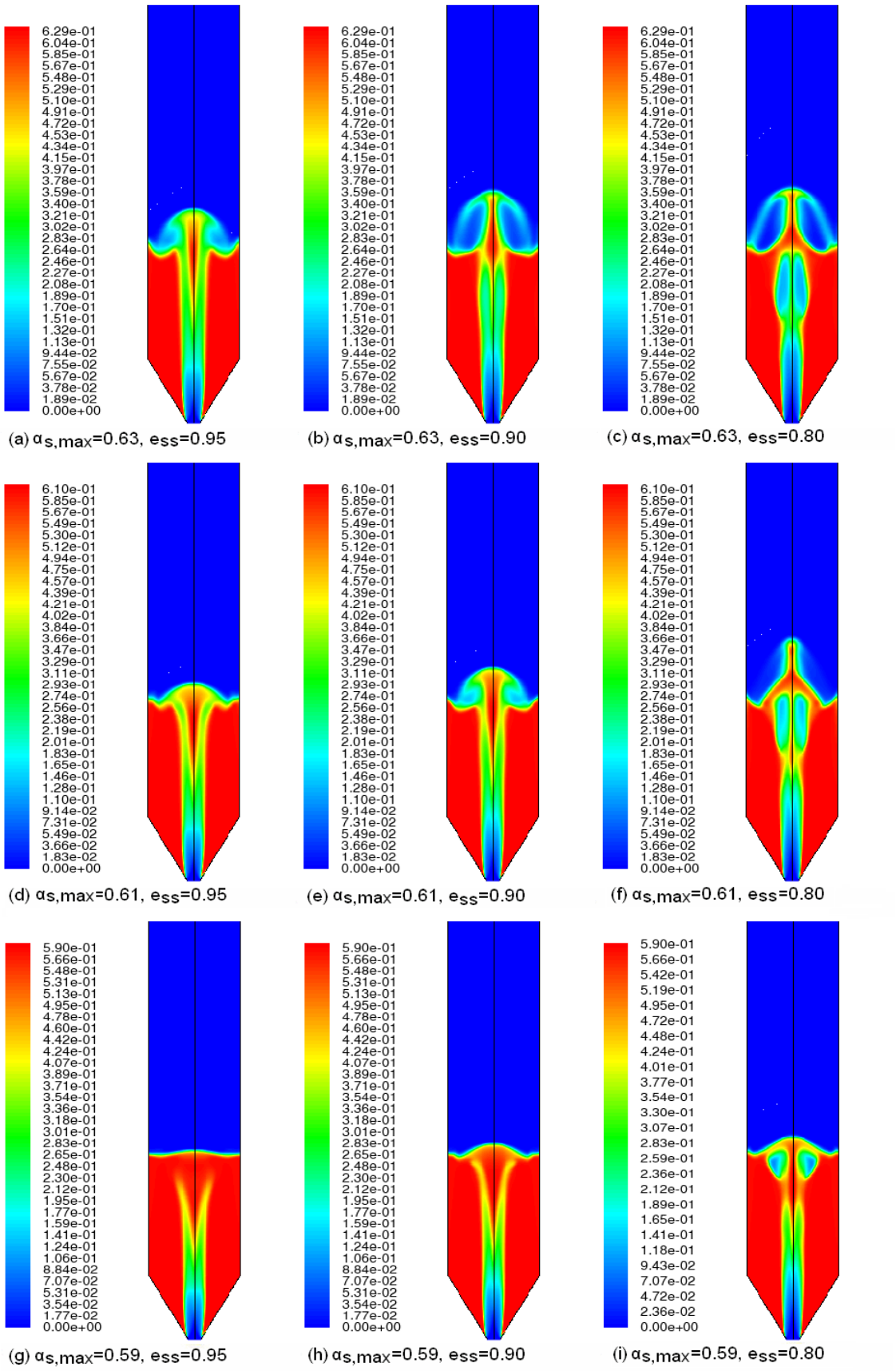

Figure 6.6 Instantaneous (t=15s) solid volume fraction distributions of Syamlal-O'Brien drag model for different e_{ss} and $\alpha_{s,max}$ values.

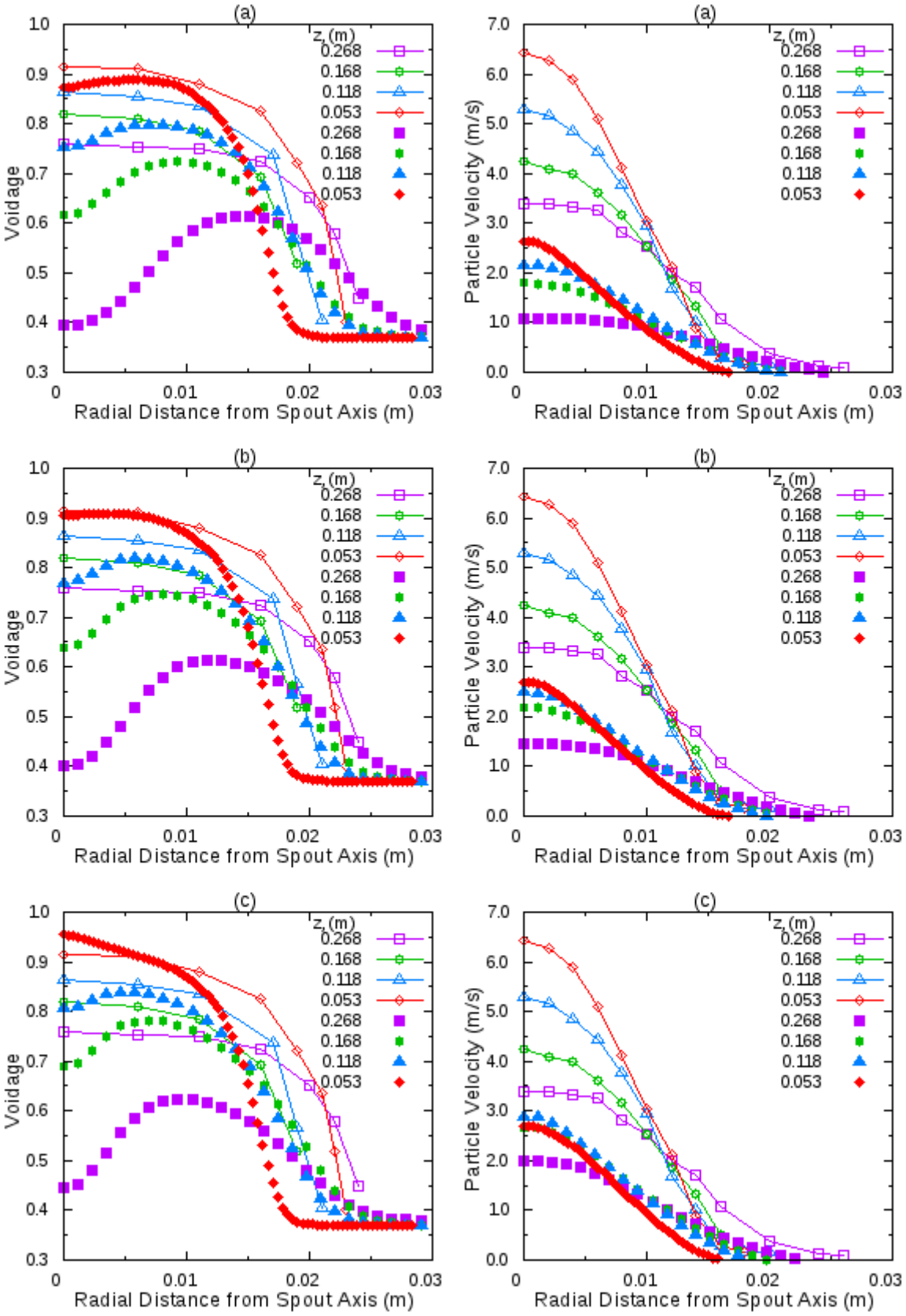

Figure 6.7 Comparison of Gidaspow drag model voidage and particle velocity profiles of $\alpha_{s,max}$=0.63 a) e_{ss} =0.95, b) e_{ss} =0.90, c) e_{ss} =0.80 case with experimental results (open pointers).

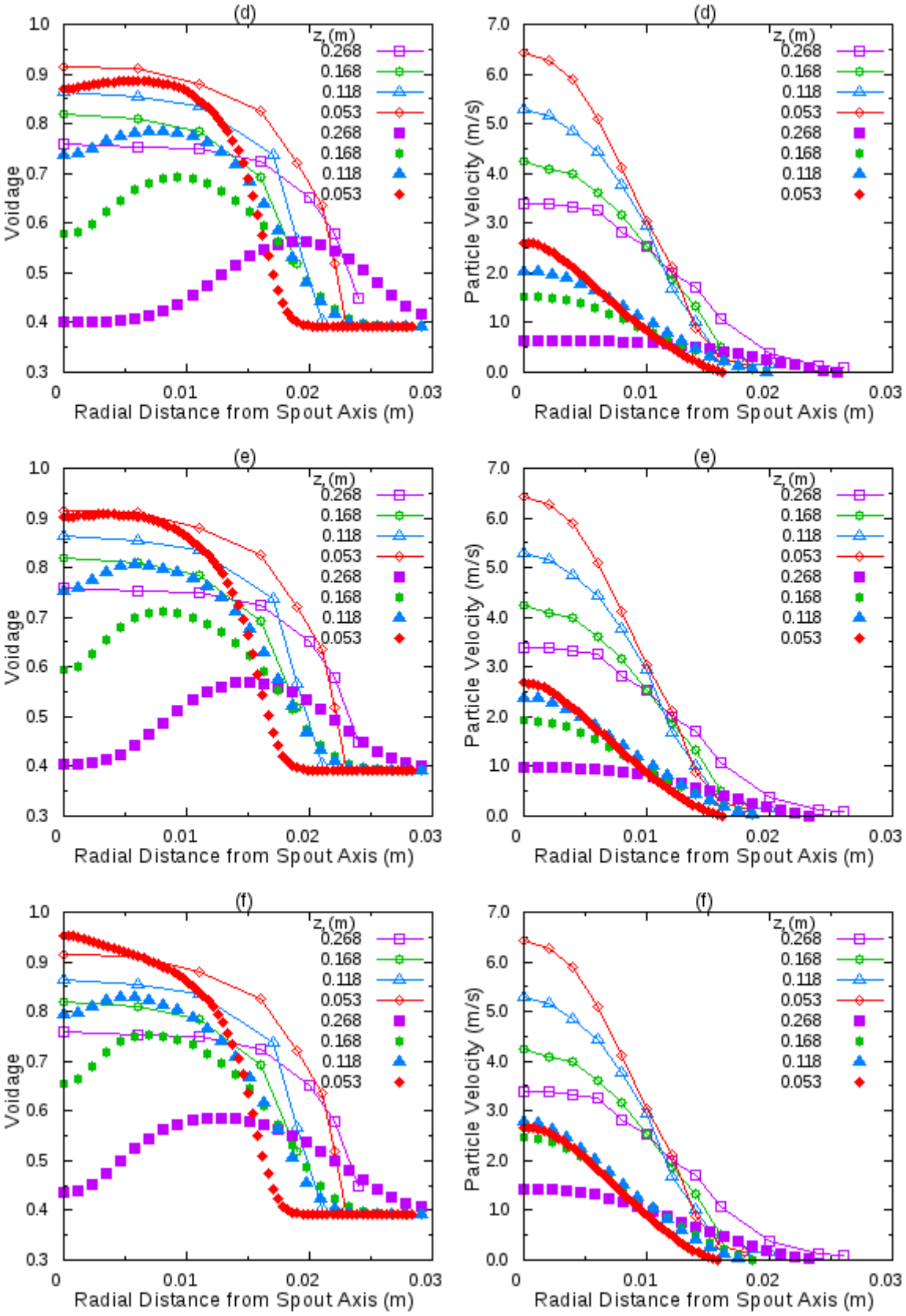

Figure 6.8 Comparison of Gidaspow drag model voidage and particle velocity profiles of $\alpha_{s,max}$=0.61 d) e_{ss} =0.95, e) e_{ss} =0.90, f) e_{ss} =0.80 case with experimental results (open pointers).

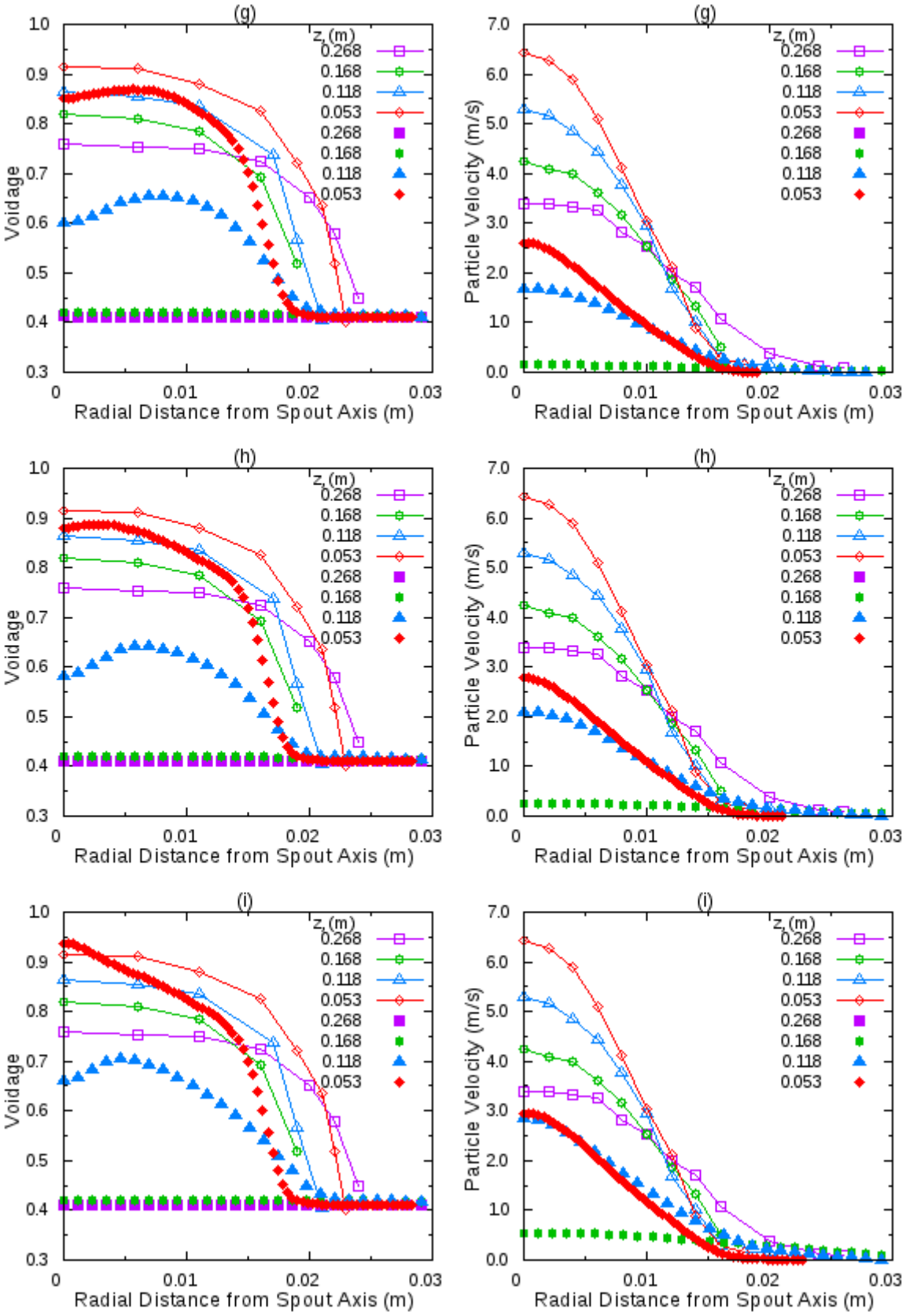

Figure 6.9 Comparison of Gidaspow drag model voidage and particle velocity profiles of $\alpha_{s,max}$=0.59 g) e_{ss} =0.95, h) e_{ss} =0.90, i) e_{ss} =0.80 case with experimental results (open pointers).

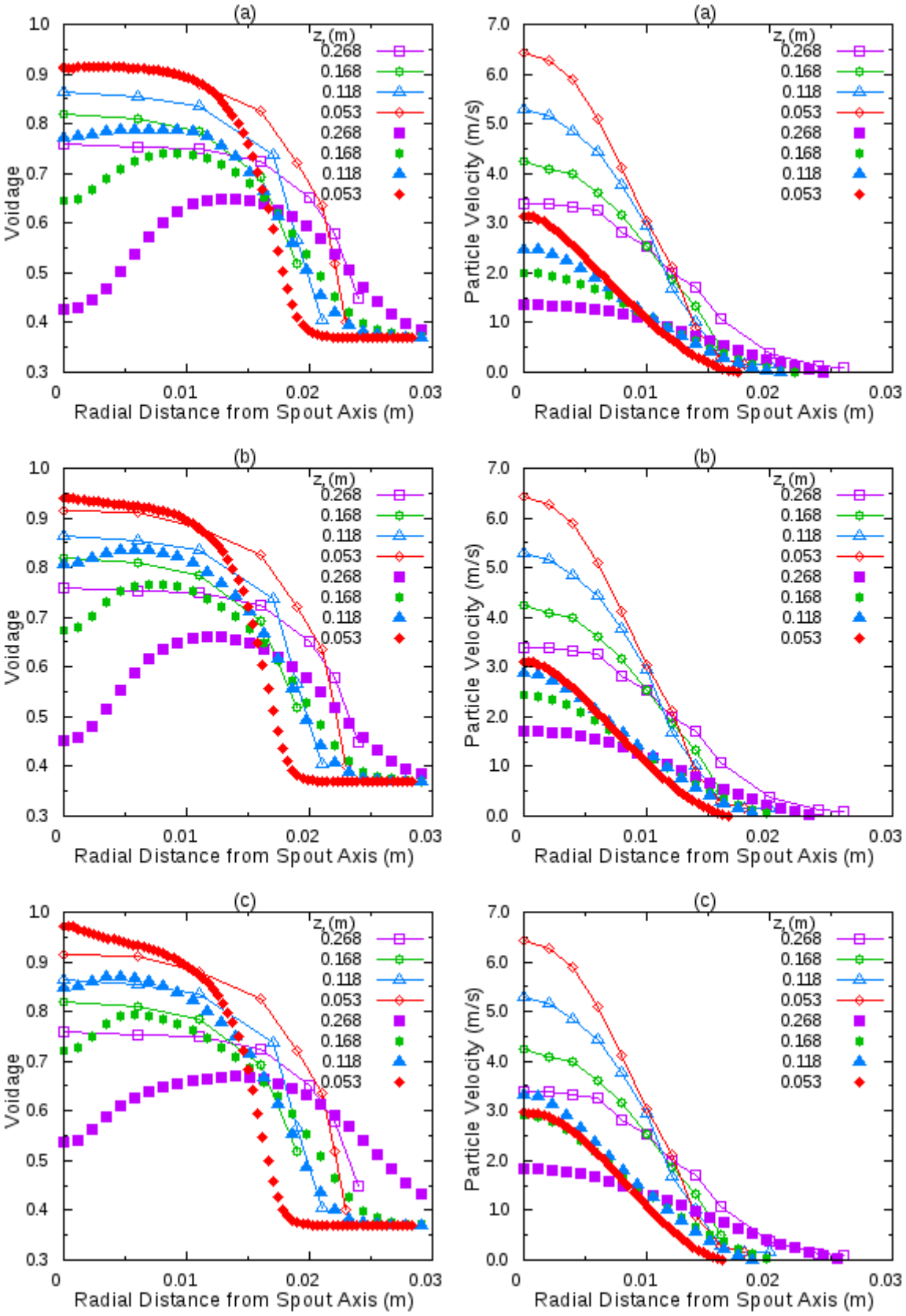

Figure 6.10 Comparison of Syamlal-O'Brien drag model voidage and particle velocity profiles of $\alpha_{s,max}$=0.63 a) e_{ss} =0.95, b) e_{ss} =0.90, c) e_{ss} =0.80 case with experimental results (open pointers).

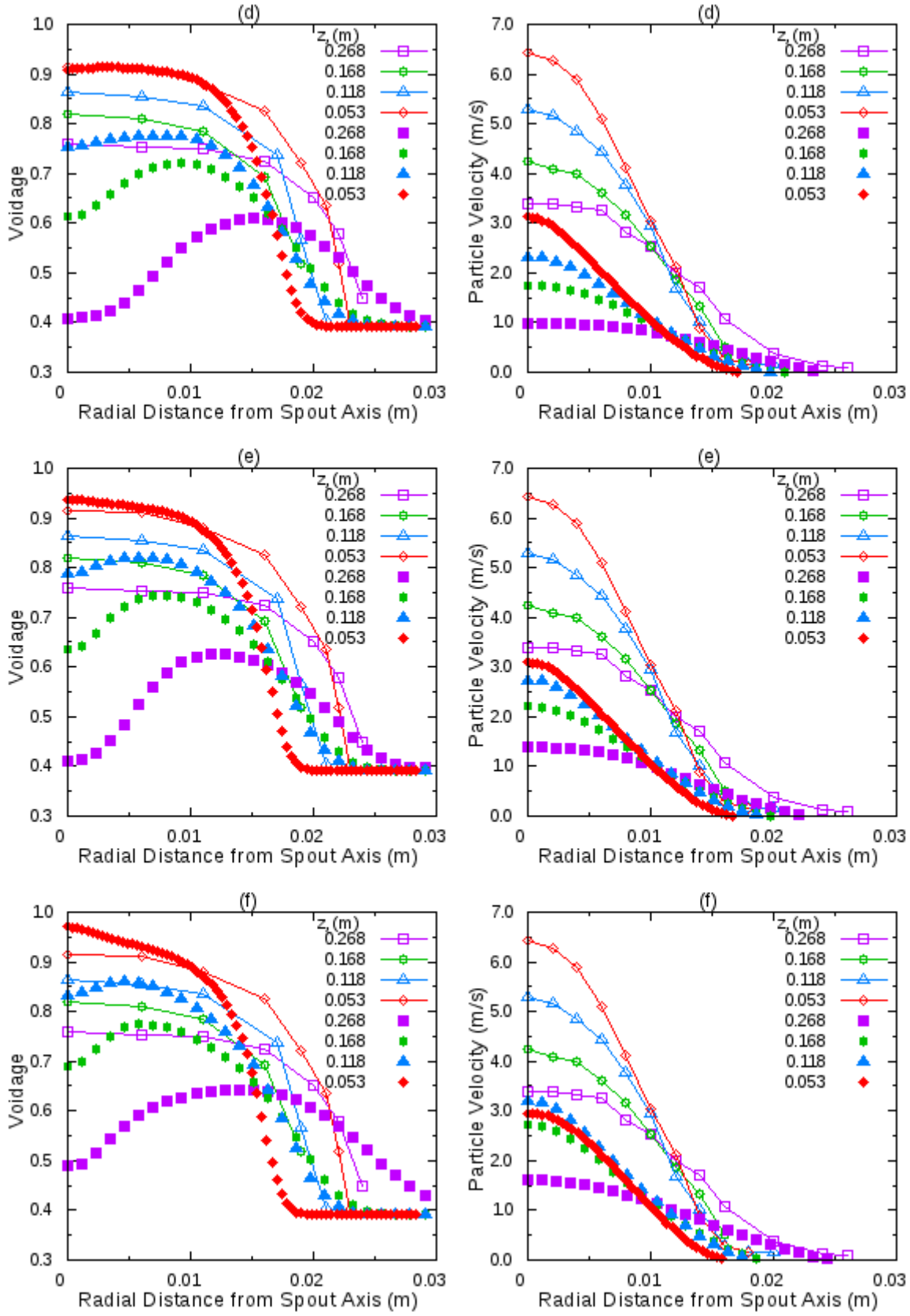

Figure 6.11 Comparison of Syamlal-O'Brien drag model voidage and particle velocity profiles of $\alpha_{s,max}$=0.61 d) e_{ss} =0.95, e) e_{ss} =0.90, f) e_{ss} =0.80 case with experimental results (open pointers).

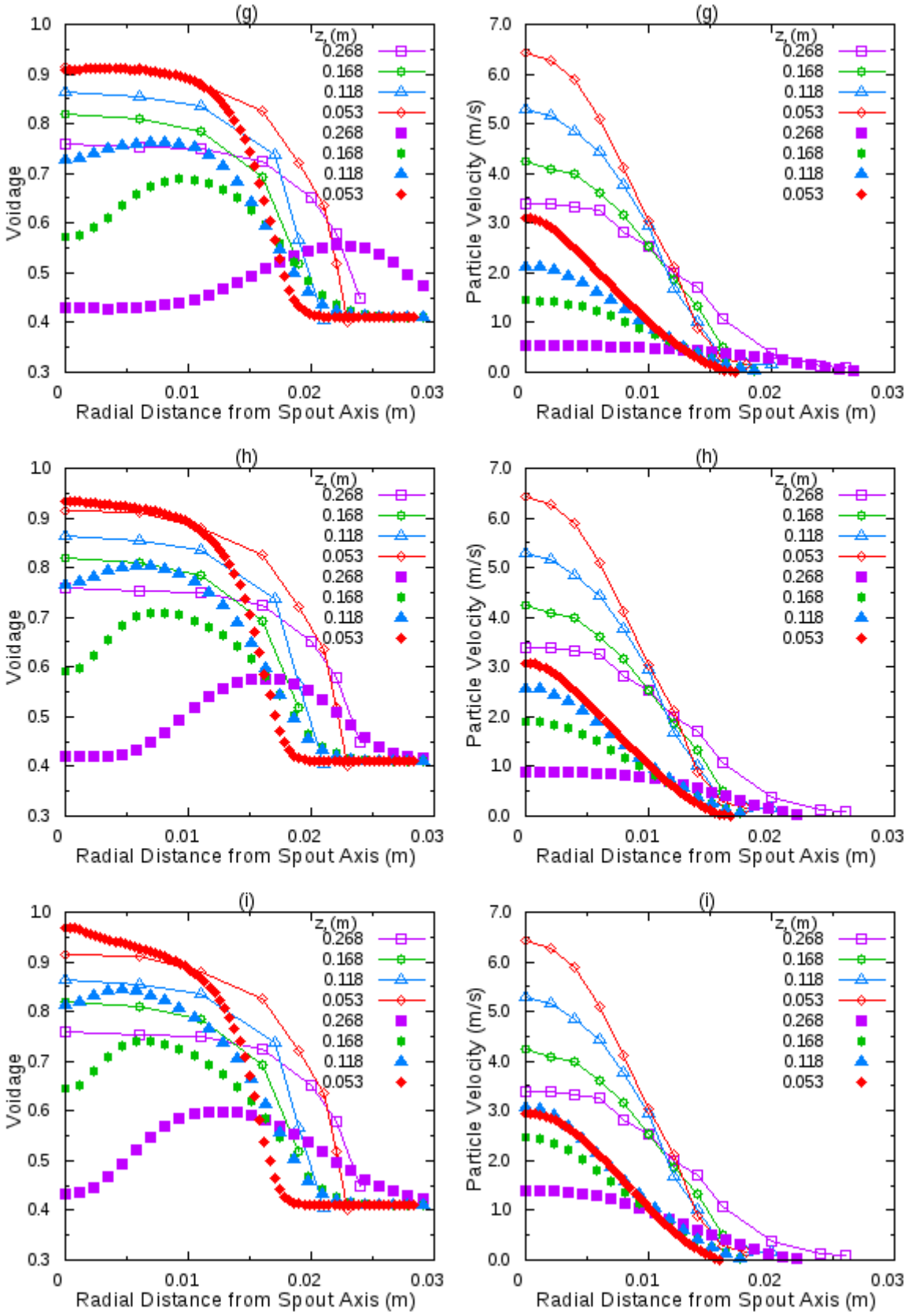

Figure 6.12 Comparison of Syamlal-O'Brien drag model voidage and particle velocity profiles of $\alpha_{s,max}$=0.59 d) e_{ss} =0.95, e) e_{ss} =0.90, f) e_{ss} =0.80 case with experimental results (open pointers).

Table 6.7 Area weighted average kinetic parameters of solid phase for Syamlal-O'Brien drag model (t=15.0 s).

Maximum Packing Limit ($\alpha_{s,max}$)	Restitution Coefficient (e_{ss})	Bulk Viscosity (kg/m-s)	Molecular Viscosity (kg/m-s)	Granular Pressure (Pa)	Granular Temperature
0.63	0.95	4.68	2.22	48.11	0.0015943
	0.90	3.83	1.82	33.90	0.0018237
	0.80	3.24	1.54	27.84	0.0014507
0.61	0.95	4.94	2.27	50.15	0.0010251
	0.90	4.08	1.87	36.12	0.0010410
	0.80	3.44	1.58	28.11	0.0011217
0.59	0.95	4.77	2.12	46.45	0.0006828
	0.90	4.19	1.86	36.20	0.0006273
	0.80	3.53	1.57	28.72	0.0004869

In conclusion, since the superficial gas velocity used for the simulations is 1.3 times of the minimum spouting velocity, for this particular case maximum packing values of 0.59 and 0.61 are not appropriate because they do not cause proper spouting as reported in the experiment.

6.3.2 The influence of restitution coefficient

Figure 6.5 and Figure 6.6 show that the fountain height increases with decreasing restitution coefficient. Figure 6.7 to Figure 6.12 indicates that particle velocity and voidage increases as restitution coefficient decreases for all measurement height results and for all combinations of drag model and maximum packing limit. The decrease in restitution coefficient results in drop of bed pressure drop as seen in Table 6.4.

The restitution coefficient indicates amount of energy loss in particle-particle collision. It has a value of one for perfectly elastic collisions. It is less than one for inelastic collisions where momentum loss occurs. Decrease in restitution coefficient results in decrease in granular temperature which is a measure of the kinetic energy contained in the fluctuating velocity of particles. On the other hand, the restitution coefficient directly affects the kinetic parameters of solid phase as seen in equation (6.2) for collisional viscosity, (6.3) for bulk viscosity, and (6.4) for solid phase pressure. Solid phase pressure is indication of momentum transferred

by the shear stress caused by the flow of particles and momentum transferred between particle collisions.

$$\mu_{s,col} = \frac{4}{5}\alpha_s \rho_s d_s g_0 (1 + e_{ss}) \left(\frac{\theta_s}{\pi}\right)^{1/2} \quad (6.2)$$

$$\lambda_s = \frac{4}{3}\alpha_s \rho_s d_s g_0 (1 + e_{ss}) \left(\frac{\theta_s}{\pi}\right)^{1/2} \quad (6.3)$$

$$p_s = \alpha_s \rho_s \theta_s + 2\rho_s (1 + e_{ss}) \alpha_s^2 g_0 \theta_s \quad (6.4)$$

It is seen in Table 6.6 and Table 6.7 that all kinetic parameters of the solid phase decrease with lowering the restitution coefficient. But this decline is small for granular temperature and its effect on kinetic parameters is less significant than the restitution coefficient itself. The argument here is that although the particle energy decreases due to lowering the restitution coefficient the particle velocity increases because the decrease in viscosity is the dominant factor on hydrodynamic calculations.

Although the decrease of restitution coefficient increases the calculated fountain height from simulations, they are still lower than 0.695 m measured during experiments. The combination referred as case c in Figure 6.5 gives 0.451 m fountain height which is the closest one to the experimental value.

6.3.3 The influence of drag model

Several well known drag models are implemented in FLUENT to be used for different applications of fluidization. It is also possible to include other models by using user defined function feature of the code. This study was focused on Gidaspow and Syamlal-O'Brien drag models which are the two commonly used ones for the spouted bed simulations.

The instantaneous particle concentrations in Figure 6.5 and Figure 6.6 show that Syamlal-O'Brien drag model results in considerably higher fountain heights for all combinations of maximum packing limit and restitution coefficient.

When particle velocity and voidage distributions in Figure 6.7 to Figure 6.12 are analyzed, it is seen that cases using Syamlal-O'Brien drag model predictions for

particle velocity is higher than the cases using Gidaspow drag model for all combinations of maximum packing limit and restitution coefficient. As a result voidages are also higher for Syamlal-O'Brien drag cases.

Bed pressure drop predictions for all Syamlal-O'Brien drag model cases are lower than Gidaspow drag model cases as seen in Table 6.4.

For all cases throughout this chapter Syamlal-O'Brien drag model cases predicted higher fountain height, higher particle velocity profile, and more bed expansion than the Gidaspow drag model cases. This is because of the fact that by its formulation Syamlal-O'Brien drag model results in higher solid-gas momentum exchange coefficient as seen in Figure 6.13. Therefore, momentum transfer from gas to solid is more for Syamlal-O'Brien drag model cases. This obviously results in higher particle velocity predictions.

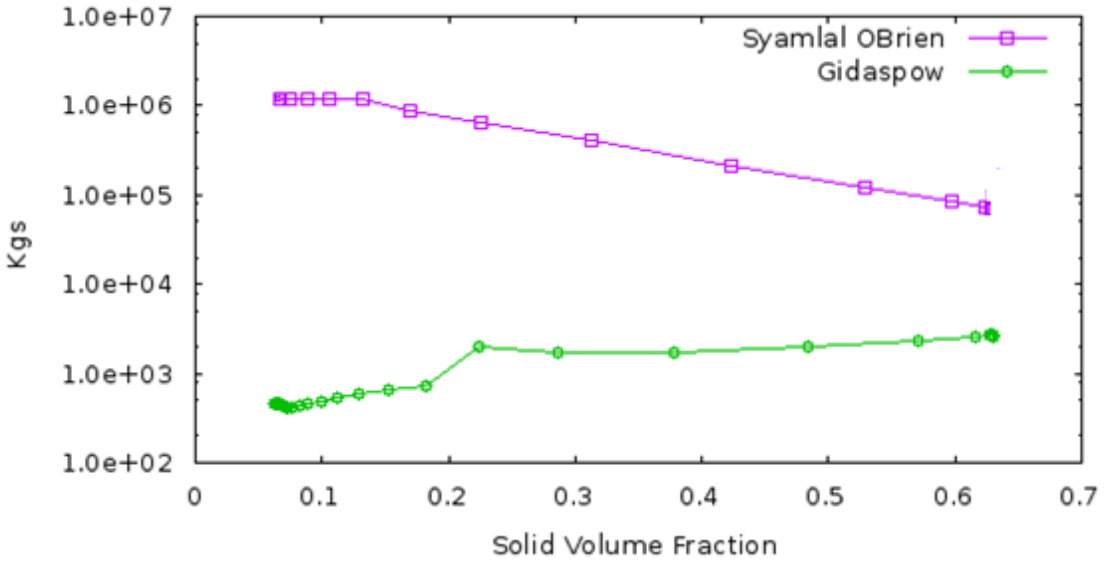

Figure 6.13 Comparison of gas-solid momentum exchange coefficient for z=0.053 m of Gidaspow and Syamlal-O'Brien drag models (t=15.0 s, e_{ss} =0.80, $\alpha_{s,max}$=0.63).

6.3.4 The influence of solid frictional viscosity

The solid shear stress tensor described before contains shear and bulk viscosities due to particle momentum exchange resulting from collision, translation and friction. A frictional component of the viscosity accounts the viscous-plastic transition when solid volume fraction reaches the maximum solid volume fraction.

In order to examine the effect of solid frictional viscosity on the results of simulations of spouted beds, Schaeffer model which is developed for very-dense gas-solid systems is adopted. Frictional part for the stress and viscosity of the solid particles are added to the kinetic theory equations. The formulation can be summarized as follows:

$$P_s = P_{kinetic} + P_{friction} \tag{6.5}$$

$$\mu_s = \mu_{kinetic} + \mu_{friction} \tag{6.6}$$

$$P_{friction} = A(\alpha_s - \alpha_{s,min})^n \tag{6.7}$$

$$\mu_{friction} = \frac{P_{friction}}{\alpha_s \sqrt{\frac{1}{6}\left[\left(\left(\frac{\partial u_s}{\partial x}\right)^2 + \left(\frac{\partial v_s}{\partial y}\right)^2\right)^2 + \left(\frac{\partial v_s}{\partial y}\right)^2 + \left(\frac{\partial u_s}{\partial x}\right)^2\right] + \frac{1}{4}\left[\left(\frac{\partial u_s}{\partial y}\right)^2 + \left(\frac{\partial v_s}{\partial x}\right)^2\right]^2}} \tag{6.8}$$

where ϕ is the internal friction angle of particles, and *A* and *n* are constants (Fluent, 2006).

A sample case referred as case b (e_{ss} =0.90, $\alpha_{s,max}$=0.63) in Figure 6.5 was used for the simulations with and without solid frictional viscosity. The influence of inclusion of frictional viscosity on the instantaneous particle concentrations can be seen in Figure 6.14 and Figure 6.15 for Gidaspow and Syamlal-O'Brien drag models. Addition of solid frictional viscosity to kinetic theory equations slightly increases the fountain height.

The voidage and particle velocity profiles in Figure 6.16 indicate that for Gidaspow drag model, inclusion of frictional stress into simulations increases the voidage especially at higher positions in the bed and has no effect on particle velocity distributions. Similar behavior is observed for voidage distributions in Syamlal-O'Brien drag model case. However, inclusion of frictional stress into simulations for the case using Syamlal-O'Brien drag model case behaves differently for particle velocity distribution predictions. Inclusion increases particle velocity especially for higher positions in the bed as seen in Figure 6.17.

Total pressure drop results from simulations with percent errors are seen in Table 6.8. As seen from the table, inclusion of frictional stress into simulations decreases pressure drop dramatically.

Table 6.8 Simulated total pressure drop values with and without solid frictional stress for sample case e_{ss} =0.90, $\alpha_{s,max}$=0.63.

	Gidaspow Drag Model	**Syamlal-O'Brien Drag Model**
Without $\mu_{s,fric}$	3565 Pa (18.8%)	3539 Pa (17.9%)
With $\mu_{s,fric}$	2838 Pa (5.4%)	2853 Pa (4.9%)

When the area weighted average kinetic parameters of the solid phase are examined, it is seen that the frictional viscosity is extremely higher than the bulk and molecular viscosity as shown in Table 6.9 and Table 6.10.

Table 6.9 Area weighted average kinetic parameters of solid phase for Gidaspow drag model (t=15.0 s, e_{ss} =0.90, $\alpha_{s,max}$=0.63).

Bulk Viscosity (kg/m-s)	**Molecular Viscosity (kg/m-s)**	**Frictional Viscosity (kg/m-s)**	**Granular Pressure (Pa)**	**Granular Temperature**
3.99	1.89	-	36.24	0.0011095
3.55	13.63	735.76	27.79	0.0011904

Table 6.10 Area weighted average kinetic parameters of solid phase for Syamlal-O'Brien drag model (t=15.0 s, e_{ss} =0.90, $\alpha_{s,max}$=0.63)

Bulk Viscosity (kg/m-s)	**Molecular Viscosity (kg/m-s)**	**Frictional Viscosity (kg/m-s)**	**Granular Pressure (Pa)**	**Granular Temperature**
3.83	1.82	-	33.90	0.0018237
3.50	13.20	702.69	27.86	0.0017121

With this high value of frictional viscosity it is expected to have smaller fountain height and lower particle velocity profiles with inclusion of solid frictional stress into simulations. On the contrary, it seemed that solid frictional stress has no significant effect on simulations other than pressure drop calculations.

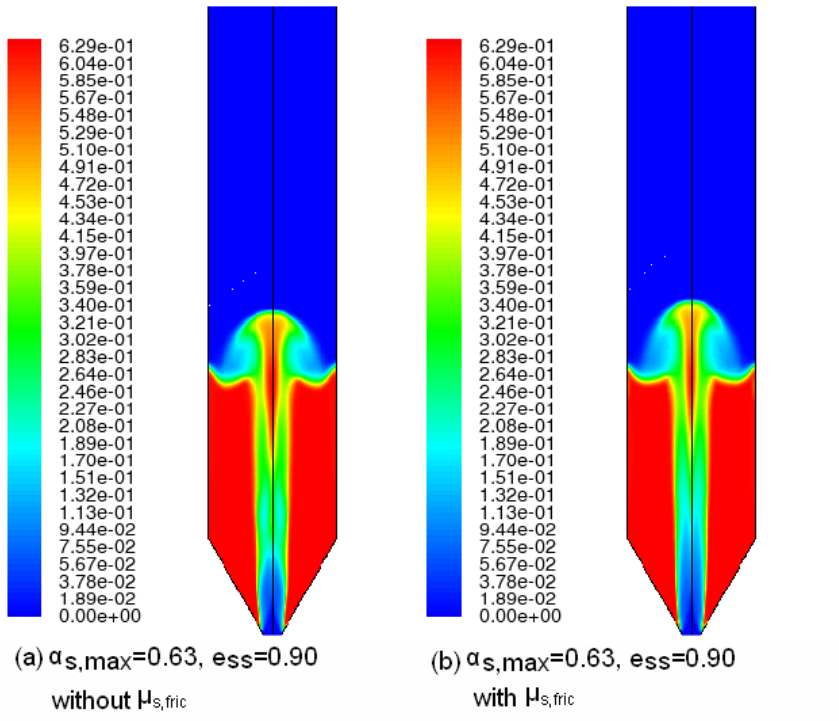

Figure 6.14 Instantaneous (t=15s) particle concentration distributions of Gidaspow drag model with and without solid frictional stress term.

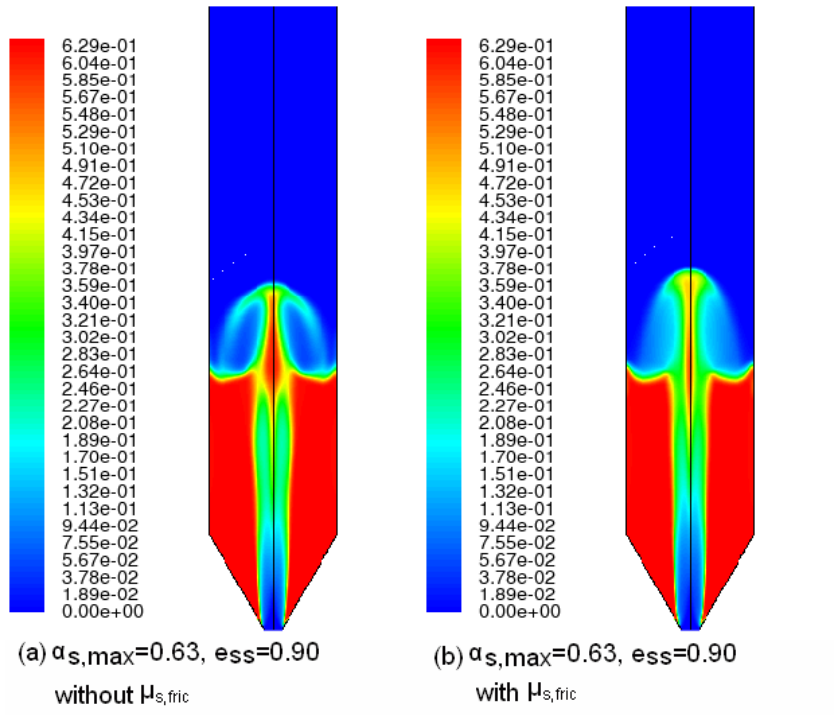

Figure 6.15 Instantaneous (t=15s) particle concentration distributions of Syamlal-O'Brien drag model with and without solid frictional stress term.

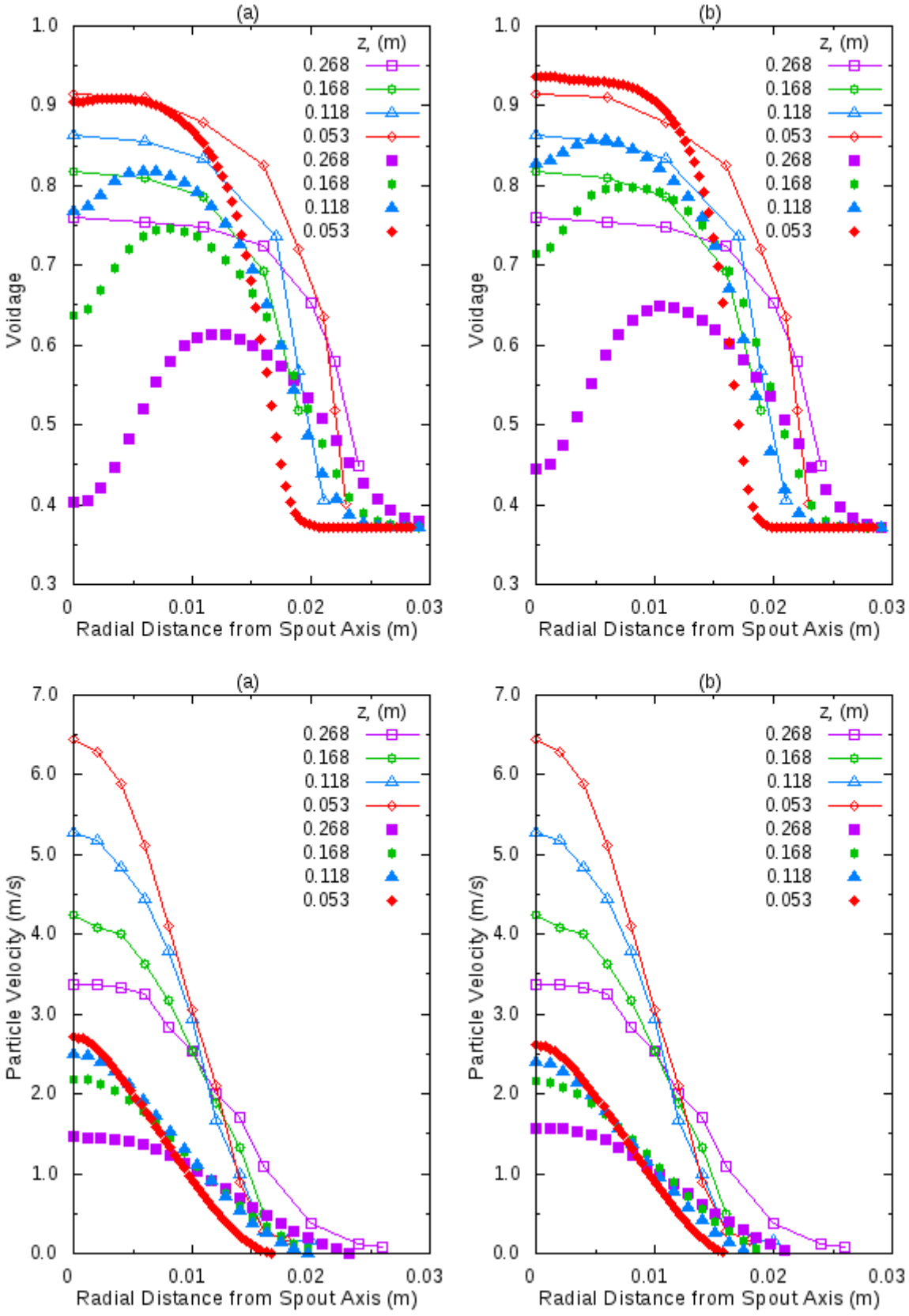

Figure 6.16 Comparison of results of Gidaspow drag model voidage and particle velocity profiles of a) without b) with solid frictional stress term with experimental results (open pointers).

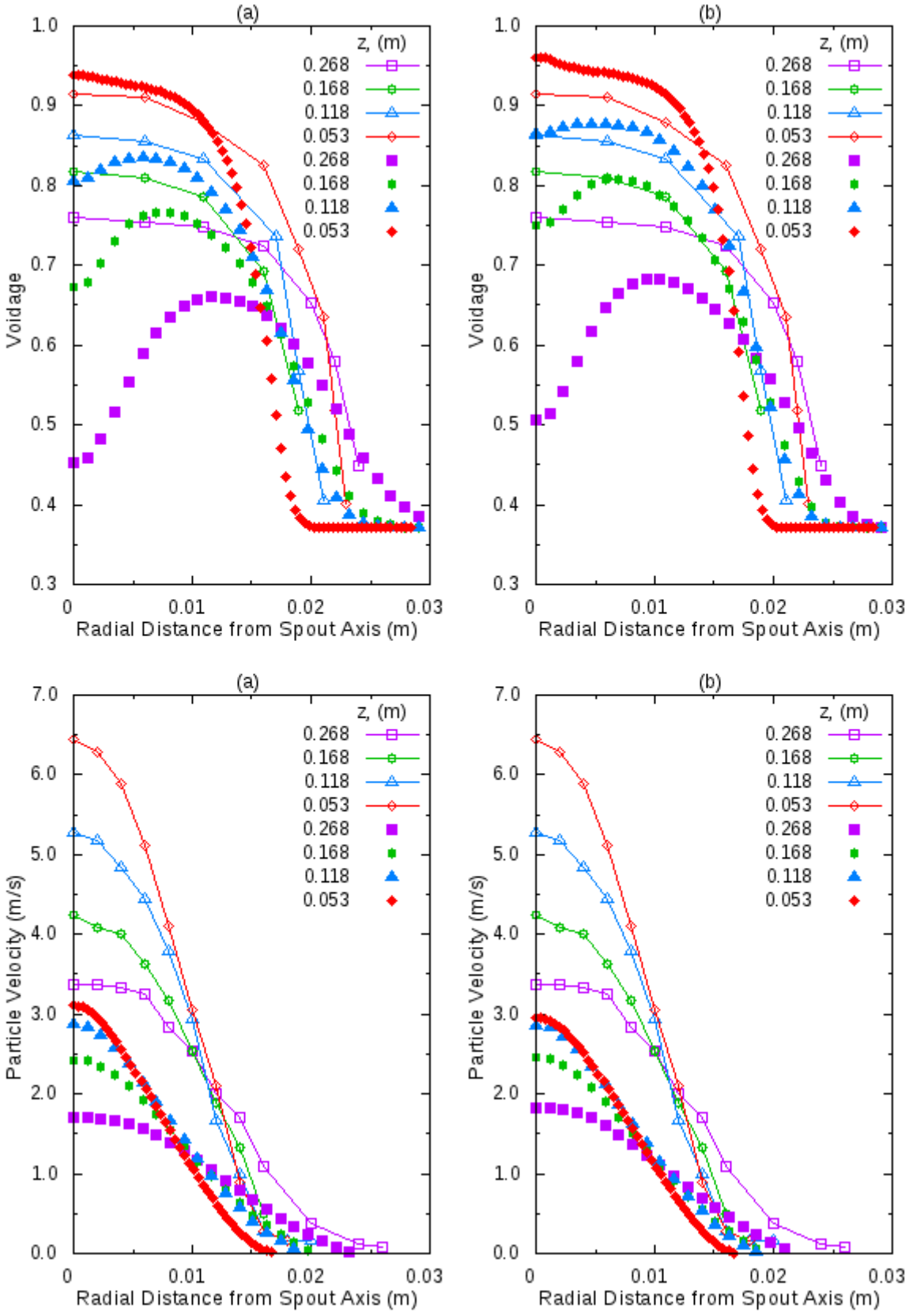

Figure 6.17 Comparison of results of Syamlal-O'Brien drag model voidage and particle velocity profiles of a) without b) with solid frictional stress term with experimental results (open pointers).

6.3.5 The influence of drag coefficient

The forces acting on phases in momentum conservation equation are the gravitational force, the external body force, the lift force, the virtual mass force, and interaction force between the phases.

When a solid particle accelerates relative to the continuous phase it accelerates a certain amount of fluid around it. This acceleration of fluid generates extra “added mass”. The virtual mass effect is significant when the secondary phase density is much smaller than the primary phase density (e.g., for a transient bubble column).

The lift force is a force on a particle that is perpendicular to motion due to vortices or shear in continuous phase. It is important if phases separate quickly.

Due to large density difference between the solid and gas phase in spouted beds, the lift force and virtual mass force are less significant than the drag force. Therefore, the drag coefficient is very important for the hydrodynamic simulation of spouted beds.

In order to analyze the influence of drag coefficient, a sample case referred as case b in Figure 6.6 was selected (Syamlal-O’Brien drag model, e_{ss}=0.9, $\alpha_{s,max}$=0.63, and without $\mu_{s,fric}$) .

The drag coefficient adopted by Syamlal-O’Brien drag model was modified by using user defined function (UDF) feature of FLUENT. A C program was written and hooked to the input file as interpreted form. Necessary changes were performed to use it for parallel computing. The 4, 3, and 2 times of the original Syamlal-O’Brien drag coefficient were generated for the simulations.

Figure 6.18 shows that when the drag force is increased the fountain height increases as expected since more drag force causes particles to move further in the spout.

Bed pressure drop results in Table 6.11 indicate that as the magnitude of drag coefficient increases, bed pressure drop increases.

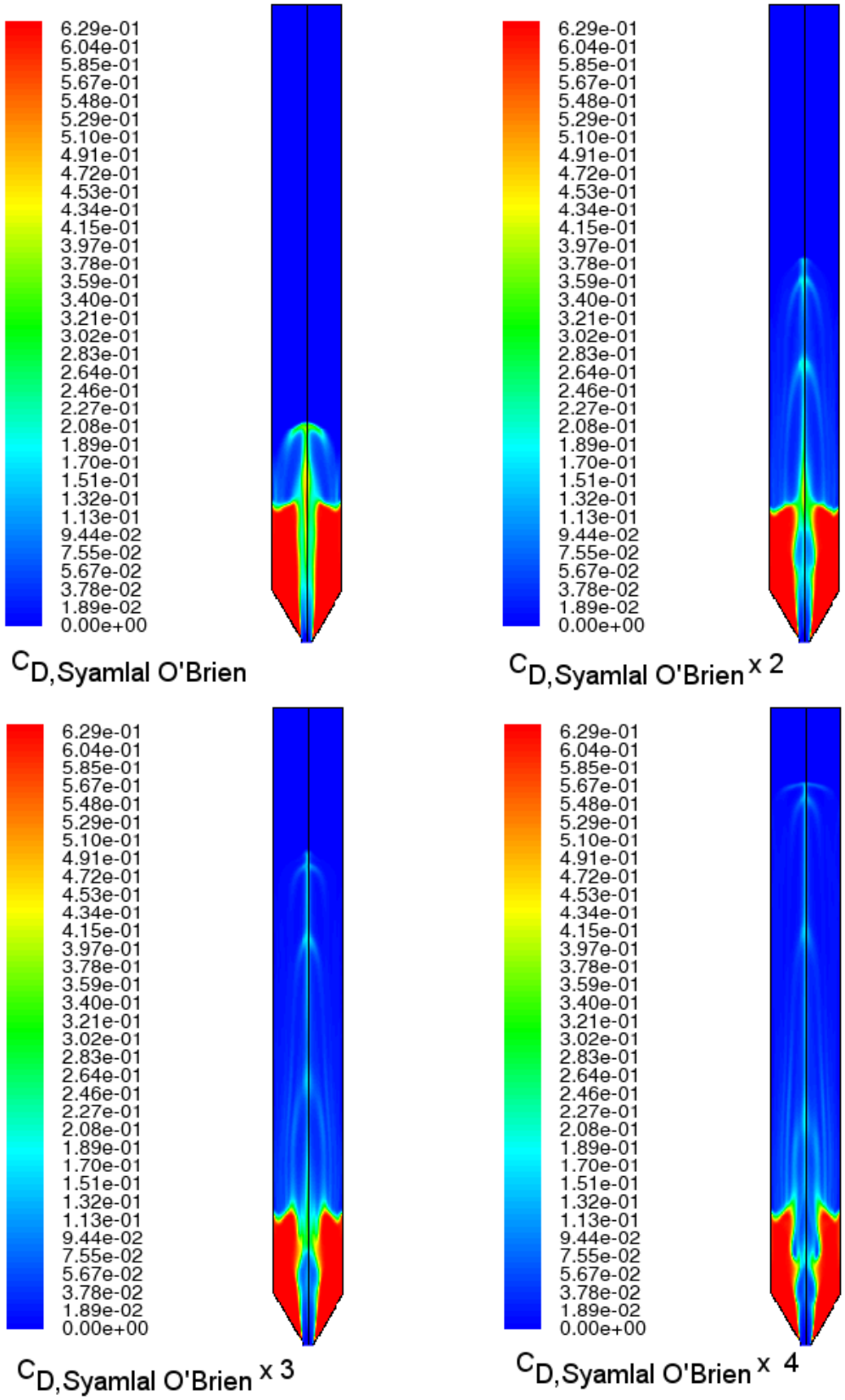

Figure 6.18 Instantaneous (t=15s) solid volume fraction of 2, 3, and 4 times of the Syamlal-O'Brien drag coefficient model without $\mu_{s,fric}$.

Table 6.11 Calculated pressure drops of cases 1, 2, 3, and 4 times of the Syamlal-O'Brien drag coefficient.

	x1	**x2**	**x3**	**x4**
Pressure Drop (Pa)	3634	3685	3699	3707

To see the effect of solid frictional viscosity together with doubling the drag coefficient, doubling the drag coefficient case with frictional stress term was tried. The results indicate that pressure drop value reduced to 2962 Pa from 3685 Pa.

It should also be pointed out that when the drag coefficient quadrupled pneumatic transport of particles out of the bed starts.

The increase in drag coefficient shifts the average voidage and particle velocity profiles up as seen in Figure 6.19 to Figure 6.22.

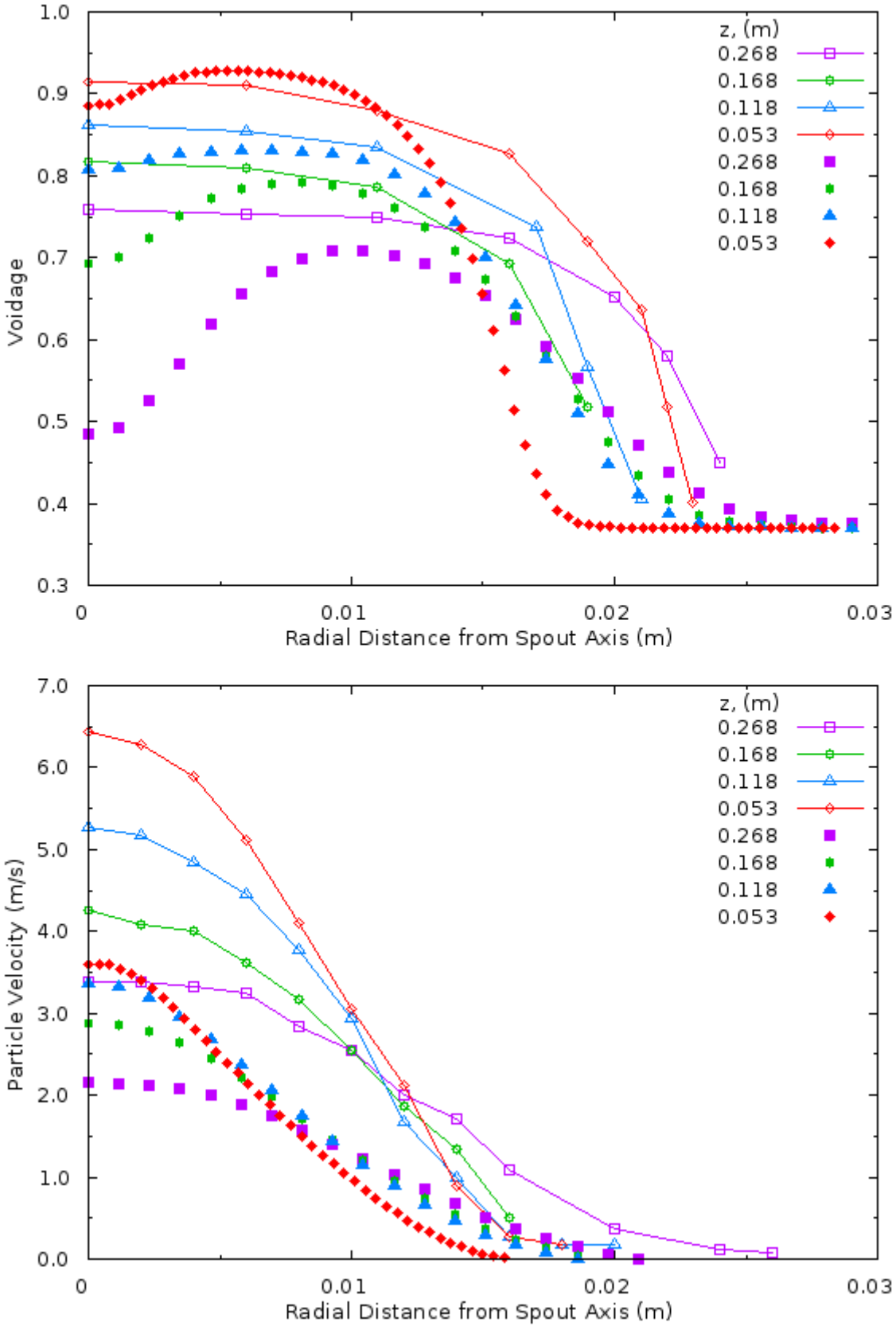

Figure 6.19 Comparison of voidage and particle velocity profiles of e_{ss} =0.90, $\alpha_{s,max}$=0.63, 1 times Syamlal-O'Brien drag model without $\mu_{s,fric}$ case with experiment (open pointers).

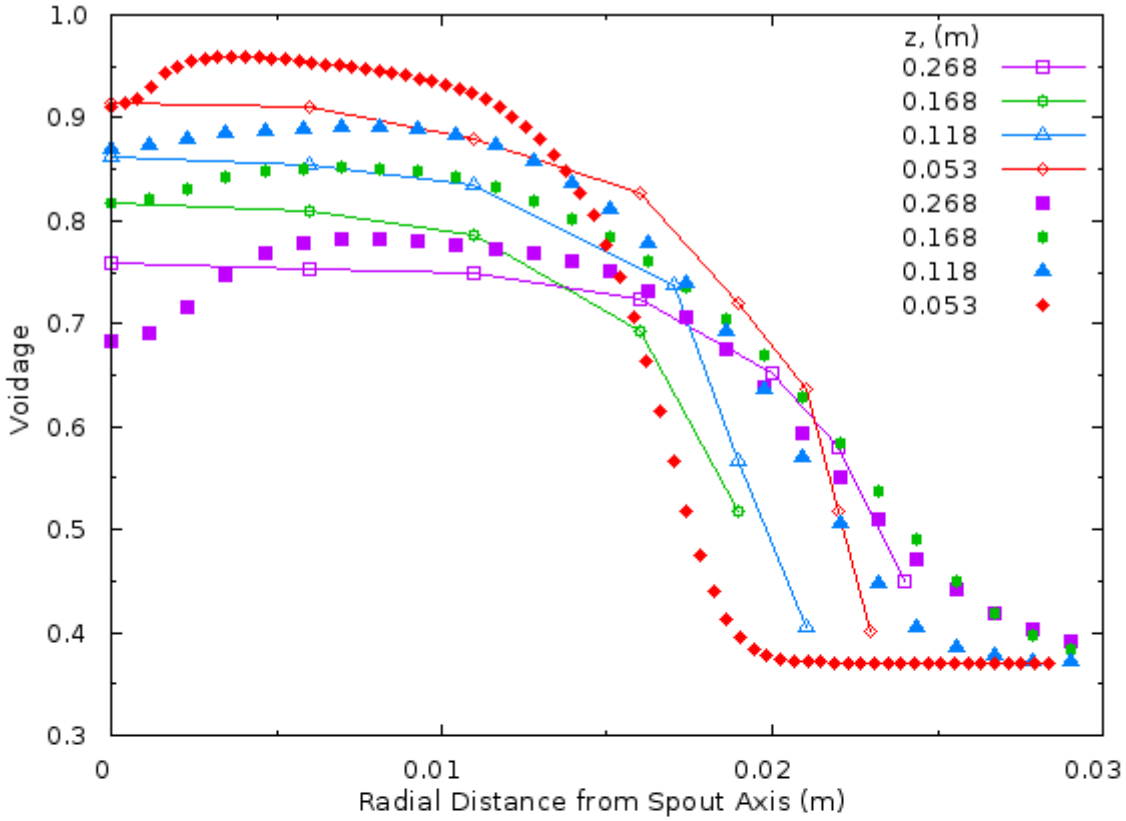

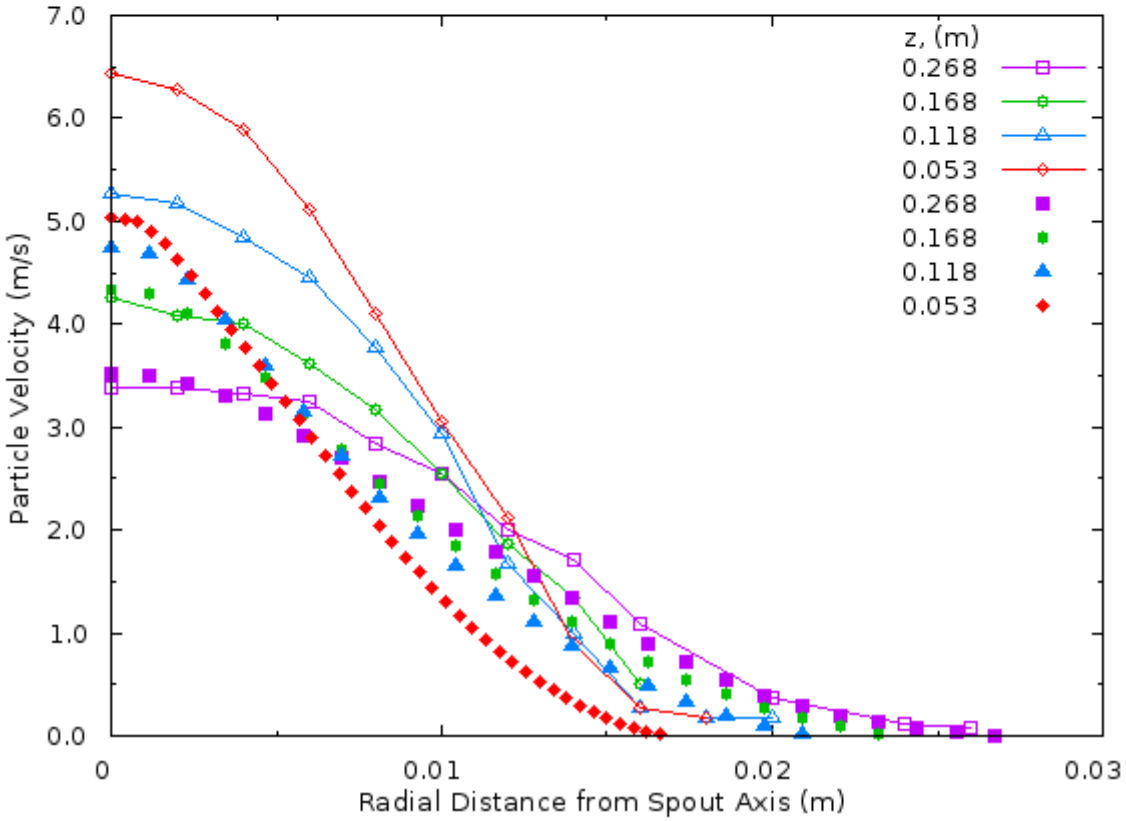

Figure 6.20 Comparison of voidage and particle velocity profiles of e_{ss} =0.90, $\alpha_{s,max}$=0.63, 2 times Syamlal-O'Brien drag model without $\mu_{s,fric}$ case with experiment (open pointers).

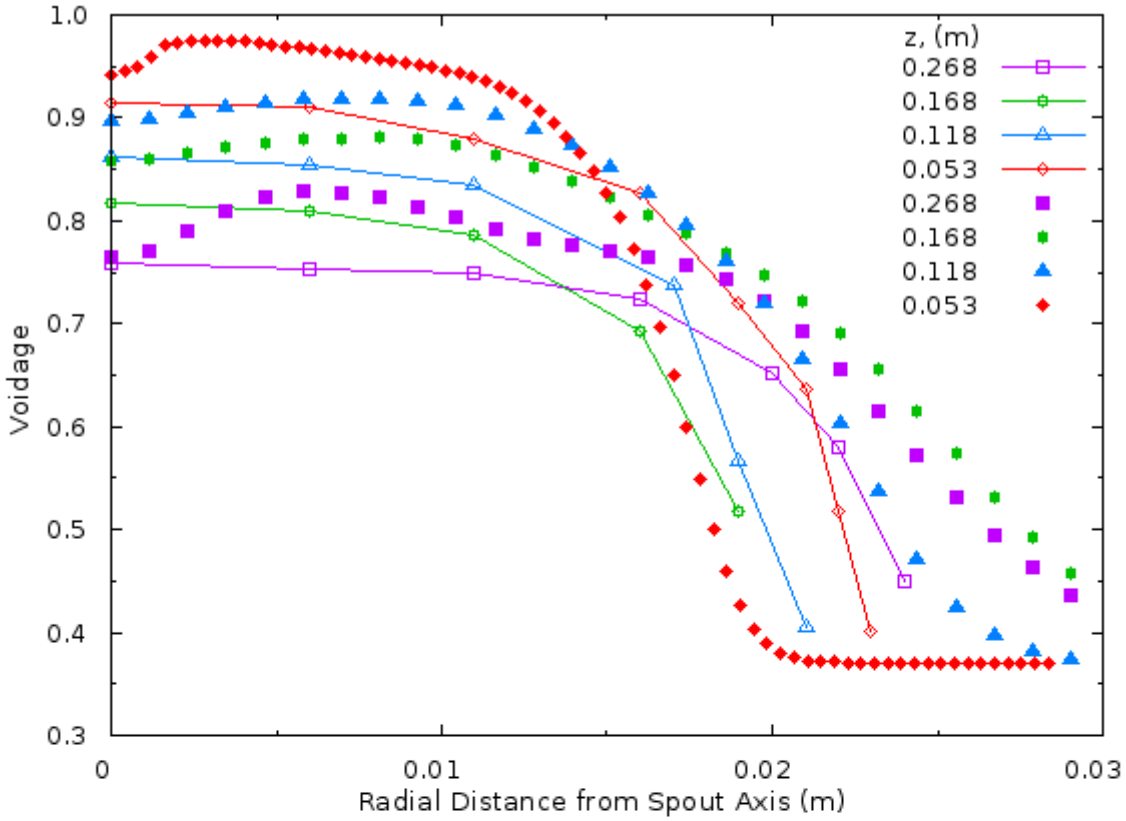

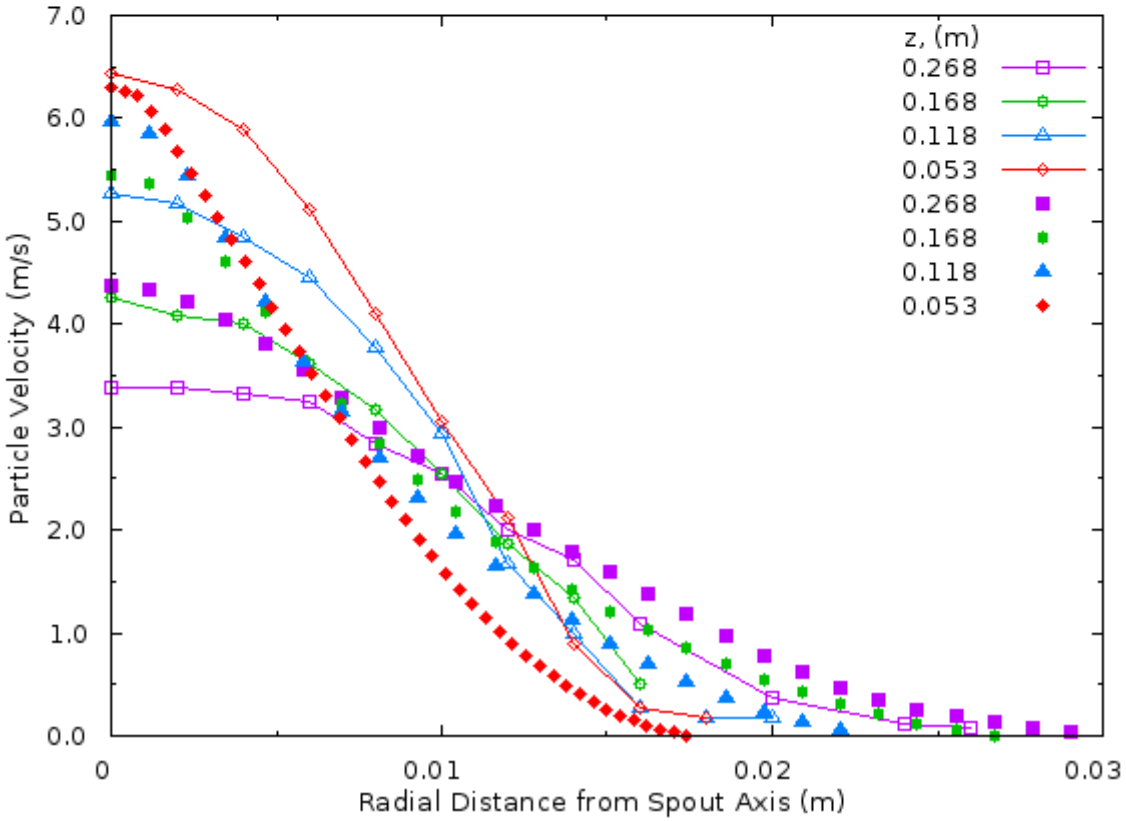

Figure 6.21 Comparison of voidage and particle velocity profiles of e_{ss} =0.90, $\alpha_{s,max}$=0.63, 3 times Syamlal-O'Brien drag model without $\mu_{s,fric}$ case with experiment (open pointers).

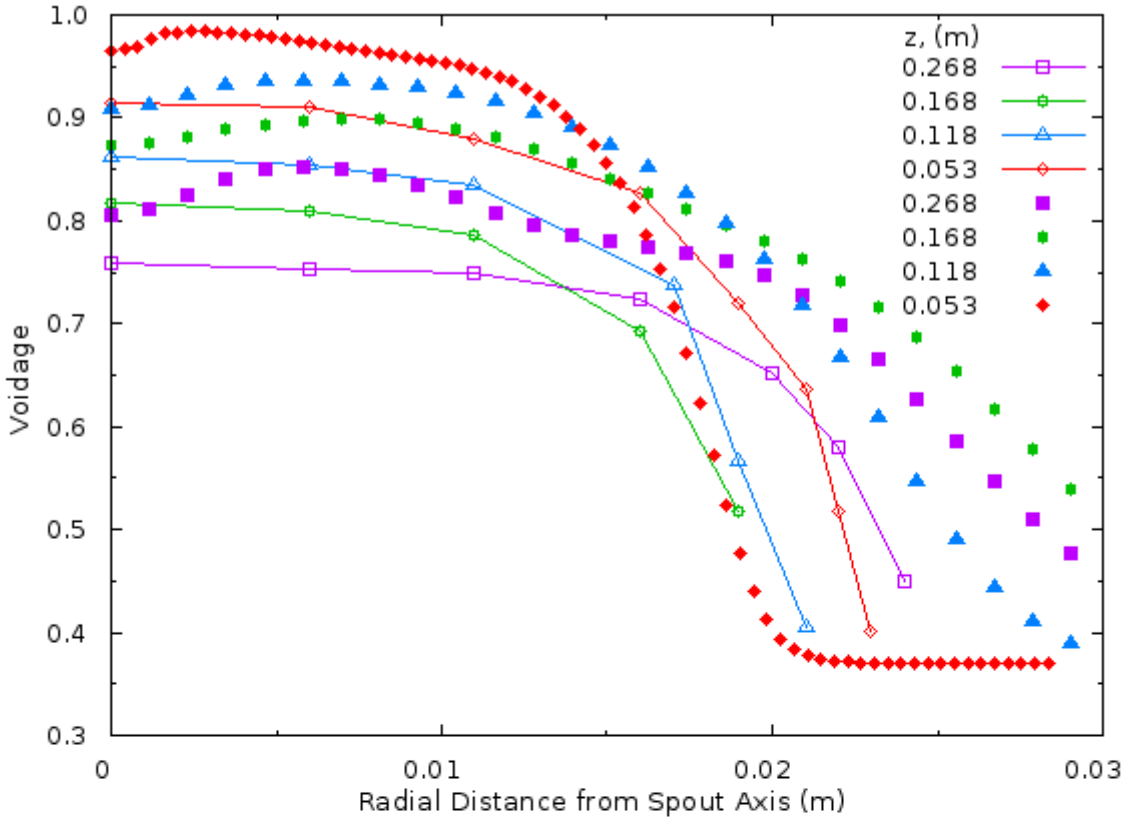

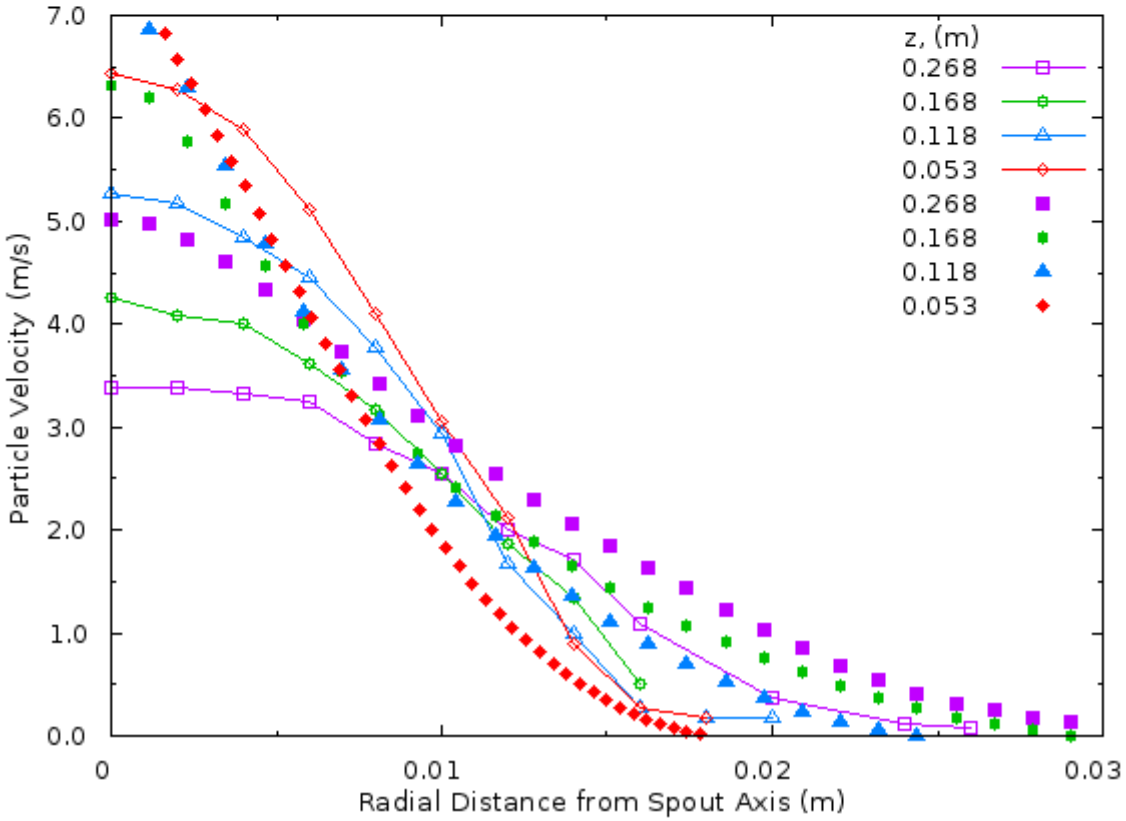

Figure 6.22 Comparison of voidage and particle velocity profiles of e_{ss} =0.90, $\alpha_{s,max}$=0.63, 4 times Syamlal-O'Brien drag model without $\mu_{s,fric}$ case with experiment (open pointers).

6.4 Results and Discussions

In this section, effects of maximum packing limit, restitution coefficient, drag model, solid frictional stress, and value of drag coefficient on hydrodynamic simulation of spouted beds filled with light particles of density 2500 kg/m^3 was investigated. For this purpose well known experimental set referred as He et al. was used.

The effects of above mentioned parameters and their concurrency with studies in the literature are summarized below. It should be mentioned that most of the studies in the literature focus on the effect of one of the above mentioned parameters on particle velocity and voidage at a time and there is not any study in the literature investigating the effects of all parameters on bed pressure drop.

1. The effect of maximum packing limit

   As maximum packing limit decreases, the values of particle velocity and voidage decrease for all combinations of restitution coefficient and drag model. This outcome is consistent with the findings of Du et al. (2006b). Its effect on bed pressure drop cannot be determined since any particular pattern could not be inferred from the results of the simulations. Its decrease causes high deviations from the experimental results for particle velocity and voidage distributions but there is not any specific pattern for bed pressure drop predictions.
2. The effect of restitution coefficient

   As the restitution coefficient decreases, the values of particle velocity and voidage increase for all combinations of drag model and maximum packing limit. This same effect of restitution coefficient on particle velocity and voidage is also observed in Du et al. (2006b) and Wang (2006). Bed pressure drop also decreases when restitution coefficient decreases. When restitution coefficient decreases all results agree better with experimental results.
3. The effect of drag model

   Syamlal-O'Brien drag model results in higher particle velocity and voidage distributions (the opposite is reported in Du et al. (2006b)) but smaller bed pressure drop. Syamlal-O'Brien drag model case predictions for particle

velocity and voidage are closer to experimental results than the Gidaspow drag model predictions but the opposite is observed for bed pressure drop predictions.

4. The effect of solid frictional stress

   Its effect changes with drag model used. For Gidaspow drag model, it seems to have no effect on particle velocity and voidage distributions. But for Syamlal-O'Brien drag model case, its inclusion increases both particle velocity and voidage distributions. The findings of Shuyan et al. (2009) show the opposite behavior. For both drag model cases, bed pressure drop decreases dramatically when solid frictional stress is included in simulations. Its inclusion in the simulations results in better estimations of particle velocity and pressure drop.

5. The effect of magnitude of drag coefficient

   The increase in magnitude of drag coefficient increases both particle velocity and voidage values (agrees well with Wang et al. (2006)) and slightly increases the bed pressure drop.

The maximum packing limit has direct influence on hydrodynamics of the spouted bed. Because, no matter what the other parameters are, lower maximum packing limit values did not cause proper external spouting. It can be said that the maximum packing limit for this particular case should be 0.63 to get a proper external spouting as reported in the original experiment. Because the value of 0.59 causes only internal spouting while 0.61 creates either internal or external spouting with very small spout height depending on other parameters.

The influence of restitution coefficient is that the decrease in its value increases the fountain height, bed expansion, and velocity although all kinetic parameters of the solid phase decrease. It is expected that decrease in granular temperature results in lower particle velocity predictions. But the simulation results showed an opposite trend which may be because of the decrease in solid viscosity, which may be more dominant in hydrodynamic simulations. Effects of restitution coefficient in CFD simulation are not very clear. The argument here is that how much it can be reduced without disturbing the actual hydrodynamics. The experimental determination of it may be a good option.

The drag models tried during this study are appropriate for the simulations of spouted beds. By its formulations, the Syamlal-O'Brien drag model results in higher drag coefficient therefore higher voidage and velocity profile predictions. As mentioned above the opposite was reported in Du et al. (2006b). The reason for this inconsistency about the effect of drag model on particle velocity could be the value of maximum packing limit used in both studies. Du used maximum packing limit value of 0.59 during simulations, the value which was found improper as a result of simulations performed in this study.

The simulation results showed that the frictional viscosity is order of magnitude higher than bulk and molecular viscosity. But its effect on particle velocity and voidage profiles is not as significant as expected. The inclusion of solid frictional stress into the simulations only helped to reduce the error in pressure drop calculations. The effect of inclusion of frictional stress into simulations observed in this study and Shuyan et al. (2009) does not agree to each other as mentioned above. The reason could be due to the value of maximum packing limit used. Shuyan used maximum packing limit value of 0.59 during simulations, the value which was found improper as a result of simulations performed in this study.

The results show that drag force is the most important force for the simulations of spouted beds and magnitude of it can affect the simulations dramatically. Increasing the drag force may cause unrealistic simulation results like pneumatic transport of particles out of the bed.

When the voidage profiles through the simulations are examined, it is clearly seen that the voidage decreases with increasing axial distance as particle velocity. This is confirmed with experimental results.

The particle velocity is underestimated for all cases tried except for the cases where the magnitude of drag coefficient increased artificially. Similar to particle velocity, voidage is underestimated for all cases except for measurement height of 0.053 m where voidage is overestimated or agrees well with experiments depending on parameters used for the simulations. In general, Syamlal-O'Brien drag model case predictions are closer to experimental results than the Gidaspow model predictions.

Quadrupling the drag coefficient over estimates both voidage and particle velocity distributions as well as causing pneumatic transport. Tripling also overestimates the voidage and particle velocity results. Doubling the drag coefficient results in better particle velocity predictions for the upper part of the spout (lines z=0.268 m and 0.168 m in Figure 6.20). The voidage profiles are still slightly overestimated for this case.

The argument here is that the effect of increasing drag coefficient on the pressure drop is not significant, on the voidage is high, and on the particle velocity and fountain height is extreme. If the drag coefficient is increased to satisfy the velocity, the spout height and the voidage are going to be even more overestimated and even pneumatic transport may occur. If the drag coefficient is decreased to satisfy the spout height, the particle velocity profile is going to be way underestimated. Therefore, it may not be possible to find the appropriate combinations of simulation parameters for this particular case.

When all simulation results are examined closely, it is seen that simulation results underestimate particle velocity distribution at every axial level as mentioned above. In order to investigate the reasons of this situation, graph of simulated particle velocity against experimental particle velocity was plotted as seen in Figure 6.23.

It is observed that experimental results and simulation results are correlated as $v_{s,simulated} = 0.53 \times v_{s,experimental}$. This suggests that there exists a systematic error either in simulations or experiments. When the experimental results were modified according to relation shown in Figure 6.23 and plotted again, the good agreement between the experiment and simulation results is achieved as seen in Figure 6.24. This outcome is consistent with the findings of Wang (2006) as seen in Figure 6.25. The correlation constant of Wang (2006) is naturally different from the one found in this study because of different models and model parameters used in Wang's study.

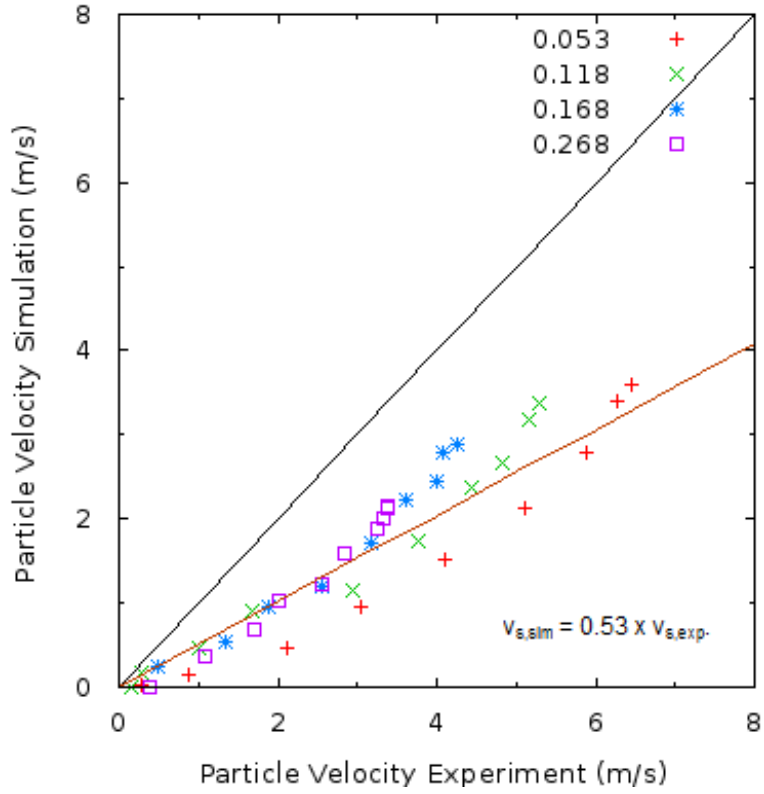

Figure 6.23 Comparison between the experimental and simulation results of particle velocity.

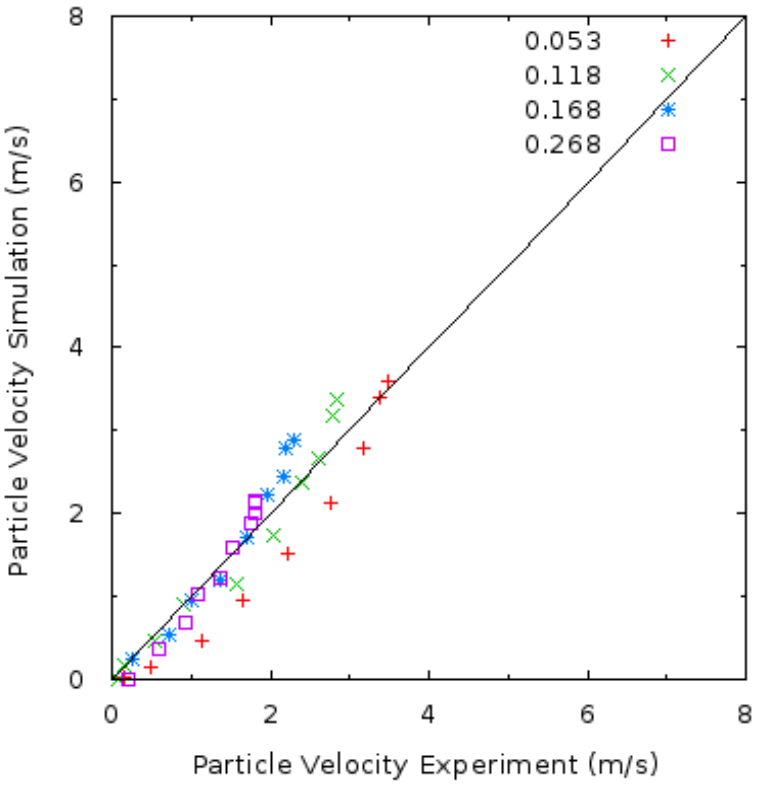

Figure 6.24 Comparison between the adjusted experimental and simulation results of particle velocity.

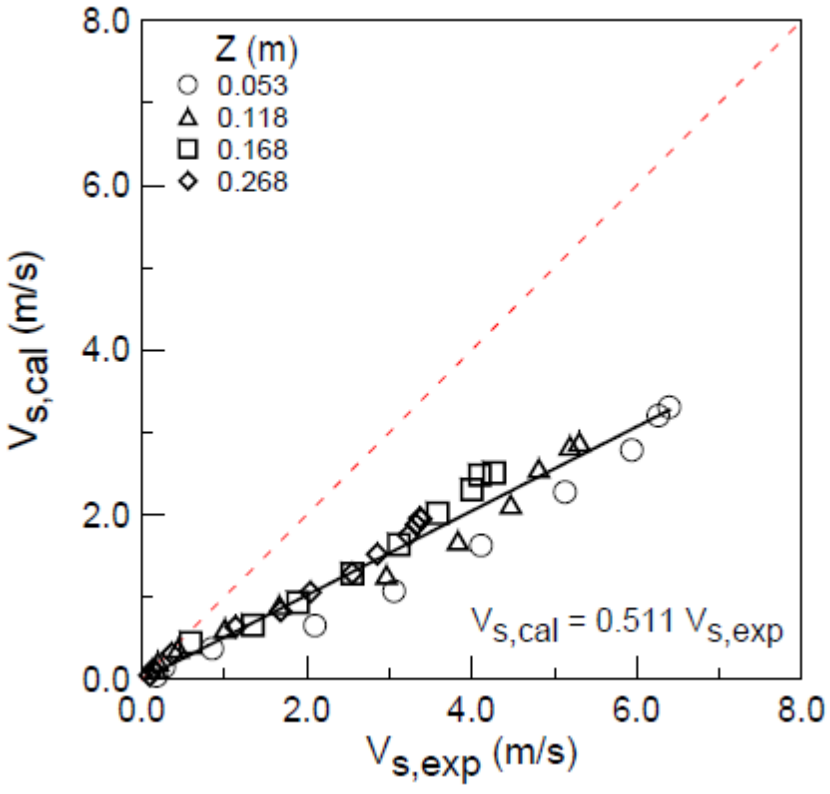

Figure 6.25 The particle velocity distribution comparison between the experimental results and simulation results of Wang (2004).

It is also seen that there is a denser particle zone surrounding the spout axis which is obvious especially for the upper part of the spout. Table 6.12 shows the literature review about the existence of denser particle zone surrounding the spout axis. It is clear from Table 6.12 that it is observed in every study using FLUENT axisymmetric geometric model, using K-FIX full or symmetric geometric model, and M-FIX full geometric model showing that is not related with geometric modeling used for CFD simulations. Moreover, it is found that symmetric model makes CFD simulations more stable. The interesting point is that denser particle zone is also confirmed in He's original experiment for the upper part of the bed especially for experimental setups having superficial gas velocity 1.1 and 1.2 times the minimum spouting velocity (He et al., 1994a). The result of this phenomenon could be related with radial movement of the particles and solid-solid collisions in spout region.

Table 6.12 Literature review about existence of denser particle zone.

Researcher	Existence of Denser Particle Zone	CFD Code	Geometric Model
Du et al. (2006a; 2006b)	Yes	FLUENT	Axisymmetric
Wang (2006)	Yes	FLUENT	Axisymmetric
Liu et al. (2011)	Yes	FLUENT	Axisymmetric
Lan et al. (2012)	Yes	FLUENT	Axisymmetric
Bettega et al. (2009b)	Yes	FLUENT	Axisymmetric
Huilin et al. (2001)	Yes	K-FIX	Full
Lu et al. (2004)	Yes	K-FIX	Symmetric
He et al. (2004)	Yes	K-FIX	N/A
Shuyan et al. (2009)	Yes	M-FIX	Full

7 CFD STUDIES ON HEAVY PARTICLE FILLED EXPERIMENTAL SETUP

The experimental investigation of hydrodynamic characteristics of conical cylindrical spouted beds was performed in Multiphase Flow Laboratory of Department of Mechanical Engineering in Hacettepe University, Ankara. The research was a part of TUBİTAK project (No: 108M435) and was completed in November 2011. Detailed information about the experimental setup and the measurement techniques can be found in Sari et al. (2011). Briefly, experiments were carried out in a Delrin (polyoxymethylene) conical cylindrical bed. Zirconia particles of two different sizes were used. For different design (different conic angles) and operating conditions (different static bed height, particle size) particle velocity, solid volume fraction, bed pressure drop, fountain height, and minimum spouting velocity were determined.

The CFD simulation of Sari's experimental setup was performed with FLUENT commercial CFD package and the results are presented in this chapter. The effects of drag model, restitution coefficient, and solid frictional stress on the simulation results were investigated. Then, the effects of conic angle, static bed height, particle size on particle velocity and solid volume fraction distributions were assessed.

7.1 The Experimental Setup

Sari's experimental setup shown in Figure 7.1 consists of an air compressor, pressure regulator, butterfly valves, orifice meters, air tank, rotameters, conical cylindrical spouted bed, and a computer system to record and process the measurements.

Simply, the air from the compressor passes though the regulator and is directed into any of the two lines though butterfly valve. Then thorough orifice meter, air tank which is placed to damp flow rate oscillations, and rotameter, it reaches the conical cylindrical spouted bed where measurements are taken.

The pressure drop measurements were performed with 0-34.5 kPa capacity pressure sensor. A 5 mm fiber optic probe system designed by Fluidization Research Center of University of British Columbia, Canada and manufactured by Institute of Process Engineering, China was used for particle velocity and solid

volume fraction measurements. The number of fibers and their sizes in probes were specifically designed to work with zircon particles. In the fiber optic probes, there are two fiber bundles which are composed of 15 μm diameter fibers arranged in a repetitive sequence of light emitter and receiver. The probes used in this experiment have small diameter fibers and contain larger number of fibers therefore they are very suitable for both particle velocity and volume fraction measurements.

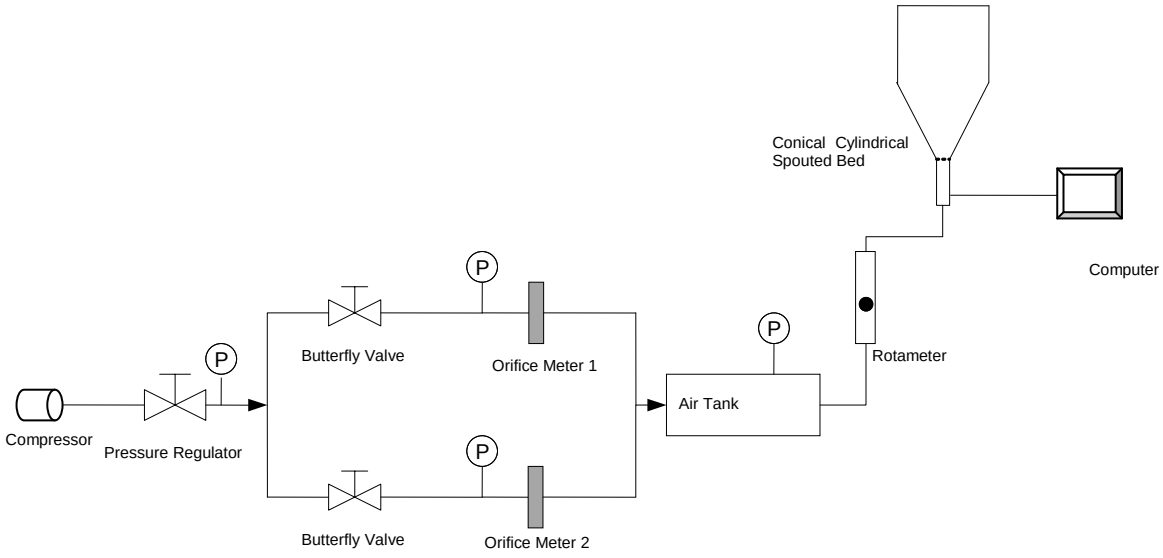

Figure 7.1 A schematic view of Sari's experimental setup (Sari et al., 2011).

A schematic view of conical cylindrical spouted bed used for the experiments is shown in Figure 7.2. The description and the values of the bed geometric parameters are summarized in Table 7.1.

Three conical cylindrical beds each of which has different conic angle were manufactured to examine the effect of conic angle on flow hydrodynamics. The bed was filled with zircon particles of different amount to generate various static bed heights to examine the effect of static bed height on flow hydrodynamics. Two particle diameters 0.5 mm and 1.0 mm were used to examine the effect of particle size on flow hydrodynamics. The spherical zircon particles of 6050 kg/m^3 density were used with air at ambient temperature as a spouting gas.

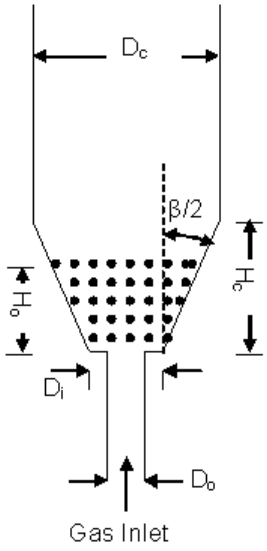

Figure 7.2 The geometry of the experimental conical cylindrical spouted bed.

Table 7.1 The geometric parameters of the Sari's experimental setup.

Symbol	Description	Value
$\mathbf{D_c}$	Bed diameter	0.15 m
$\mathbf{D_i}$	Bed base diameter	0.025 m
$\mathbf{D_o}$	Gas inlet diameter	0.015 m
$\boldsymbol{\beta}$	Conic angle	30^o, 45^o, 60^o
$\mathbf{H_c}$	Conic height	0.23325 m, 0.15089 m, 0.10825 m
$\mathbf{H_o}$	Static bed height	Changes for every experimental set

In order to perform pressure drop, particle velocity, and solid volume fraction measurements, holes were drilled on the sides of the conical section of the beds as shown in Figure 7.3.

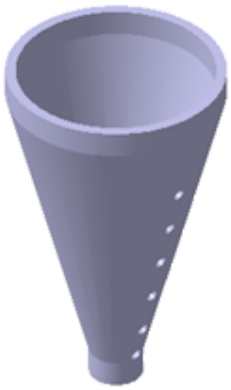

Figure 7.3 The schematic view of measurement holes (Sari et al., 2011).

The fiber optic probe was inserted into the bed from any of the holes to make measurements as seen in Figure 7.4. Moving the probe to different radial positions allowed the acquisition of measurements of radial distribution of particle velocity and volume fraction.

Figure 7.4 The picture of measurement with fiber optic probe.

There are seven experimental sets according to combinations of particle diameter (d_s), conic angle (β), and static bed height (H_o) to perform measurements and examine the hydrodynamics of the spouted beds as seen in Table 7.2.

Table 7.2 The definition of experimental sets.

Experimental Set Number	d_s (mm)	β (^{o})	H_o (mm)	Measurement Heights (mm)
1	1.0	30	140	100
2	1.0	45	60	42
3	1.0	45	100	42 & 80
4	1.0	45	140	42, 82 &120
5	1.0	60	60	50
6	1.0	60	100	50 & 93
7	0.5	60	100	50 & 93

There are 12 measurements in total for these seven experimental sets. For a set, the experimental results of different measurement heights are given. Experimental

conditions of each measurement number are explained in Table 7.3. H_p is defined as measurement height and U_o is the air velocity based on bed inlet diameter.

Since it is important to predict the behavior of a spouted bed at operating conditions, which is achieved after spouting occurs; the inlet gas velocity for the experiments is set to 1.25 times of the minimum spouting velocity.

Table 7.3 The description of parameters of measurements.

Measurement No.	Exp. Set No.	d_s (mm)	β (^{o})	H_o (mm)	H_p (mm)	U_o (m/s)	H_p/H_o	U_o/U_{ms}
1	1	1.0	30	140	100	38.6	0.71	1.25
2	2	1.0	45	60	42	20.1	0.70	1.25
3	3	1.0	45	100	42	36.9	0.42	1.25
4	3	1.0	45	100	80	36.9	0.80	1.25
5	4	1.0	45	140	42	57.0	0.30	1.25
6	4	1.0	45	140	82	57.0	0.59	1.25
7	4	1.0	45	140	120	57.0	0.86	1.25
8	5	1.0	60	60	50	26.8	0.83	1.25
9	6	1.0	60	100	50	45.3	0.50	1.25
10	6	1.0	60	100	93	45.3	0.93	1.25
11	7	0.5	60	100	50	25.3	0.50	1.25
12	7	0.5	60	100	93	25.3	0.93	1.25

7.2 The Preparations for CFD Simulations

The CFD simulation of the experimental setup was performed with FLUENT commercial CFD package version 6.3. First step of every CFD simulation is the generation of computational grid which can be defined as converting the simulation geometry into computational mesh. Although there are several programs to do this, GAMBIT, a general purpose preprocessor for CFD analysis, version 2.4 was used in this study.

All the simulations are performed with 2D axial symmetric computational grid. Therefore, half of the geometry was modeled. A sample computational grid used for all bed geometries is shown in Figure 7.5. Scaled schematic of all bed geometries is shown in Figure 7.6. For simulations, the length of cylindrical section at the top of the conical section was chosen twice as high as conical bed height.

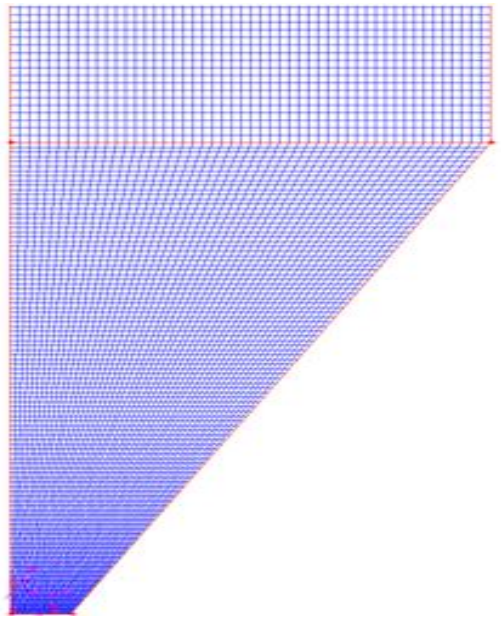

Figure 7.5 A sample computational mesh generated for calculations.

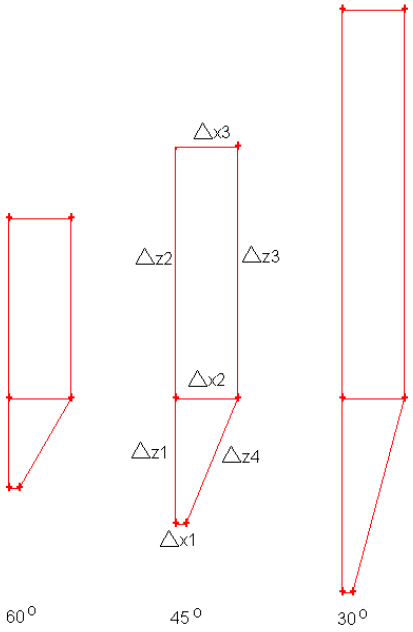

Figure 7.6 The scaled schematic view of each bed.

Grid independence studies were performed by using CFD model of experimental set 1 described in Table 7.2. Three different computational grids were generated – coarse mesh (18000 cells), fine mesh (45000 cells), and very-fine mesh (209700 cells). The computational times and calculated pressure drop values are shown in

Table 7.4 and particle velocity and solid volume fraction distributions are shown in Figure 7.7.

Table 7.4 Pressure drop and computational time comparison of three mesh sizes.

	Coarse Mesh	**Fine Mesh**	**Very-fine Mesh**
Computational Time (s)	74193	182573	1020282
Pressure Drop (Pa)	3533	3610	3734

Figure 7.7 shows that results of fine and very-fine mesh are close to each other. Table 7.4 indicates that computational time for very-fine mesh is 6 times more than the computational time of fine mesh. Therefore, fine mesh is used in this study.

The grid size kept the same for all bed geometries as seen in Table 7.5 . Since the bed heights are different for each bed due to conic angle, different number of computational elements was generated for each bed

Table 7.5 The grid size values and total number of computational elements for each bed.

Cone Angle (^{o})	**Δx1 (m)**	**Δx2 & Δx3 (m)**	**Δz1, Δz2, Δz3 & Δz4 (m)**	**Total Number of Elements**
30	1.0×10^{-4}	1.0×10^{-3}	1.0×10^{-3}	45000
45	1.0×10^{-4}	1.0×10^{-3}	1.0×10^{-3}	33750
60	1.0×10^{-4}	1.0×10^{-3}	1.0×10^{-3}	24300

The set of governing equations of Eulerian-Eulerian multiphase model were solved by a finite volume method. General transport equations of mass, momentum, and energy were applied to each computational cell by using first order implicit node based unsteady, pressure based solver. The phase coupled SIMPLE algorithm was applied to solve pressure-velocity coupling. First order discretization scheme was set up for momentum, energy, and volume fraction variables.

The gas inlet boundary was defined as velocity inlet such that the gas is injected only in axial direction and solid inlet velocity was set to zero. At the outlet, the outflow boundary condition was applied which implies the velocity gradients for the two phases in the axial direction are zeros. For the walls of the bed, no slip boundary condition was used. The symmetry axis requires the velocity gradients

for the two phases and the granular temperature gradient along the radial direction to be zeros.

For 15 seconds of total simulation time, 30000 time steps with 5×10^{-4} s time step size were used.

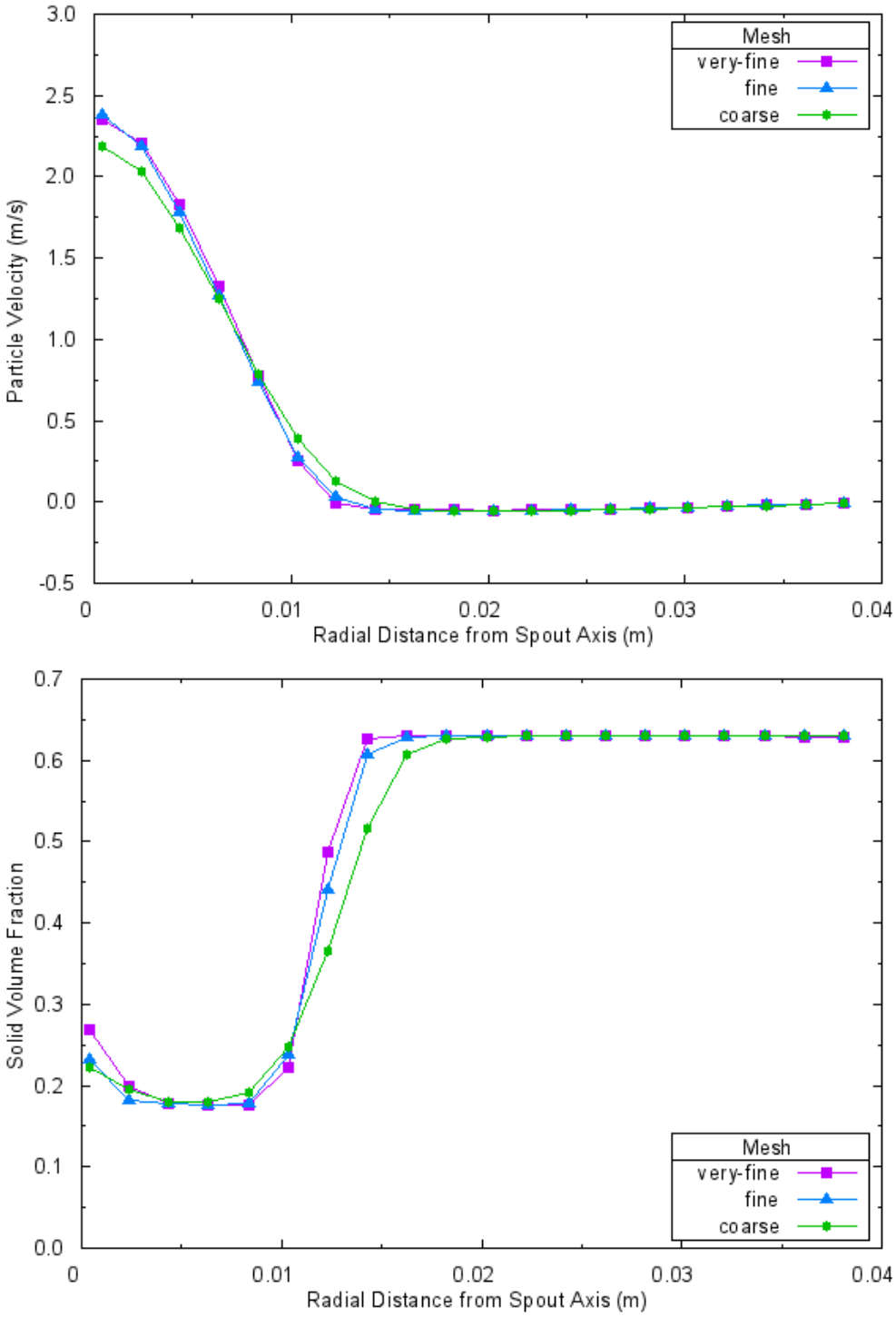

Figure 7.7 Comparison of particle velocity and solid volume fraction profiles of three mesh sizes.

The major drawback of the CFD simulations is longer computation time. In order to reduce the computation time of CFD simulations, parallel processing was performed on 8 HP ProLiant BL680C G5 systems with 4 quad-core Intel Xeon E7300 CPU that contains 128 cores. In order to determine the optimum number of cores, a test case was run on 1, 2, 4, 6, 8, 10, 12, 14, and 16 cores. For each simulation different input files were generated. METIS partitioning technique implemented in FLUENT was used for partitioning the geometry for a given number of processors. The number of processors versus speed-up factor graph was generated for a sample case. It is seen from Figure 6.4 that the speed-up factor reaches saturation around 12 cores. Since the addition of extra cores after 12 deteriorates the simulation time, all the simulations in this study were performed by using 12 cores. Depending on the experimental set, each 15 s run was completed in one to two days.

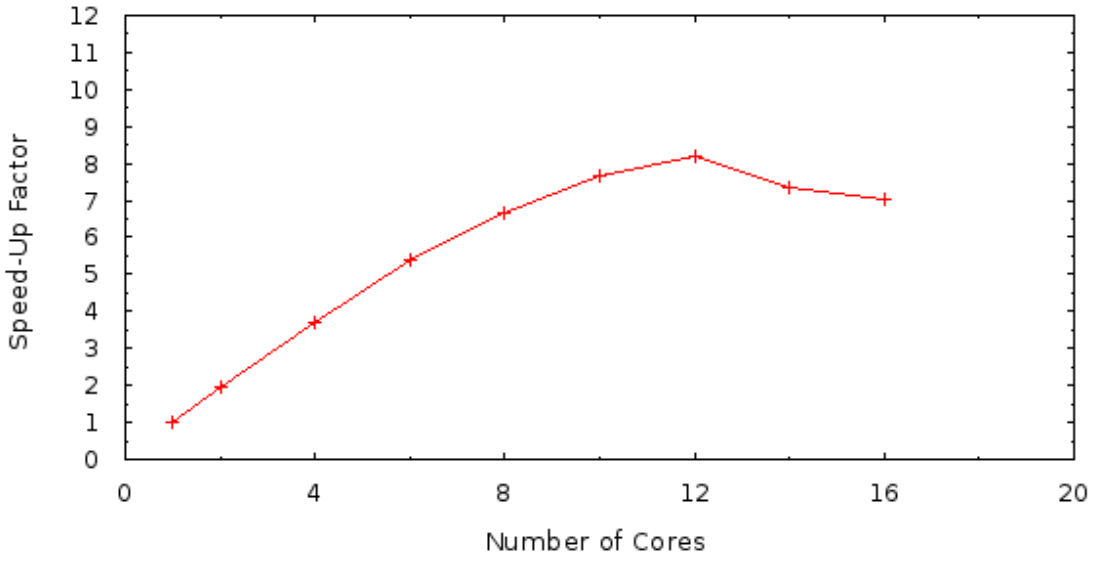

Figure 7.8 The speed-up graph of FLUENT on 8 HP ProLiant BL680C G5 system.

7.3 Findings from CFD Simulations

In this section, CFD simulation results of each experimental set defined in Table 7.3 are going to be presented. And the effect of drag model, restitution coefficient, and inclusion solid frictional stress into the simulations are going to be investigated.

Twelve computational runs as a result of combination of different drag models, restitution coefficient values, and inclusion/not-inclusion of solid frictional stress were performed for every experimental set. Each computational run is represented with a case number as seen in Table 7.6. Gidaspow and Syamlal-O'Brien drag models were selected because they are recommended for heavy solid phase and dense bed simulations. The restitution coefficient values ranging from 0.80 to 0.95 were selected to cover the range in which particle collusions go from plastic to nearly elastic.

Table 7.6 The parameters of cases used for CFD simulations.

Case Number	Drag Model	Restitution Coefficient	Solid Frictional Stress
1	Gidaspow	0.80	Not included
2	Gidaspow	0.90	Not included
3	Gidaspow	0.95	Not included
4	Syamlal-O'Brien	0.80	Not included
5	Syamlal-O'Brien	0.90	Not included
6	Syamlal-O'Brien	0.95	Not included
7	Gidaspow	0.80	Included
8	Gidaspow	0.90	Included
9	Gidaspow	0.95	Included
10	Syamlal-O'Brien	0.80	Included
11	Syamlal-O'Brien	0.90	Included
12	Syamlal-O'Brien	0.95	Included

For all these cases, the value of bed pressure drop and the distribution of particle velocity and solid volume fraction are going to be compared to understand the effect of each parameter on simulations.

For the particle velocity and solid volume fraction distributions, time averaging was applied to the results of the last 5 seconds of simulations.

7.3.1 The Experimental Set 1

As described in Table 7.3, the experimental set 1 contains a bed of 30^{o} conic angle, 140 mm static bed height, and 1.0 mm diameter particles. The air inlet velocity is 38.6 m/s. The measurement height is 100 mm.

The bed pressure drop results from simulations are shown in Table 7.7. Syamlal-O'Brien drag model predictions for bed pressure drop are slightly higher than Gidaspow drag model predictions for each restitution coefficient and frictional stress condition combinations (comparison between case 1 & 4, case 2 & 6, ...,case 9 & 12).

When restitution coefficient increases, bed pressure drop decreases for every case except Gidaspow drag model without friction cases (1, 2, and 3). But results are consistent.

Table 7.7 Calculated bed pressure drops for experimental set 1.

Case Number	Bed Pressure Drop (Pa)
1	3390
2	3504
3	3539
4	3827
5	3618
6	3610
7	2565
8	2424
9	2409
10	2544
11	2458
12	2498

When solid frictional stress is included into the simulations, calculated pressure drop values decrease dramatically for each case (comparison between case 1 & 7, case 2 & 8, ..., case6 & 12). The difference between the results is around 30%.

Figure 7.9 and Figure 7.10 show the effect of drag model on particle velocity and volume fraction radial distributions at a measurement height 100 mm. It is observed from Figure 7.9 that Syamlal-O'Brien drag model velocity predictions are higher than the Gidaspow model predictions in spout region. But the results are very close in annulus region. The spout radius which is a boundary where particle velocity becomes negative (particles move downwards) is almost the same for both drag model cases.

It is seen in Figure 7.10 that, the solid volume fraction values of Syamlal-O'Brien drag model cases are lower than the values of Gidaspow drag model cases close to spout center. Therefore, it can be said that spout region is more dilute for Syamlal-O'Brien drag model cases.

The increase in the value of restitution coefficient results in lower particle velocity predictions as seen in Figure 7.11 in spout region. On the contrary, when restitution coefficient value increases the solid volume fraction prediction increases as shown in Figure 7.12. The results are very similar for annulus region.

Inclusion of solid frictional stress into simulations slightly decreases the particle velocity distribution as seen in Figure 7.13. Figure 7.14 indicates that its effect on solid volume fraction is more significant. Inclusion of solid frictional stress reduces the solid volume fraction in spout region.

The distribution of particle velocity and solid volume fraction on Figure 7.9 to Figure 7.14 is consistent in all cases about particle velocity is being decreasing towards the bed wall unlike solid volume fraction.

Contours of solid volume fraction snap shots at simulation time of 15 seconds for all cases in Figure 7.15 indicate that stable external spouting is achieved for all cases. When the contours of solid volume fraction is examined, it is observed that Syamlal-O'Brien drag model fountain height predictions is higher than Gidaspow drag model ones regardless of the combination of restitution coefficient and solid frictional stress condition as seen in Figure 7.15.

For all cases, as restitution coefficient increases fountain height decreases. But, the results of the cases with restitution coefficient equal to 0.90 and 0.95 are very close to each other.

Inclusion of solid frictional stress into simulations decreases fountain height for all Gidaspow drag model cases but increases fountain height for all Syamlal-O'Brien drag model cases.

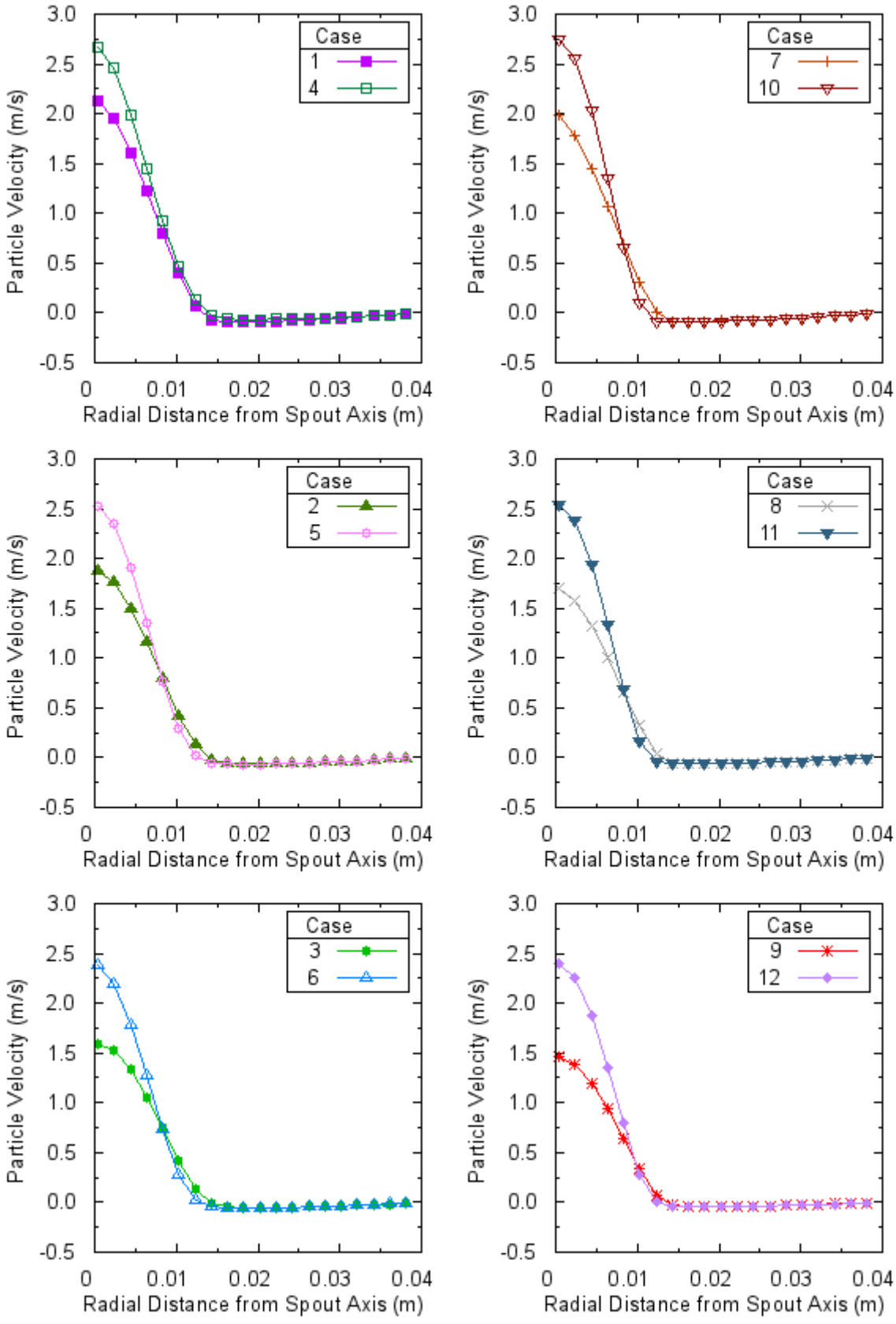

Figure 7.9 The effect of drag model on particle velocity distribution for experimental set 1, measurement height 100 mm.

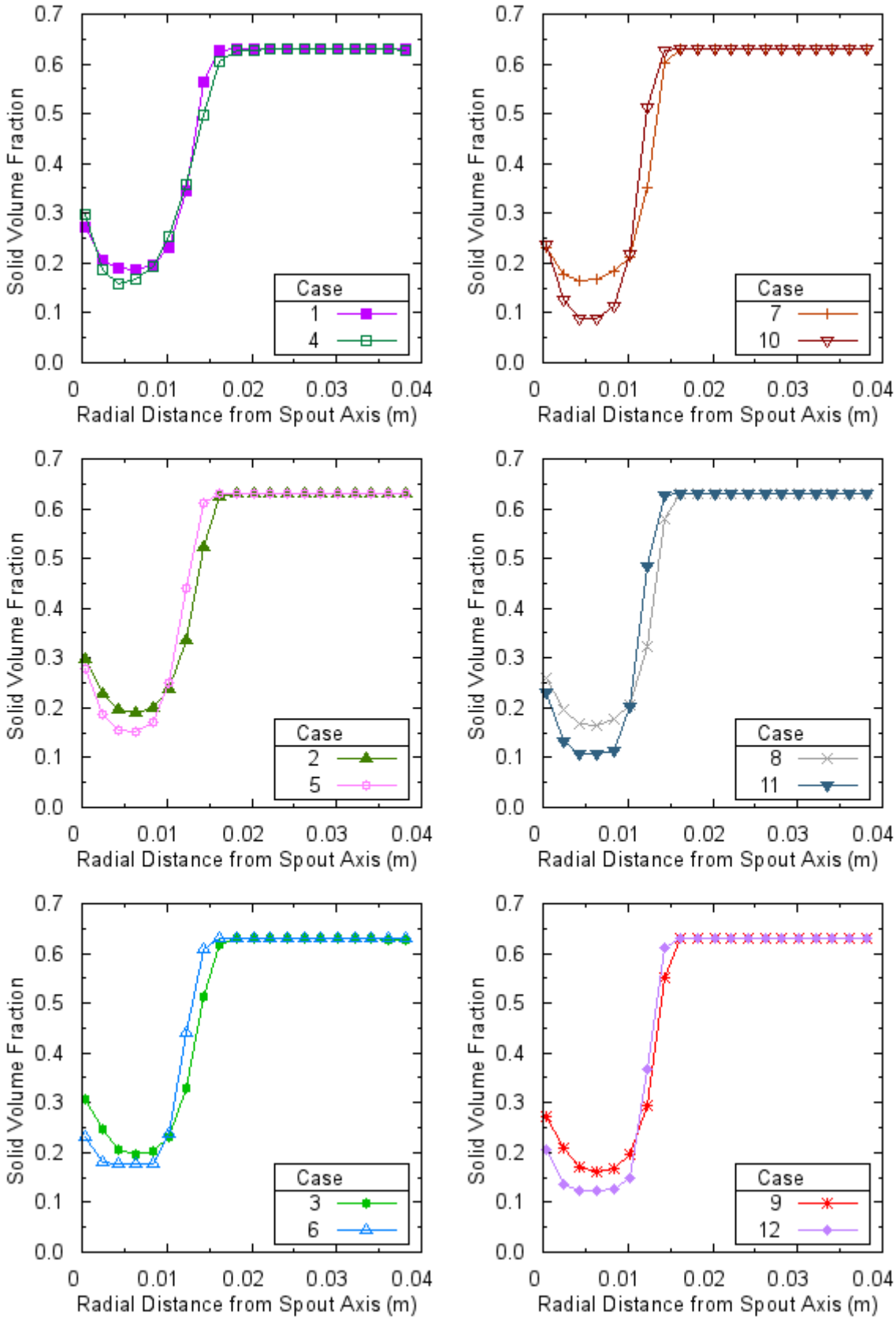

Figure 7.10 The effect of drag model on solid volume fraction distribution for experimental set 1, measurement height 100 mm.

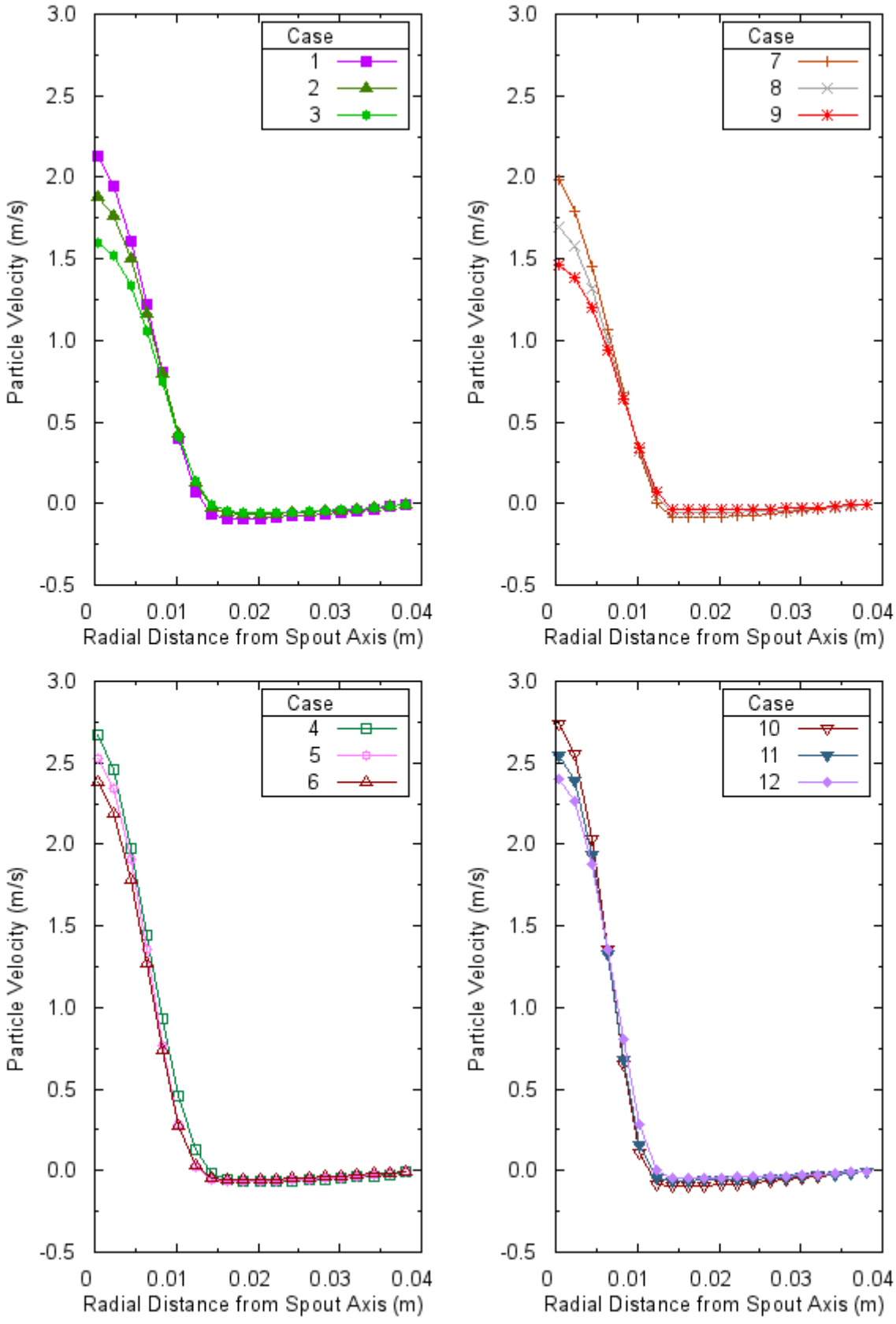

Figure 7.11 The effect of restitution coefficient on particle velocity distribution for experimental set 1, measurement height 100 mm.

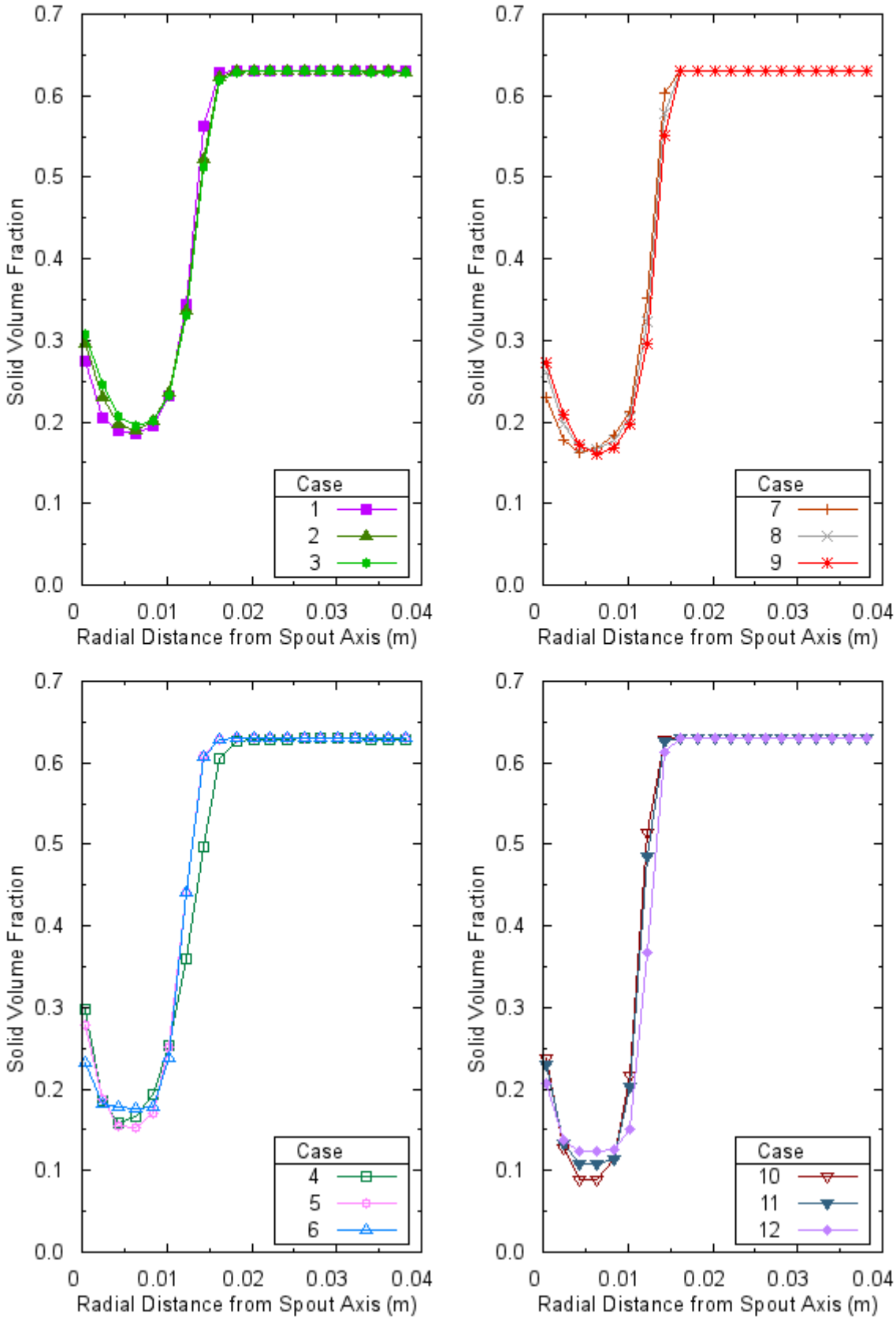

Figure 7.12 The effect of restitution coefficient on solid volume fraction distribution for experimental set 1, measurement height 100 mm.

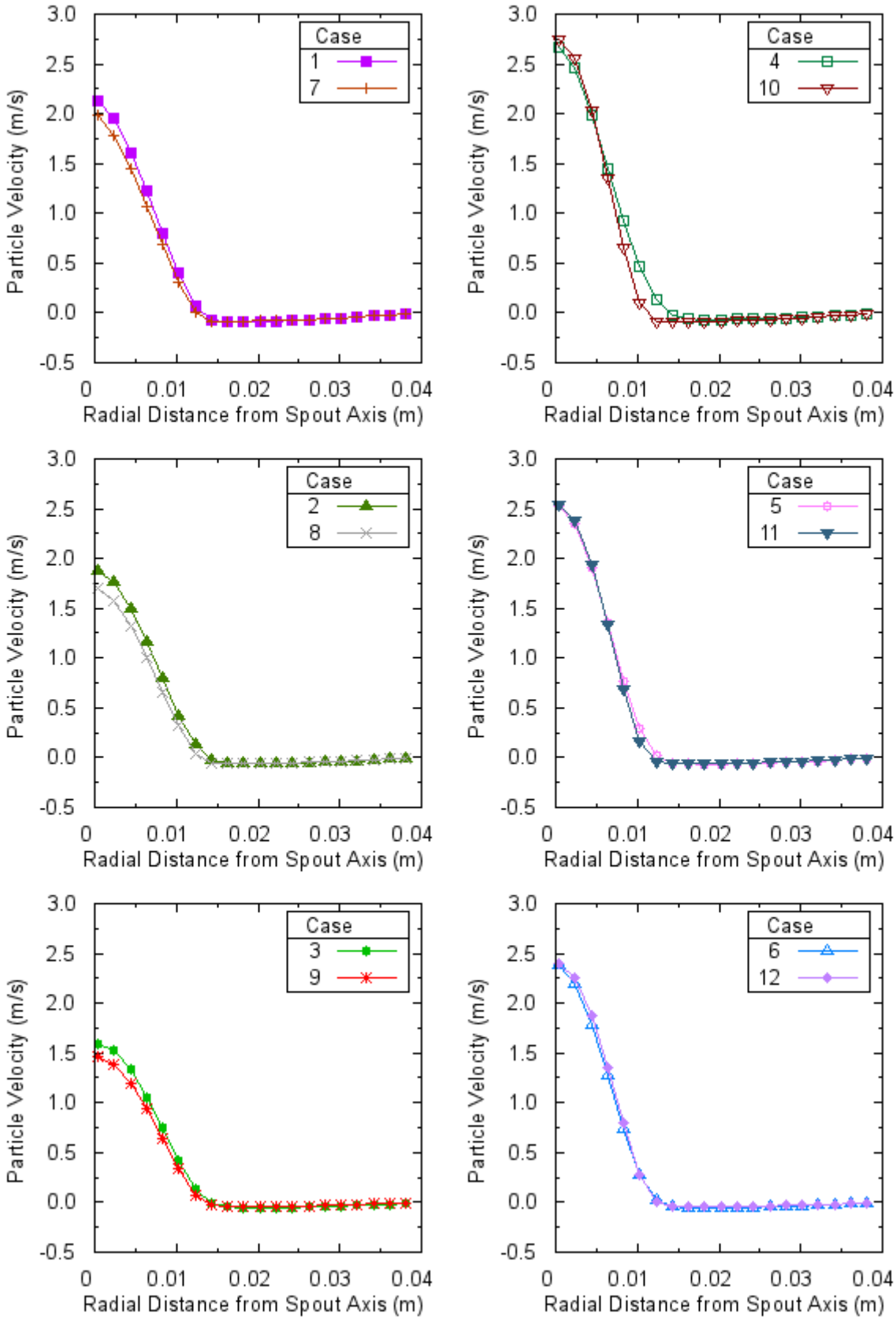

Figure 7.13 The effect of solid frictional stress on particle velocity distribution for experimental set 1, measurement height 100 mm.

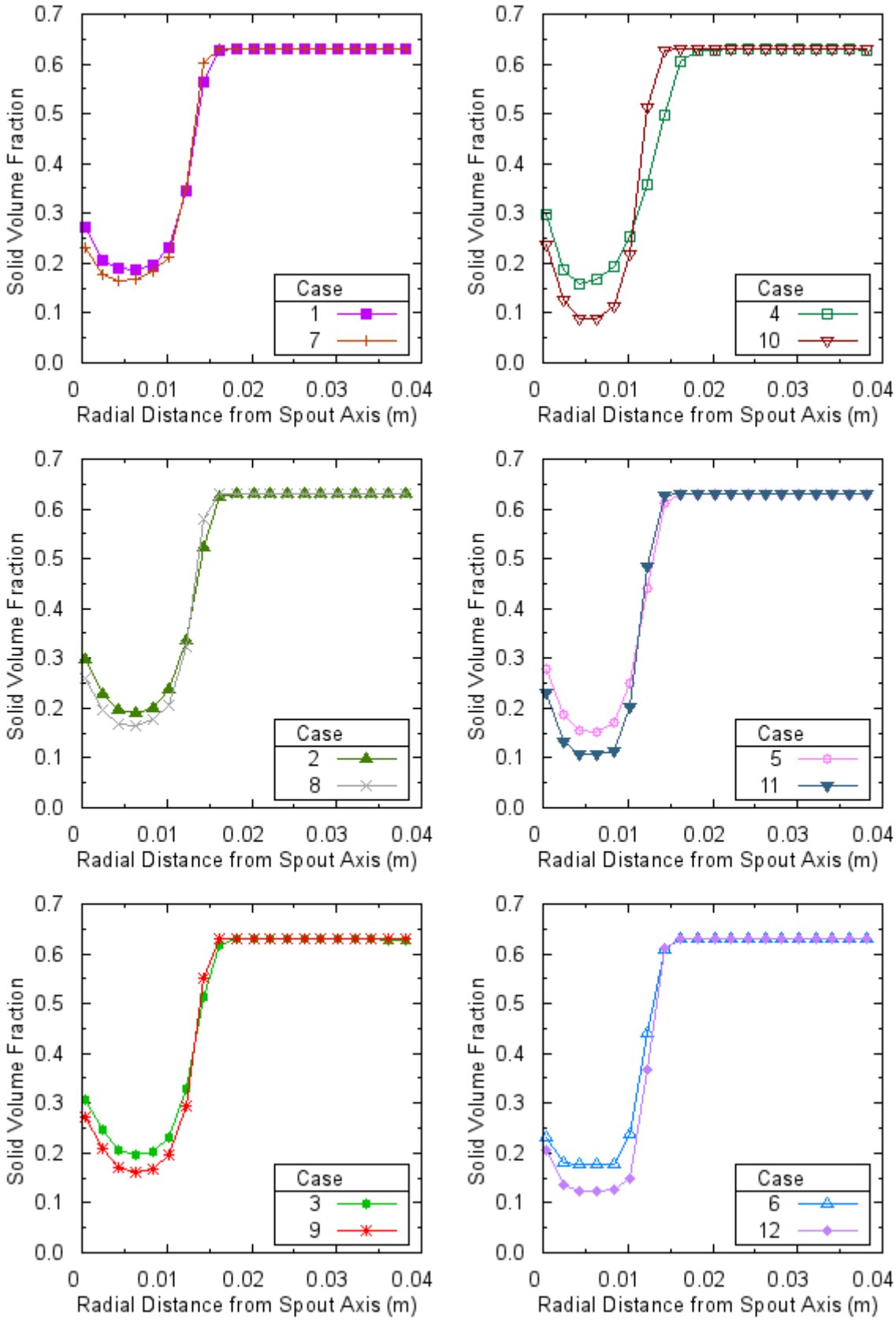

Figure 7.14 The effect of solid frictional stress on solid volume fraction distribution for experimental set 1, measurement height 100 mm.

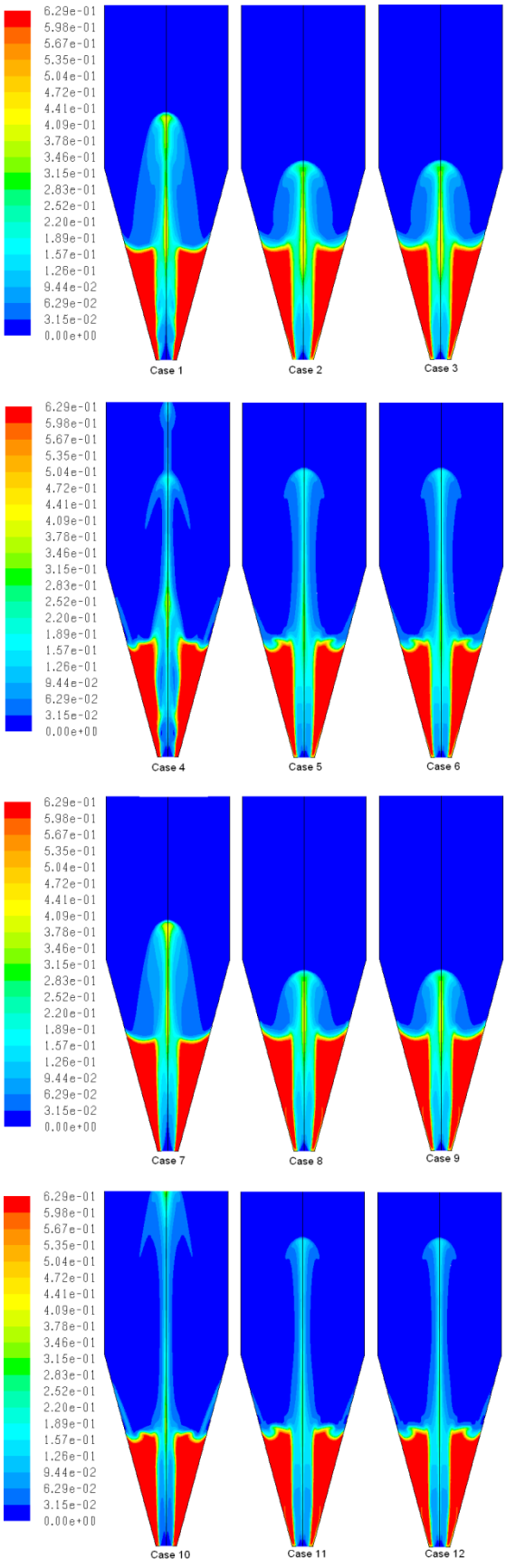

Figure 7.15 Contours of solid volume fraction at t= 15 s for experimental set 1.

7.3.2 The Experimental Set 2

For this set, the conic angle is 45^{o}, particle diameter is 1.0 mm, static bed height is 60 mm, and air inlet velocity is 20.1 m/s. There is only one measurement point at z=42 mm.

The bed pressure drop values from the simulations are presented in Table 7.8. For every combination of restitution coefficient and solid frictional stress condition, Syamlal-O'Brien drag model cases' results are higher than Gidaspow drag model cases' results. The difference between results reduces when restitution coefficient increases.

Table 7.8 Calculated bed pressure drops for experimental set 2.

Case Number	Bed Pressure Drop (Pa)
1	1301
2	1319
3	1334
4	1424
5	1397
6	1370
7	958
8	871
9	837
10	994
11	924
12	853

The effect of restitution coefficient differs depending on the drag model used. For Gidaspow cases without friction (case 1, 2, & 3), bed pressure drop increase with increasing restitution coefficient. However, for all other cases bed pressure drop decreases with increasing restitution coefficient.

With inclusion of solid frictional stress, bed pressure drop values decrease around 25 to 38 % depending on combinations of drag model and restitution coefficient value.

Figure 7.16 shows the effect of drag model on particle velocity for experimental set 2, measurement height 42 mm. Syamlal-O'Brien drag model particle velocity

values are higher than Gidaspow drag model values in spout region regardless of the value of the restitution coefficient and solid frictional stress condition. The distribution is similar for annulus region. The spout radius is not differing significantly with drag model choice. As seen in Figure 7.17, solid volume fraction values for Gidaspow drag model cases are higher than Syamlal-O'Brien drag model cases in spout region. The results are very close in annulus region.

The effect of restitution coefficient on simulation results can be seen in Figure 7.18 and Figure 7.19. When restitution coefficient value increases, particle velocity predictions reduce. Solid volume fraction distribution slightly increases with increasing restitution coefficient. The effect of restitution coefficient on particle velocity is more significant than the effect of it on solid volume fraction.

When the solid frictional stress is included into simulations, particle velocity values as well as solid volume fraction values have a reduction tendency as seen in Figure 7.20 and Figure 7.21. The resulting distribution of both are quiet close in annulus region.

Figure 7.22, contours of solid volume fraction at t=15 seconds, shows that external spouting is achieved for all cases. It also demonstrates that fountain heights for Syamlal-O'Brien drag model cases are higher than Gidaspow drag model cases for all combinations of restitution coefficient and frictional stress condition.

The fountain height of higher restitution coefficient value cases is smaller for all drag model and frictional stress condition combinations. The fountain height values for cases having restitution coefficient 0.90 and 0.95 are very close to each other.

Inclusion of frictional stress in simulations decreases fountain height for all drag model and restitution coefficient combinations but the effect is not so significant for Syamlal-O'Brien drag model cases.

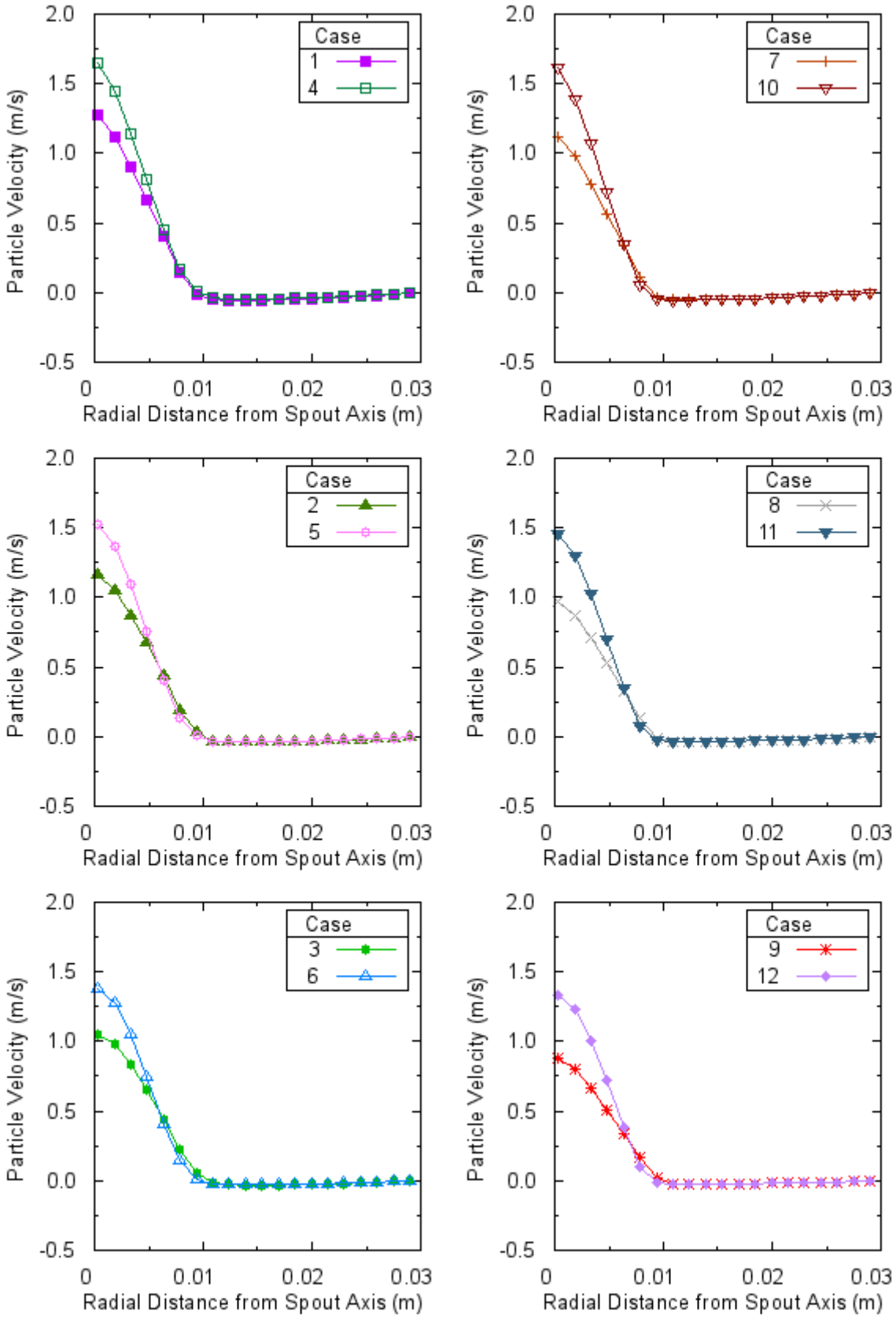

Figure 7.16 The effect of drag model on particle velocity distribution for experimental set 2, measurement height 42 mm.

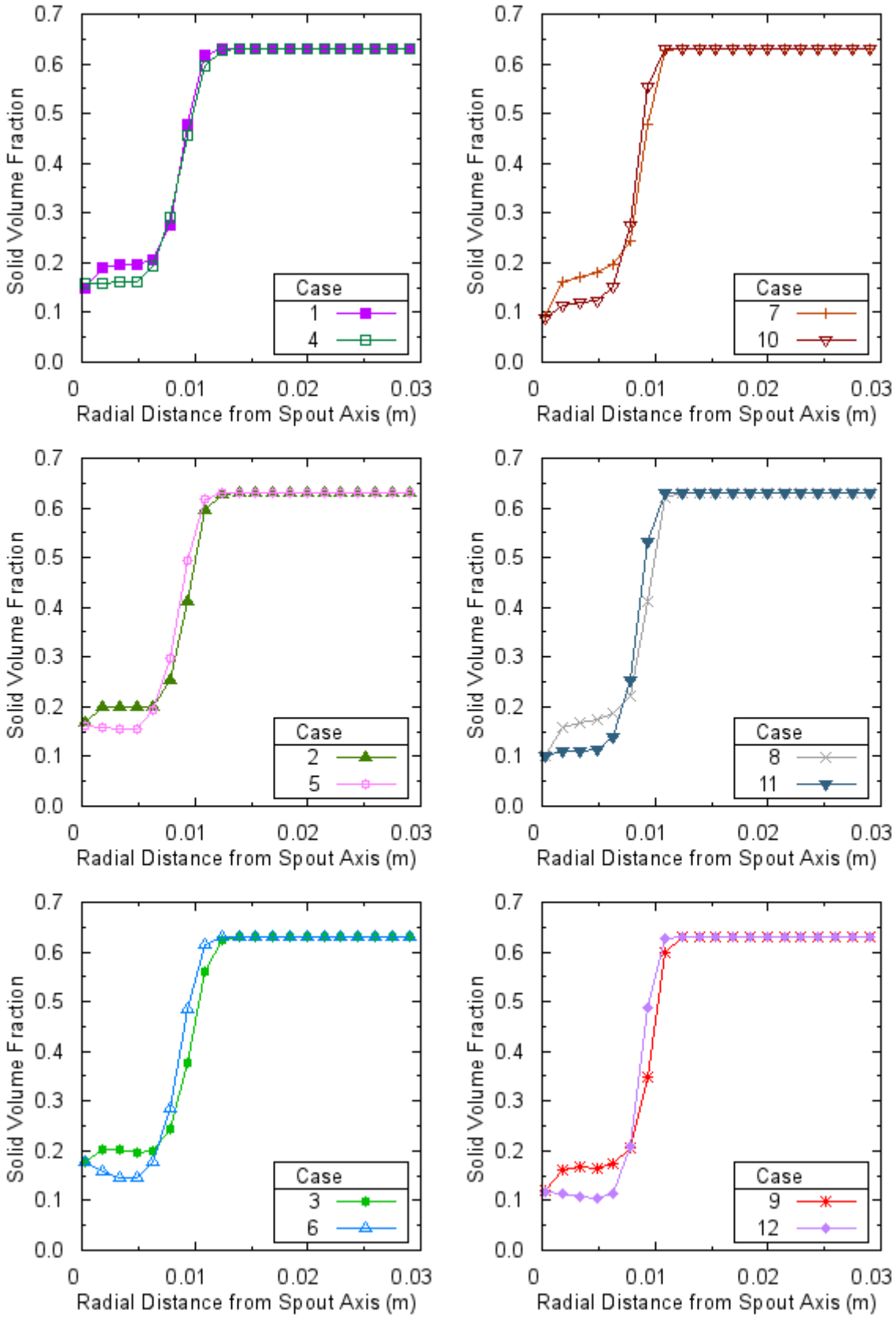

Figure 7.17 The effect of drag model on solid volume fraction distribution for experimental set 2, measurement height 42 mm.

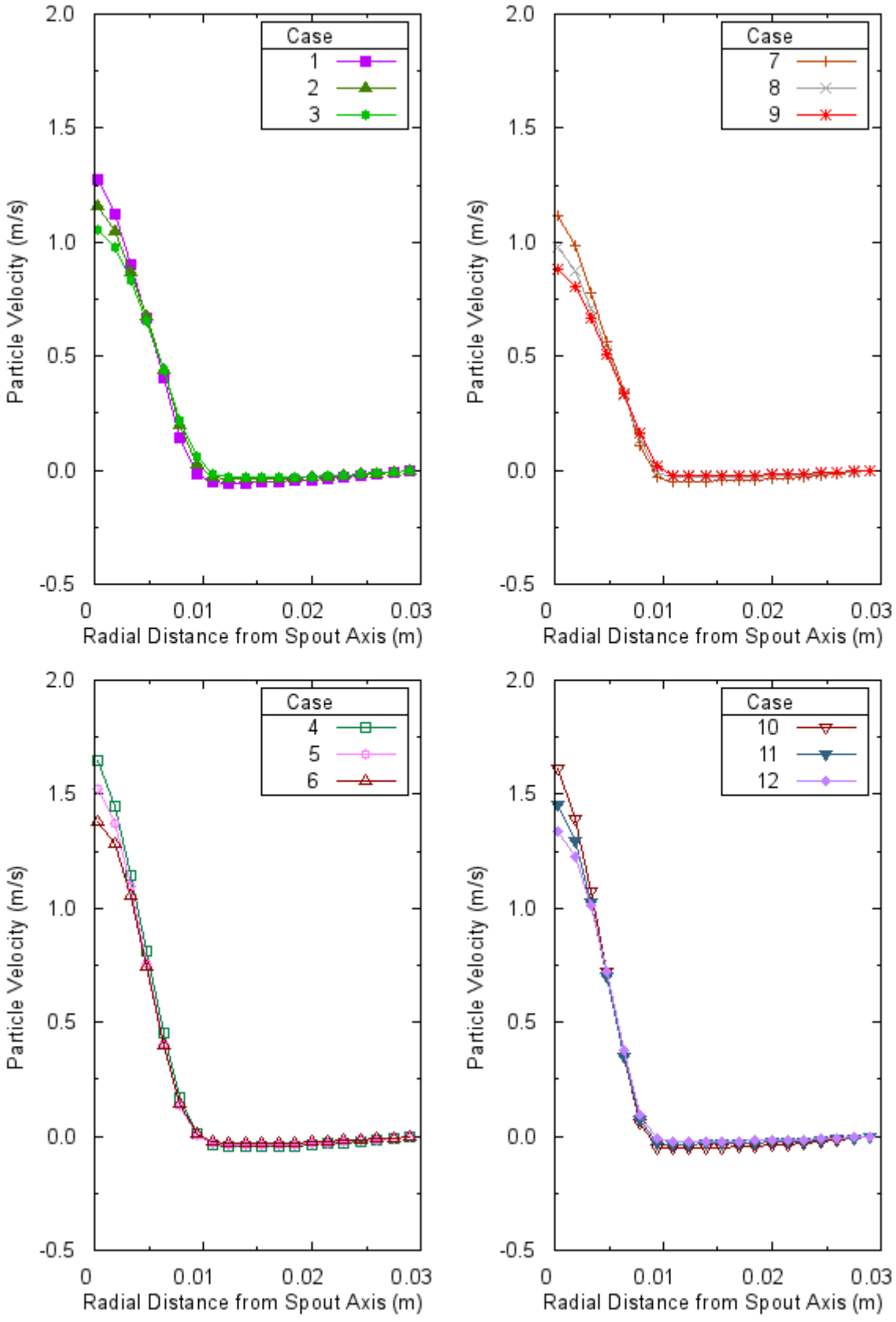

Figure 7.18 The effect of restitution coefficient on particle velocity distribution for experimental set 2, measurement height 42 mm.

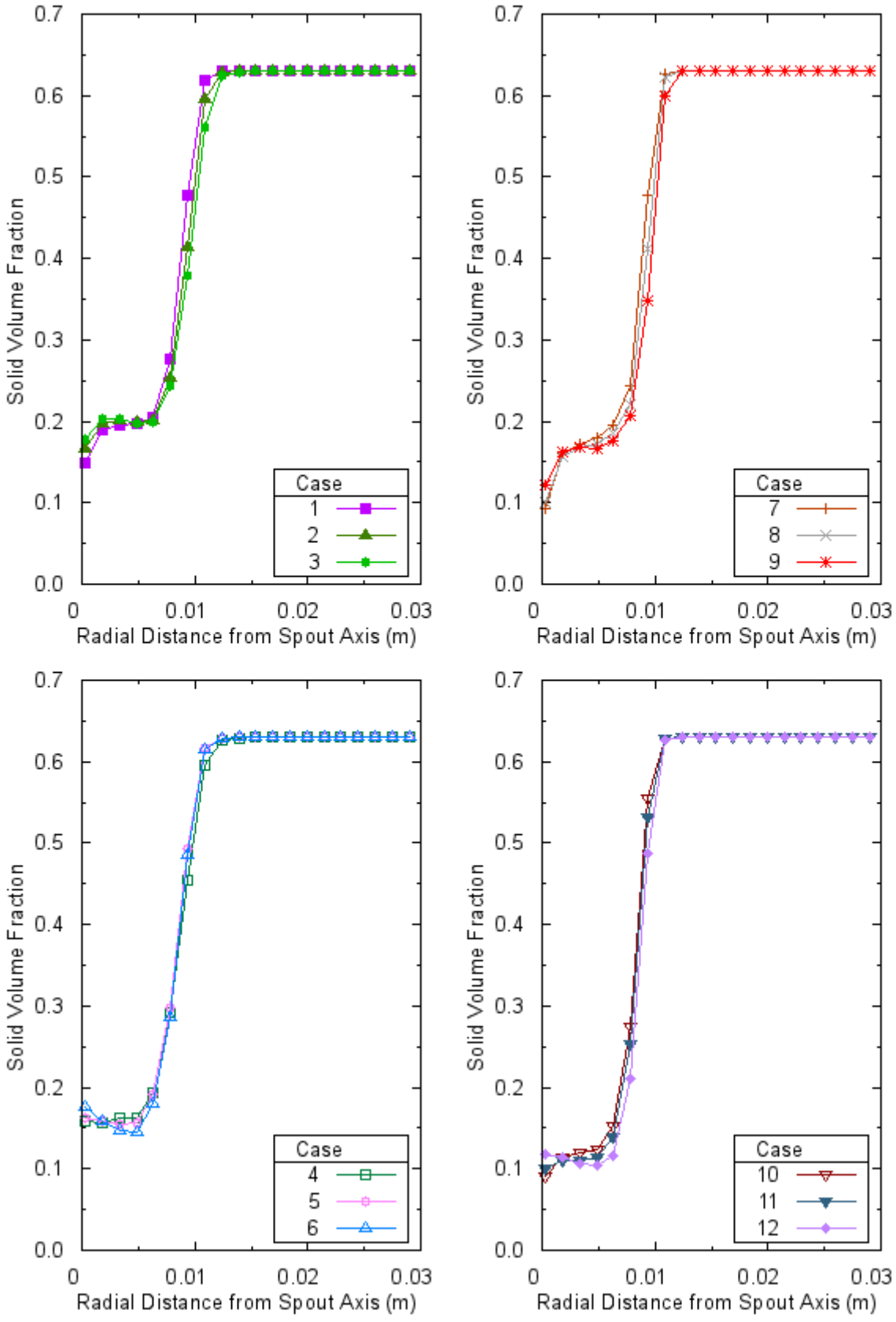

Figure 7.19 The effect of restitution coefficient on solid volume fraction distribution for experimental set 2, measurement height 42 mm.

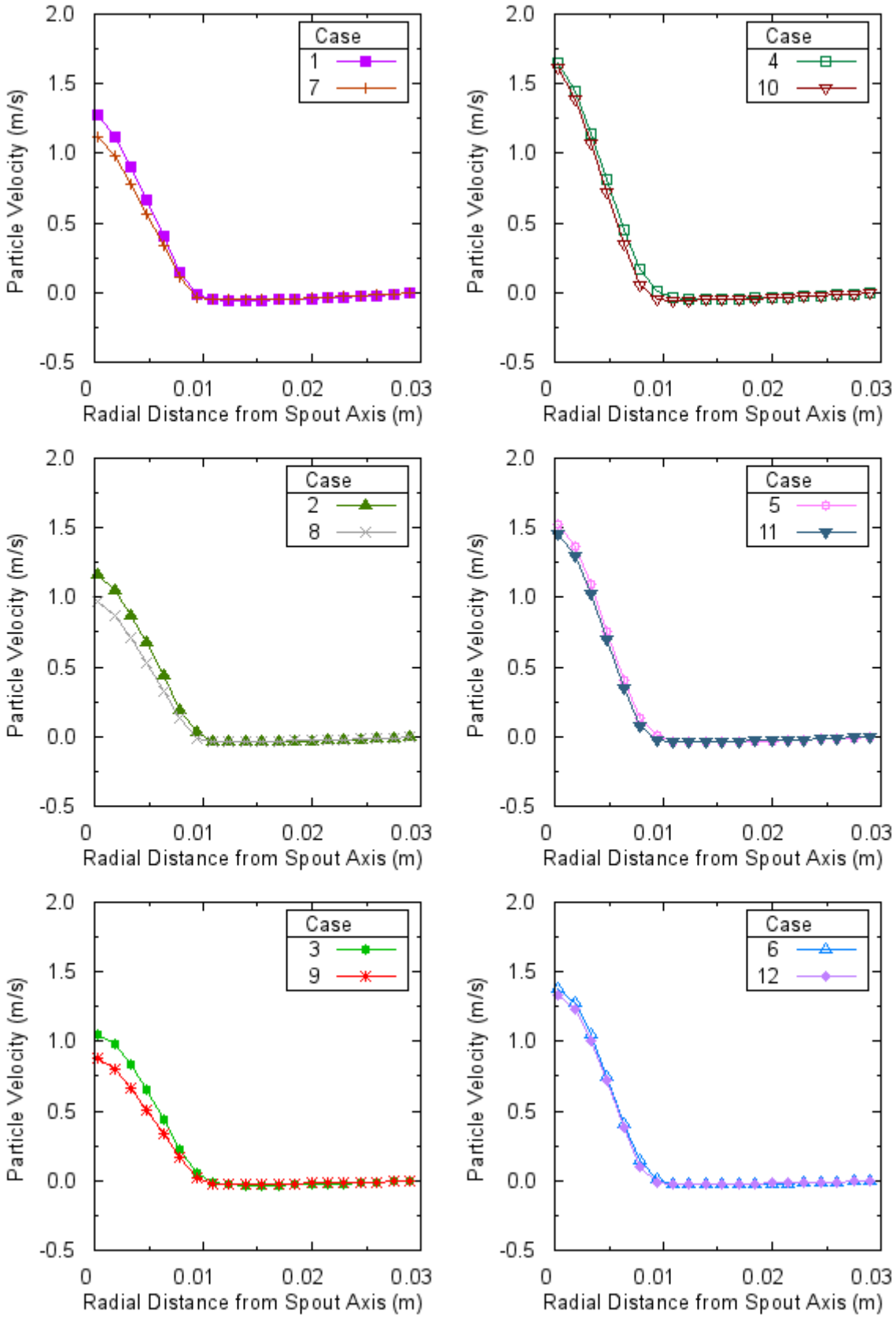

Figure 7.20 The effect of solid frictional stress on particle velocity distribution for experimental set 2, measurement height 42 mm.

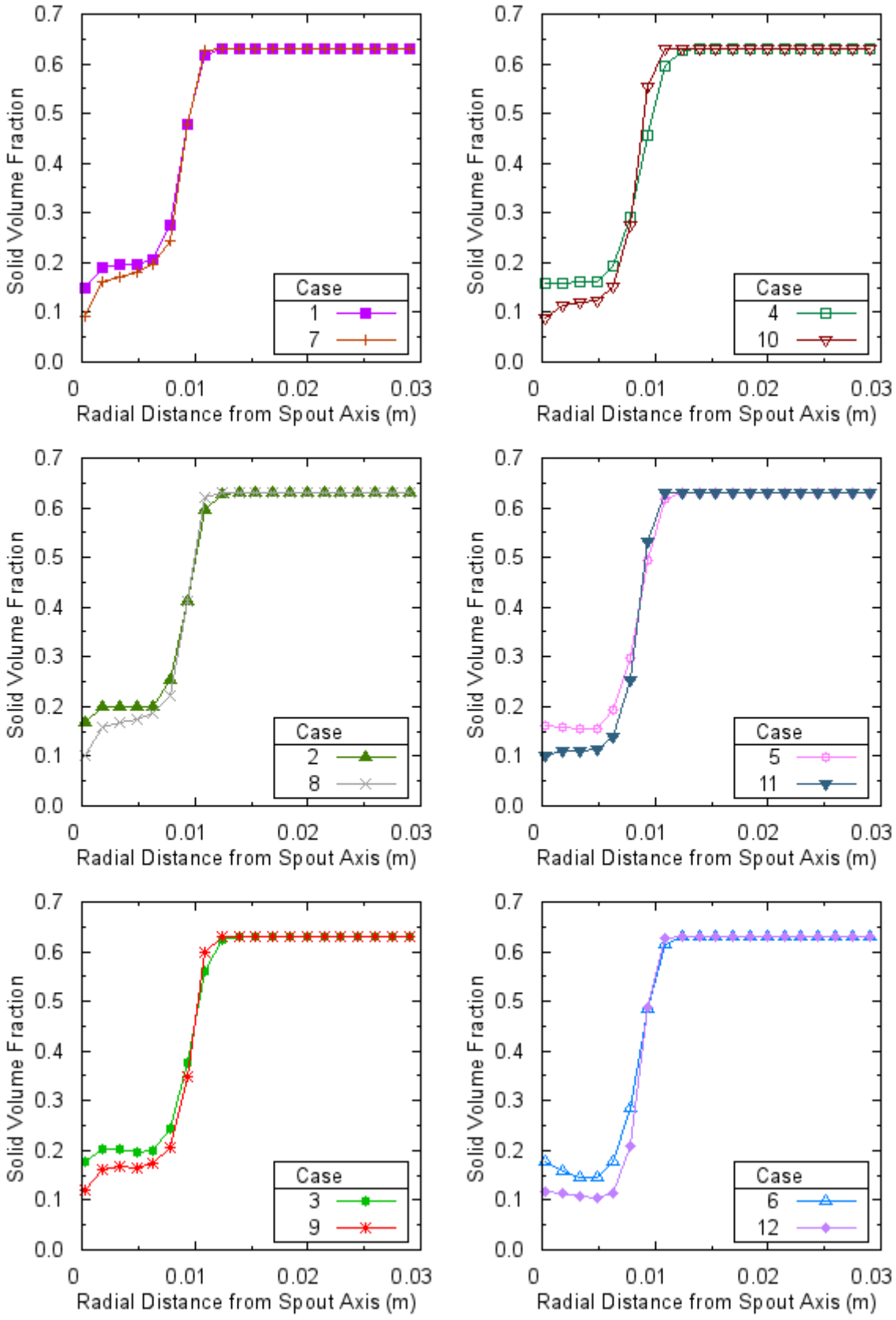

Figure 7.21 The effect of solid frictional stress on solid volume fraction distribution for experimental set 2, measurement height 42 mm.

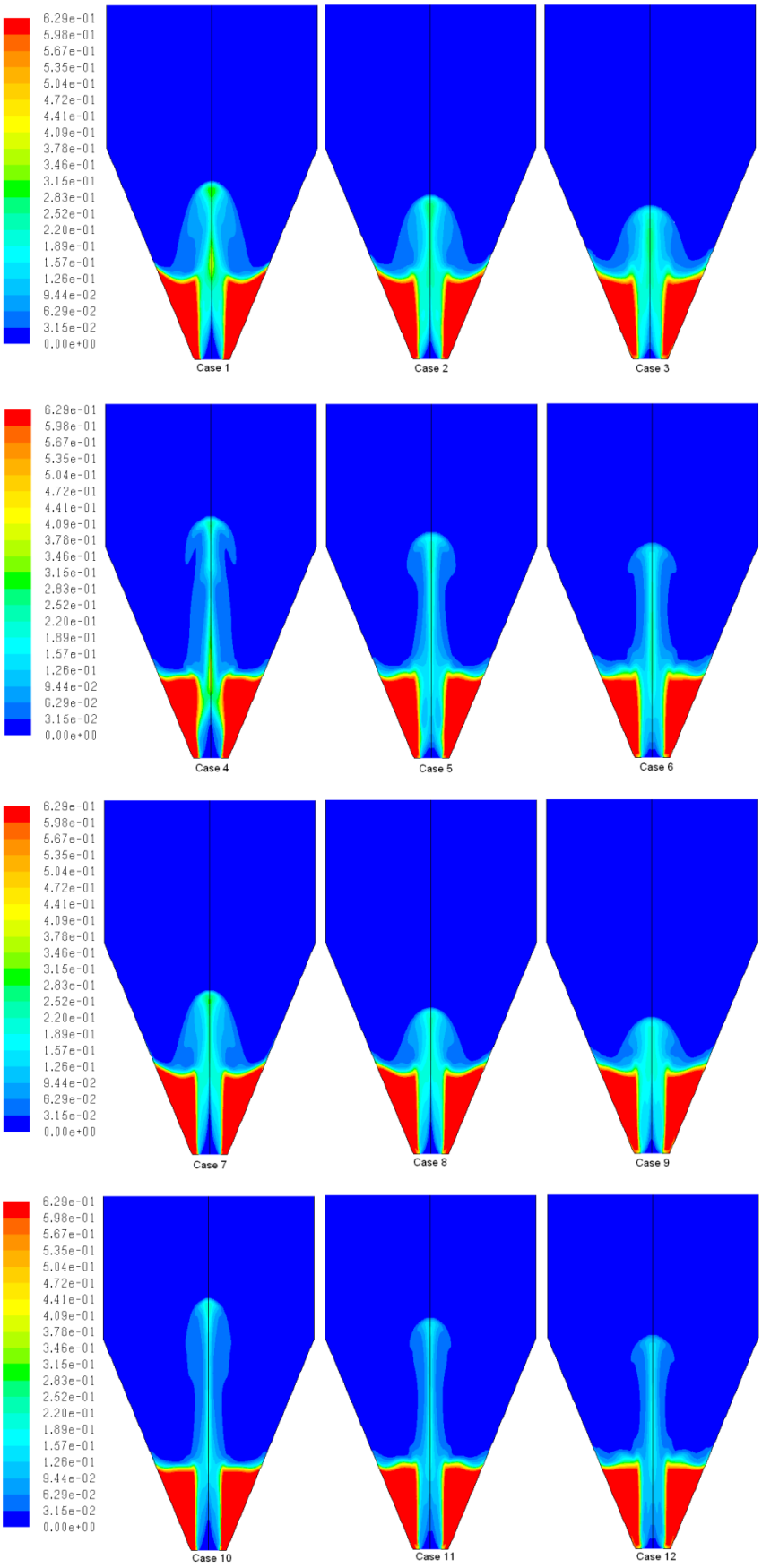

Figure 7.22 Contours of solid volume fraction at t= 15 s for experimental set 2.

7.3.3 The Experimental Set 3

The experimental set 3 is made up of 45^{o} angle bed containing 1.0 mm diameter particles. The static bed height is 100 mm and air inlet velocity is 36.9 m/s. Radial distributions of particle velocity and solid volume fraction are present for measurement heights of 42 mm and 80 mm.

An interesting simulation result was observed for case 10 that some particles flew out of the spouted bed. The difference in volume of particles at the beginning and at the end of the simulation is around 10^{-8} m^3. As a result of this, particle volume in the system was reduced only 0.019 %. Therefore, volume reduction is ignored and case 10 is included in the comparisons.

As seen in Table 7.9 the results of cases using Syamlal-O'Brien drag model is higher than the results of cases using Gidaspow drag model. This is valid for all combinations of solid frictional stress condition and value of restitution coefficient.

Table 7.9 Calculated bed pressure drops for experimental set 3.

Case Number	Bed Pressure Drop (Pa)
1	2286
2	2353
3	2355
4	2466
5	2453
6	2459
7	1604
8	1465
9	1395
10	1655
11	1544
12	1459

As restitution coefficient increases, except the cases having only Gidaspow drag model (case 1, 2, & 3), bed pressure drop decreases for cases having only Syamlal-O'Brien drag model, Gidaspow drag model with solid frictional stress, and Syamlal-O'Brien drag model with solid frictional stress. Although restitution coefficient in case 6 is lower than the restitution coefficient in case 5, the resulting bed pressure drop is higher.

30 to 40 % reduction in bed pressure drop occurs when solid frictional stress is included into the simulations regardless of other parameter combinations.

Figure 7.23 to Figure 7.26 shows the effect of drag model on particle velocity and solid volume fraction for measurement heights 42 mm and 80 mm. For both of them, Syamlal-O'Brien drag model predictions for particle velocity is higher than Gidaspow drag model predictions. For all cases, spout region for Syamlal-O'Brien drag model is mode dilute than the Gidaspow drag model spout region.

These figures also indicate that, particle velocity decreases as measurement height increases. Particle velocity values at measurement height 42 mm are higher than particle velocity values at measurement height 80 mm for every case. On the contrary, solid volume fraction increases as measurement height increases.

The effect of restitution coefficient in Figure 7.27 to Figure 7.30 is that particle velocity predictions reduce with increase in restitution coefficient for both measurement heights unlike solid volume fraction predictions. Its effect on solid volume fraction distribution for measurement height 80 mm is not as clear as its effect on solid volume fraction distribution for measurement height 42 mm.

The inclusion of solid frictional stress decreases both particle velocity and solid volume fraction for every case for each measurement height. But, this reduction is extremely low on particle velocity. For some cases, the results are almost the same as seen in Figure 7.31 to Figure 7.34.

Contours of solid volume fraction in Figure 7.35 show external spouting for all cases. Syamlal-O'Brien drag model cases have higher fountain height values for every combination of restitution coefficient and frictional stress condition.

As restitution coefficient increases fountain height decreases for all combinations of other parameters.

Inclusion of frictional stress also reduces the fountain height. But this reduction is not clear for cases having Syamlal-O'Brien as a drag model.

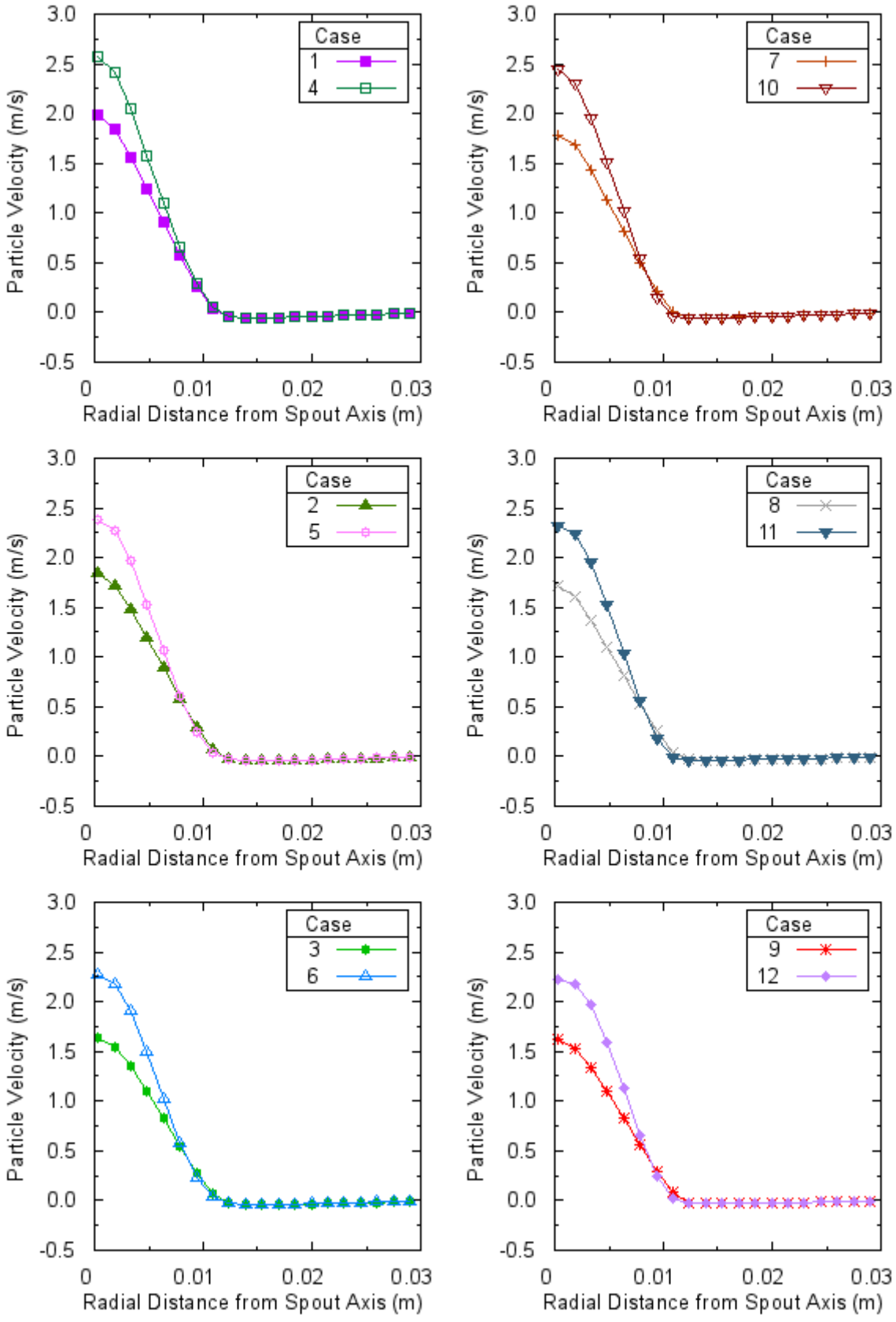

Figure 7.23 The effect of drag model on particle velocity distribution for experimental set 3, measurement height 42 mm.

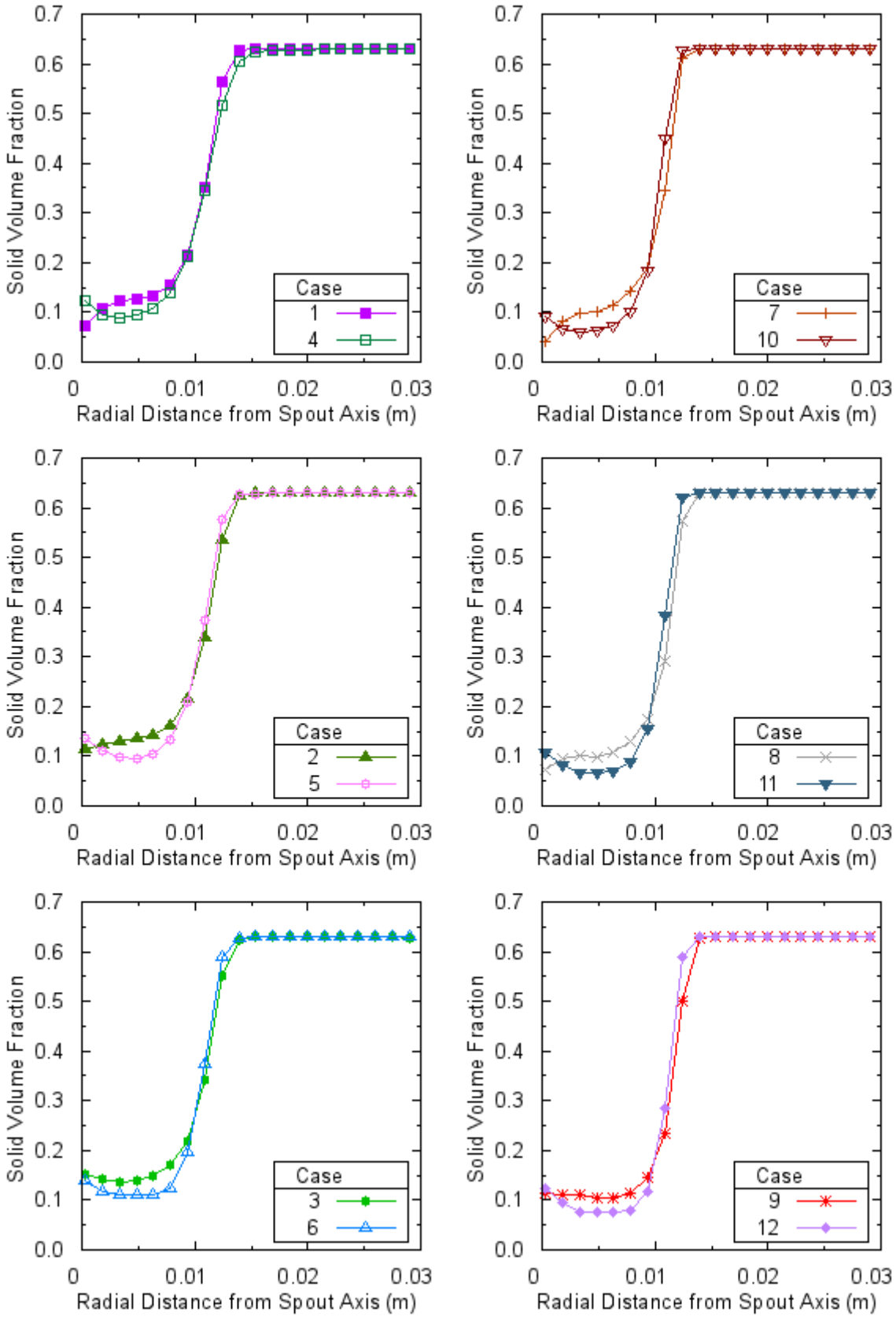

Figure 7.24 The effect of drag model on solid volume fraction distribution for experimental set 3, measurement height 42 mm.

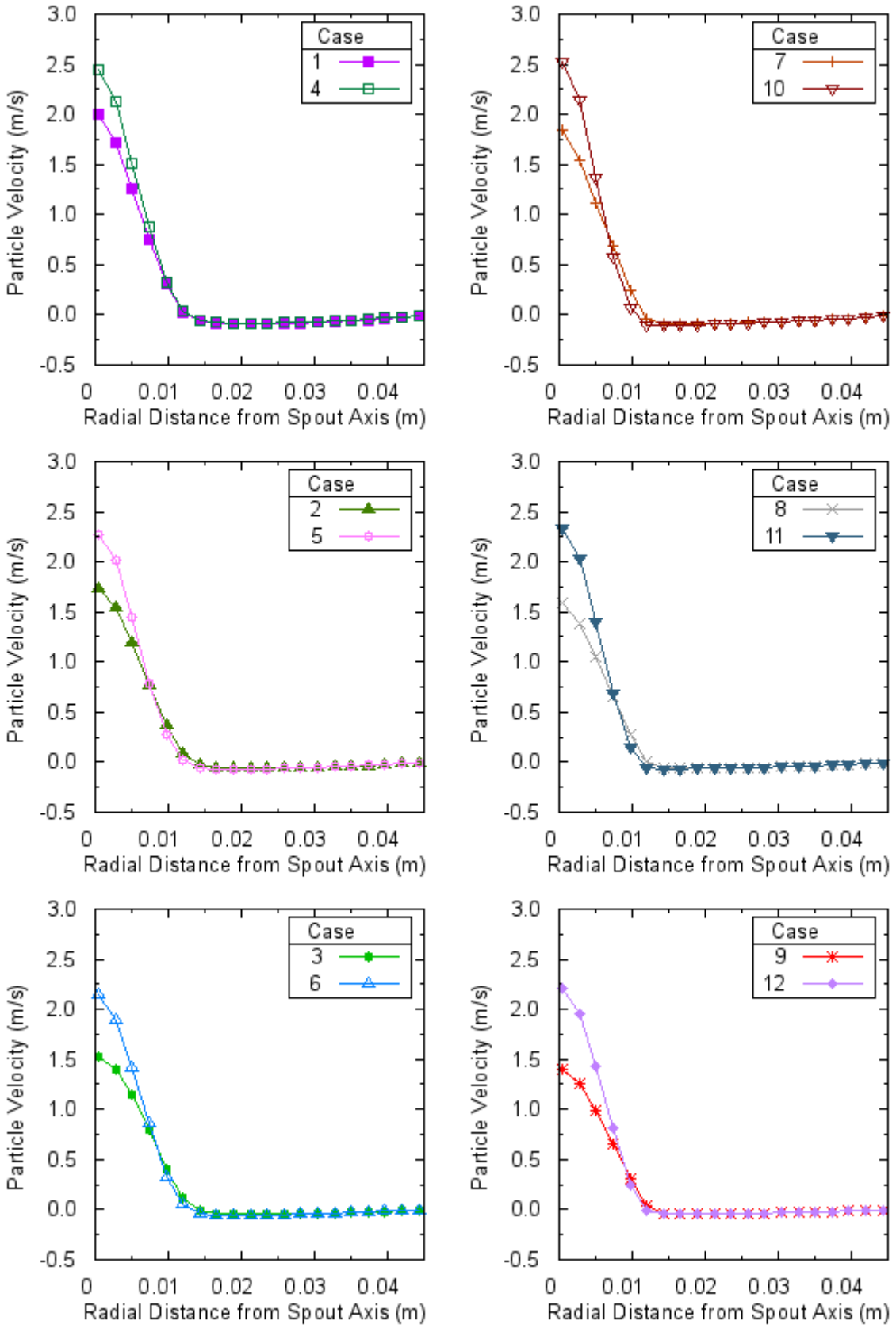

Figure 7.25 The effect of drag model on particle velocity distribution for experimental set 3, measurement height 80 mm.

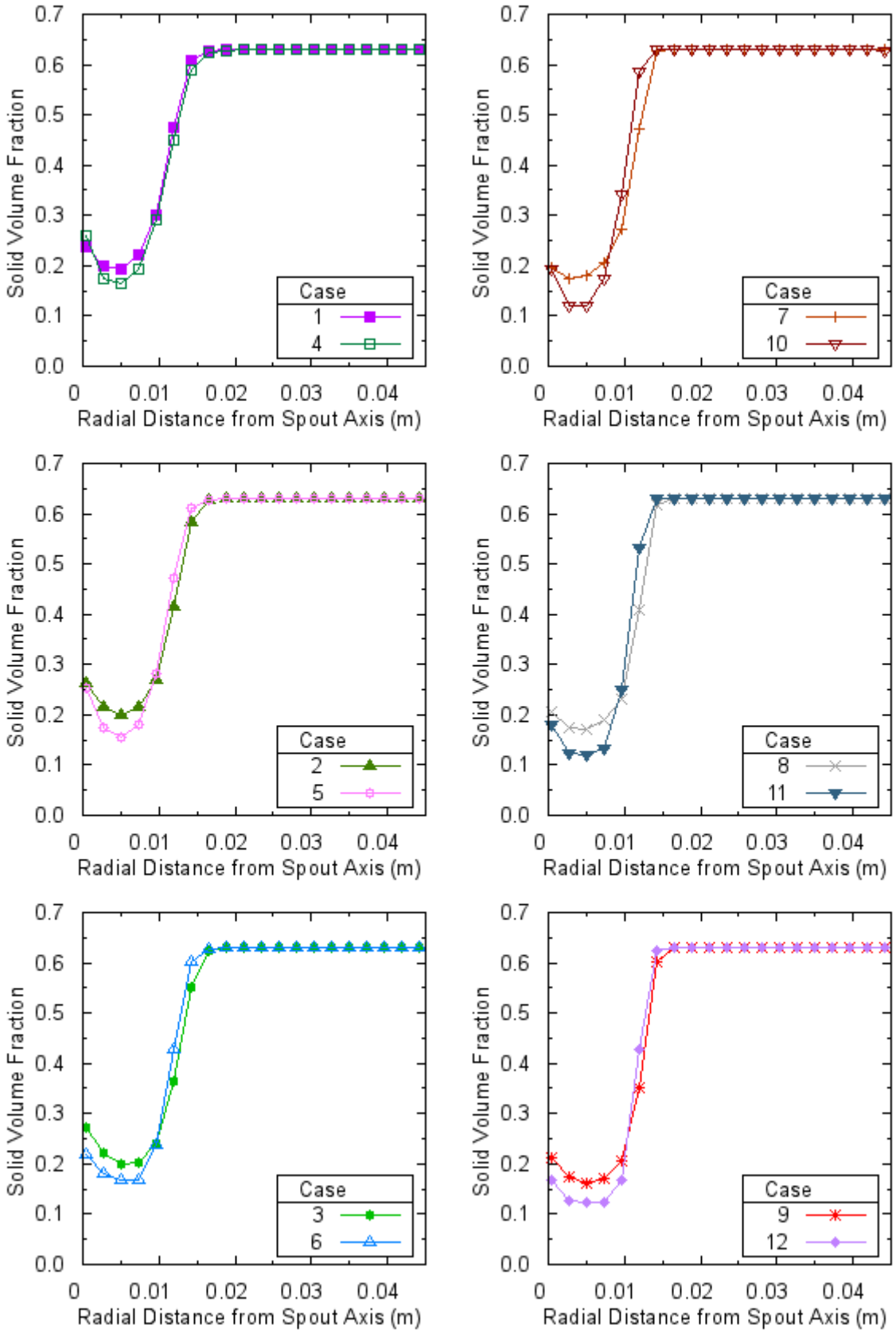

Figure 7.26 The effect of drag model on solid volume fraction distribution for experimental set 3, measurement height 80 mm.

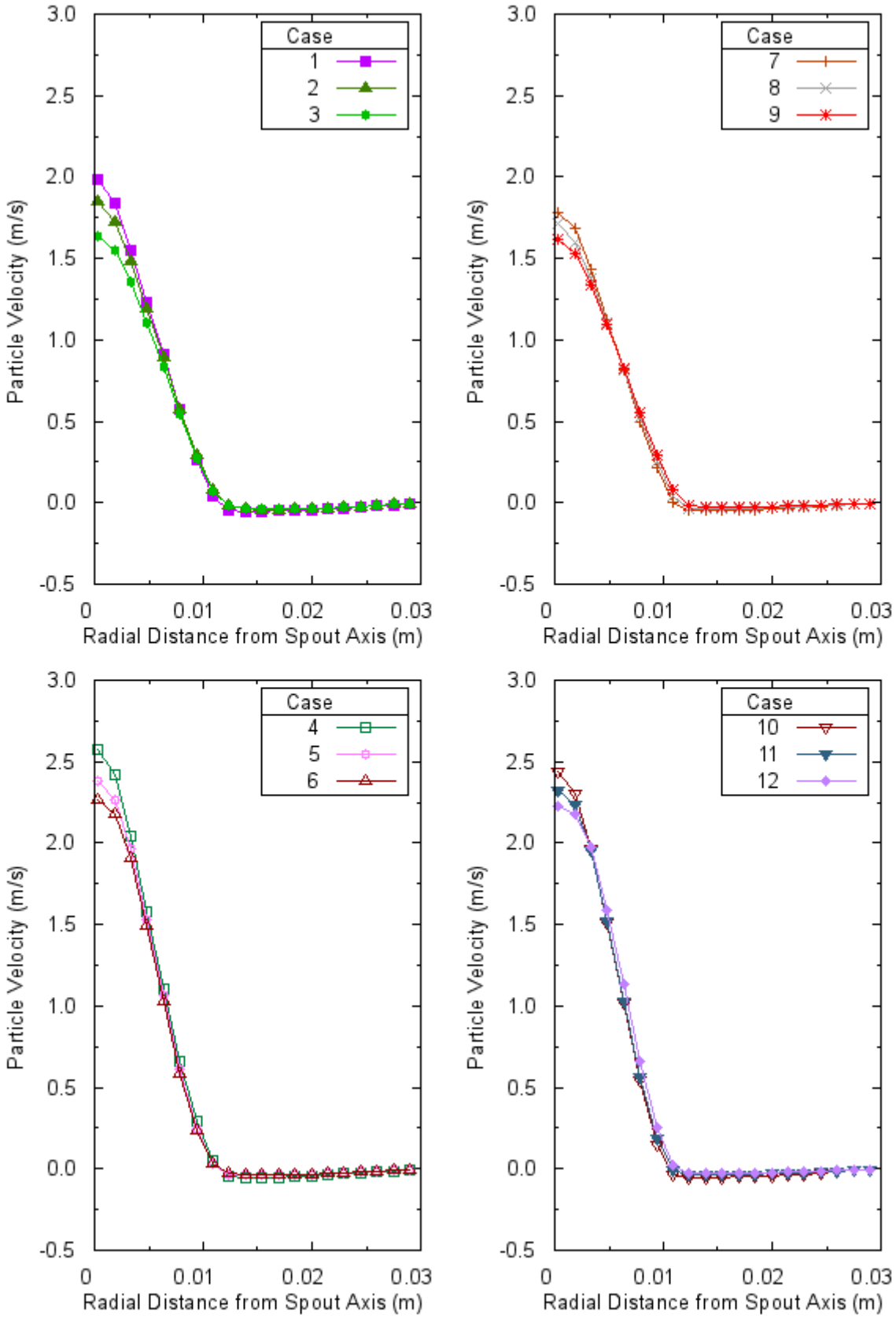

Figure 7.27 The effect of restitution coefficient on particle velocity distribution for experimental set 3, measurement height 42 mm.

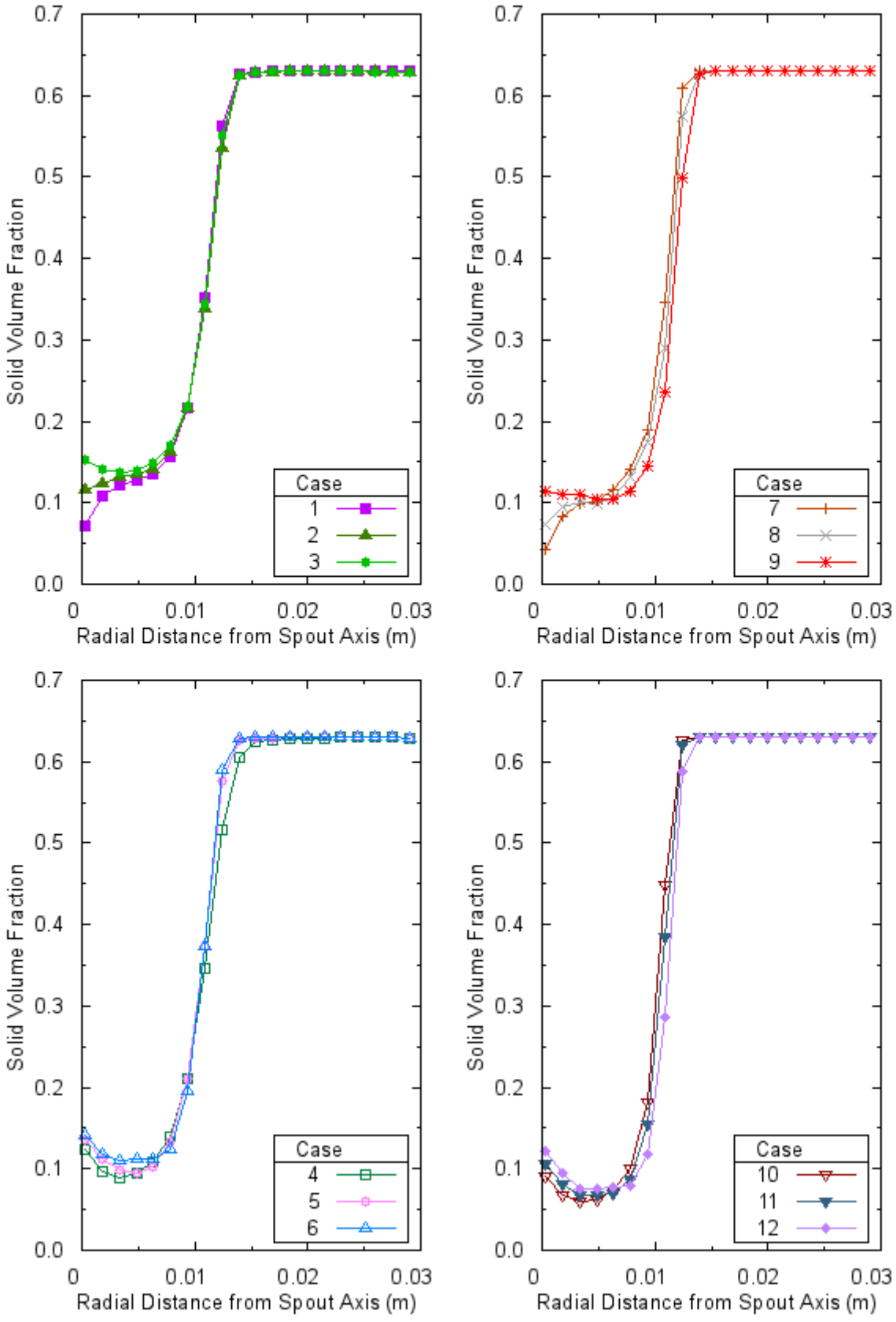

Figure 7.28 The effect of restitution coefficient on solid volume fraction distribution for experimental set 3, measurement height 42 mm.

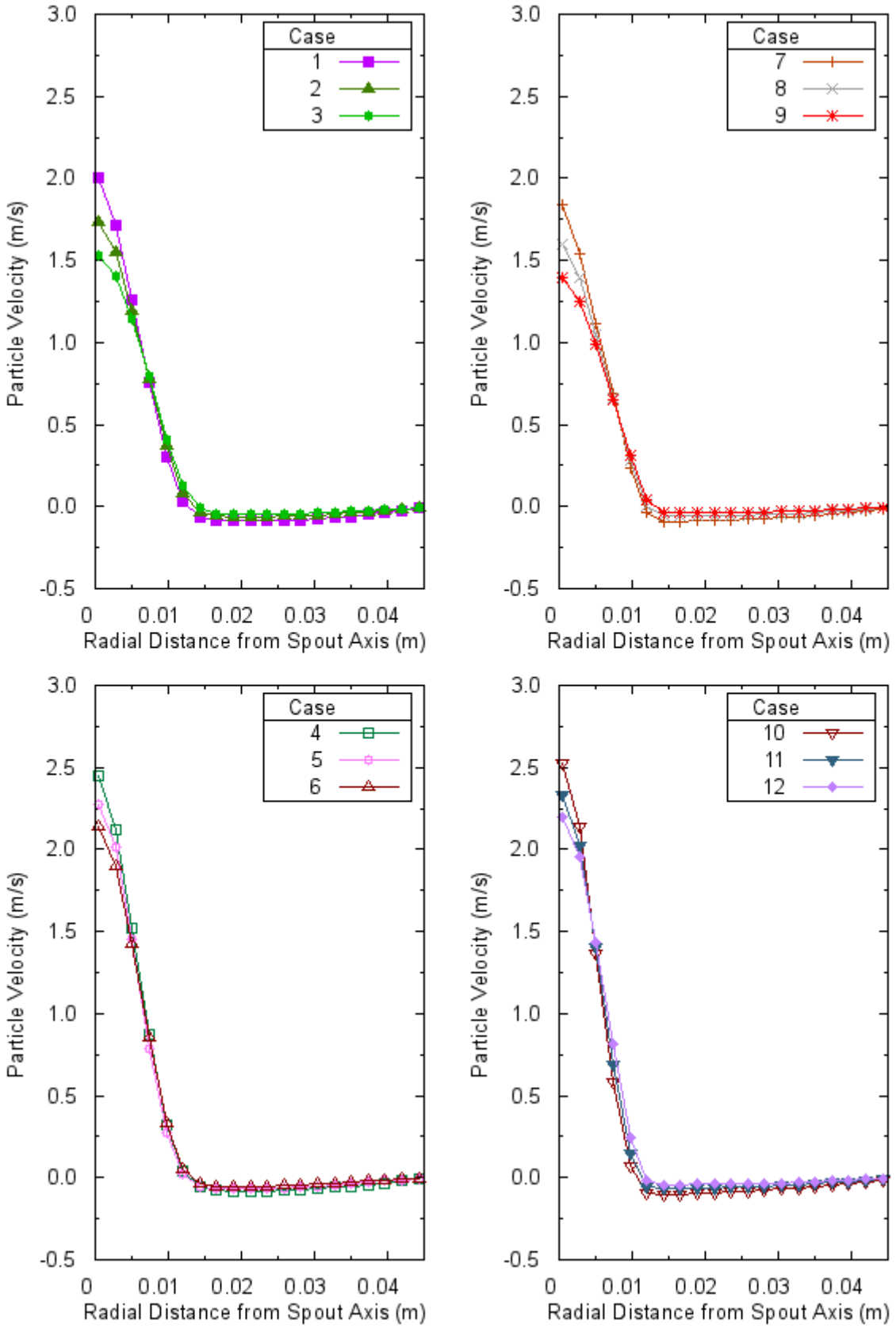

Figure 7.29 The effect of restitution coefficient on particle velocity distribution for experimental set 3, measurement height 80 mm.

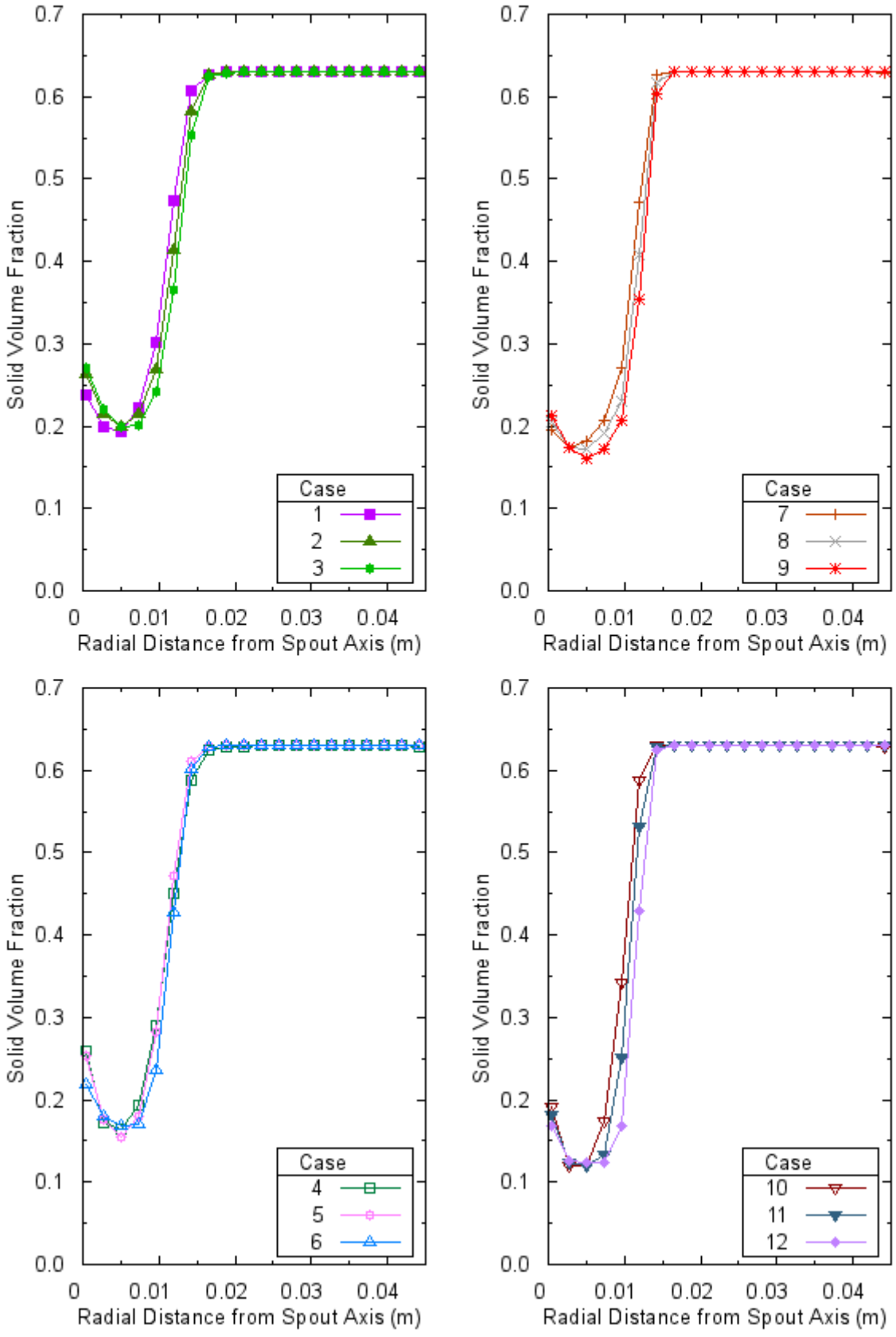

Figure 7.30 The effect of restitution coefficient on solid volume fraction distribution for experimental set 3, measurement height 80 mm.

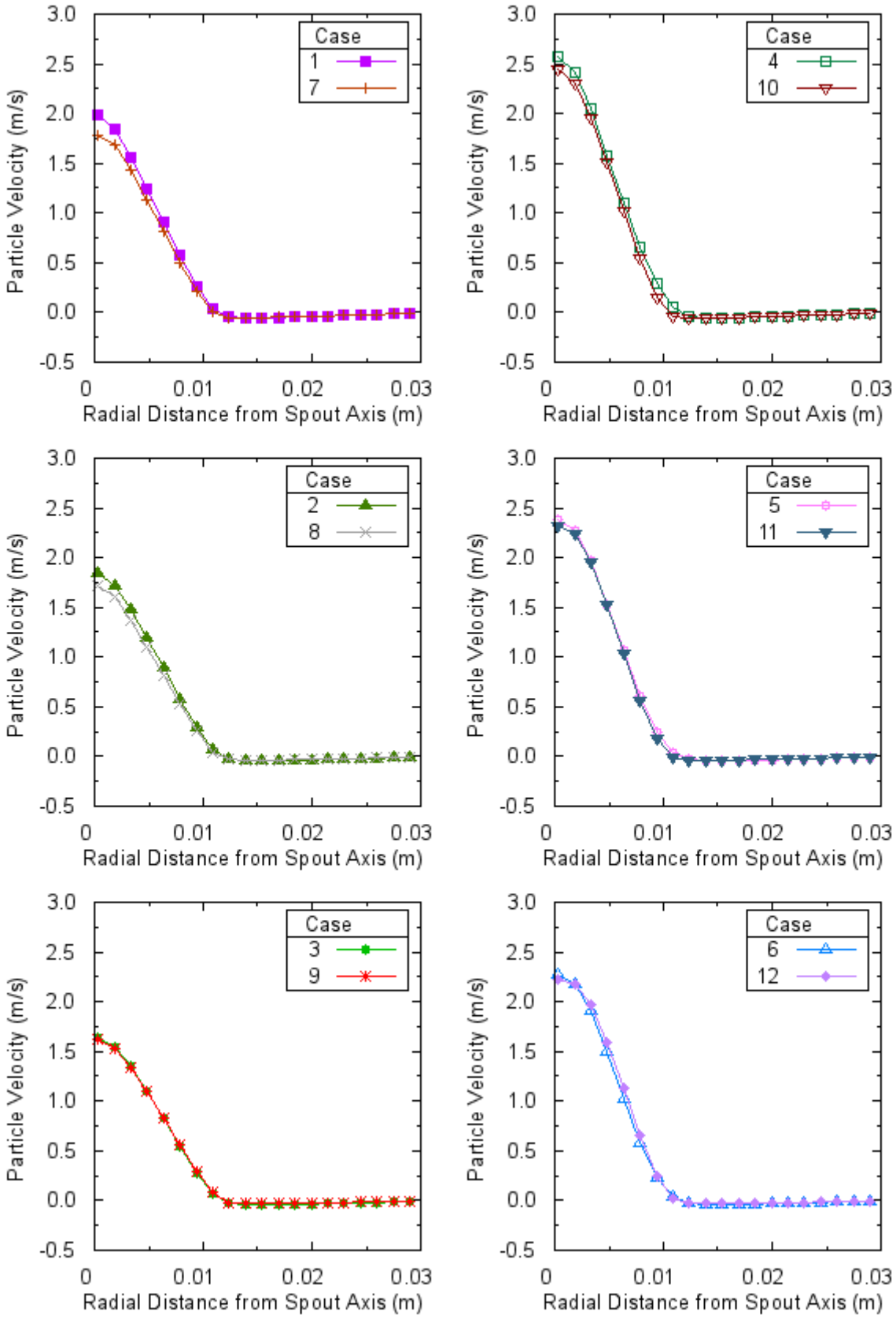

Figure 7.31 The effect of solid frictional stress on particle velocity distribution for experimental set 3, measurement height 42 mm.

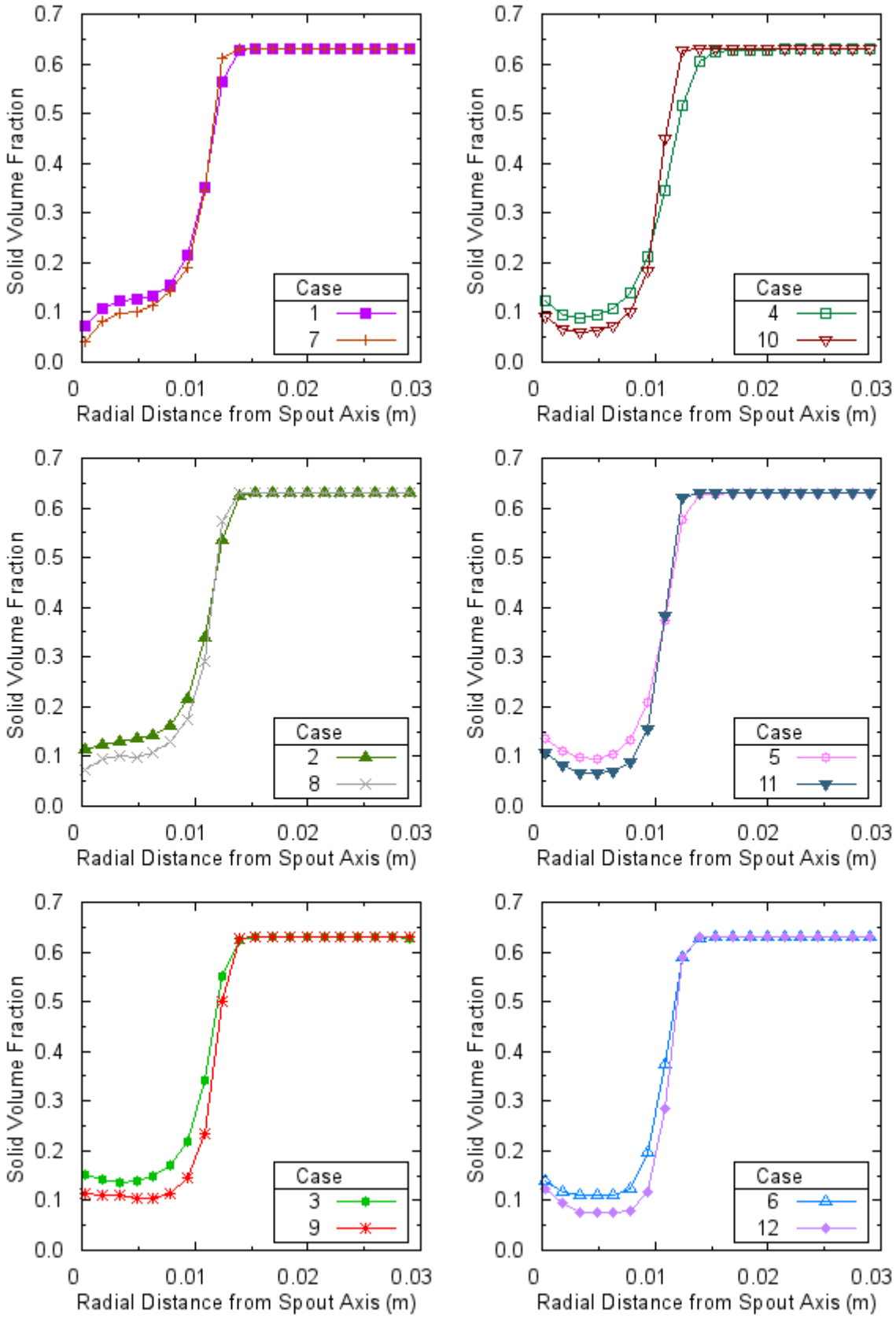

Figure 7.32 The effect of solid frictional stress on solid volume fraction distribution for experimental set 3, measurement height 42 mm.

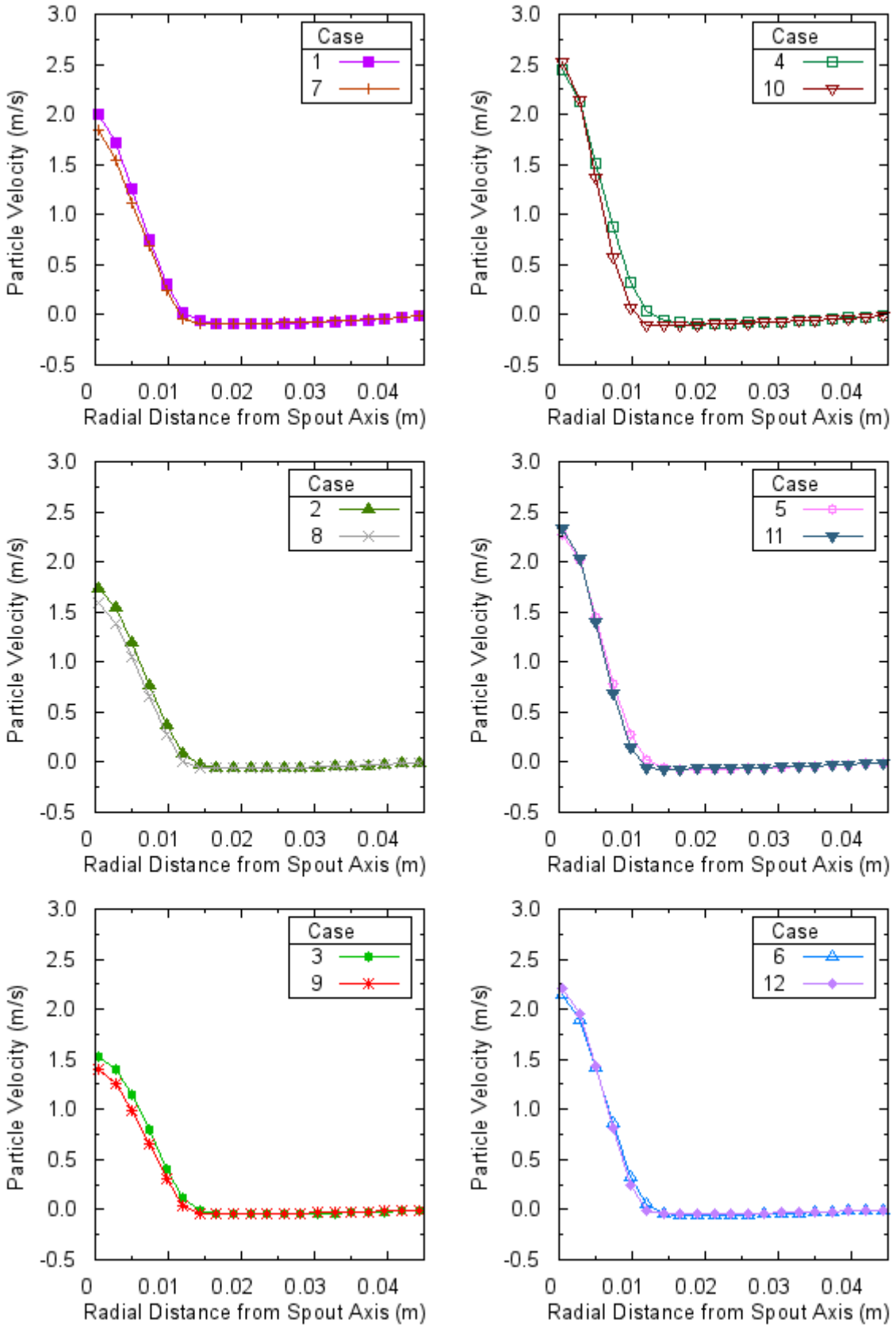

Figure 7.33 The effect of solid frictional stress on particle velocity distribution for experimental set 3, measurement height 80 mm.

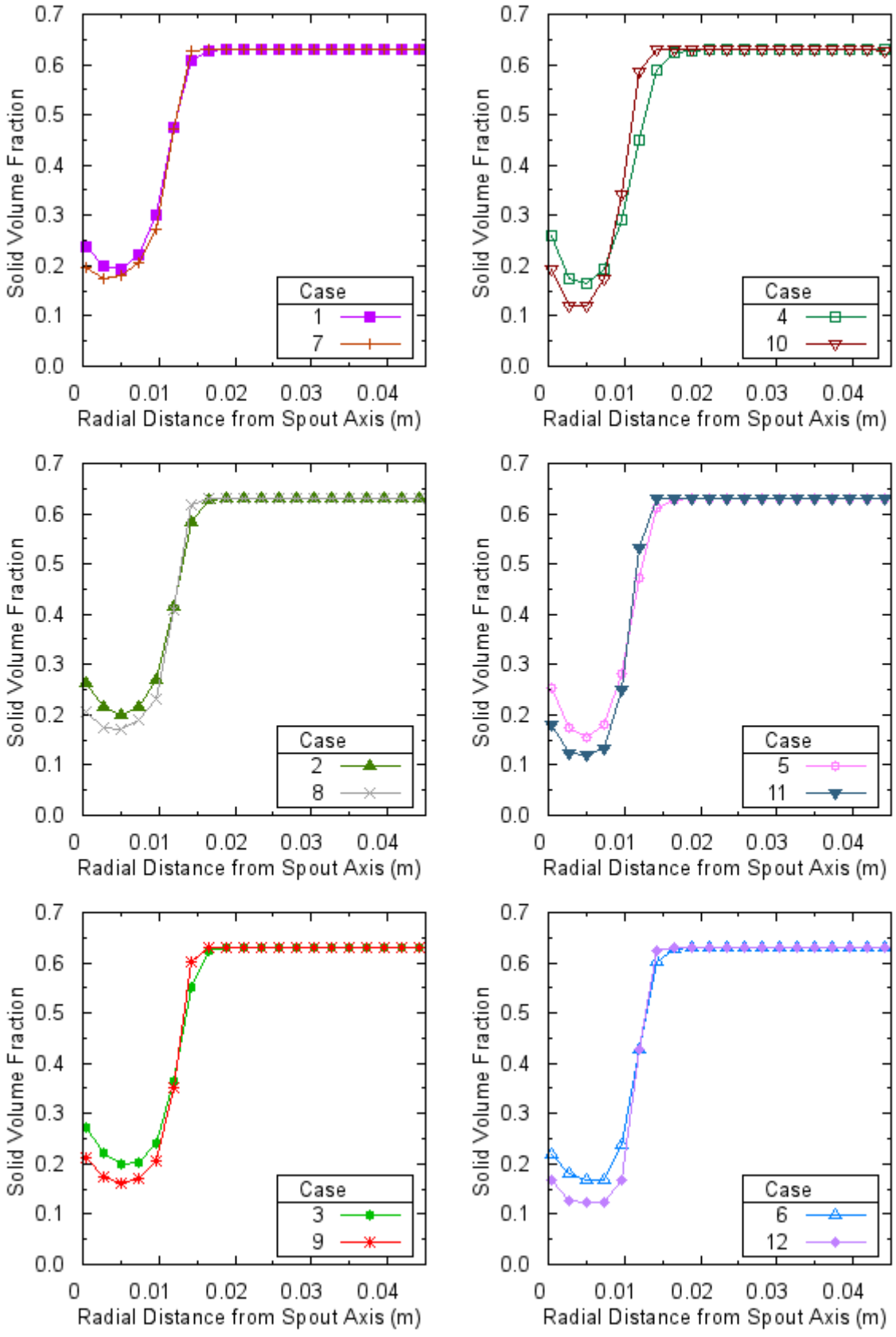

Figure 7.34 The effect of solid frictional stress on solid volume fraction distribution for experimental set 3, measurement height 80 mm.

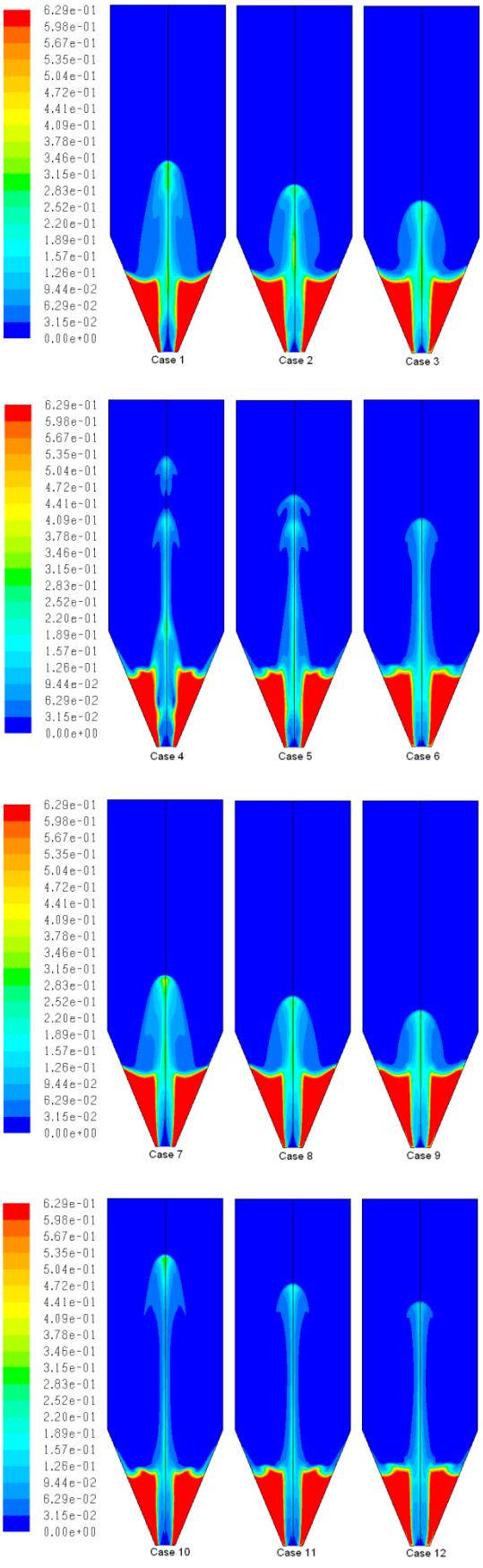

Figure 7.35 Contours of solid volume fraction at t=15 s for experimental set 3.

7.3.4 The Experimental Set 4

The experimental set consists of 45^{o} conic angle, 1.0 mm diameter particles filled in up to the height of 140 mm, and air inlet velocity of 57 m/s. Three heights 42 mm, 82 mm, and 120 mm are used for measurements.

During CFD simulations of the experimental set 4, particles flew out of the system for 8 out of 12 cases (cases 1, 4, 5, 6, 7, 10, 11, and 12). The resulting percent reduction of the solid particle mass in the bed is shown in Table 7.10. For case 1 and 7 total loss in mass is not so significant but for all other cases almost all solid particles flew out of the bed. These cases all use Syamlal-O'Brien drag model and combinations of different restitution coefficient and solid frictional stress condition. However, it is observed from Table 7.10 that as restitution coefficient increases less particles flow out of the system. This observation is valid for Gidaspow drag model cases as well because only the cases having restitution coefficient 0.80 (case 1 and case 7) show the outflow behavior. Another observation is that the particle flow out problem deteriorates when solid frictional stress is included into simulations. Under these circumstances, only the cases 1, 2, 3, 7, 8, and 9 are going to be used for comparison.

Table 7.10 The percent reduction in mass of solid particles due to outflow from the bed for experimental set 4.

Case Number	% Reduction in Solid Particle Mass
1	0.15
4	99.96
5	93.92
6	74.33
7	0.02
10	99.99
11	99.80
12	82.15

The total bed pressure drop values form simulations are shown in Table 7.11. Since all Syamlal-O'Brien drag model cases have outflow condition, there is nothing to compare between drag models.

The effect of restitution coefficient on bed pressure drop for cases with Gidaspow drag model without solid frictional stress does not have specific pattern because it first increases then decreases as restitution coefficient increases. But, increase in restitution coefficient for cases with Gidaspow drag model with solid frictional stress result in a decreasing tendency on bed pressure drop.

There is 30 to 40 % decrease in bed pressure drop values when solid frictional stress is included into the simulations.

Table 7.11 Calculated bed pressure drops for experimental set 4.

Case Number	Bed Pressure Drop (Pa)
1	3187
2	3307
3	3274
7	2180
8	2006
9	1942

Since all Syamlal-O'Brien drag model cases have outflow condition, there is nothing to compare between drag models for particle velocity and solid volume fraction.

The effect of restitution coefficient on simulations for all three measurement heights are shown in Figure 7.36 for particle velocity and Figure 7.37 for solid volume fraction. For all measurement heights, particle velocity predictions decrease as restitution coefficient increases. The effect is not so clear for the measurement height 42 mm which is the closest the bed inlet. For solid volume fraction, there is an increase in values for every measurement height. The effect of restitution coefficient on solid volume fraction distributions are not significant for z=82 mm and z=120 mm.

The effect of inclusion of solid frictional stress into simulations on both particle velocity and solid volume fraction distributions are represented in Figure 7.38 for z=42 mm, in Figure 7.39 for z=82 mm, and in Figure 7.40 for z=120 mm. Its inclusion decreases particle velocity and solid volume fraction for every height. But the effect is very small on particle velocity distributions.

It can be concluded from all simulations that particle velocity decreases as measurement height increases. Controversially, solid volume fraction increases in the spout region as measurement height increases.

Both increase in restitution coefficient and inclusion of solid frictional stress reduce the spout height as seen in Figure 7.41.

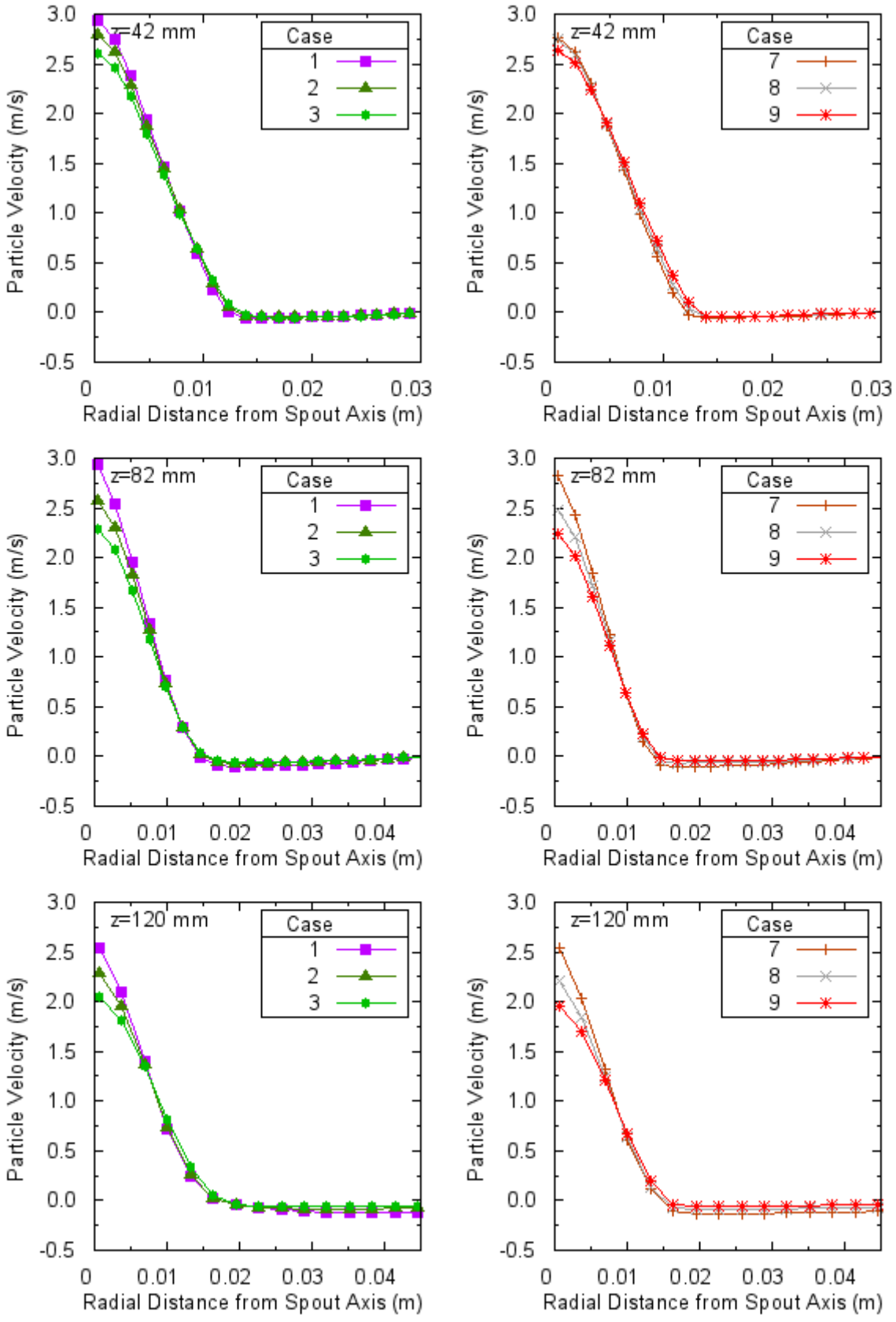

Figure 7.36 The effect of restitution coefficient on particle velocity distribution for experimental set 4, measurement height 42 mm, 82 mm, and 120 mm.

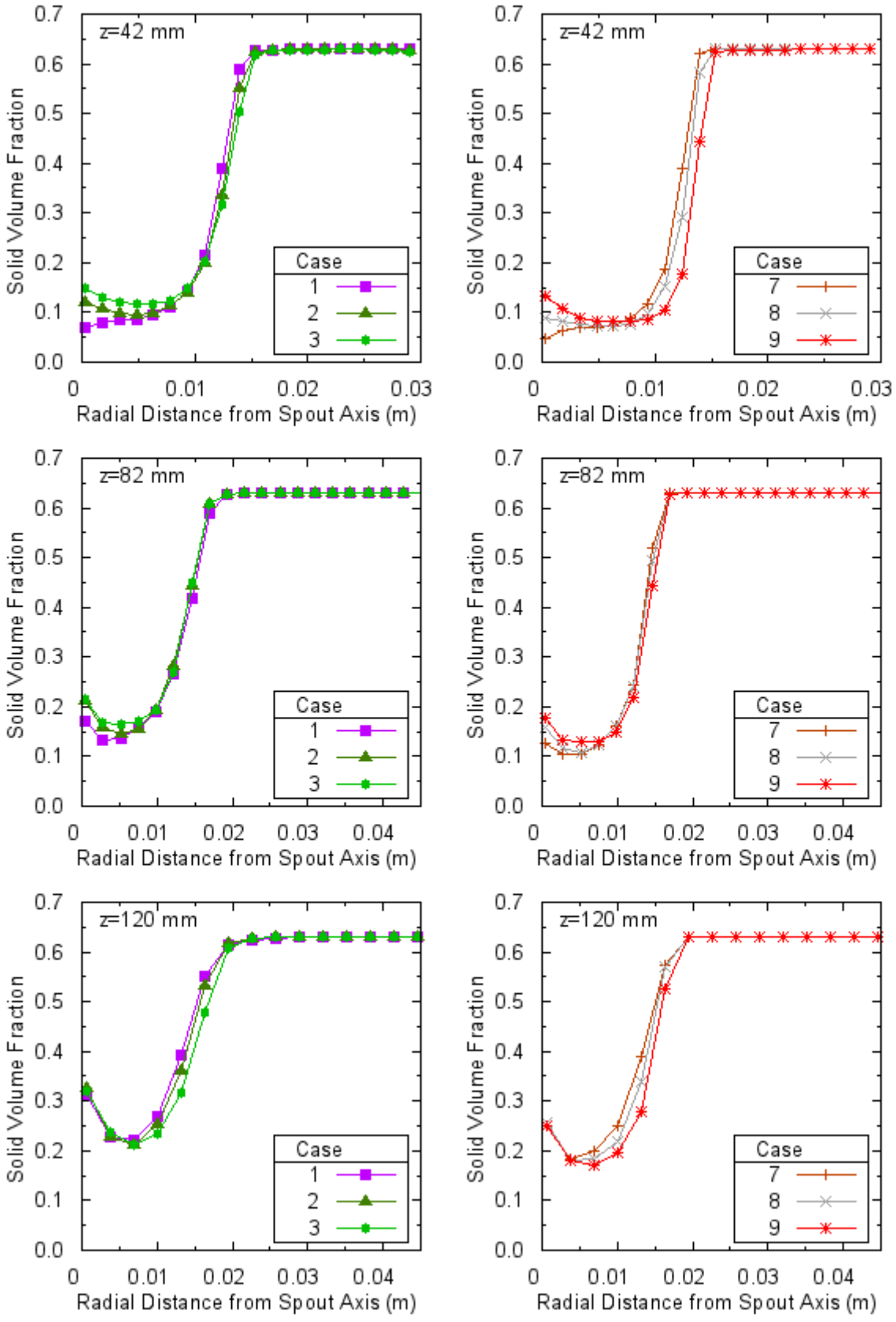

Figure 7.37 The effect of restitution coefficient on solid volume fraction distribution for experimental set 4, measurement height 42 mm, 82 mm, and 120 mm.

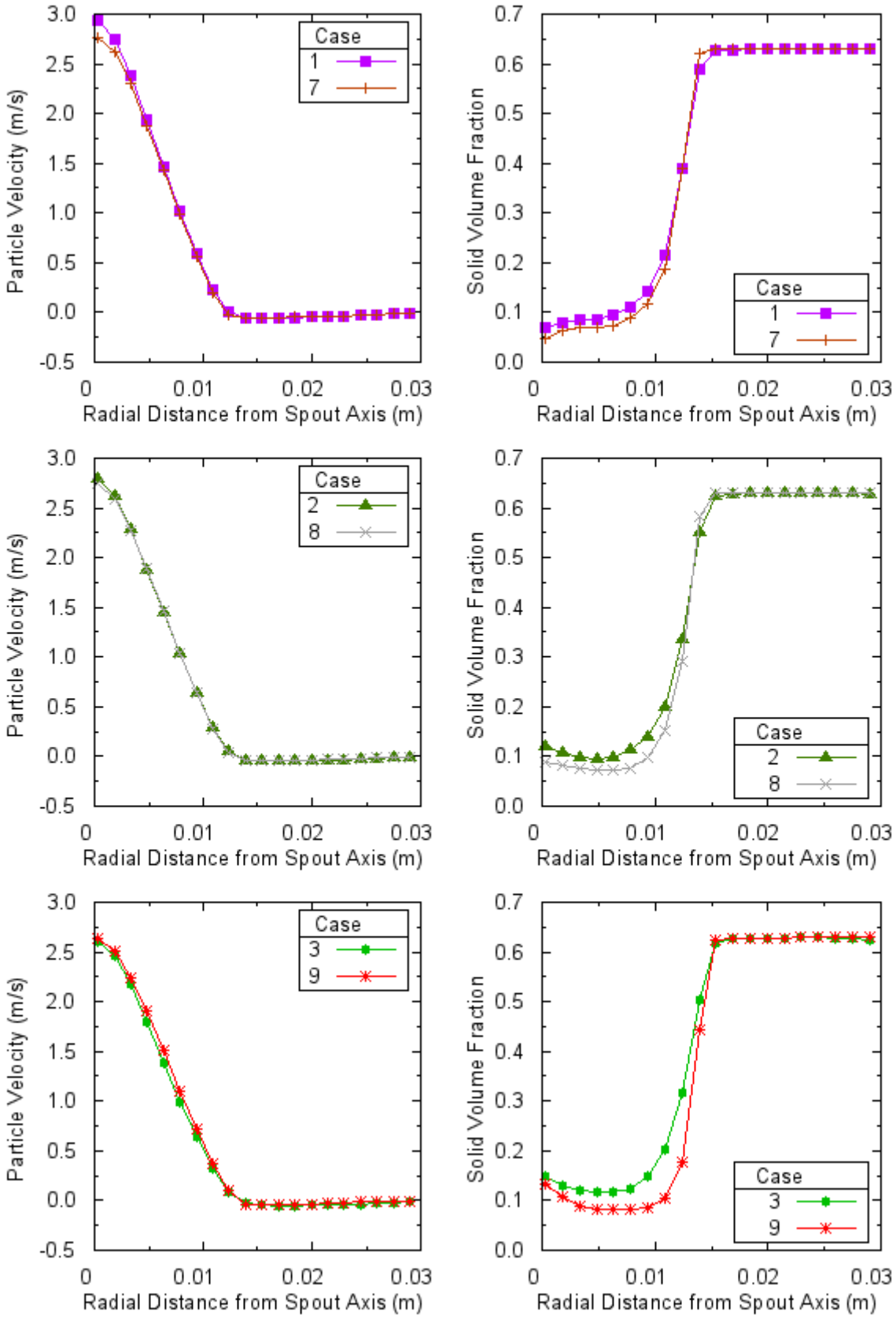

Figure 7.38 The effect of frictional stress on particle velocity and solid volume fraction distributions for experimental set 4, measurement height 42 mm.

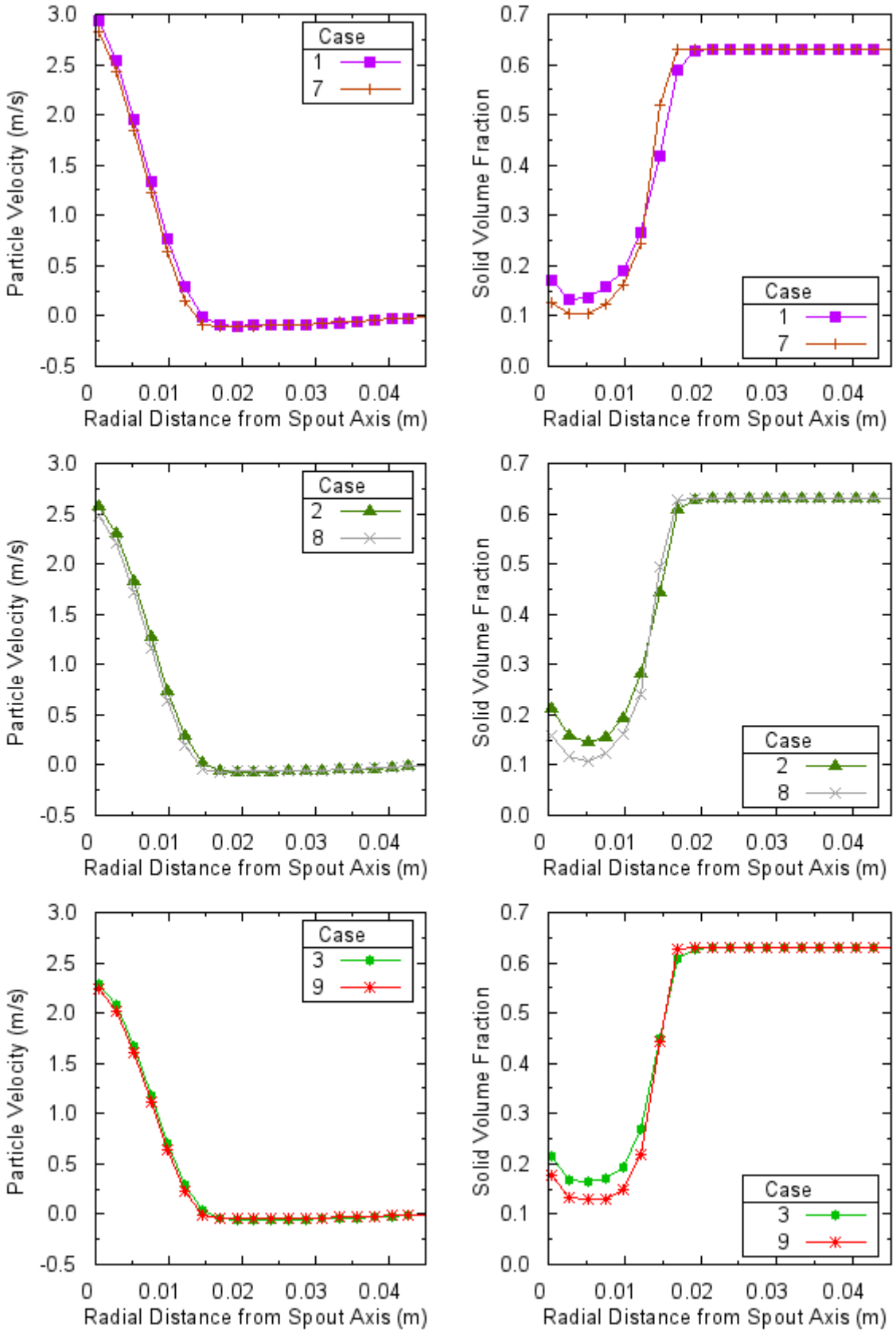

Figure 7.39 The effect of frictional stress on particle velocity and solid volume fraction distributions for experimental set 4, measurement height 82 mm.

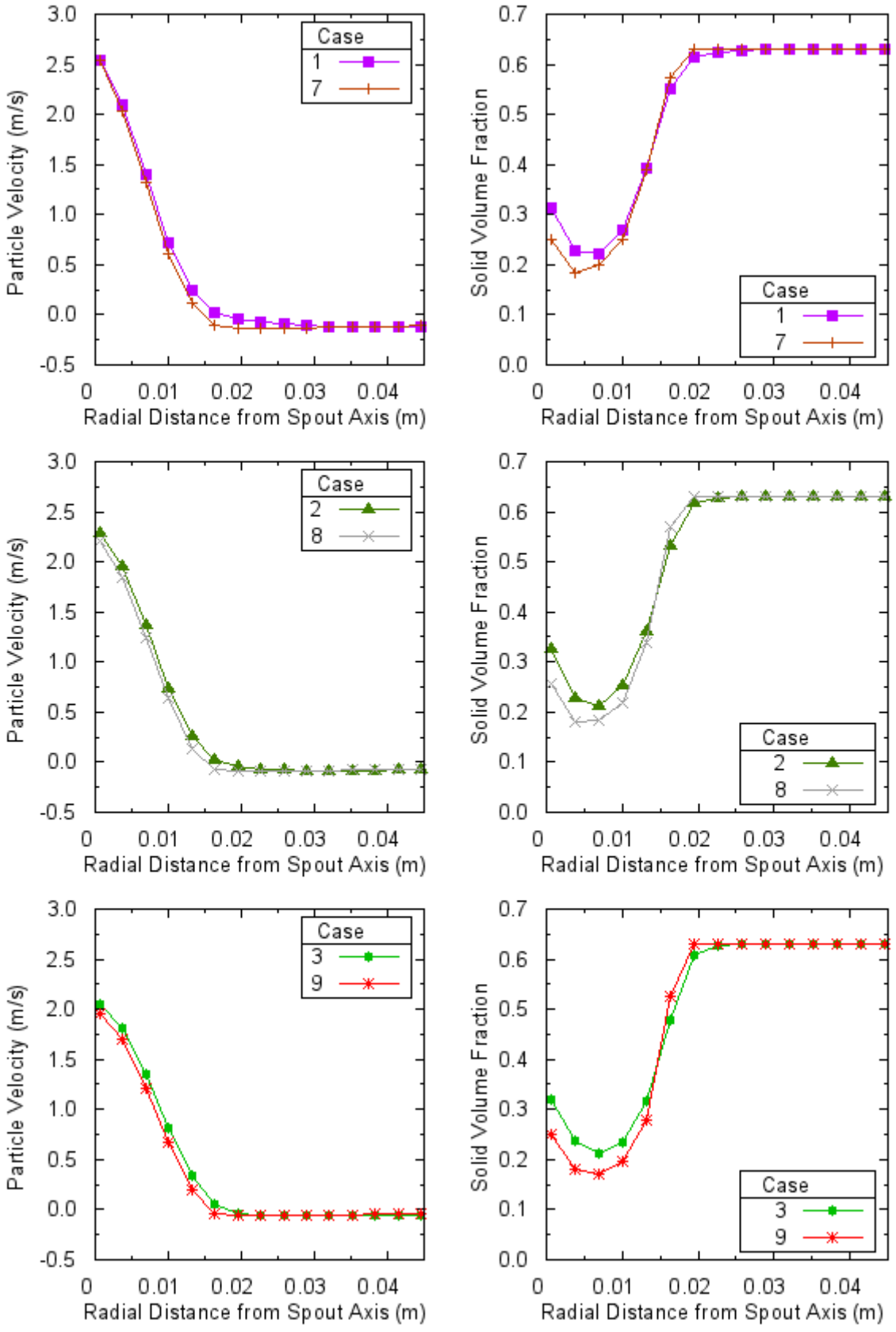

Figure 7.40 The effect of frictional stress on particle velocity and solid volume fraction distributions for experimental set 4, measurement height 120 mm.

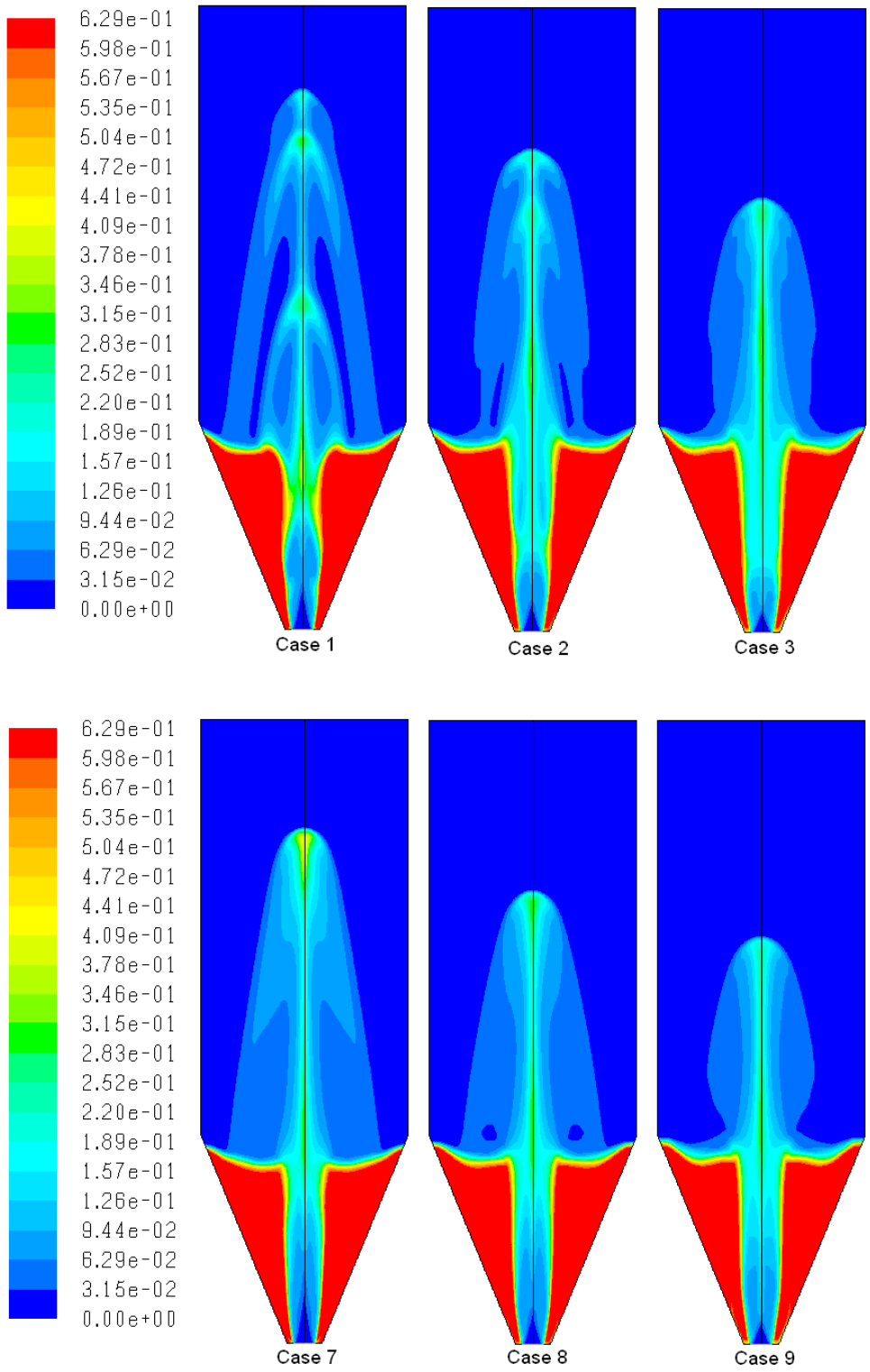

Figure 7.41 Contours of solid volume fraction at t=15 s for experimental set 4.

7.3.5 The Experimental Set 5

This experimental set has 60^o conic angle, is filled with 1.0 mm diameter particles up to the height of 60 mm, and the bed is fluidized with air at 26.8 m/s velocity. The measurement height of 50 mm is used.

The calculated pressure drop results in Table 7.12 indicate that Syamlal-O'Brien drag model predictions for bed pressure drop are higher than Gidaspow drag model predictions.

As restitution coefficient increases, pressure drop results decrease for all cases except the cases using only Gidaspow drag model without solid frictional stress. For this case pressure drop results are very close and it first decreases and then increases.

Addition of solid frictional stress in simulations drops the pressure drop results 30 to 45 %.

Table 7.12 Calculated bed pressure drops for experimental set 5.

Case Number	Bed Pressure Drop (Pa)
1	1225
2	1223
3	1233
4	1334
5	1307
6	1289
7	851
8	734
9	674
10	856
11	797
12	711

Syamlal-O'Brien drag model particle velocity results are higher than the Gidaspow drag model results as seen in Figure 7.42. But the spout radiuses are very close as well as velocity results in annulus region. Spout region for Syamlal-O'Brien case is more dilute as seen in Figure 7.43.

Figure 7.44 indicates that the increase in restitution coefficient reduces the particle velocity results. Although there is a small increase in solid volume fraction with increase in restitution coefficient but the effect is not so significant for solid volume fraction shown in Figure 7.45.

Both particle velocity and solid volume fraction predictions reduce when solid frictional stress is included in simulations as seen in Figure 7.46 and Figure 7.47.

The contours of solid volume fraction at 15^{th} second of the simulation for all cases are shown in Figure 7.48. Syamlal-O'Brien drag model fountain height is higher than Gidaspow drag model fountain height for every other combination of restitution coefficient and solid frictional stress condition.

As restitution coefficient increases fountain height decreases.

Inclusion of solid frictional stress in simulations results in lower fountain height.

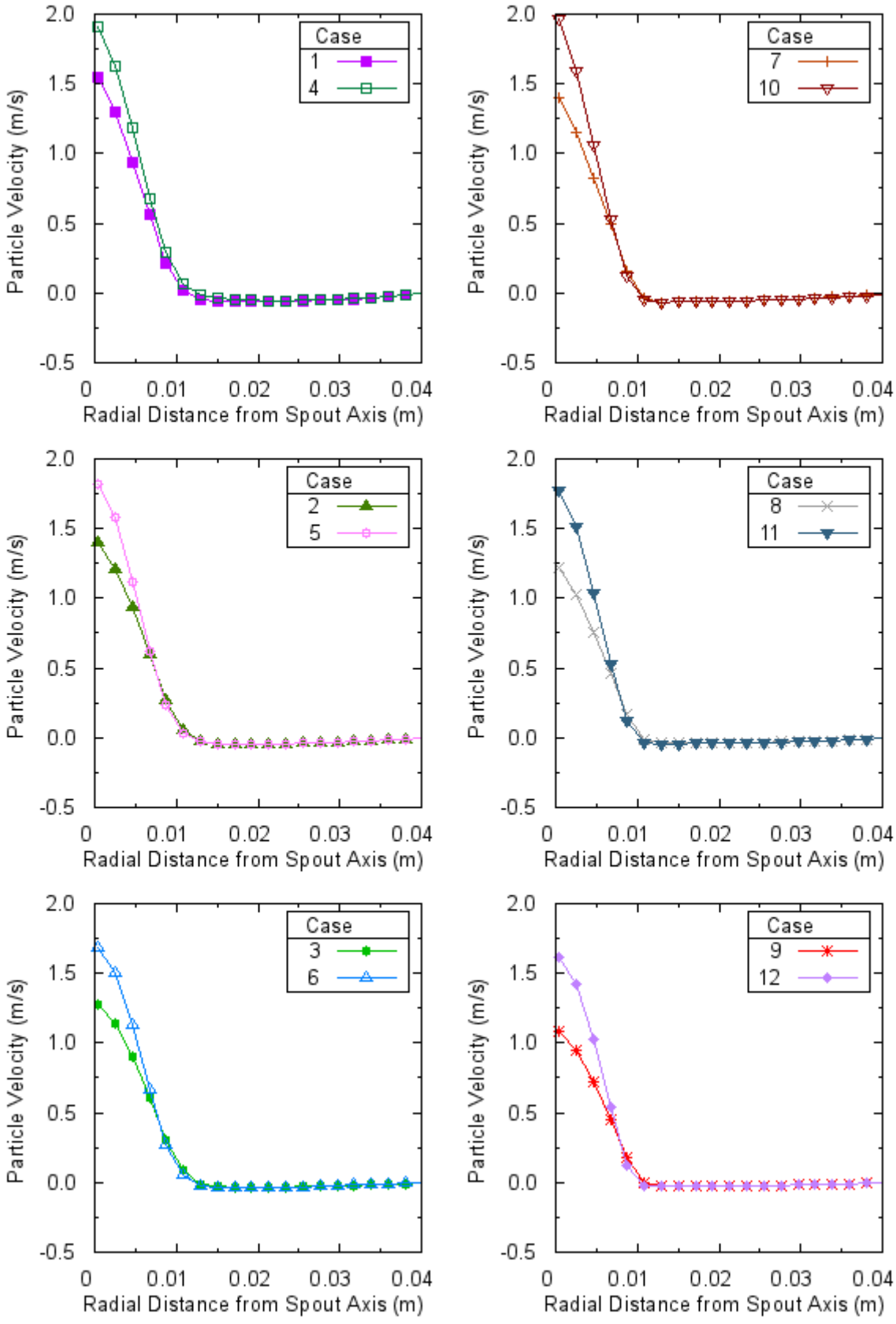

Figure 7.42 The effect of drag model on particle velocity distribution for experimental set 5, measurement height 50 mm.

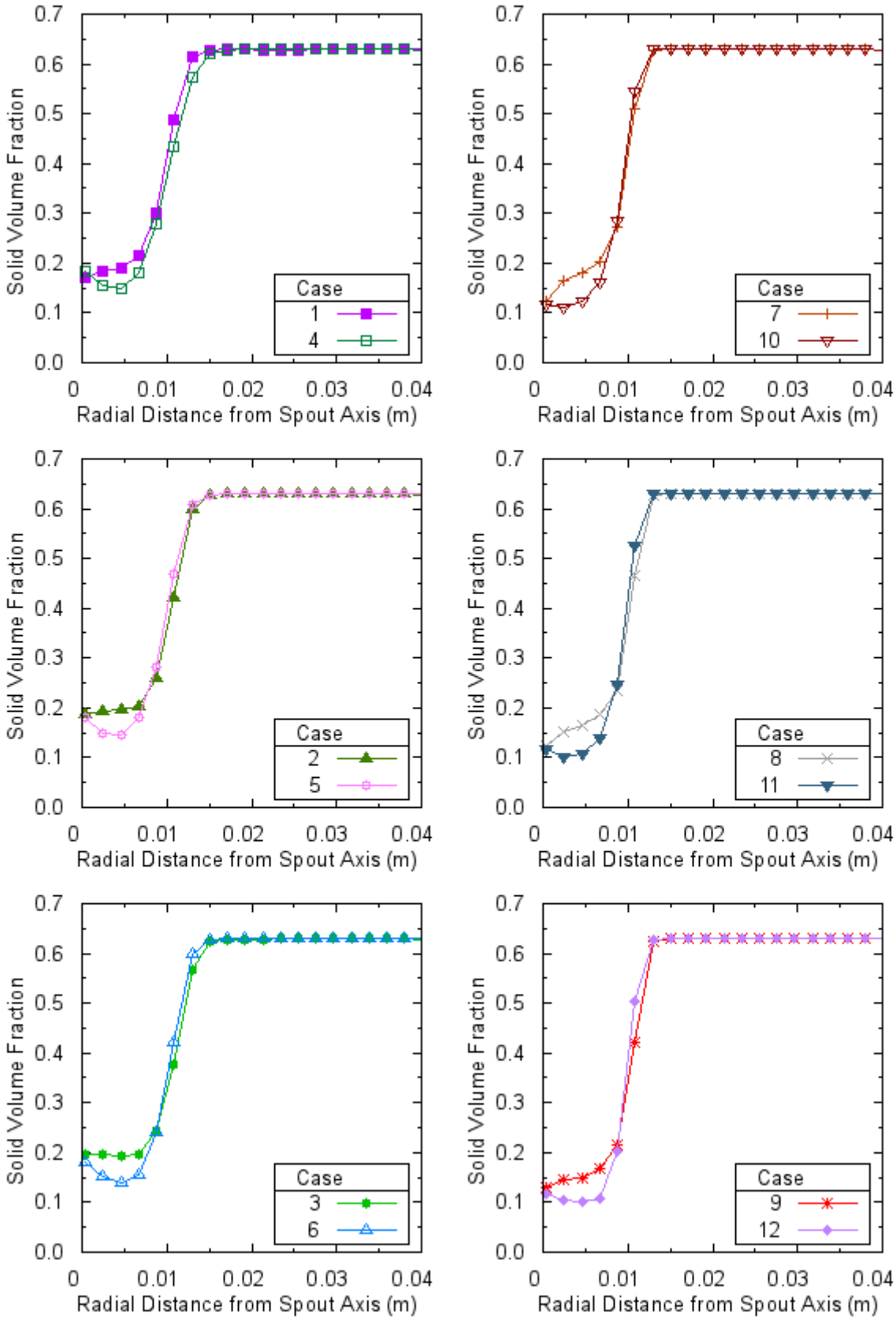

Figure 7.43 The effect of drag model on solid volume fraction distribution for experimental set 5, measurement height 50 mm.

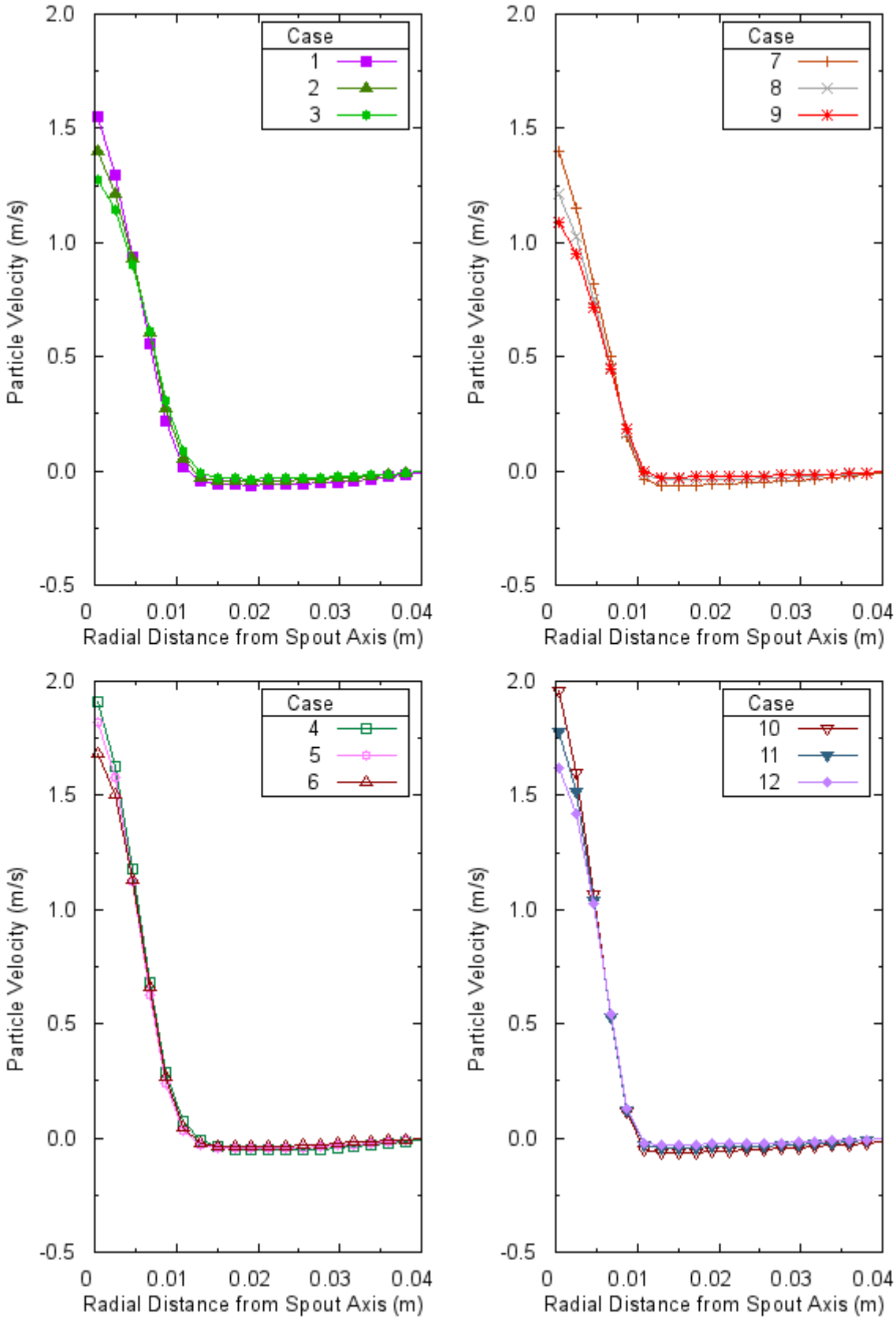

Figure 7.44 The effect of restitution coefficient on particle velocity distribution for experimental set 5, measurement height 50 mm.

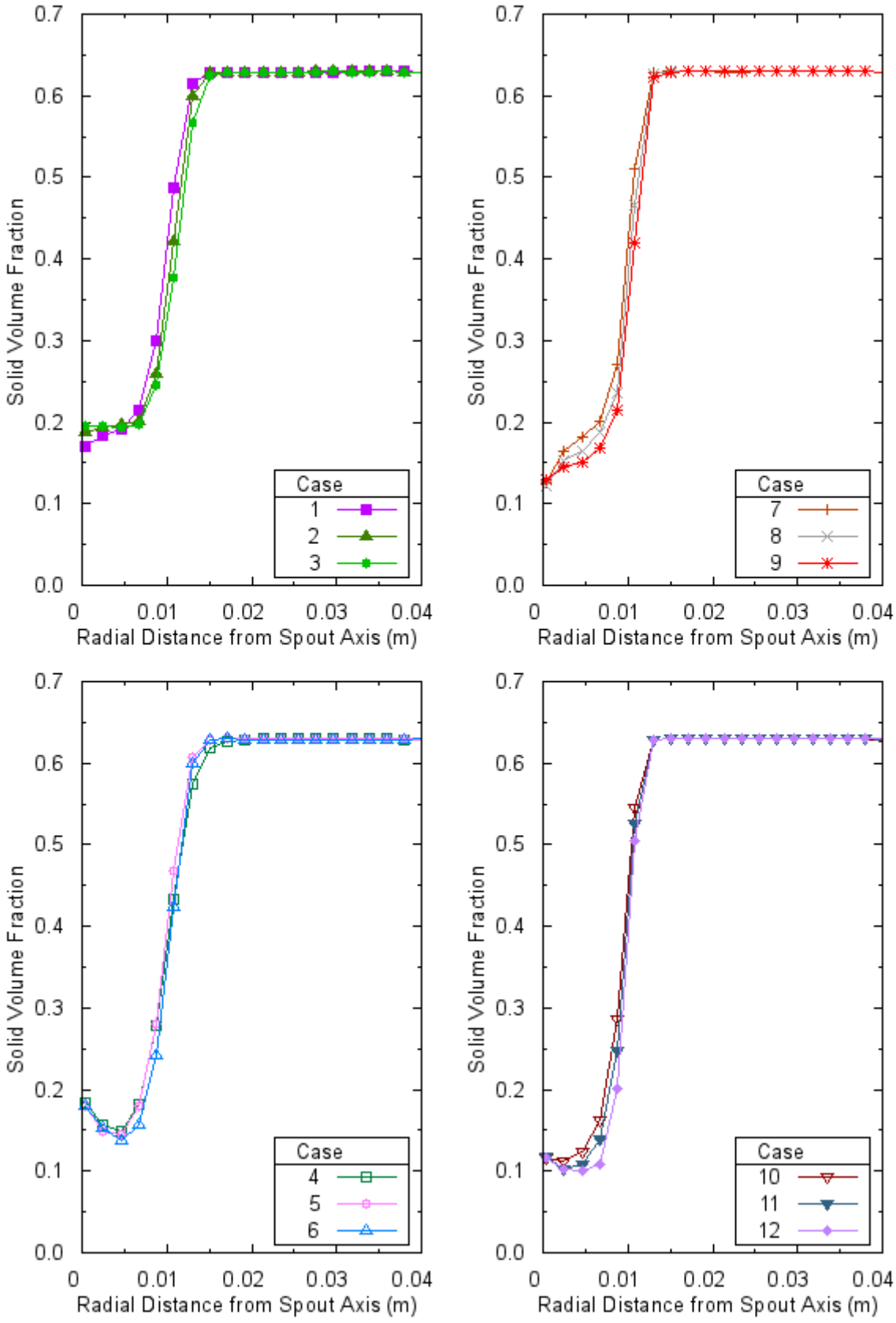

Figure 7.45 The effect of restitution coefficient on solid volume fraction distribution for experimental set 5, measurement height 50 mm.

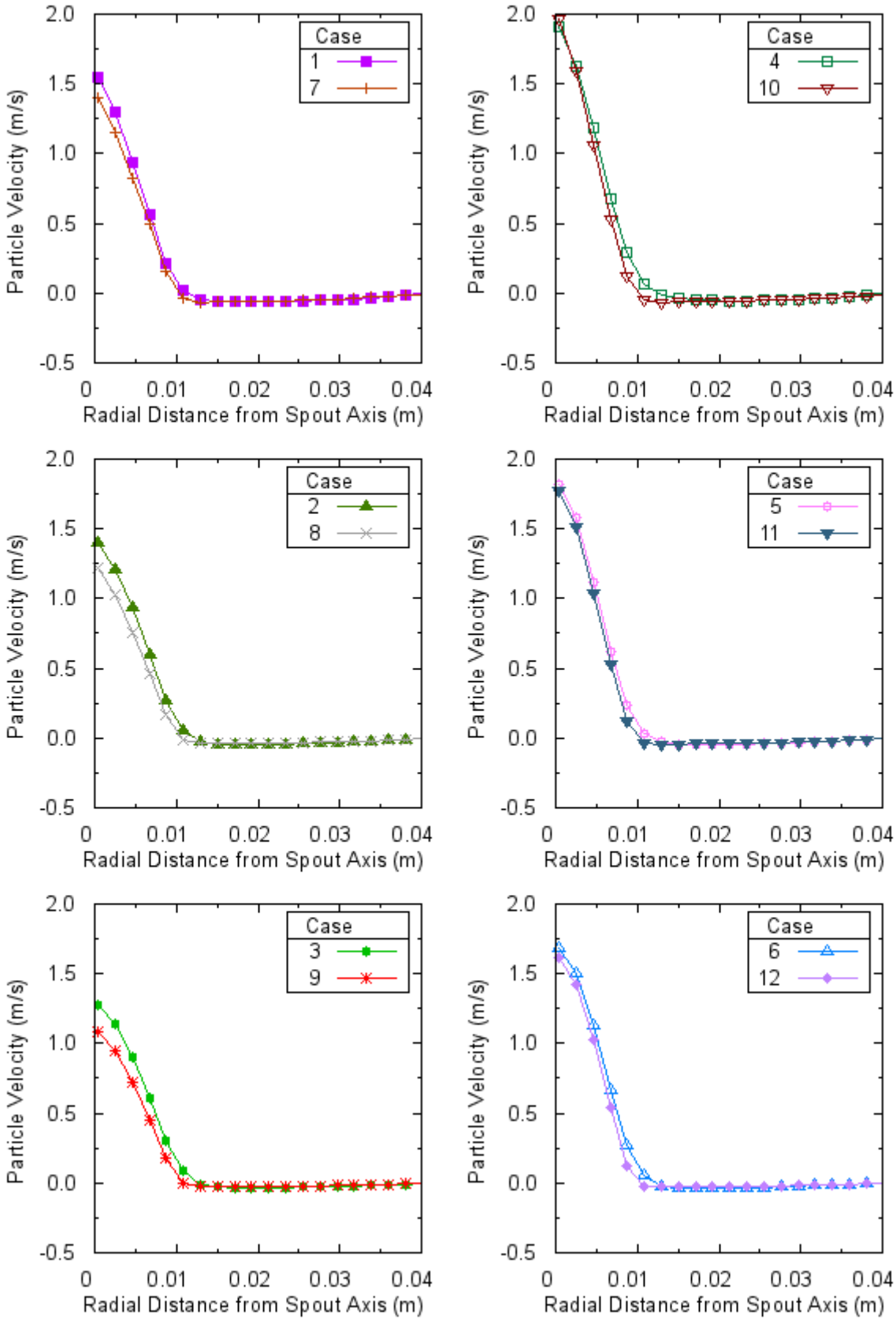

Figure 7.46 The effect of solid frictional stress on particle velocity distribution for experimental set 5, measurement height 50 mm.

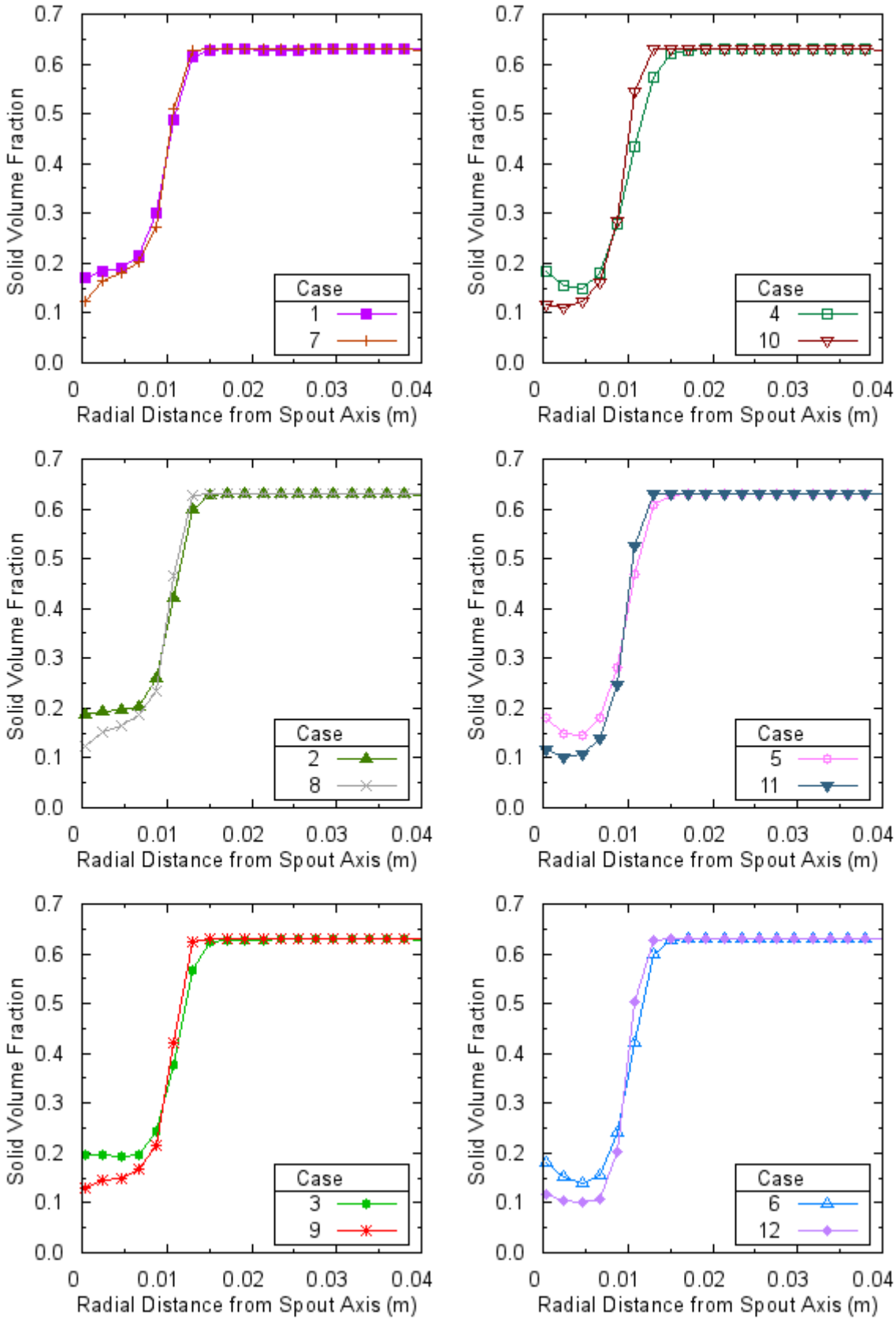

Figure 7.47 The effect of solid frictional stress on solid volume fraction distribution for experimental set 5, measurement height 50 mm.

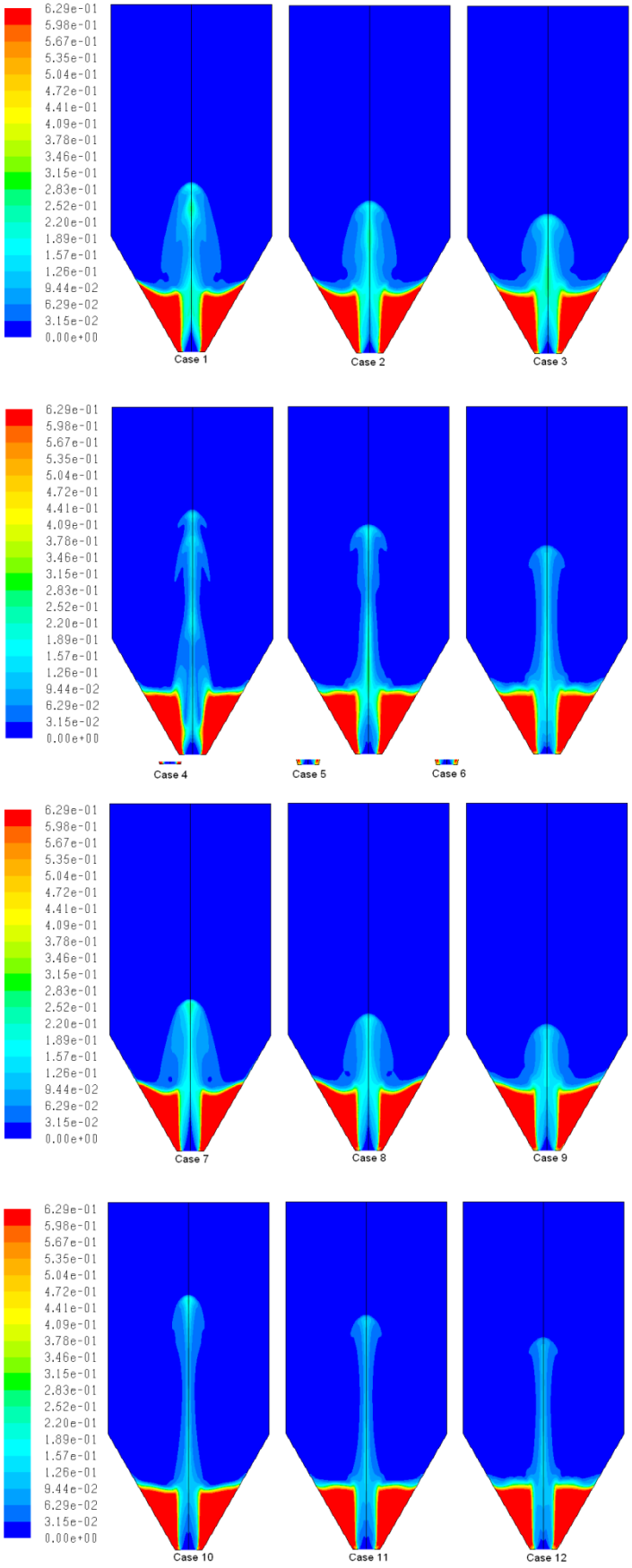

Figure 7.48 Contours of solid volume fraction at t=15 s for experimental set 5.

7.3.6 The Experimental Set 6

60^o conic angle experimental set is filled with 1.0 mm diameter particles. It has 100 mm static bed height and inlet velocity is 45.3 m/s. Two measurement heights 50 mm and 93 mm are used.

The particles flew out of the bed for the cases having Syamlal-O'Brien drag model no matter what the restitution coefficient is or whether solid frictional stress is included into simulations or not. The percent reduction in solid particle mass is shown in Table 7.13. It is clear from the table that an increase in restitution coefficient results in less particle outflow. Controversially, inclusion of solid frictional stress results in more particle outflow. Since the mass of particles are reduces significantly, the cases having Syamlal-O'Brien drag model are not going to be considered for examination of simulation results.

Table 7.13 The percent reduction in mass of solid particles due to outflow from the bed for experimental set 6.

Case Number	% Reduction in Solid Particle Mass
4	99.99
5	89.29
6	57.55
10	99.99
11	93.17
12	67.41

Calculated bed pressure drop values for experimental set 6 for cases having only Gidaspow drag model are presented in Table 7.14. Both increase in restitution coefficient and inclusion of solid frictional stress into simulations reduce the bed pressure drop results. Only exception is case 2. For this case, pressure drop result increases as restitution coefficient increases. The most drastic parameter for bed pressure calculations is solid frictional stress condition since the reductions are around 30 to 40 % depending on the value of the restitution coefficient.

The effect of restitution coefficient and inclusion of solid frictional stress into simulations on particle velocity and solid volume fraction for measurement heights 50 and 93 mm are presented in Figure 7.49 to Figure 7.52.

Table 7.14 Calculated bed pressure drops for experimental set 6.

Case Number	Bed Pressure Drop (Pa)
1	2275
2	2305
3	2268
7	1584
8	1371
9	1191

The increase in restitution coefficient decreases the particle velocity for both z=50 mm and z=93 mm as seen in Figure 7.49. The particle velocity distribution at z=93 mm first decreases and then increases in annulus region. This is more significant for case 1 and case 7 where restitution coefficient is at minimum. The solid volume fraction distribution for two measurement heights show great difference as presented in Figure 7.50. In the spout region, solid volume fraction distributions are very similar to what observed in all experimental set simulations. But in the annulus region solid volume fraction drops sharply as if there is another spout region inside the annulus. Then it reaches to a value close to maximum packing limit near the bed wall. This is because of the fact that measurement line at 93 mm is very close to bed surface. Since the bed surface is not stable due to particle movements, there are small peaks of solid particles at the surface. The simulations results catch these ups and downs in solid volume fraction. Therefore, comparison is not going to be performed for annulus region of measurement height of 93 mm. The increase in restitution coefficient seems to be more significant for measurement height 50 mm as it increases the solid volume fraction more than it does for measurement height 93 mm.

Inclusion of frictional stress into simulations reduces the particle velocity and solid volume fraction as seen in Figure 7.51 and Figure 7.52. At z=93 mm, the behavior of solid volume fraction is very chaotic therefore the effect of inclusion of solid frictional stress on solid volume fraction is not clear for annulus region.

As observed in Figure 7.53, an increase in restitution coefficient reduces fountain height. An inclusion of solid frictional stress in simulations also reduces fountain height but the effect is not so clear.

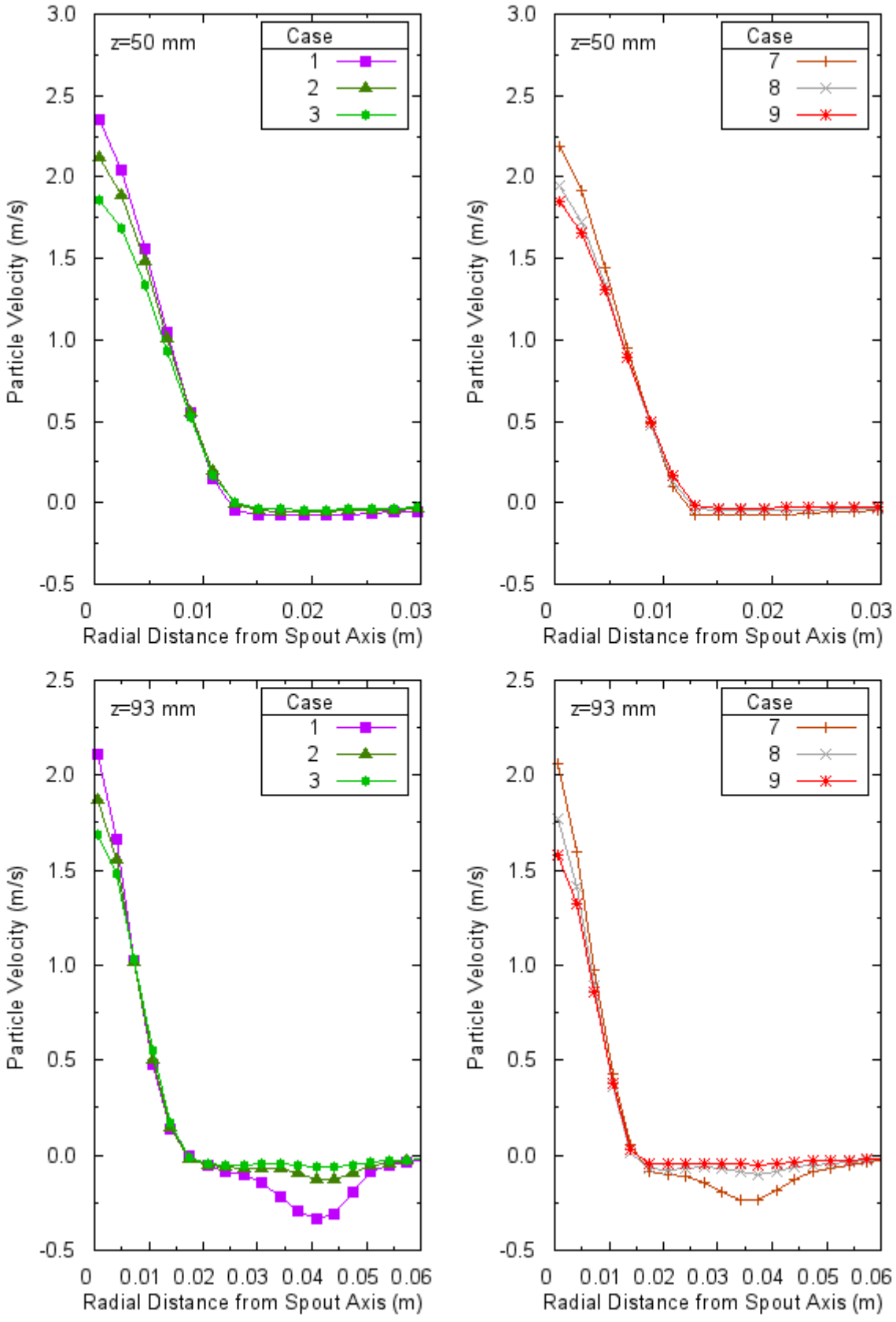

Figure 7.49 The effect of restitution coefficient on particle velocity distribution for experimental set 6, measurement height 50 mm, 93 mm.

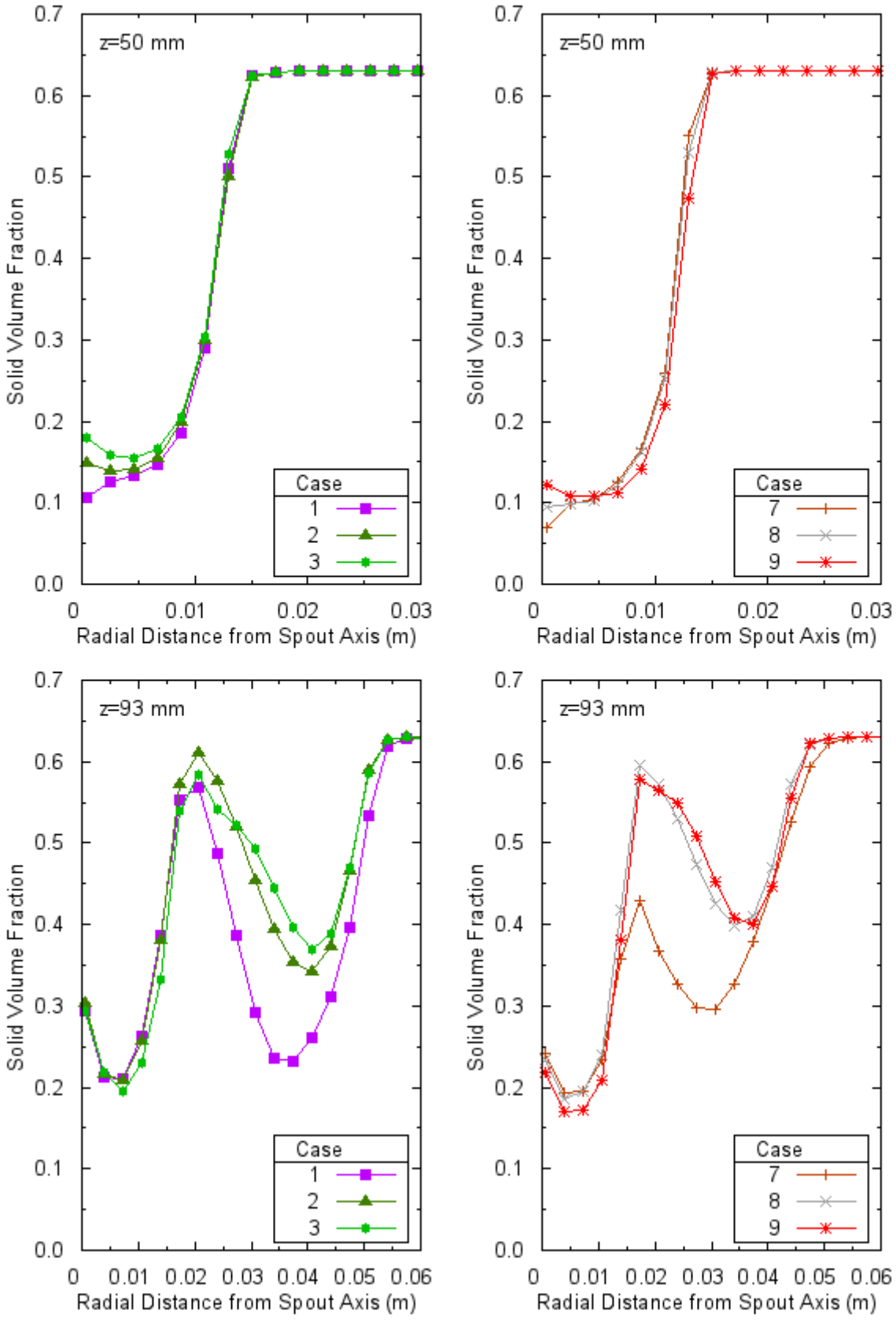

Figure 7.50 The effect of restitution coefficient on solid volume fraction distribution for experimental set 6, measurement height 50 mm, 93 mm.

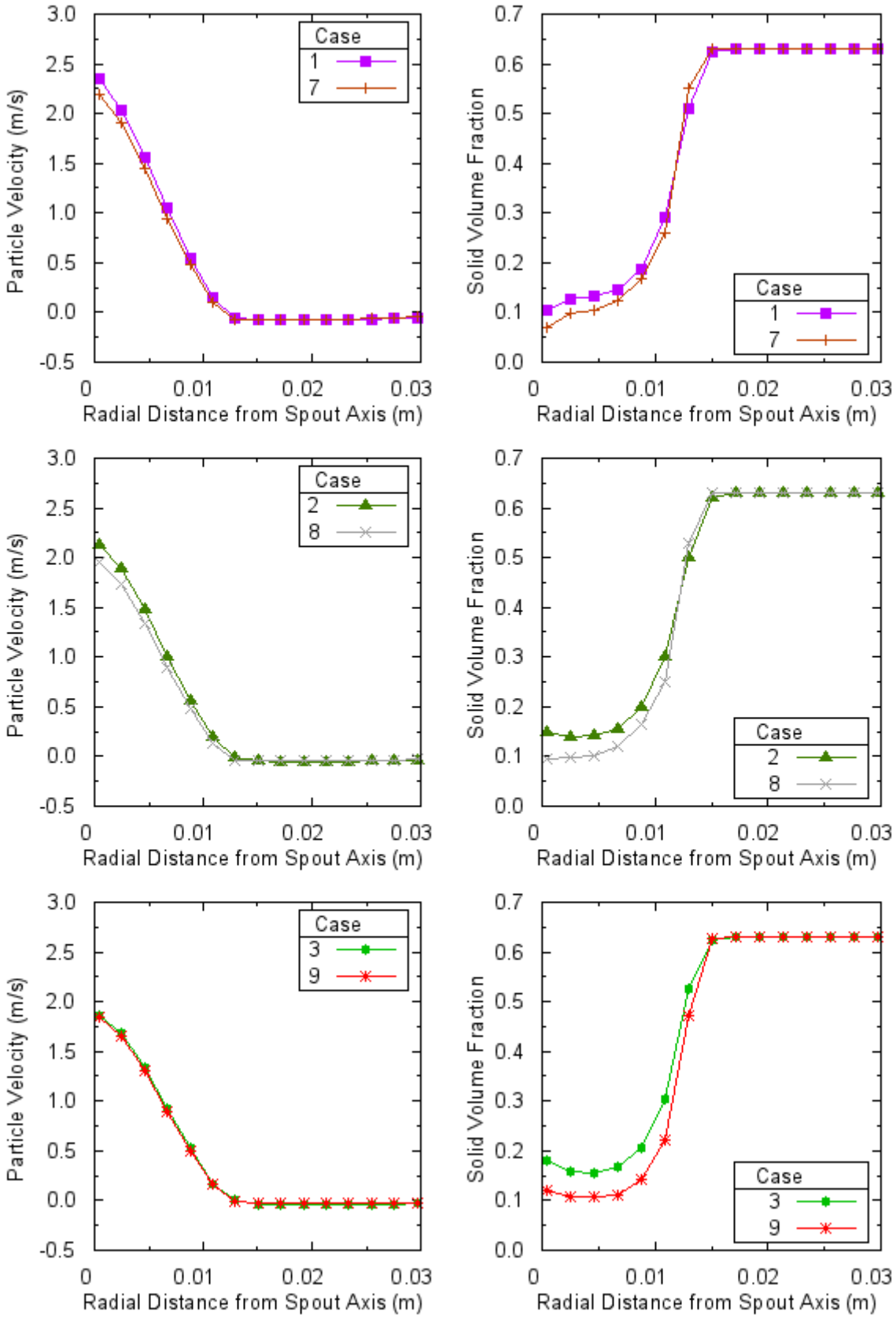

Figure 7.51 The effect of frictional stress on particle velocity and solid volume fraction distributions for experimental set 6, measurement height 50 mm.

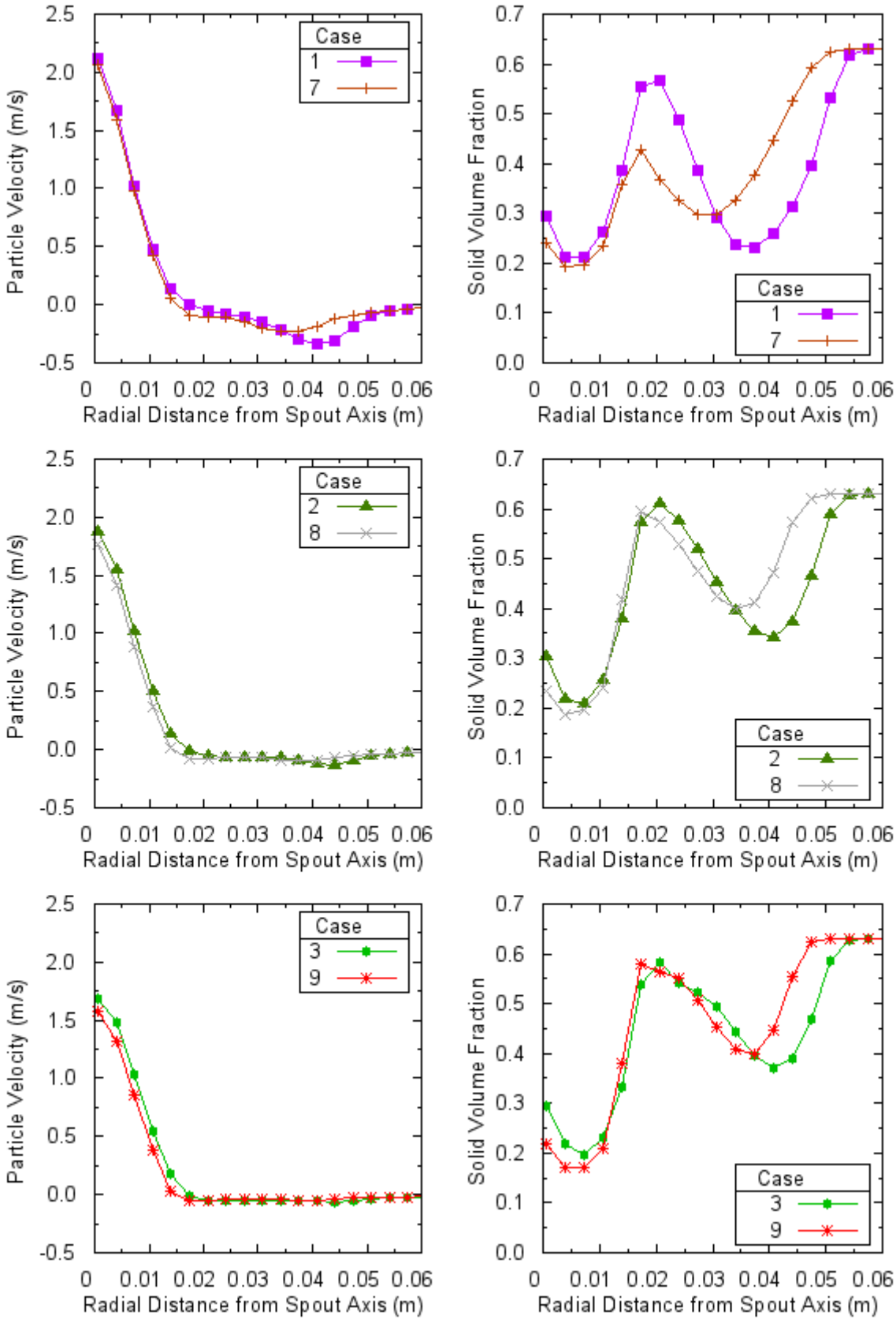

Figure 7.52 The effect of frictional stress on particle velocity and solid volume fraction distributions for experimental set 6, measurement height 93 mm.

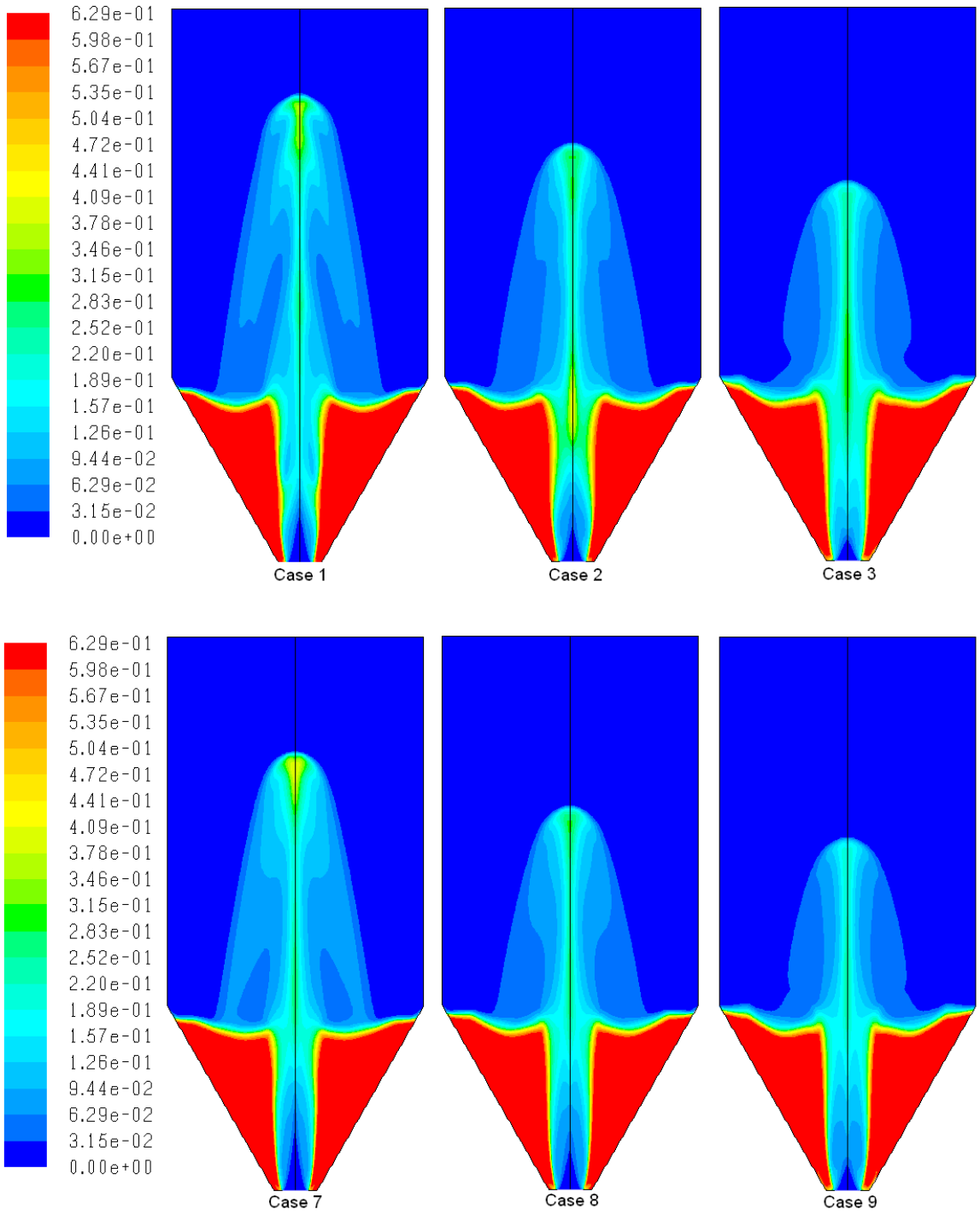

Figure 7.53 Contours of solid volume fraction at t=15 s for experimental set 6.

7.3.7 The Experimental Set 7

60^o conic angle experimental set is the only experimental set containing 0.5 mm diameter particles. The static bed height for it is 100 mm and air inlet velocity is 25.3 m/s. The measurement heights are 50 mm and 93 mm.

Solid particles flew out of the bed during simulations of all 12 cases. The percent reduction in mass of particles is shown in Table 7.15. The rate is higher for cases having Syamlal-O'Brien drag model. Inclusion of solid frictional stress deteriorates the escape. Increase in restitution coefficient has positive effect on flow out except the cases having Gidaspow drag model with no solid frictional stress which does not have specific pattern.

Table 7.15 The percent reduction in mass of solid particles due to outflow from the bed for experimental set 7.

Case Number	% Reduction in Solid Particle Mass
1	4.84
2	0.43
3	1.27
4	75.47
5	61.97
6	56.25
7	67.06
8	40.51
9	7.84
10	96.67
11	88.49
12	76.72

It is clear that the inclusion of solid frictional stress and reduction of restitution coefficient cannot prevent particle outflow. The restitution coefficient cannot be increased more than 1 and drag models cannot be changed to achieve a stable spouting. But, the magnitude of drag coefficient can be altered. In order to do this, user defined function feature of FLUENT code was used. A small C program that can calculate drag coefficient was written in a parallelized way. Therefore, it was possible to use it for parallel processing. Case 3 (Gidaspow drag model, restitution coefficient 0.95, no solid frictional stress) was selected for investigation of the effect of magnitude of drag coefficient on simulations. The magnitude of drag

coefficient was modified to 0.9, 0.8, and 0.7 times of the original drag coefficient. The drag coefficient was reduced because particle outflow occurred when original drag magnitude was used.

The particles did not flow out of the system when the drag coefficient was reduced. The resulting bed pressure drop values are shown in Table 7.16. The numbers 09, 08, and 07 at the end of the case numbers mean that drag magnitude is 0.9, 0.8, and 0.7 times the original drag magnitude. It is seen from Table 7.16 that the magnitude of drag coefficient has slight effect on bed pressure drop.

Table 7.16 The effect of magnitude of drag coefficient on bed pressure drop results for experimental set 7.

Case Number	Bed Pressure Drop (Pa)
3	2805
3-d09	2810
3-d08	2808
3-d07	2788

The effect of magnitude of drag coefficient on particle velocity and solid volume fraction distributions are shown in Figure 7.54 for measurement height 50 mm and in Figure 7.55 for measurement height 93 mm. The decrease in drag coefficient magnitude causes reduction in particle velocity for both measurement heights. The effect is clearer for spout region. On the other hand, solid volume fraction increases as drag coefficient magnitude reduces for both measurement heights.

As magnitude of drag coefficient decreases, fountain height decreases as shown in Figure 7.56.

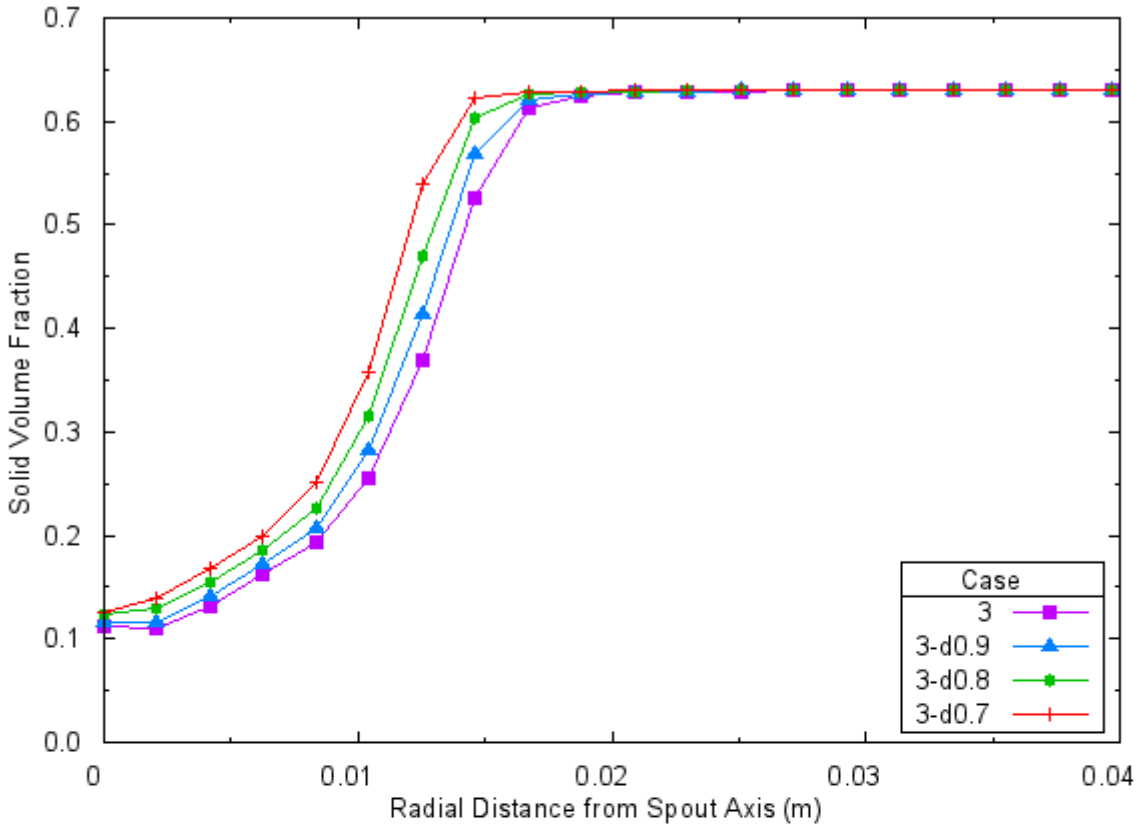

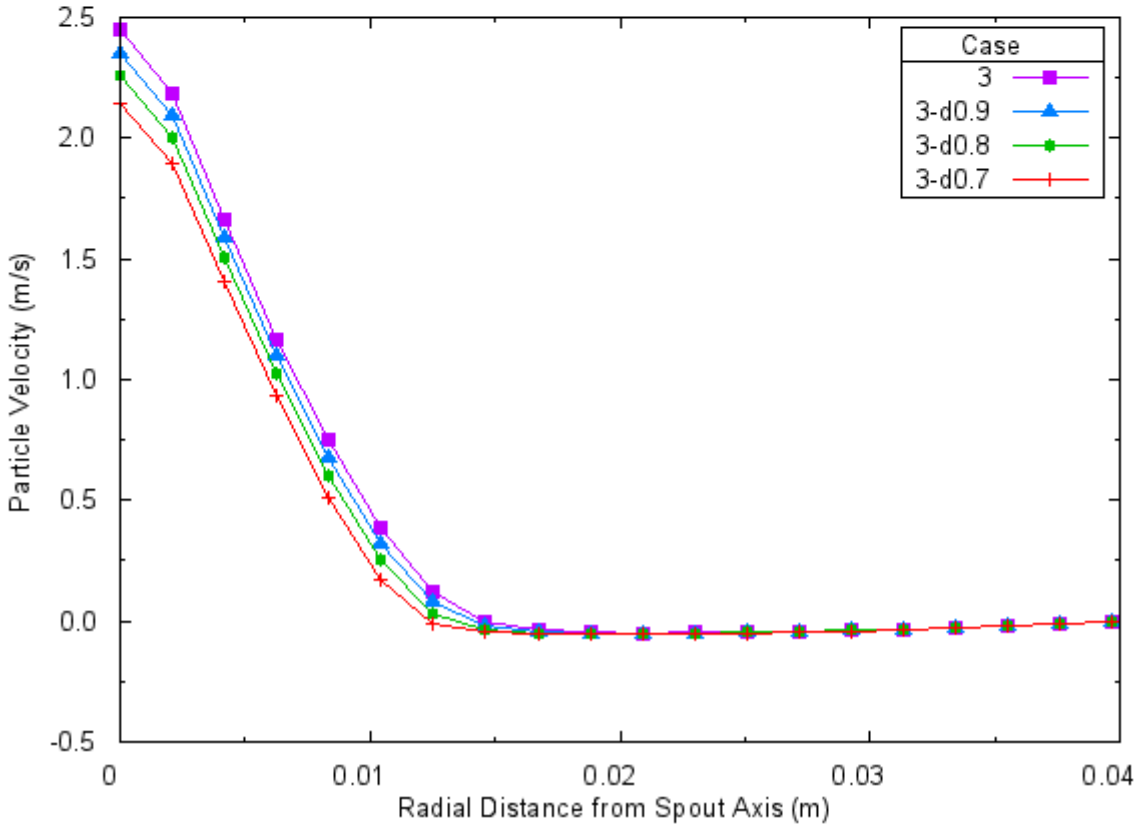

Figure 7.54 The effect of magnitude of drag coefficient on particle velocity and solid volume fraction distributions for experimental set 7, measurement height 50 mm.

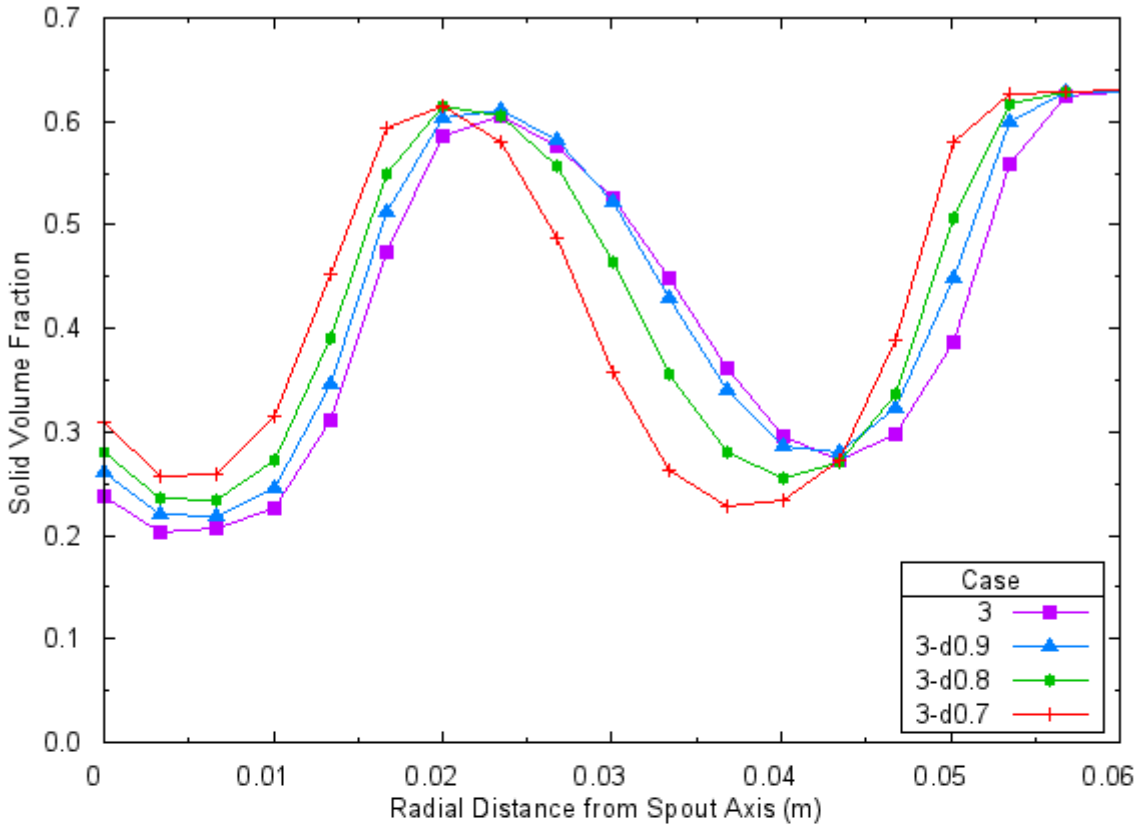

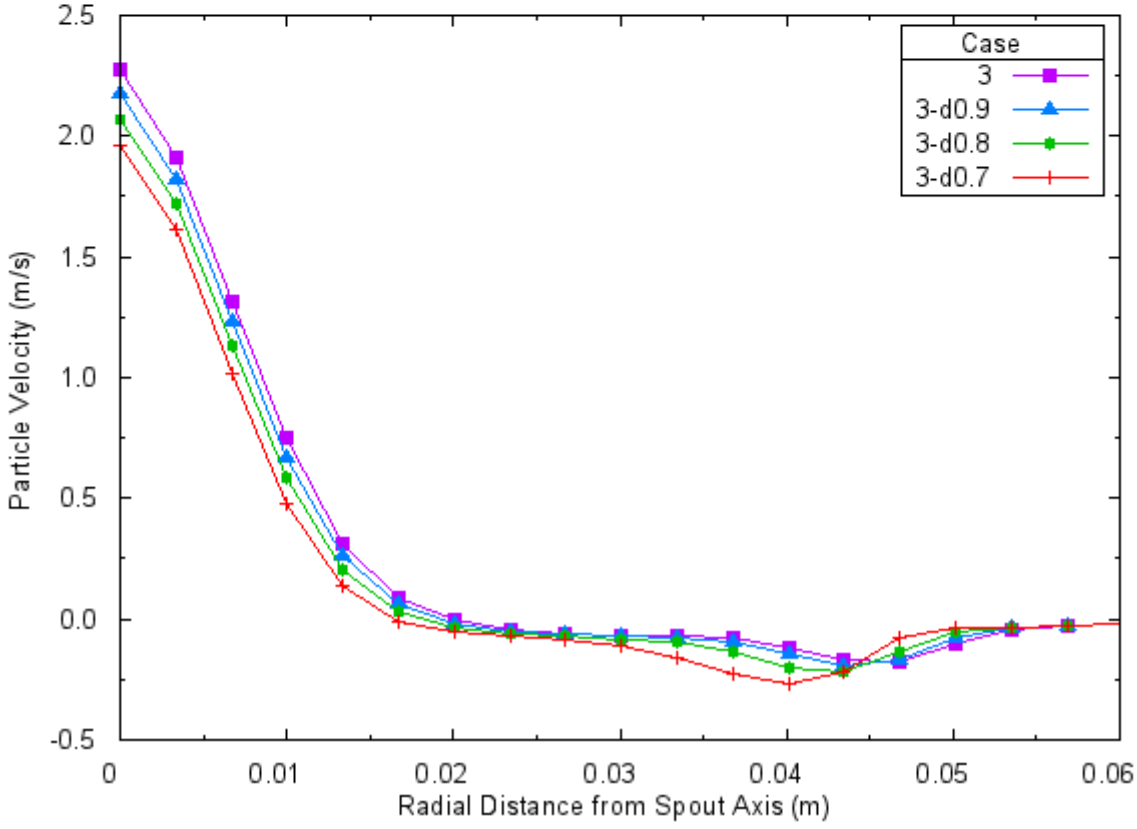

Figure 7.55 The effect of magnitude of drag coefficient on particle velocity and solid volume fraction distributions for experimental set 7, measurement height 93 mm.

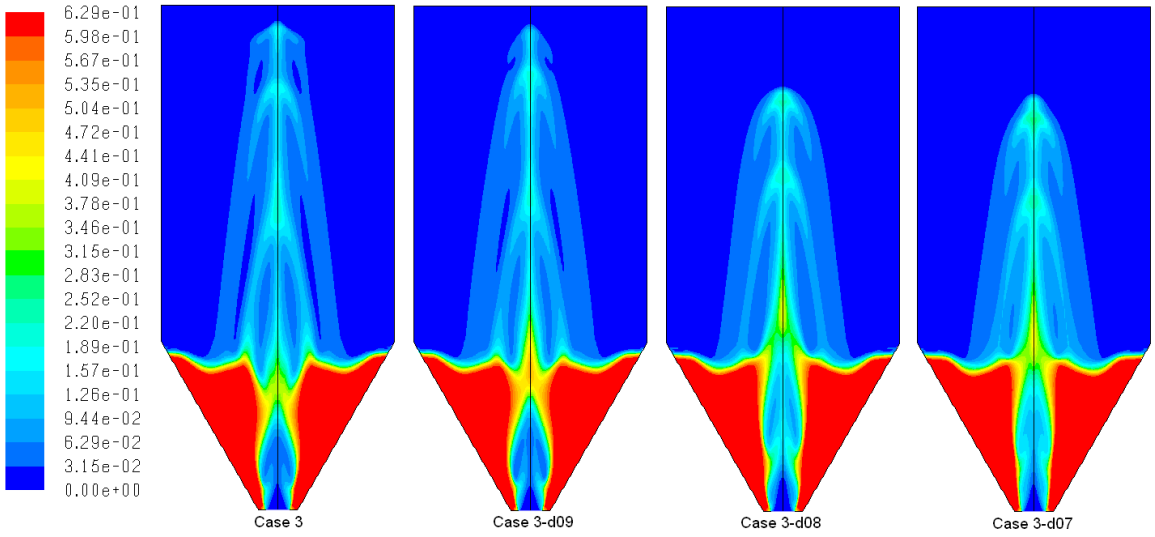

Figure 7.56 Contours of solid volume fraction at t=15 s for experimental set 7.

7.4 Results and Discussions

In this chapter, the effects of drag model, restitution coefficient, inclusion of solid frictional stress into simulations, and magnitude of drag coefficient on hydrodynamics of the spouted beds filled with heavy particles of density 6050 kg/m^3 were investigated. For this purpose CFD simulations of experimental setup defined in Sari et al. (2011) were performed with FLUENT commercial CFD package.

All the gas inlet velocities used for the simulations are 1.25 times of the minimum spouting velocity. Therefore, well defined spout, annulus, and fountain zones are expected from the simulations. Indeed, for all simulation cases of experimental sets there exist spout, annulus, and fountain zones. In the spout zone, particles move upwards, particle velocity decreases away from the spout center unlike solid volume fraction. In annulus, particles move slowly downwards, particle velocity decreases towards the wall of the bed, and solid volume fraction has a constant value close to maximum packing. In the fountain, particles move upwards near the core of the fountain and downwards near the sides of the fountain. This behavior is consistent with typical conical cylindrical spouted bed behavior defined in literature.

The common behavior from all simulations for particle velocity distribution is that predictions of cases having Syamlal-O'Brien drag model are higher than the predictions of cases having Gidaspow drag model regardless of other simulation parameters. The opposite is observed for solid volume fraction distribution. Figure 7.57 shows the comparison gas-solid exchange coefficient between two drag models for same conditions. By formulation, Syamlal-O'Brien drag model results in higher gas-solid exchange coefficients than Gidaspow drag model. Therefore, momentum transfer to particles from gas is higher for Syamlal-O'Brien drag model calculations. This results in higher particle velocity values. Since solid mass flux, G_s, equals to solid volume fraction times solid velocity, $G_s = \alpha_s \times v_s$, for the same mass flux, increase in solid velocity results in decrease in solid volume fraction. Therefore, solid volume fraction values are smaller for Syamlal-O'Brien drag model cases. The comparison between two drag models also revealed that bed pressure drop predictions of cases using Syamlal-O'Brien drag model are higher than the ones using Gidaspow drag model no matter what the restitution coefficient and what the solid frictional stress condition are.

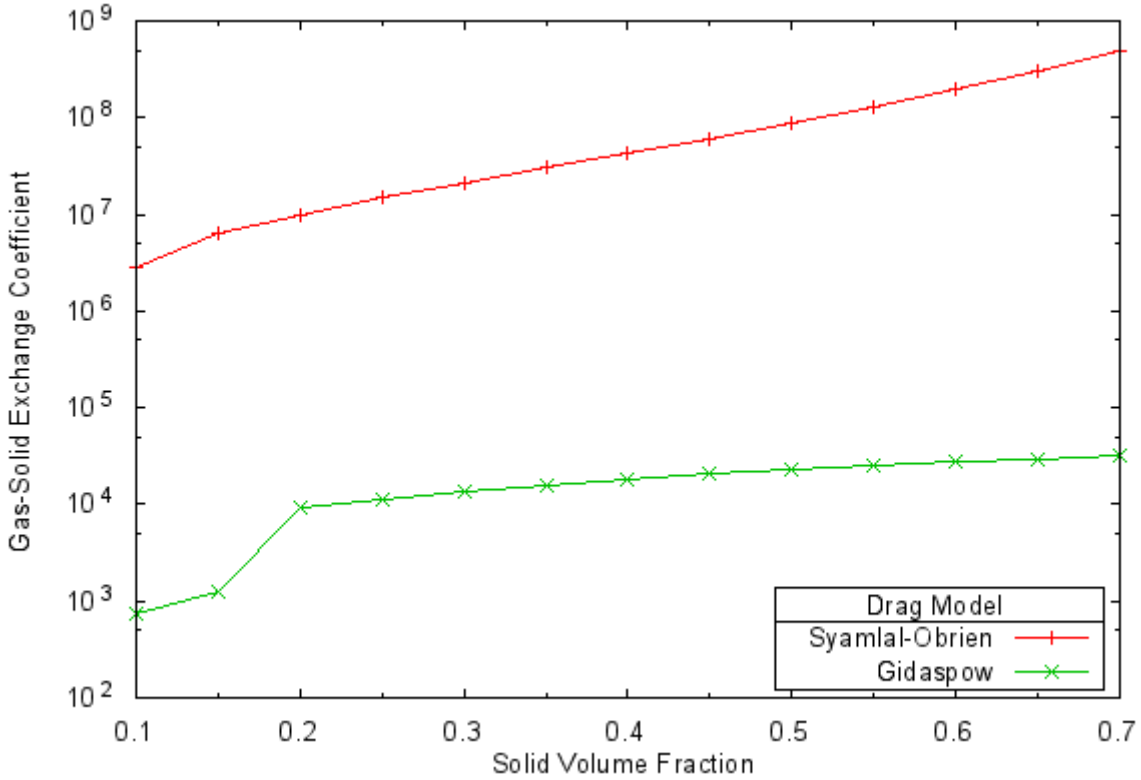

Figure 7.57 The gas-solid exchange coefficient comparison between Syamlal-O'Brien and Gidaspow drag models.

One finding from simulations is that as restitution coefficient increases particle velocity decreases and solid volume fraction increases for all cases tried for all experimental sets. Restitution coefficient influences the momentum conservation and granular temperature conservation of solid phase. Figure 7.58 shows the increase in granular temperature as a result of increase in restitution coefficient. When granular temperature distribution is analyzed, it is seen that granular temperature increases to a point where solid volume fraction reaches its minimum value and then decreases as solid volume fraction increases. It is because of the fact that, as solid volume fraction increases dissipation of granular temperature increases due to particle-particle collisions. Under these circumstances, particle velocity should increase in regions where granular temperature increases and solid volume fraction decreases but the opposite is observed. The effect of increase of restitution coefficient on bed pressure drop is reduction for all cases except cases 1, 2, and 3 which have Gidaspow as drag model and no solid frictional stress. There isn't any logical explanation why pressure drop increases for the cases 1, 2, and 3.

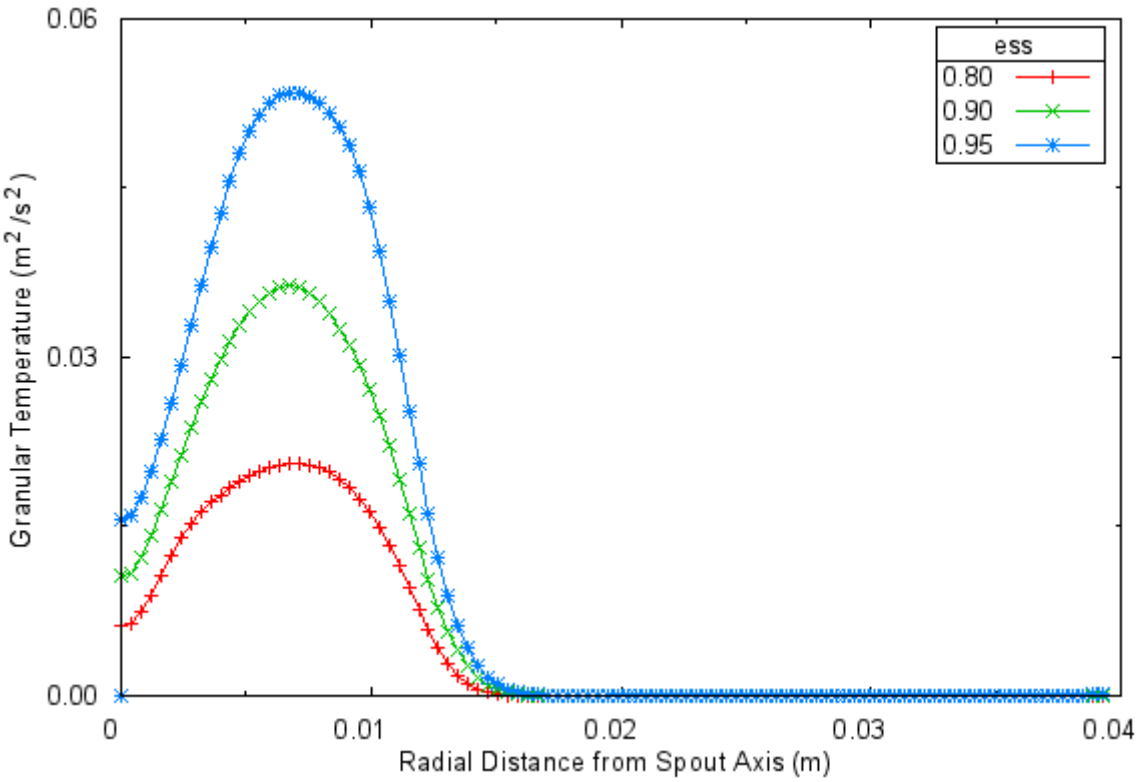

Figure 7.58 The effect of restitution coefficient on granular temperature.

Another finding from simulations is that inclusion of solid frictional stress into simulations decreases solid velocity, solid volume fraction, and bed pressure drop. Although the reduction in particle velocity is not very significant, it is very drastic for pressure drop results. The bed pressure drop decreases 30 to 50 % when the solid frictional stress is included in CFD simulations. Inclusion of frictional stress into simulations decreases the upward force exerted by the gas on the particles therefore decreases particle velocity.

The other interesting observation is that for some experimental sets (4, 6, and 7) particles flew out of the bed during simulations. These simulations are generally the cases containing Syamlal-O'Brien drag model except experimental set 7 which contains particles with 0.5 mm diameter. For this experimental set, all cases resulted in particle outflow. Since the effect of other parameters like restitution coefficient and solid frictional stress does not affect the outcome, it can be said that drag is the most important parameter defining hydrodynamics of the bed. The reduction in magnitude of drag coefficient reduces particle velocity and prevents particle outflow.

For all simulations, whenever the particle velocity decreased due to an effect, fountain height decreased, too.

The bed pressure drop predictions for all 12 CFD cases for each experimental set are compared with the experimental results and percent error values are shown in Table 7.17. There wasn't any measured pressure drop value for experimental set 2 therefore the comparison was not performed for it. Since all the cases resulted in particle outflow, the comparison was not performed for experimental set 7, either. The case with the smallest percent error for each experimental set is highlighted in the table. It can be said that, Gidaspow drag model without solid frictional stress cases have smaller percent error compared to other cases.

Comparison of particle velocity and solid volume fraction distributions of all simulations with experimental results are shown in Figure 7.59 to Figure 7.70

Table 7.17 Percent error in bed pressure drop calculations for each case.

	Experimental Set						
Case	**1**	**2**	**3**	**4**	**5**	**6**	**7**
1	9.9	N/A	**0.6**	7.6	16.4	33.2	N/A
2	6.9	N/A	3.5	**4.1**	**16.3**	34.9	N/A
3	6.0	N/A	3.6	5.1	17.2	32.7	N/A
4	**1.7**	N/A	8.5	N/A	26.8	N/A	N/A
5	3.9	N/A	7.9	N/A	24.2	N/A	N/A
6	4.1	N/A	8.2	N/A	22.5	N/A	N/A
7	31.9	N/A	29.4	36.8	19.1	**7.20**	N/A
8	35.6	N/A	35.6	41.8	30.2	19.7	N/A
9	36.0	N/A	38.6	43.7	35.9	30.2	N/A
10	32.4	N/A	27.2	N/A	18.6	N/A	N/A
11	34.7	N/A	32.1	N/A	24.2	N/A	N/A
12	33.6	N/A	35.8	N/A	32.4	N/A	N/A

The findings out of comparison of solid volume fraction and particle velocity distributions with experimental results for each experimental set are summarized below.

1. Experimental Set 1

All Gidaspow drag model cases overestimate the solid volume fraction at spout center then underestimate the solid volume fraction up to the radial distance 0.01 m, agree well with experimental results at the border of spout and annulus regions, and overestimate it in annulus region. All Syamlal-O'Brien drag model cases behave similar to Gidaspow drag model cases in spout-annulus border and annulus. However, unlike Syamlal-O'Brien drag model without friction cases Syamlal-O'Brien drag model with friction cases underestimate solid volume fraction at spout center.

All Gidaspow drag model cases except case 9 and 3 overestimate particle velocity up to the distance 0.005 m. Underestimation in all cases then continues till the bed wall. All Syamlal-O'Brien drag model cases overestimate particle velocity in spout region and underestimate up to the bed wall.

Gidaspow drag model cases' predictions are much closer to experimental results than Syamlal-O'Brien drag model cases' predictions.

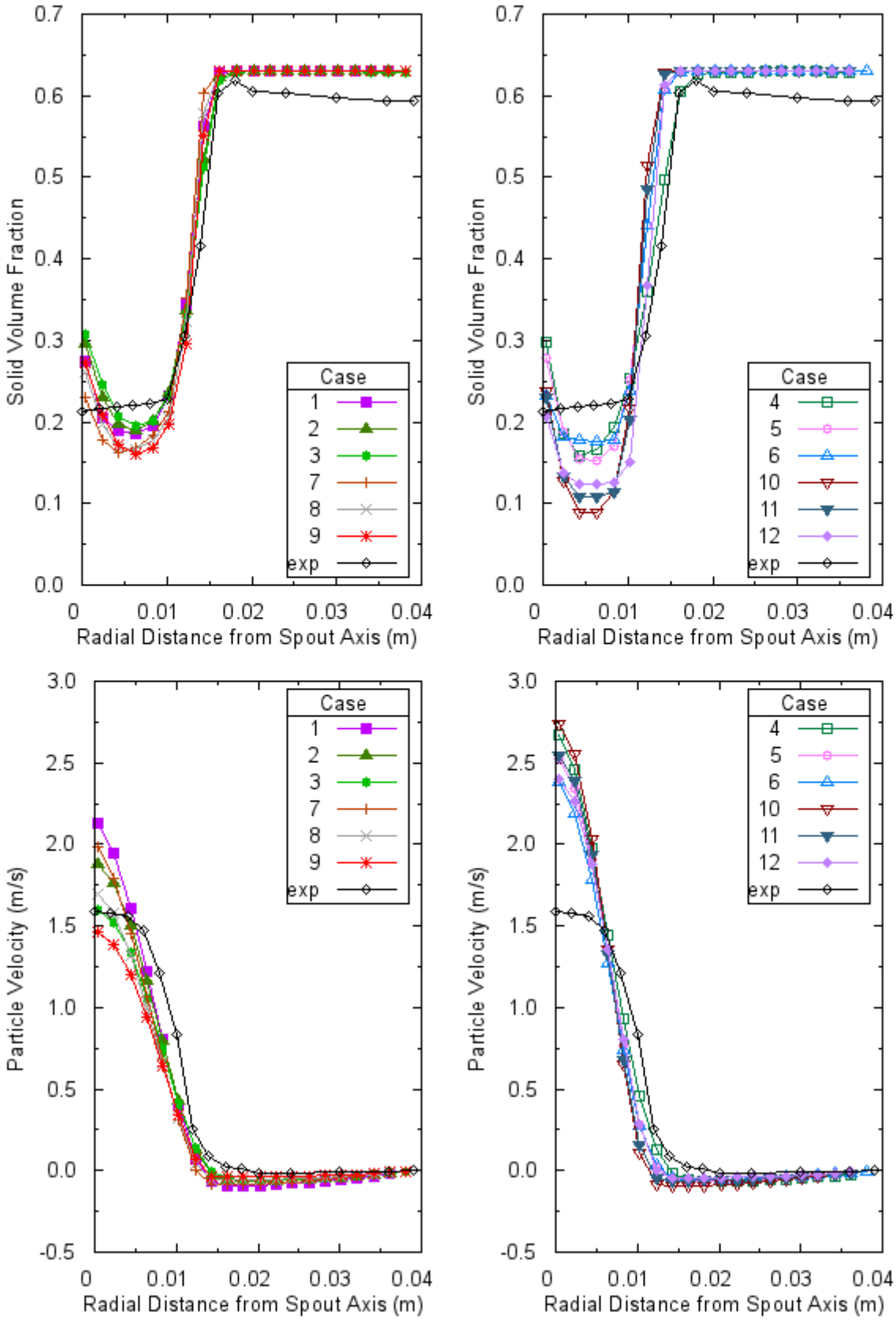

Figure 7.59 Comparison of CFD results with experimental results for experimental set 1, measurement height 50 mm- left: Gidaspow drag model, right: Syamlal-O'Brien drag model.

2. Experimental Set 2

Most of the Gidaspow drag model cases and all Syamlal-O'Brien drag model cases underestimate solid volume fraction in the spout region. All of the both drag model cases overestimate the solid volume fraction in spout annulus border and in annulus region.

Most of the Gidaspow drag model cases overestimate particle velocity in spout region, underestimate it in spout-annulus border and in annulus. All Syamlal-O'Brien drag model cases overestimate particle velocity in the spout region. On the other hand, underestimate it in spout-annulus border and in annulus.

Gidaspow drag model cases' predictions are much closer to experimental results than Syamlal-O'Brien drag model cases' predictions.

3. Experimental Set 3

For measurement height 42 mm, all Gidaspow drag model and Syamlal-O'Brien drag model case results of solid volume fraction are underestimated in spout region and overestimated in spout-annulus border and annulus regions.

All Gidaspow drag model cases underestimate particle velocity till the bed wall. All Syamlal-O'Brien drag model cases first overestimate (radius less than 0.005 m) then underestimate the particle velocity (from 0.005 m to bed wall).

For measurement height 80 mm, all Gidaspow drag model cases overestimate solid volume fraction in spout, some of them overestimate it in spout-annulus border, and all of them overestimate it in annulus similar to Syamlal-O'Brien drag model cases.

Gidaspow drag model case results for particle velocity are generally underestimated in all regions like Syamlal-O'Brien drag model cases except very near the spout center where the values are overestimated.

Gidaspow drag model cases' predictions for both measurement heights are much closer to experimental results than Syamlal-O'Brien drag model cases' predictions.

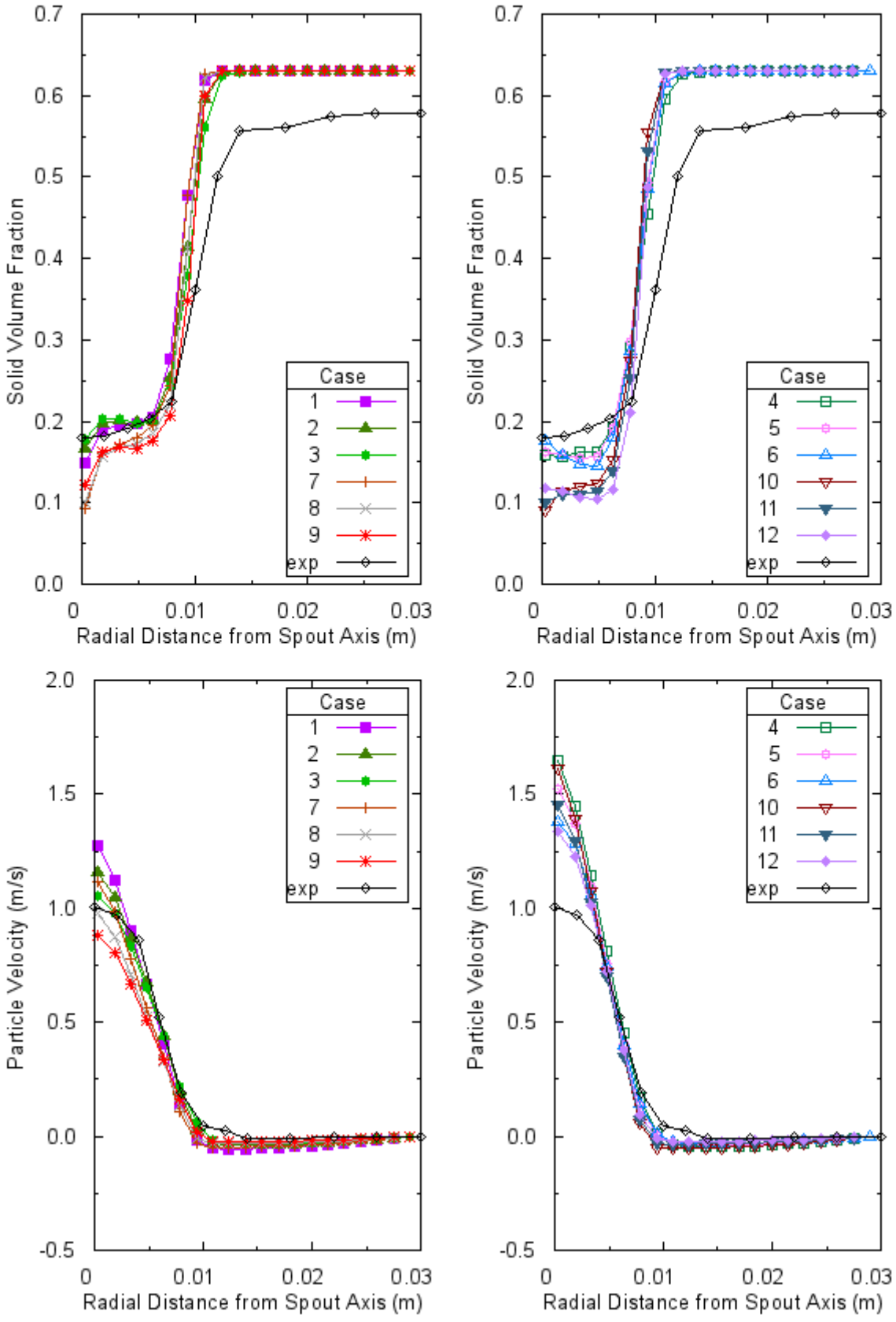

Figure 7.60 Comparison of CFD results with experimental results for experimental set 2, measurement height 42 mm- left: Gidaspow drag model, right: Syamlal-O'Brien drag model.

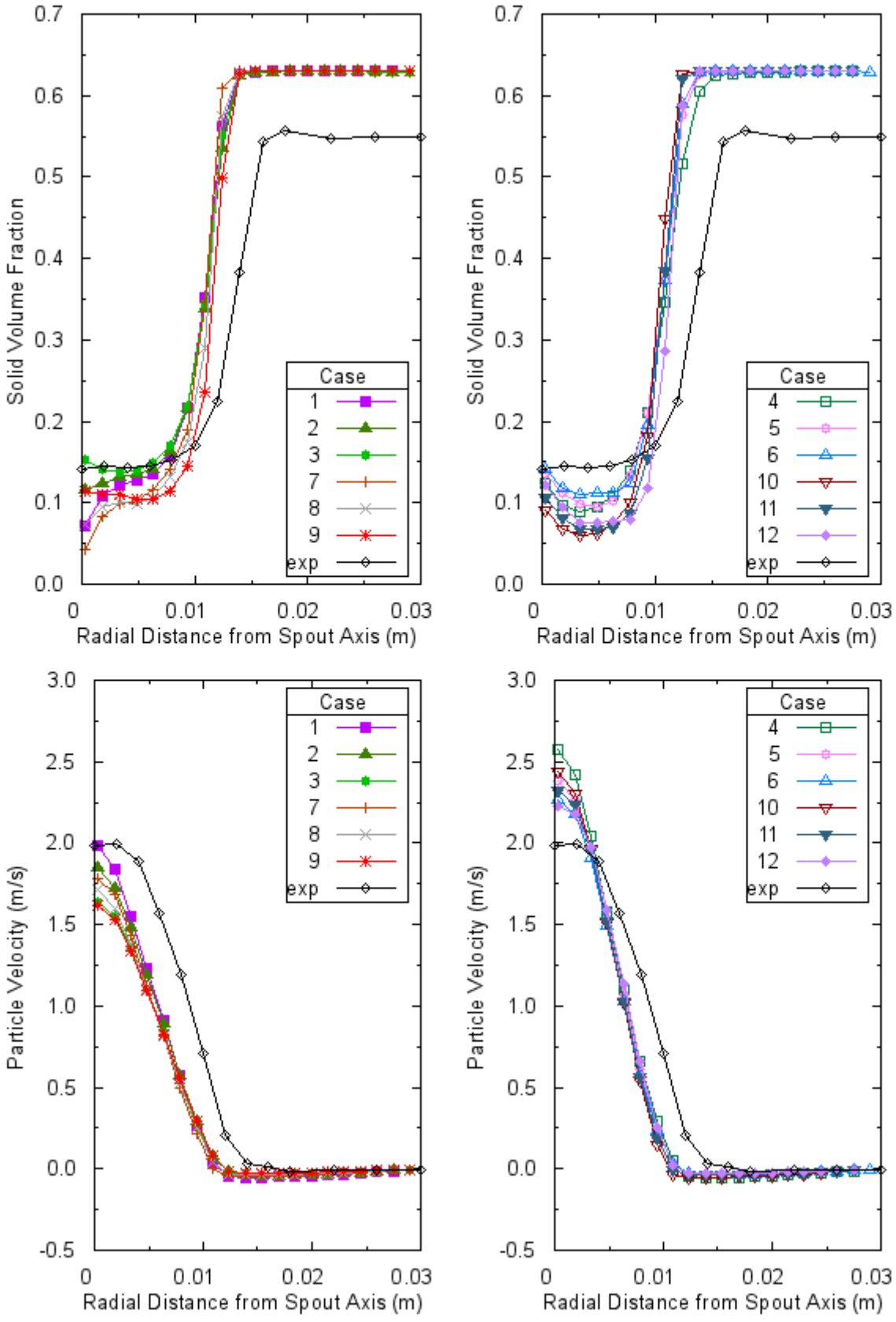

Figure 7.61 Comparison of CFD results with experimental results for experimental set 3, measurement height 42 mm- left: Gidaspow drag model, right: Syamlal-O'Brien drag model.

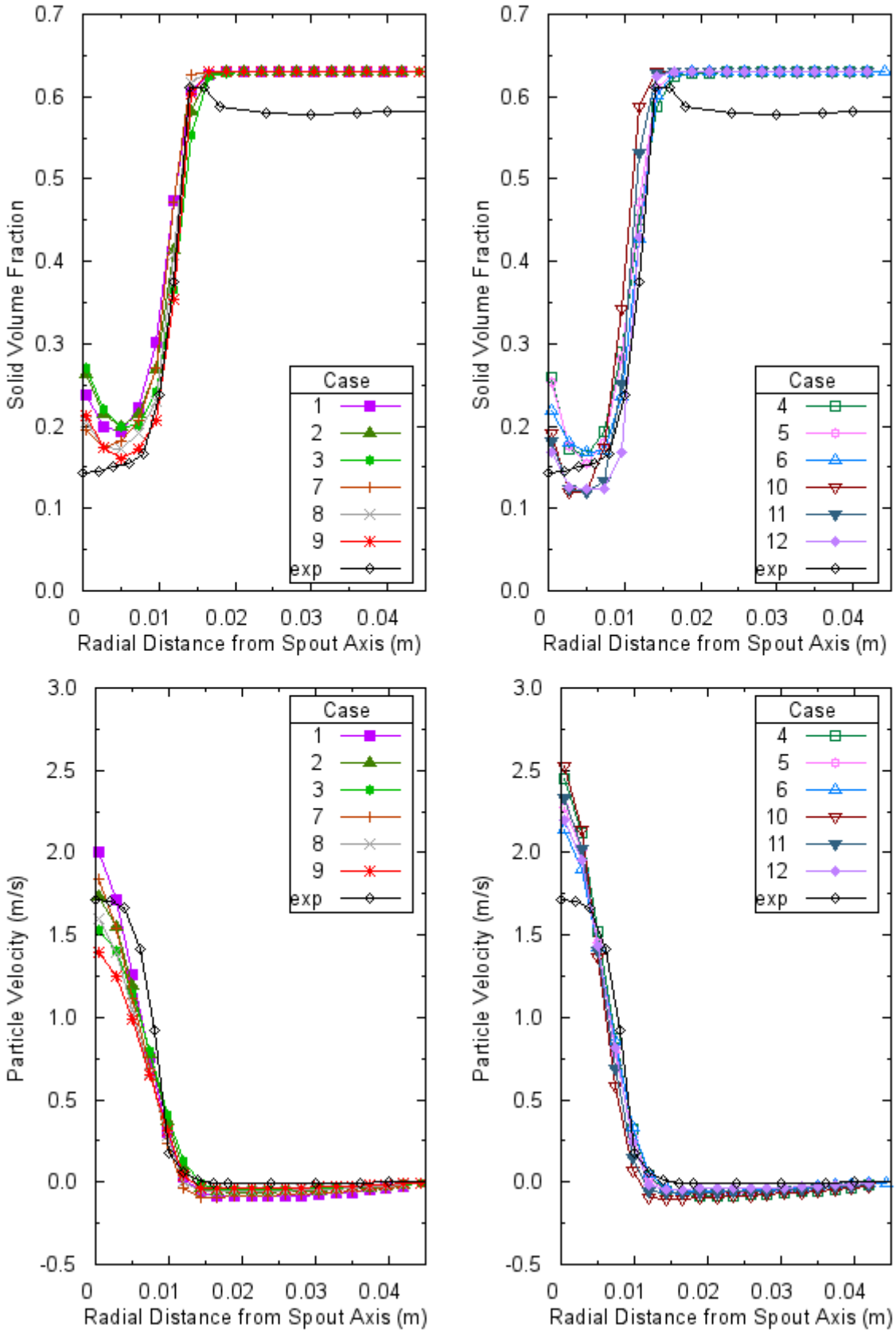

Figure 7.62 Comparison of CFD results with experimental results for experimental set 3, measurement height 80 mm - left: Gidaspow drag model, right: Syamlal-O'Brien drag model.

4. Experimental Set 4

Only Gidaspow drag model cases are compared with experimental results because for all Syamlal-O'Brien drag model cases particle outflow is occurred.

For measurement height 42 mm, solid volume fraction results underestimated or overestimated depending on other parameters in spout region and spout-annulus border but overestimated by all cases in annulus region. Particle velocity results are overestimated up to radial distance 0.005 m then are underestimated till the bed wall.

For measurement height 82 mm, same behavior of measurement height 42 mm is observed for solid volume fraction distribution in spout and annulus regions. But, in spout-annulus border results are underestimated. Overestimation in particle velocity results continues till spout-annulus border and then results are underestimated in annulus.

For measurement height 120 mm, solid volume fraction distribution follows the same path observed in measurement height of 82 mm. Particle velocity distribution of measurement height 120 mm is similar to particle velocity distribution of measurement height 82 mm but magnitude of overestimation increases.

5. Experimental Set 5

All Gidaspow cases overestimate solid volume fraction in spout region, agree well with experimental results in spout-annulus border, and overestimate it in annulus regions. All Syamlal-O'Brien drag model cases agree with Gidaspow drag model cases in annulus region and in spout-annulus border but in spout region some Syamlal-O'Brien drag model cases underestimate solid volume fraction.

All Gidaspow drag model cases underestimate particle velocity in spout region, agree well with experimental results in spout-annulus border, and underestimate particle velocity in annulus region. Similar behavior is observed for Syamlal-O'Brien drag model cases except in spout center where particle velocity is overestimated. Gidaspow drag model cases' predictions are much closer to experimental results than Syamlal-O'Brien drag model cases' predictions.

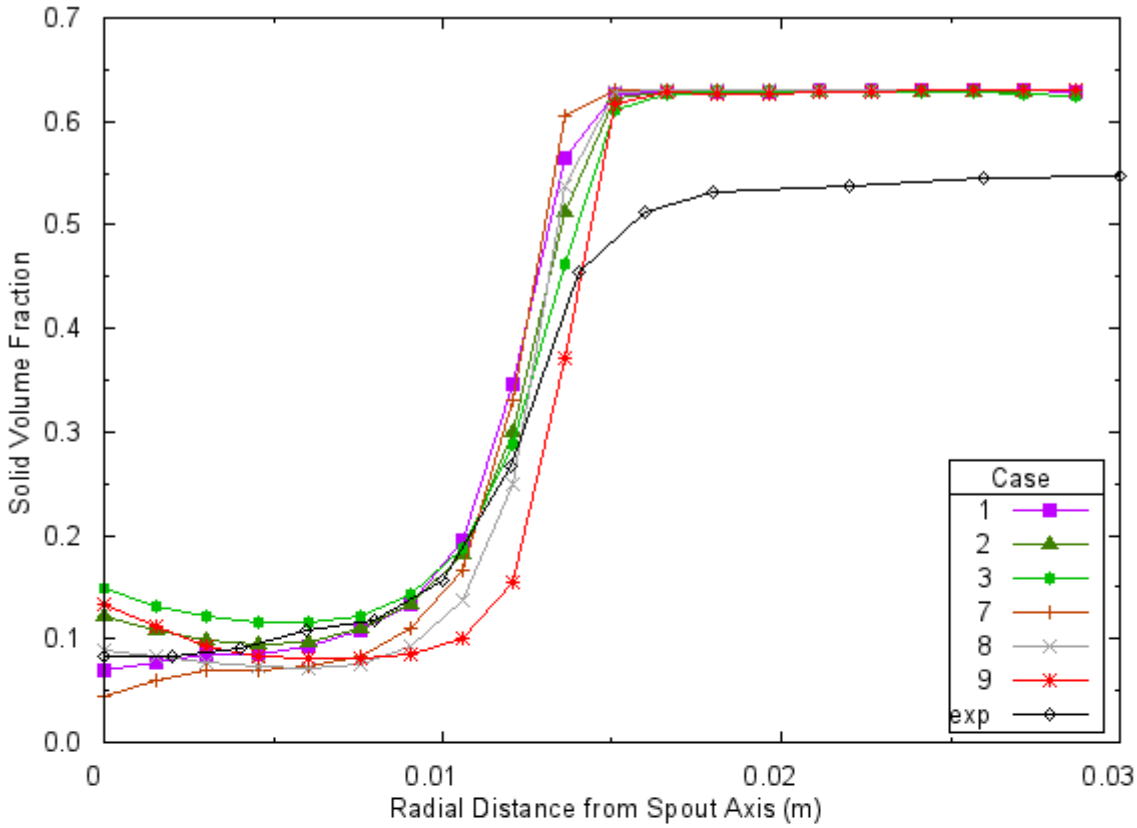

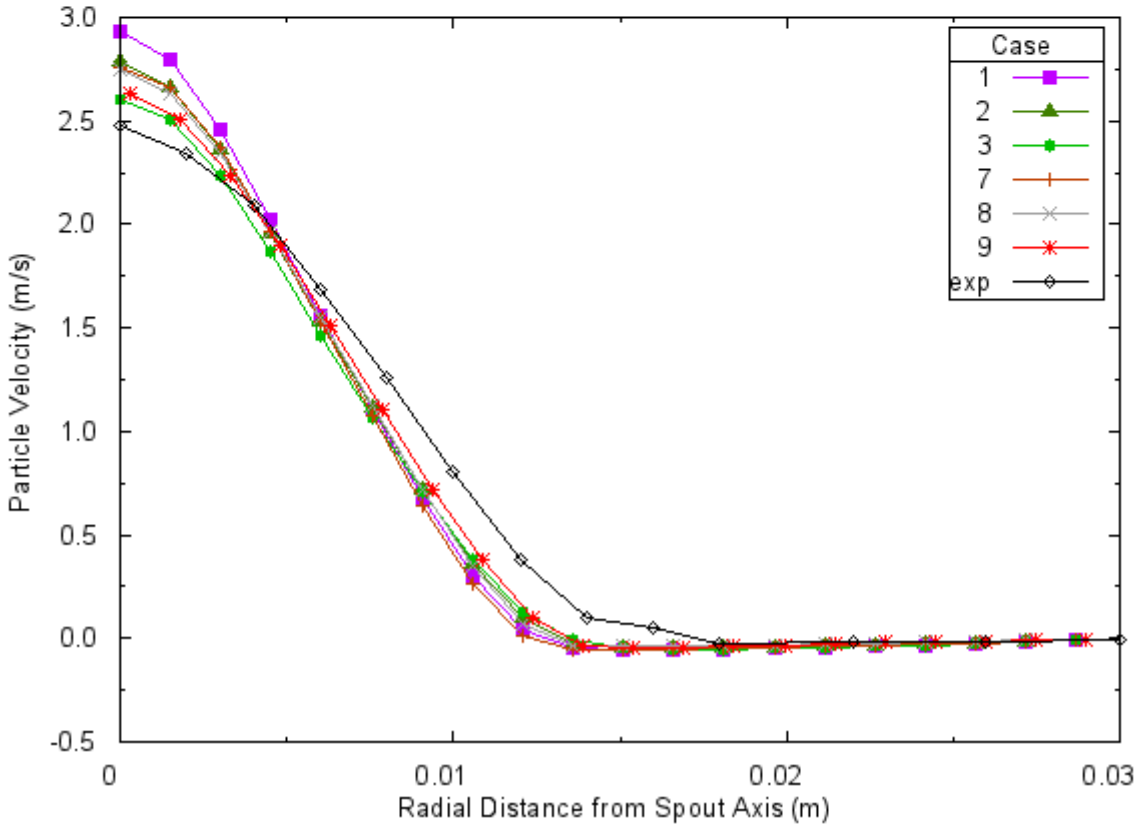

Figure 7.63 Comparison of CFD results with experimental results for experimental set 4, measurement height 42 mm - Gidaspow drag model.

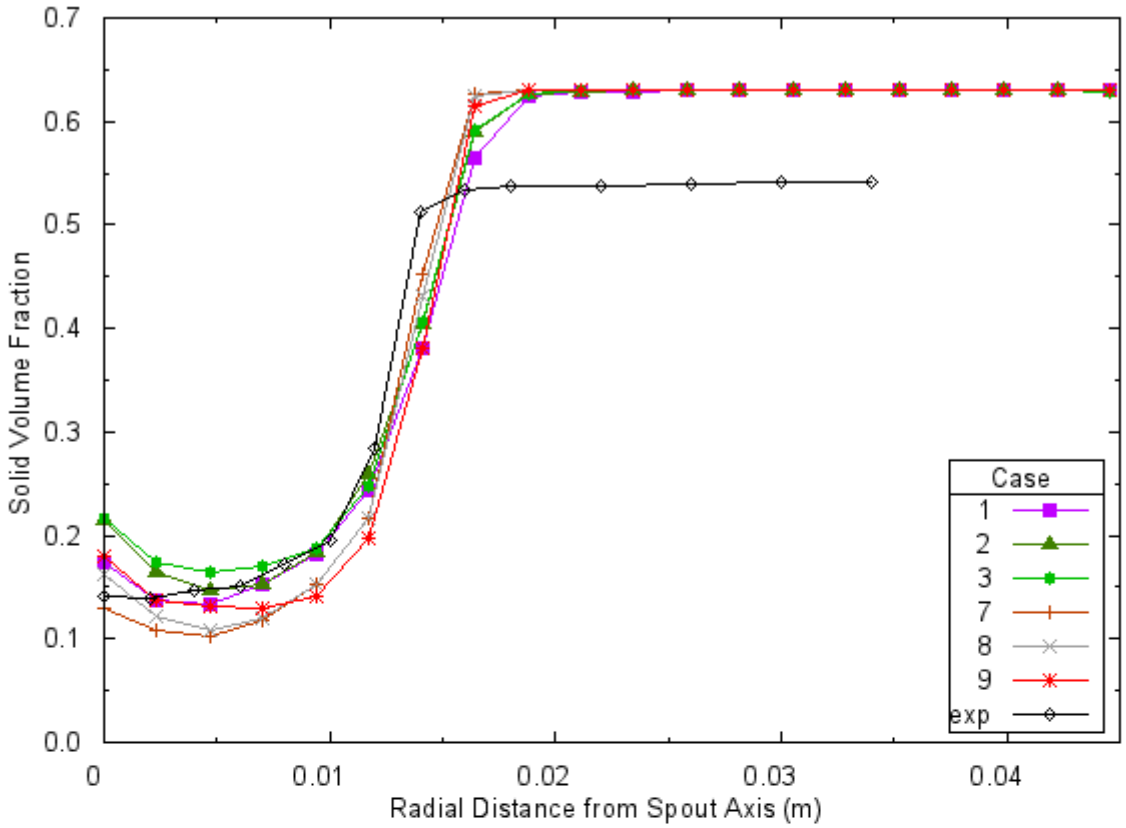

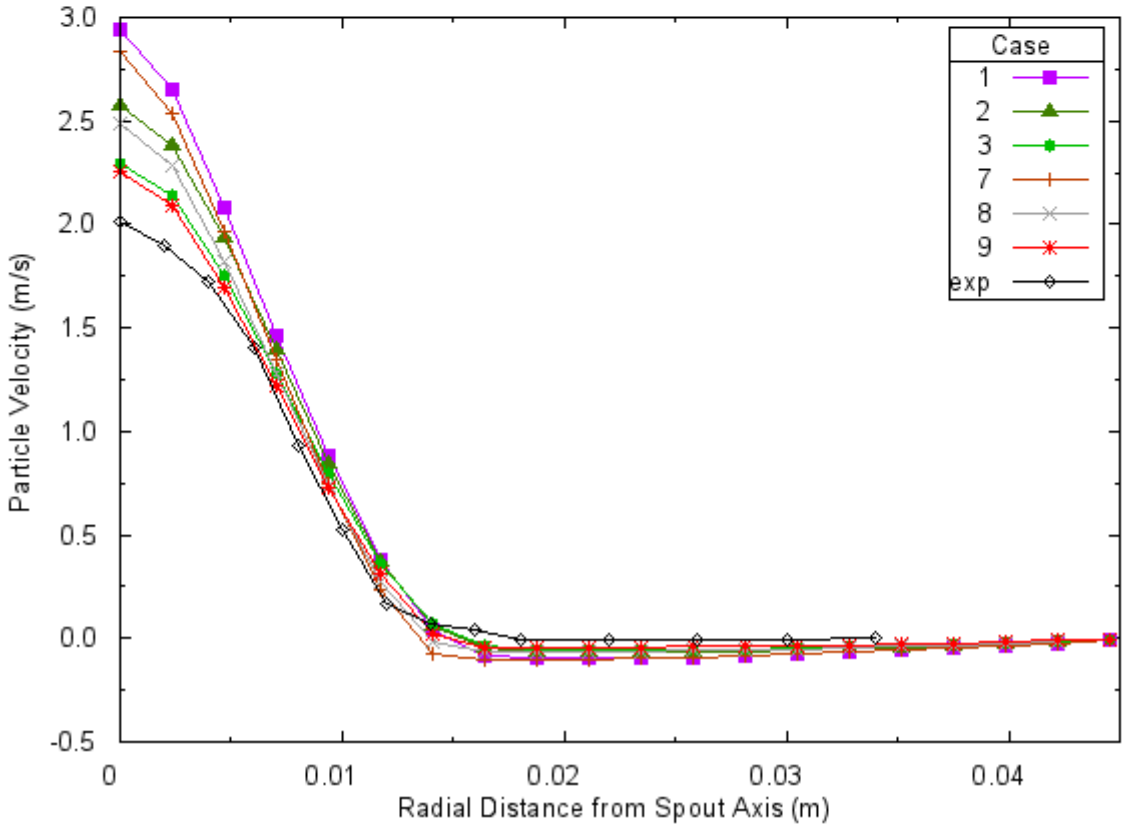

Figure 7.64 Comparison of CFD results with experimental results for experimental set 4, measurement height 82 mm - Gidaspow drag model.

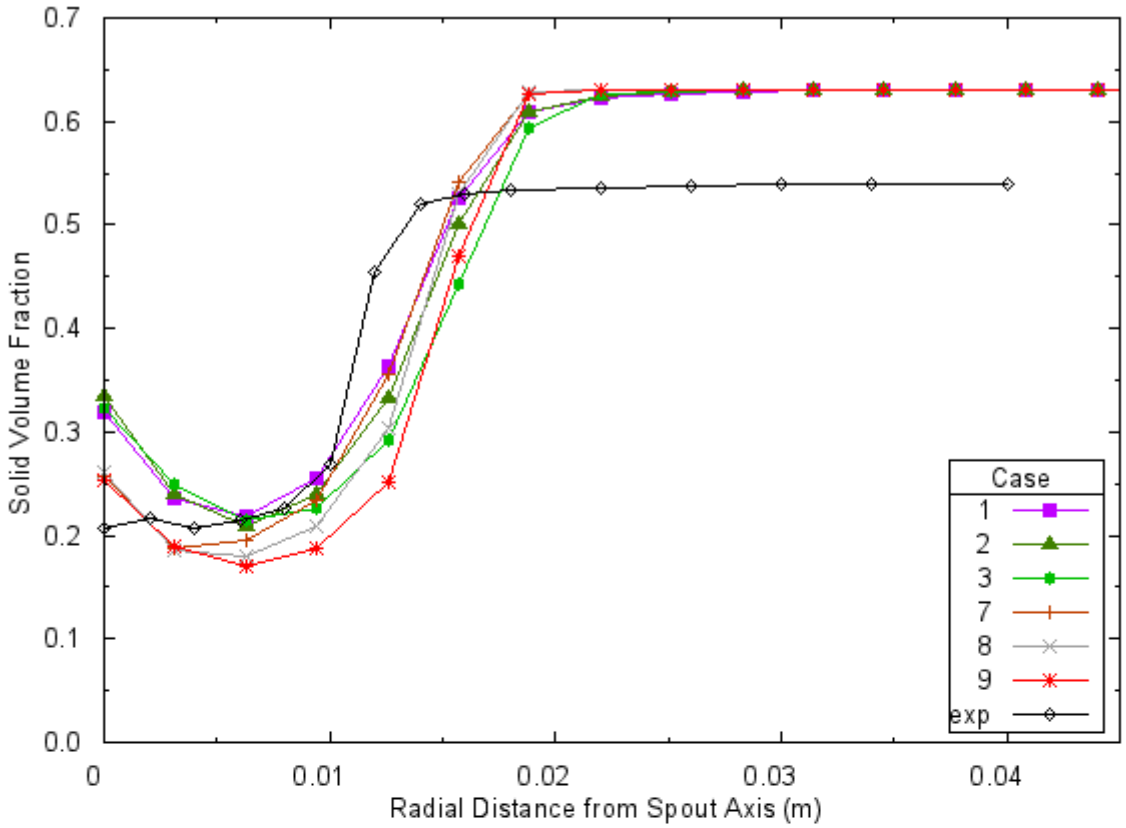

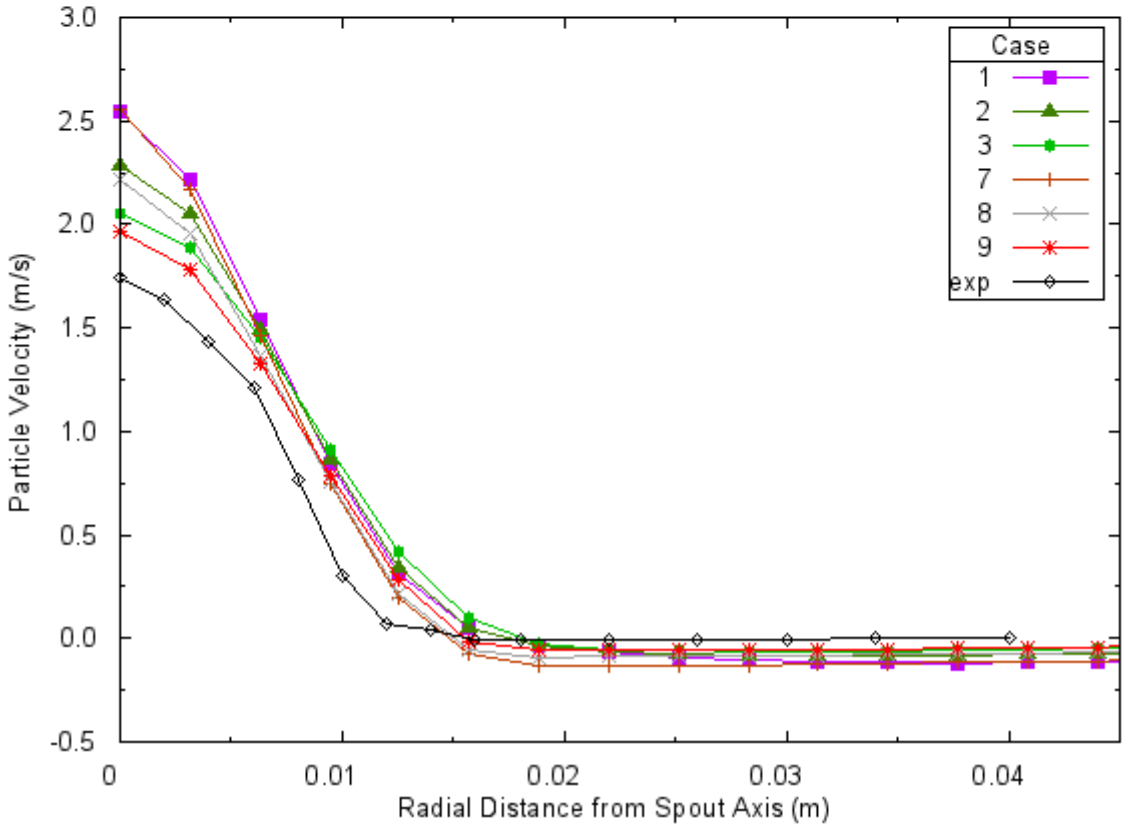

Figure 7.65 Comparison of CFD results with experimental results for experimental set 4, measurement height 120 mm - Gidaspow drag model.

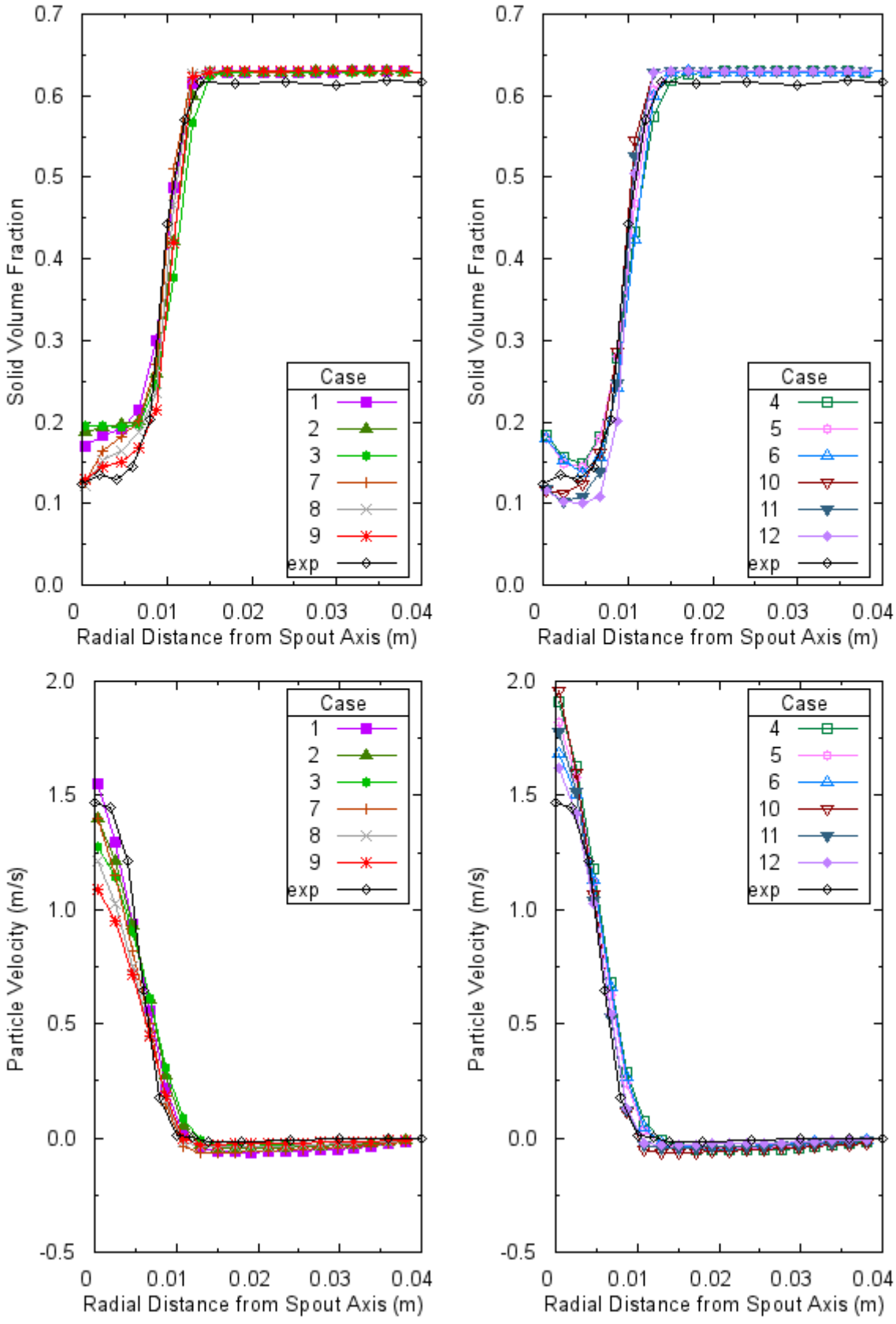

Figure 7.66 Comparison of CFD results with experimental results for experimental set 5, measurement height 50 mm - left: Gidaspow drag model, right: Syamlal-O'Brien drag model.

6. Experimental Set 6

Only Gidaspow drag model cases are compared with experimental results because for all Syamlal-O'Brien drag model cases particle outflow is occurred.

For measurement height 50 mm, solid volume fraction is overestimated in all regions. Particle velocity is underestimated in all regions.

For measurement height 93 mm, since the measurement height is very close the static bed height value of 100 mm, there are fluctuations in solid volume fraction results in annulus region. Contours of solid volume fractions figures show wave-like behavior on the surface of the bed therefore comparison cannot be performed for annulus region. Solid volume fraction is overestimated in spout region and underestimated in spout-annulus border. Particle velocity is underestimated in spout region and is overestimated in spout-annulus border.

7. Experimental Set 7

Since all combinations of every parameter resulted in particle outflow, different drag coefficient magnitude results are compared with experimental results.

For measurement height 50 mm, as drag magnitude decreases, overestimation of solid volume fraction increases in all regions. On the other hand, underestimation of particle velocity increases in all regions.

The case with the highest drag coefficient estimates both solid volume fraction and particle velocity better.

For measurement height 93 mm, as drag coefficient magnitude decreases, overestimation in solid volume fraction in spout region increases but underestimation in spout-annulus border decreases and overestimation decreases. For particle velocity overestimation decreases with decrease in drag magnitude.

The case with the lowest drag coefficient estimates both solid volume fraction and particle velocity better for all measurement heights.

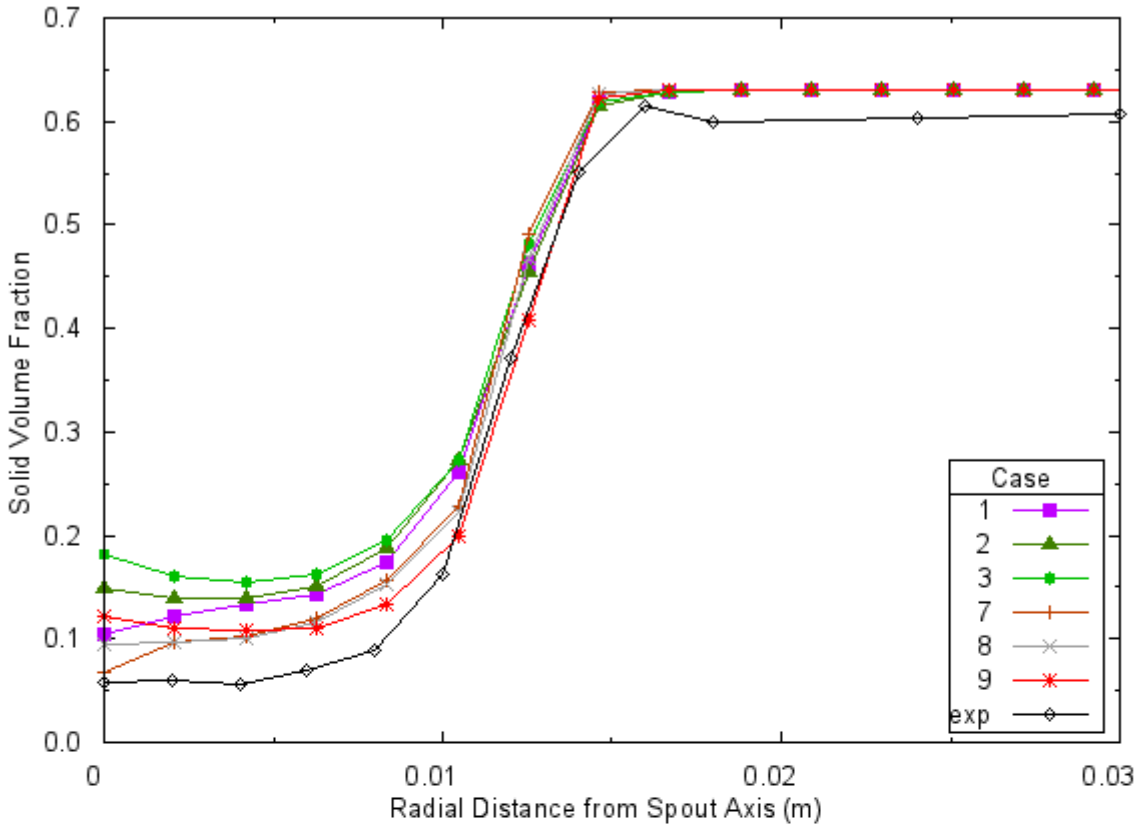

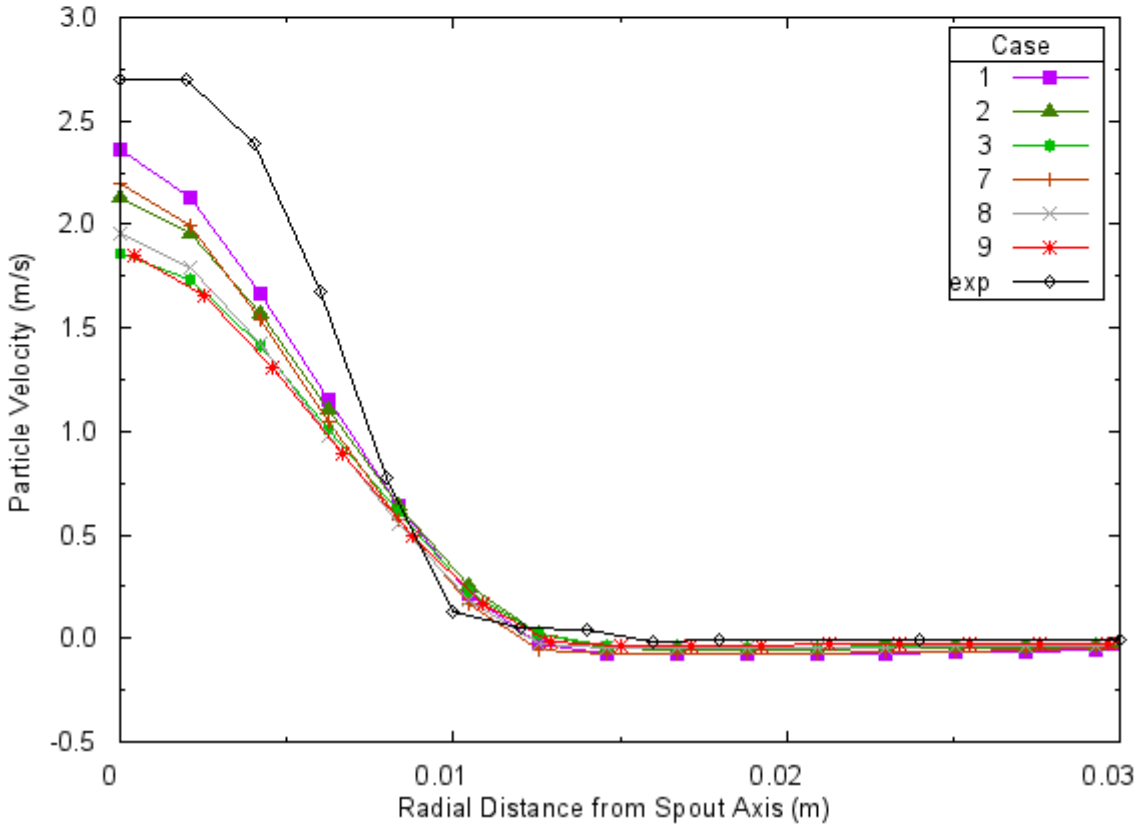

Figure 7.67 Comparison of CFD results with experimental results for experimental set 6, measurement height 50 mm - Gidaspow drag model.

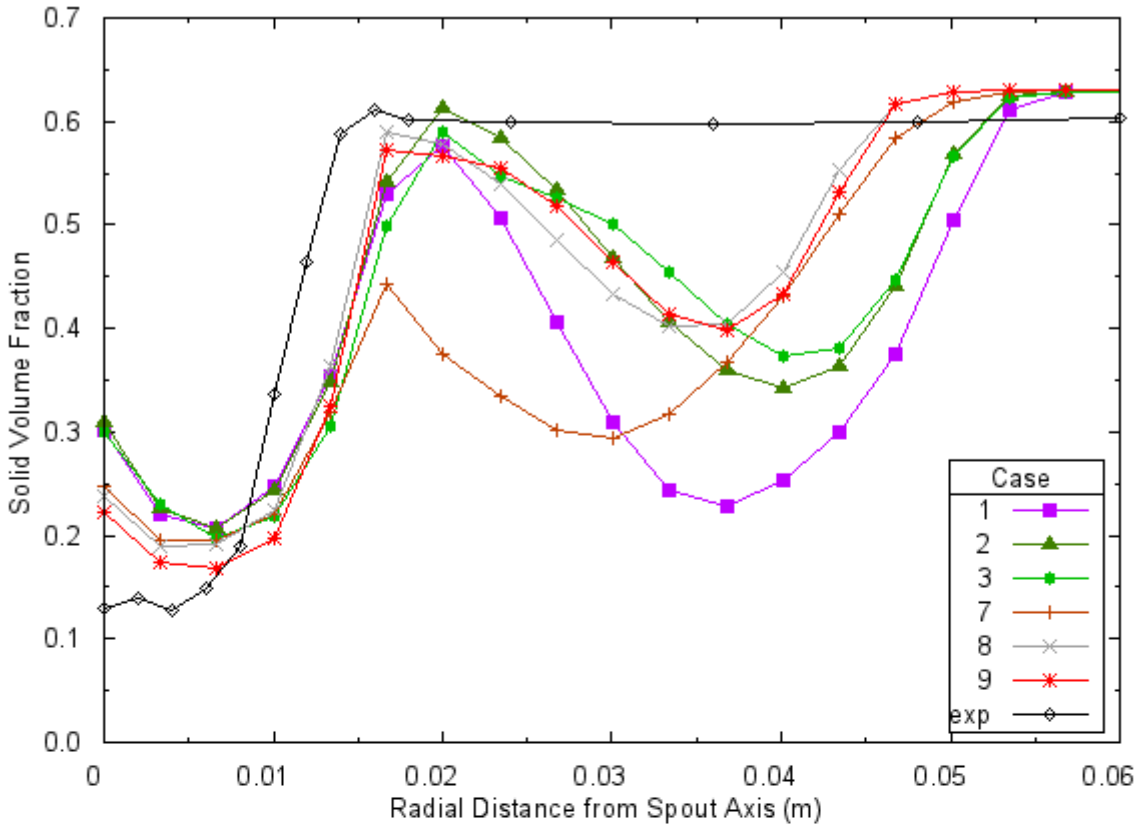

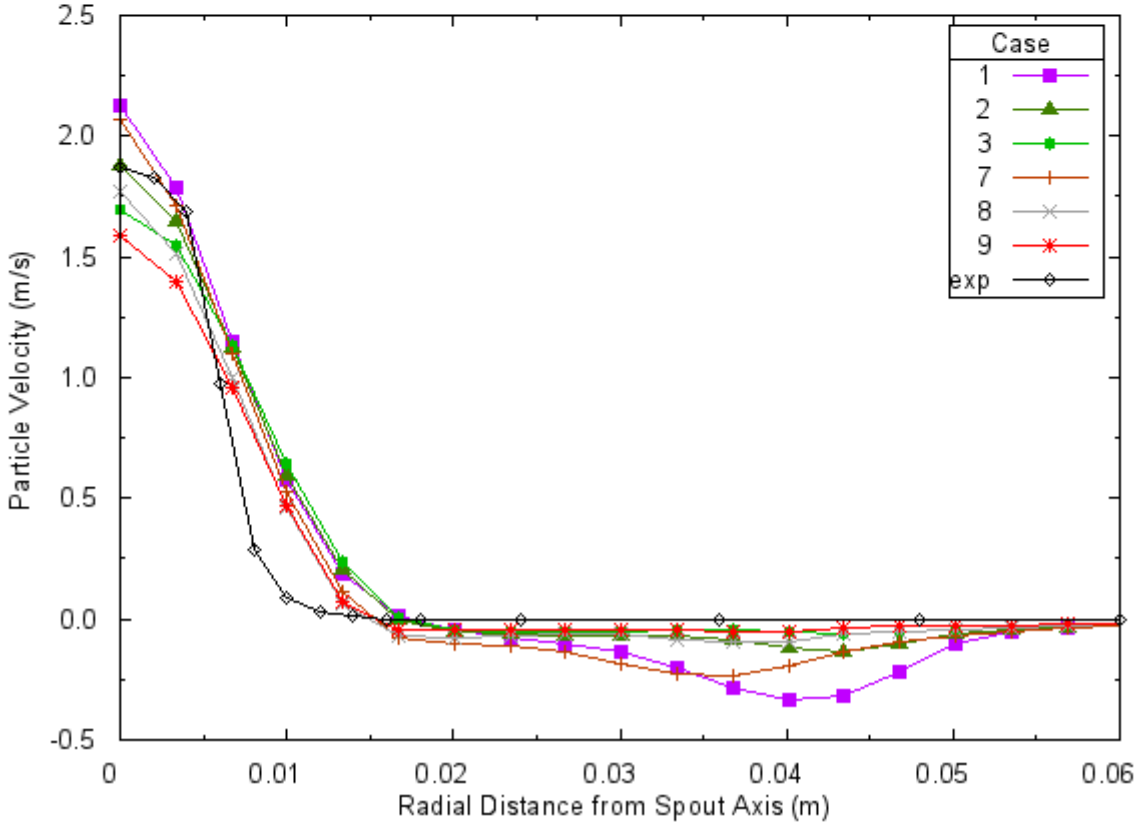

Figure 7.68 Comparison of CFD results with experimental results for experimental set 6, measurement height 93 mm - Gidaspow drag model.

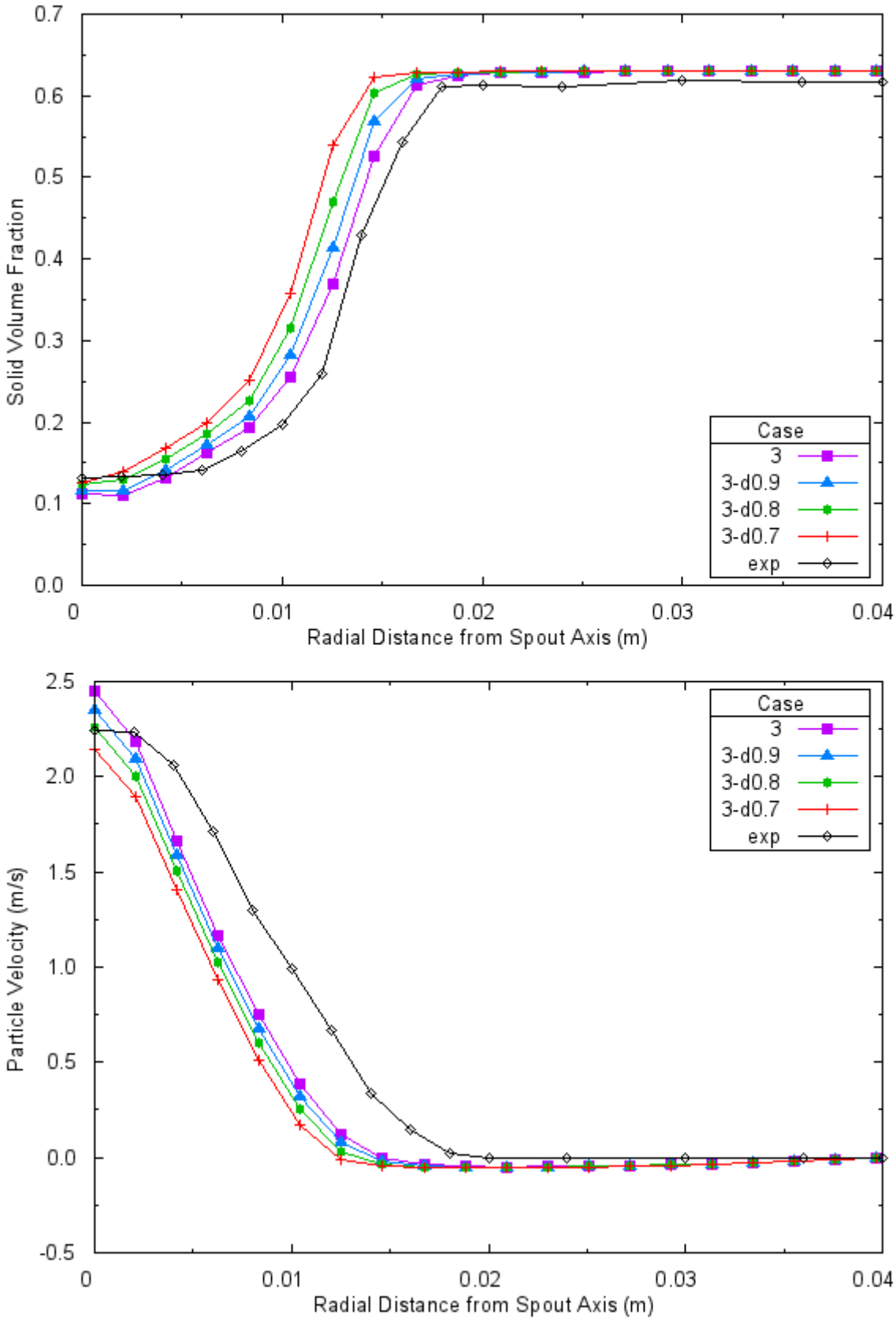

Figure 7.69 Comparison of CFD results with experimental results for experimental set 7, measurement height 50 mm - Gidaspow drag model.

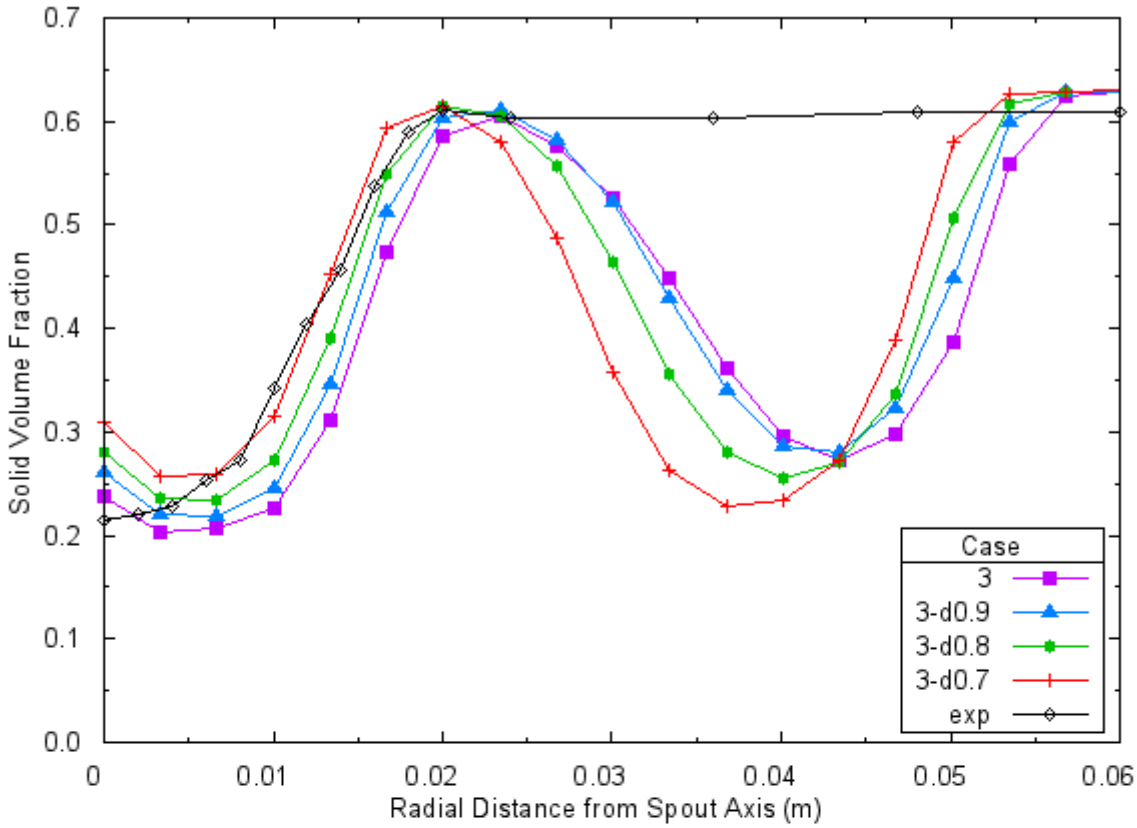

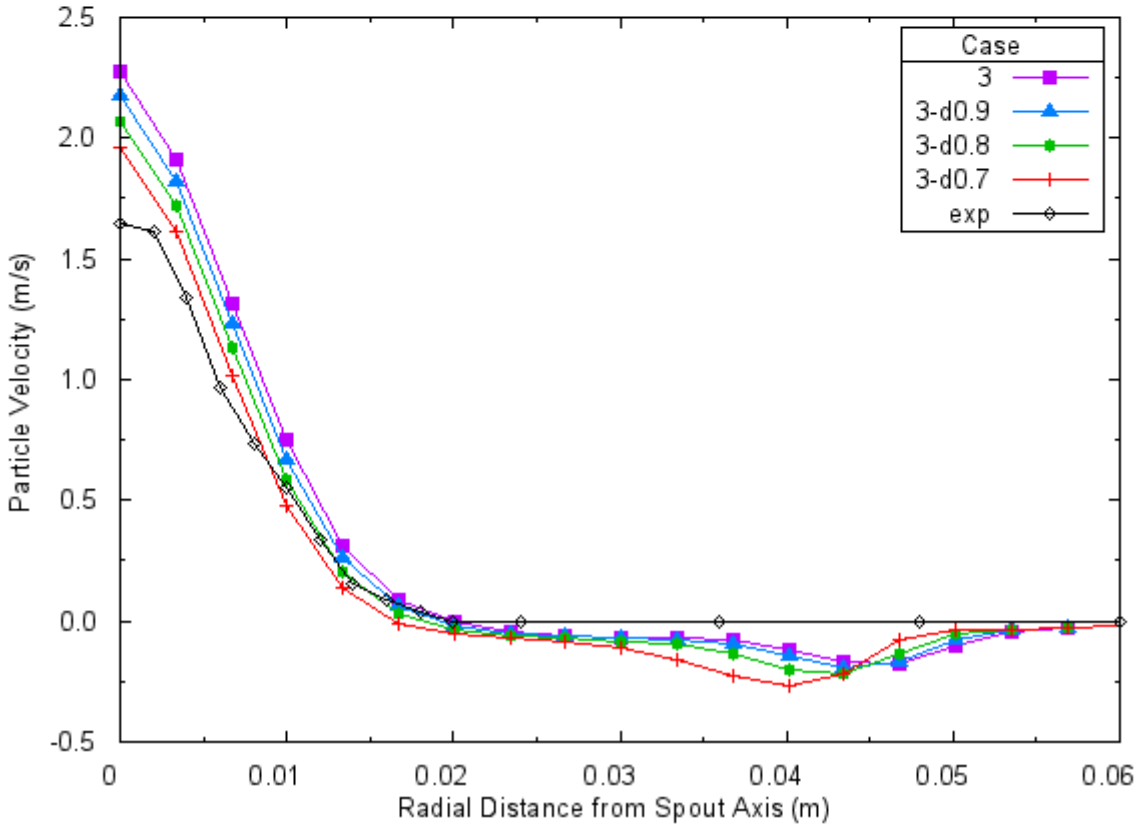

Figure 7.70 Comparison of CFD results with experimental results for experimental set 7, measurement height 93 mm - Gidaspow drag model.

The summary about effects of the restitution coefficient, drag model, inclusion of frictional stress into simulations, and magnitude of drag coefficient on hydrodynamics of spouted beds and resulting concurrency with experiments can be presented as follows.

1. The effect of restitution coefficient

   As restitution coefficient decreases, particle velocity and voidage increases. On the other hand, the bed pressure drop decreases for all cases expect Gidaspow drag model with no frictional stress cases. When restitution coefficient decreases particle velocity and voidage distributions deviates from experimental results. But, error in bed pressure drop predictions decreases as restitution coefficient decreases.
2. The effect of drag model

   Syamlal-O'Brien drag model predictions of particle velocity and voidage are higher than Gidaspow drag model predictions as well as bed pressure drop predictions. Gidaspow model results for particle velocity and voidage are closer to experimental results than Syamlal-O'Brien drag model results. The pattern on error in bed pressure drop predictions is not clear.
3. The effect of solid frictional stress

   Inclusion of solid frictional stress into simulations decreases particle velocity and voidage predictions. The bed pressure drop predictions reduce dramatically (30-50 %) when solid frictional stress is included into simulations. Its inclusion increases error in bed pressure drop. But, the effect on concurrency with experimental results in particle velocity and voidage does not have specific pattern.
4. The effect of magnitude of drag coefficient

   As magnitude of drag coefficient increases, particle velocity and voidage increase however no specific pattern is determined about its effect on bed pressure drop.

7.5 Comparison of Effects of CFD Model Parameters on Light and Heavy Particle Simulations

Throughout this study, two sets of experimental setups defined in He et al. (1994a; 1994b) and Sari et al. (2011) were used. Although there are some geometrical and operational differences, the main difference between these two setups is particle

density. As mentioned before, He's experiment contains glass beads of 2500 kg/m^3 density and Sari's experiment contains Zirconia particles of 6050 kg/m^3 density. Up to now, neither applicability of CFD models for simulations of heavy particle filled conical cylindrical spouted beds nor comparison of effects of simulation parameters on hydrodynamics of heavy and light particle filled spouted beds was tested computationally. By using the results of Chapter 6 and Chapter 7, it is going to be evaluated here.

Throughout simulations different values of restitution coefficient (0.95, 0.90, and 0.80), different drag models (Gidaspow and Syamlal-O'Brien), inclusion of solid friction into simulations, and different drag magnitudes were used to investigate the effects of these parameters on hydrodynamics of conical cylindrical spouted beds for two different particles having different densities. It should be noted that maximum packing limit value of 0.63 was used for simulation of Sari's experiment because this is the loosely packed solid volume fraction. Therefore, its effect was not assessed for heavy particles.

The characteristic flow pattern of solid particles in spouted beds is described in three zones. The spout zone where particles move upward, the annulus zone where particles move slowly downward, and the fountain zone where at its core particles move upward and at its sides particles move downward. This typical flow pattern was established during both light and heavy particle simulations.

Other characteristic of spouted beds is that in the spout zone particle velocity decreases axially away from the gas inlet and radially away from the spout center and solid volume fraction follows the opposite. This was observed during simulations of both heavy and light particles.

Another characteristic of spouted beds is that in the annulus zone particle velocity decreases towards the wall of the bed and solid volume fraction reaches a constant value close to maximum packing limit. This was the case for both light and heavy particle simulations.

As a result, it can be said that Eulerian-Eulerian two-fluid model with kinetic theory of granular flows approach is capable of simulating flow in the conical cylindrical spouted beds filled with both light and heavy particles.

The effect of model parameters i.e. restitution coefficient, drag model, inclusion of solid friction into simulations, and magnitude of drag coefficient on light and heavy particle simulations is presented in Table 7.18.

As seen in Table 7.18, the effect of restitution coefficient on particle velocity and bed pressure drop is the same for both light and heavy particles. Its decrease increases particle velocity and decreases bed pressure drop.

The effect of drag model on particle velocity is the same for light and heavy particle simulations but the effect differs for bed pressure drop results. Syamlal-O'Brien drag model predictions for particle velocity are higher than Gidaspow drag model predictions for both particles. For light particles Gidaspow drag model predictions for bed pressure drop is higher than Syamlal-O'Brien drag model predictions. On the other hand, the opposite is valid for heavy particles.

Inclusion of solid frictional stress into simulations decreases particle velocity for heavy particles no matter what the drag model is, but its effect changes with drag model for light particles. With inclusion of frictional stress into simulations, for Gidaspow drag model case particle velocities decrease but for Syamlal-O'Brien drag model case particle velocities increase. The effect of its inclusion on pressure drop is the same for both particle densities.

Increase in drag coefficient magnitude increases particle velocity for both light and heavy particles. Its effect on pressure drop is an increase for light particles but no specific pattern was found for heavy particles.

When all the results of both experiments are analyzed it can be said that the best simulation parameters for He's experiment are Syamlal-O'Brien drag model, restitution coefficient of 0.90, and solid frictional stress should be included into simulations. The best simulation parameters for Sari's experiment are Gidaspow drag model, restitution coefficient of 0.95, and solid frictional stress should not be included into simulations.

Table 7.18 The comparison of effects of model parameters on particle velocity and bed pressure drop for light and heavy particle simulations.

Parameter	Effect on particle velocity		Effect on bed pressure drop	
	Light Particles	**Heavy Particles**	**Light Particles**	**Heavy Particles**
Decrease in restitution coefficient	increase	increase	decrease	decrease
Drag model	Syamlal-O'Brien drag model predictions are higher than Gidaspow drag model predictions	Syamlal-O'Brien drag model predictions are higher than Gidaspow drag model predictions	Gidaspow drag model predictions are higher than Syamlal-O'Brien drag model predictions	Syamlal-O'Brien drag model predictions are higher than Gidaspow drag model predictions
Inclusion of solid frictional stress	Increase or decrease	decrease	decrease	decrease
Increase in magnitude of drag coefficient	increase	increase	increase	can't defined

7.6 The Findings about Hydrodynamics of Spouted Beds

Sari's experiments were used to examine experimentally the effect of conic angle, static bed height, and particle size on hydrodynamics of conical cylindrical spouted beds. The CFD simulations were used to do similar examinations on computer. The findings from experiments and CFD simulations were compared and reported in this section.

As a result of findings from CFD simulations in Section 7.4, case 3 (Gidaspow drag model, restitution coefficient of 0.95, and no solid frictional stress) which estimated bed pressure drop, solid volume fraction, and particle velocity better than other cases for most of the experimental sets was selected to investigate the effect of the above mentioned parameters on hydrodynamics of the spouted beds.

Table 7.19 shows the experimental and simulation results of bed pressure drop for every experimental set.

The effect of static bed height on bed pressure drop is that total bed pressure drop increases with increase in static bed height. Obviously, the higher the static bed height, the higher the total particle weight in the bed. Since the bed weight and forces between particles must be overcome for spouting, total bed pressure drop increases with static bed height. This finding agrees well with experimental findings and with findings of Rojas (2010).

Table 7.19 The experimental and CFD results for bed pressure drop.

Experimental Set Number	Experimental Pressure Drop (Pa)	CFD Pressure Drop (Pa)
1	3764	3539
2	N/A	1334
3	2273	2355
4	3449	3274
5	1052	1233
6	1708	2268
7	2125	2805

The effect of particle size on bed pressure drop is that as particle size increases, bed pressure drop decreases. Same deduction can be done from experimental results. This finding agrees well with the findings of Rojas (2010) and Zhou (2008). It is because of the fact that when particle size increases, it became easy for gas to pass through the openings between solids therefore bed pressure drop decreases.

The effect of conic angle on bed pressure drop is that total bed pressure drop decreases with increasing conic angle. This is confirmed with experimental results. In addition, the same outcome is reported in Zhou (2008). It is due to the fact that for the same static bed height more particles are carried out by the walls of the bed when conic angle increases. This reduces the bed pressure drop.

The findings about the effect of static bed height, particle size, conic angle, and measurement height on particle velocity and solid volume faction distributions from CFD simulations and experiments are given in Figure 7.71 to Figure 7.78. The particle velocity distribution in spout and annulus regions is presented separately

on the same graph. The filled pointers represent particle velocity in spout region and open pointers represent particle velocity in annulus region.

The effect of static bed height on solid volume fraction and particle velocity distributions is shown in Figure 7.71 and Figure 7.72. Particle velocity increases in spout and annulus regions as static bed height increases. Solid volume fraction follows the reverse of the particle velocity and decreases as static bed height increases. These findings from CFD simulations agree well with the experimental results.

The effect of particle size on solid volume fraction and particle velocity distributions is shown in Figure 7.73 and Figure 7.74. As particle size increases, particles move slower upward in spout and slower downward in annulus regions. Solid volume fraction increases as particle size increases. These findings are exact opposite of the experimental results.

The effect of conic angle on solid volume fraction and particle velocity is shown in Figure 7.75 and Figure 7.76. According to CFD simulations, the higher the conic angle the higher the particle velocity in spout and annulus regions. This is verified with experimental results. As conic angle increases solid volume fraction decreases. Similar behavior is concluded from experiments.

The behavior of solid volume fraction and particle velocity distributions with increase in measurement height is also examined. As measurement height is increased, particle velocity is decreased in spout region. This is also observed in experimental results as seen in Figure 7.78. But in annulus region, CDF simulations results show increase in particle velocity as measurement height increases. The opposite is true for experimental results. On the other hand increase in solid volume fraction with increasing measurement height conclusion agrees well with experimental results as seen in Figure 7.77.

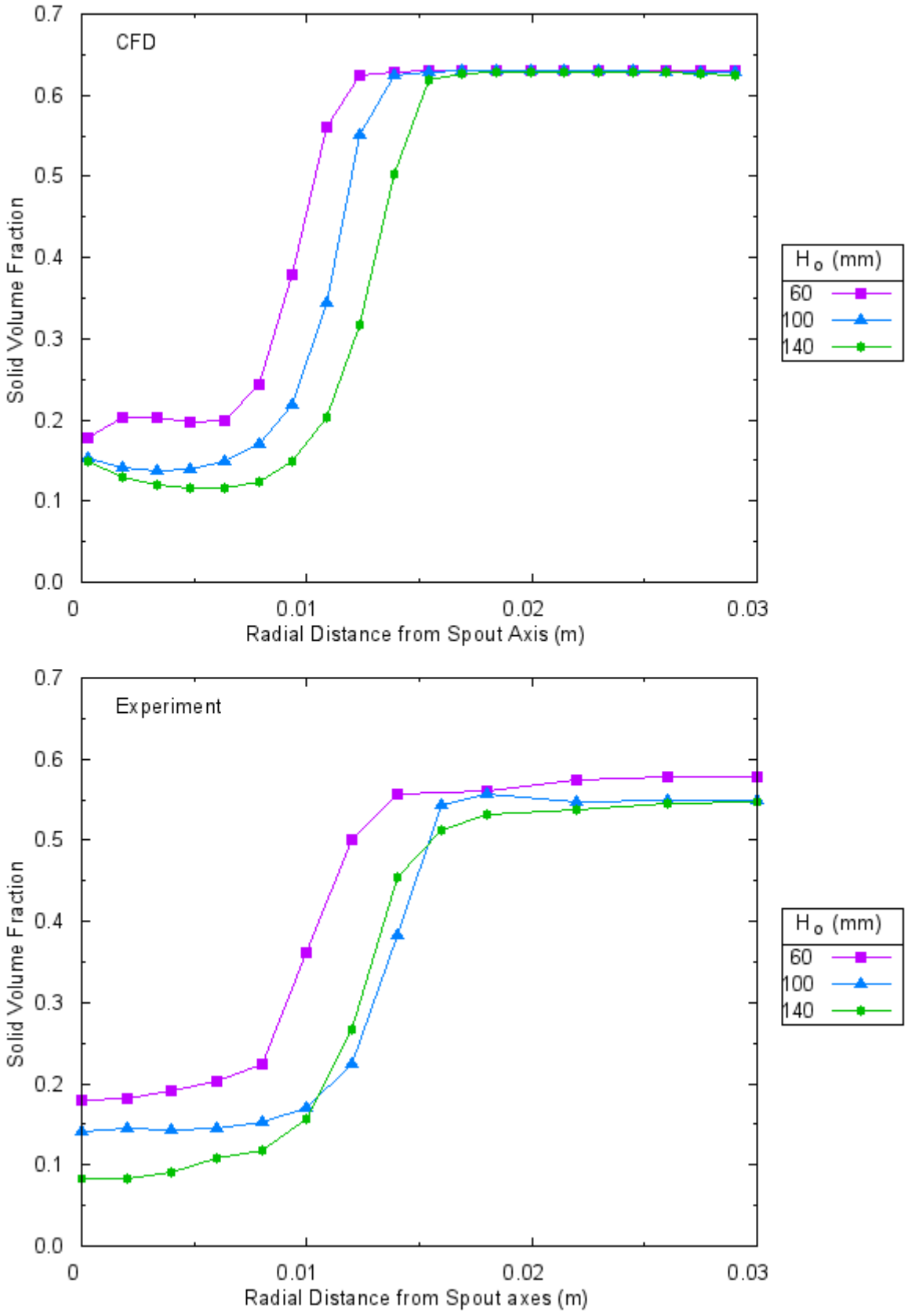

Figure 7.71 The effect of static bed height on solid volume fraction distribution.

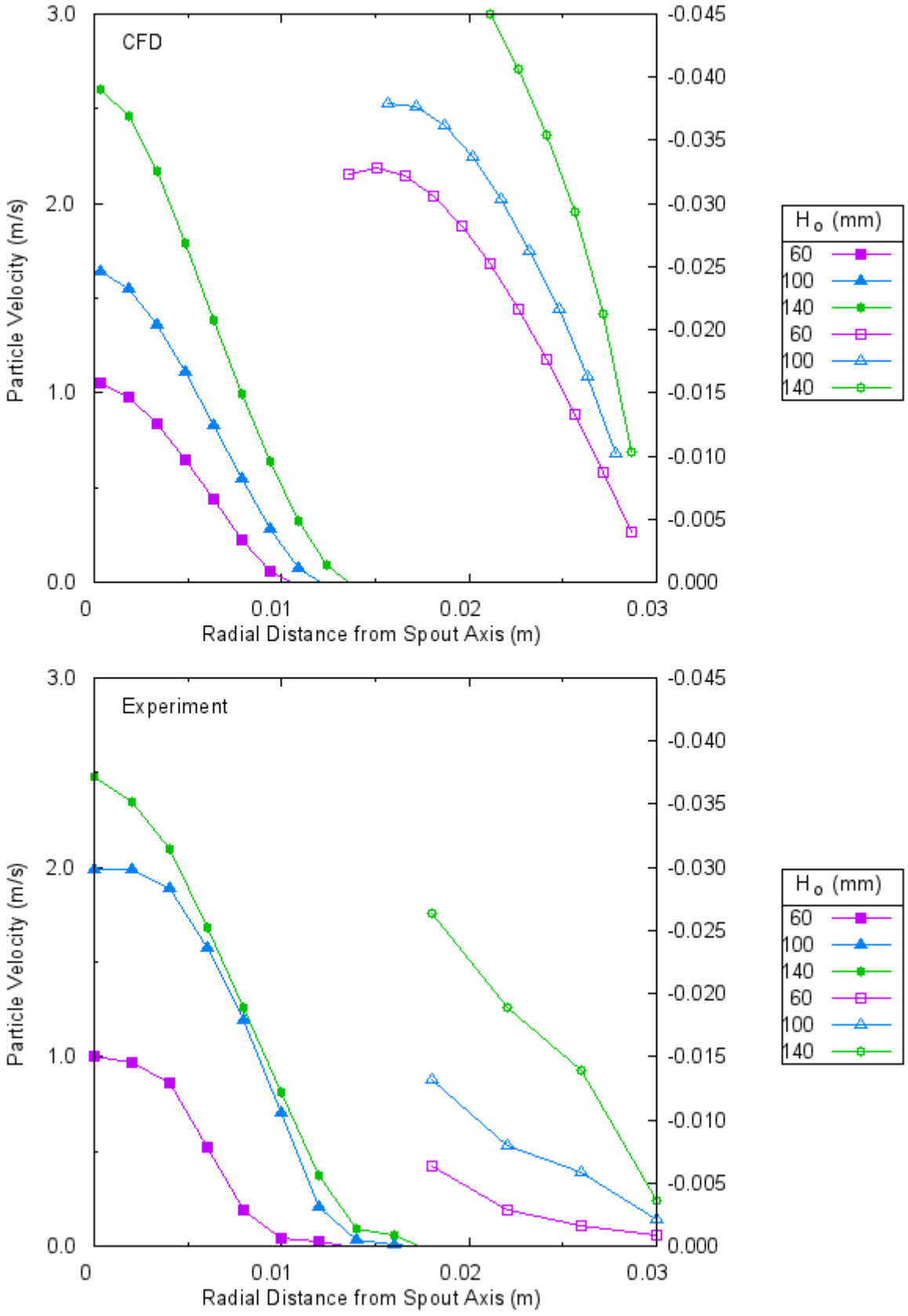

Figure 7.72 The effect of static bed height on particle velocity distribution.

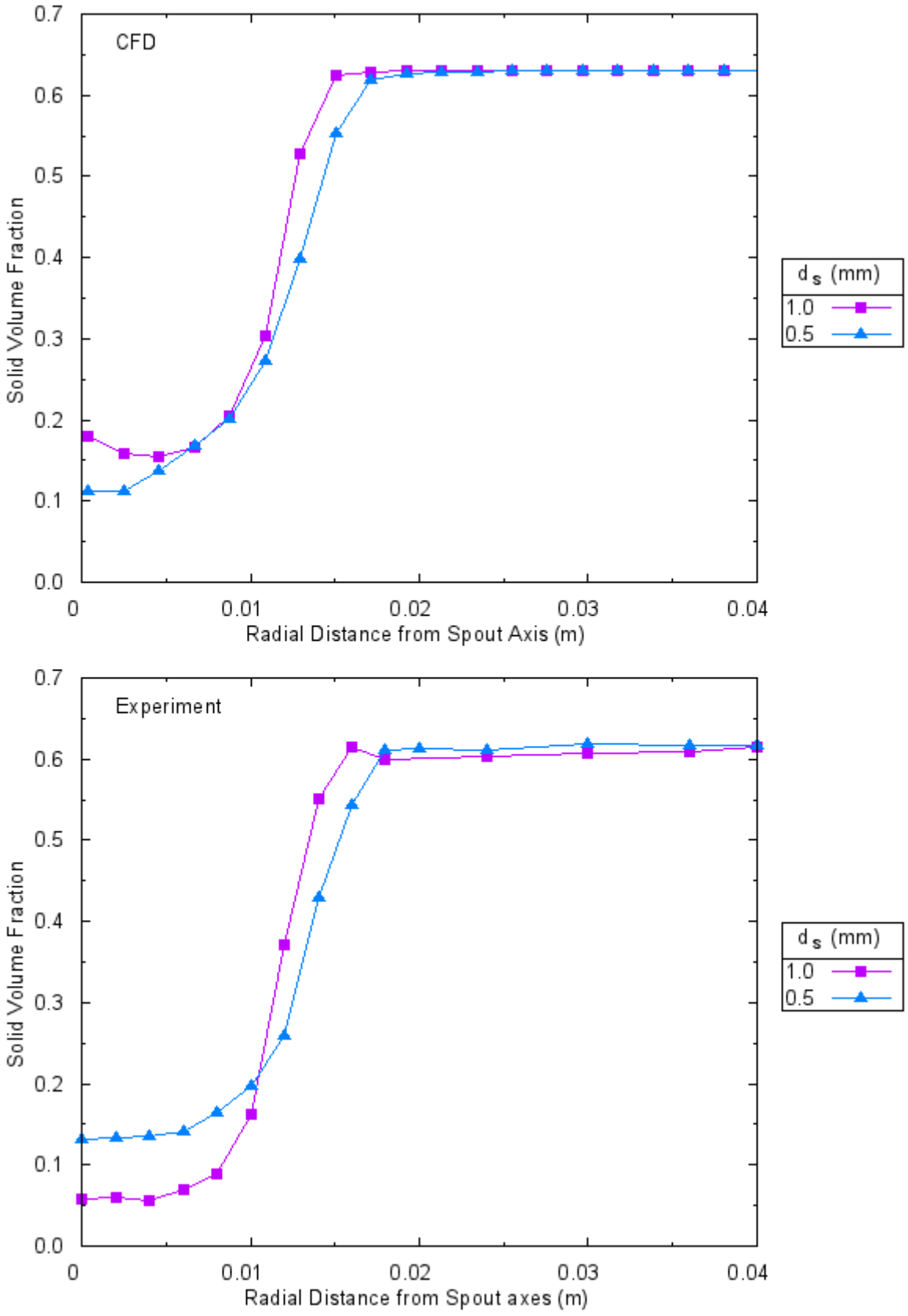

Figure 7.73 The effect of particle size on solid volume fraction distribution.

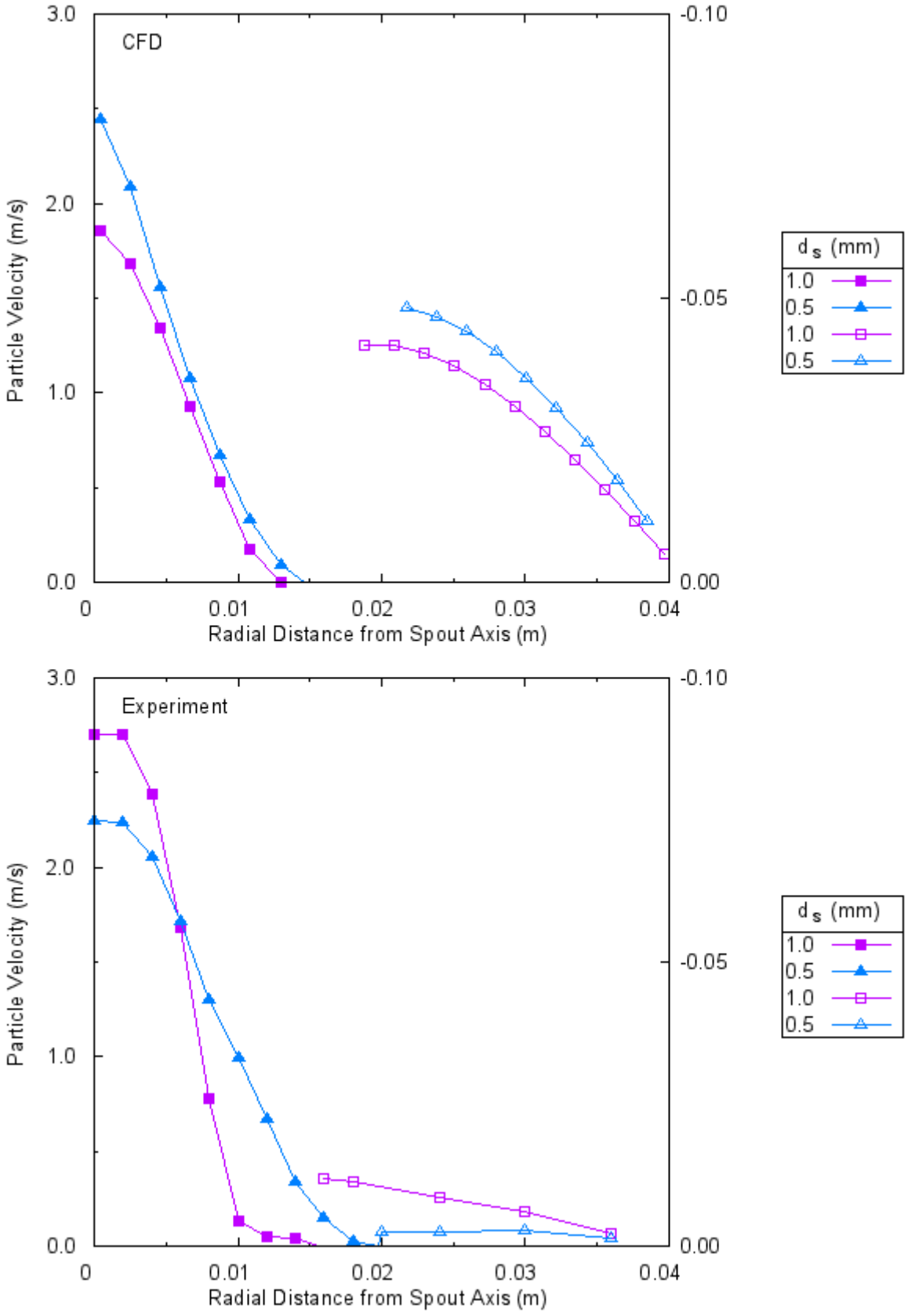

Figure 7.74 The effect of particle size on particle velocity distribution.

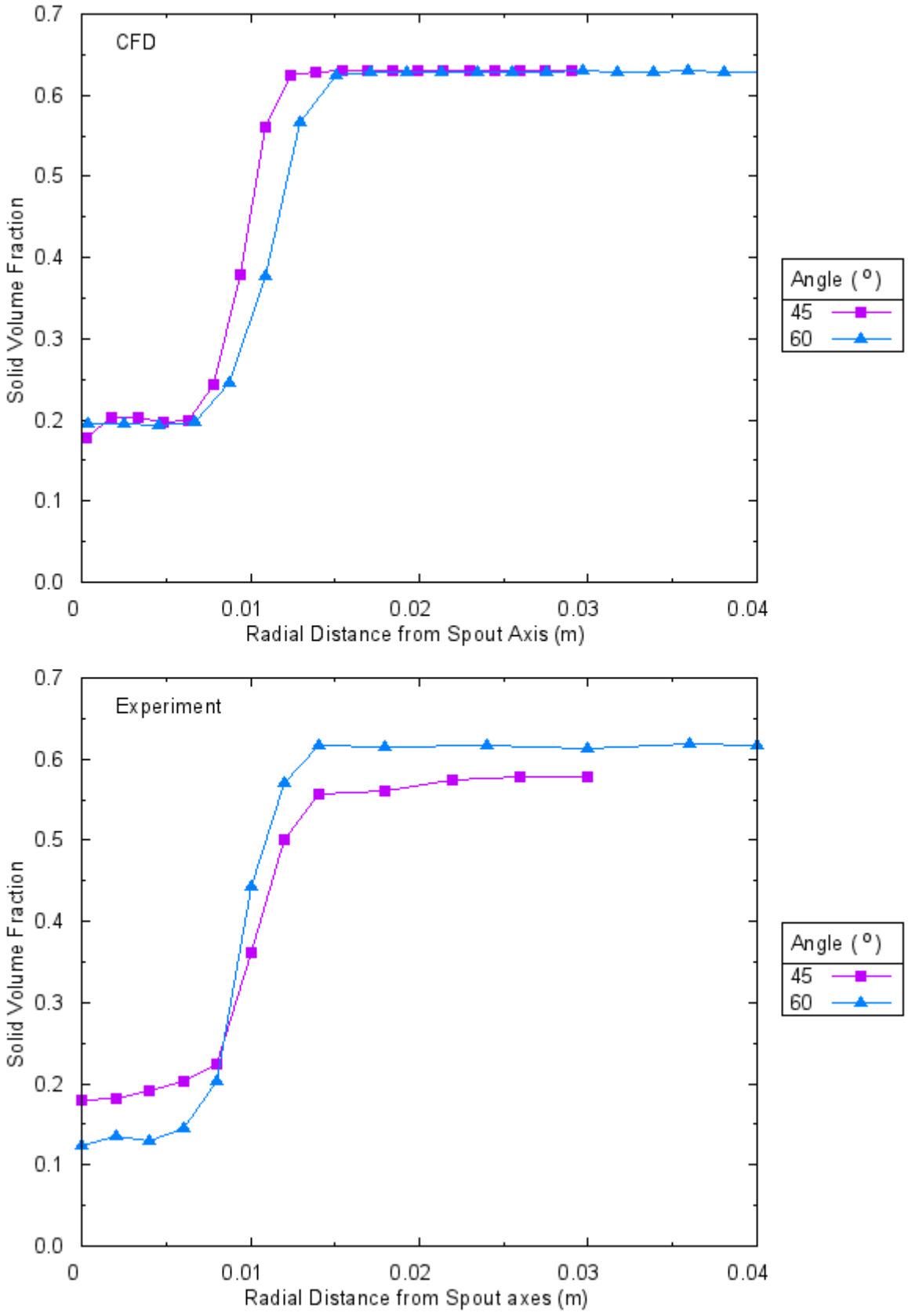

Figure 7.75 The effect of conic angle on solid volume fraction distribution.

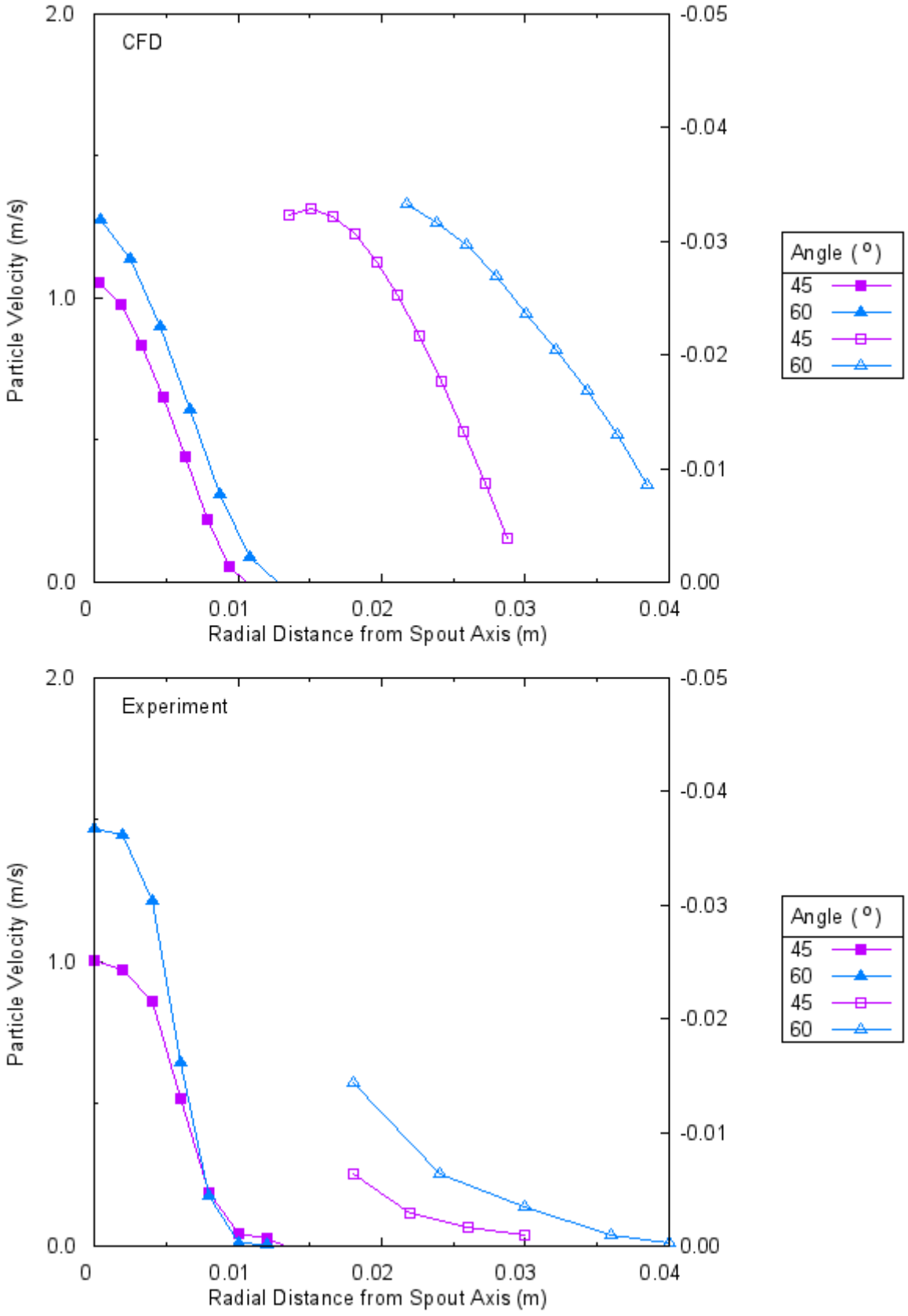

Figure 7.76 The effect of conic angle on particle velocity distribution.

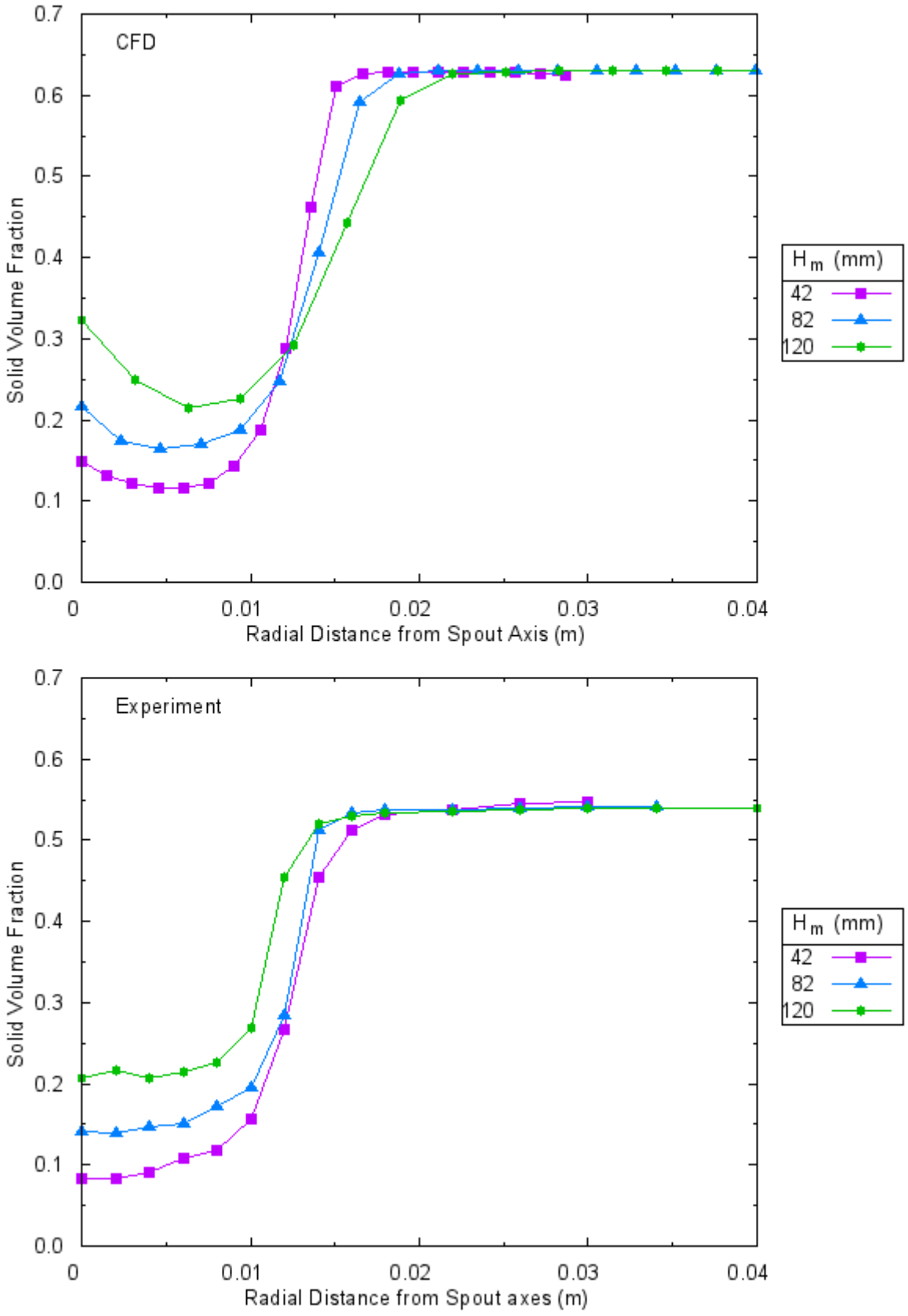

Figure 7.77 Change in solid volume fraction distribution with measurement height.

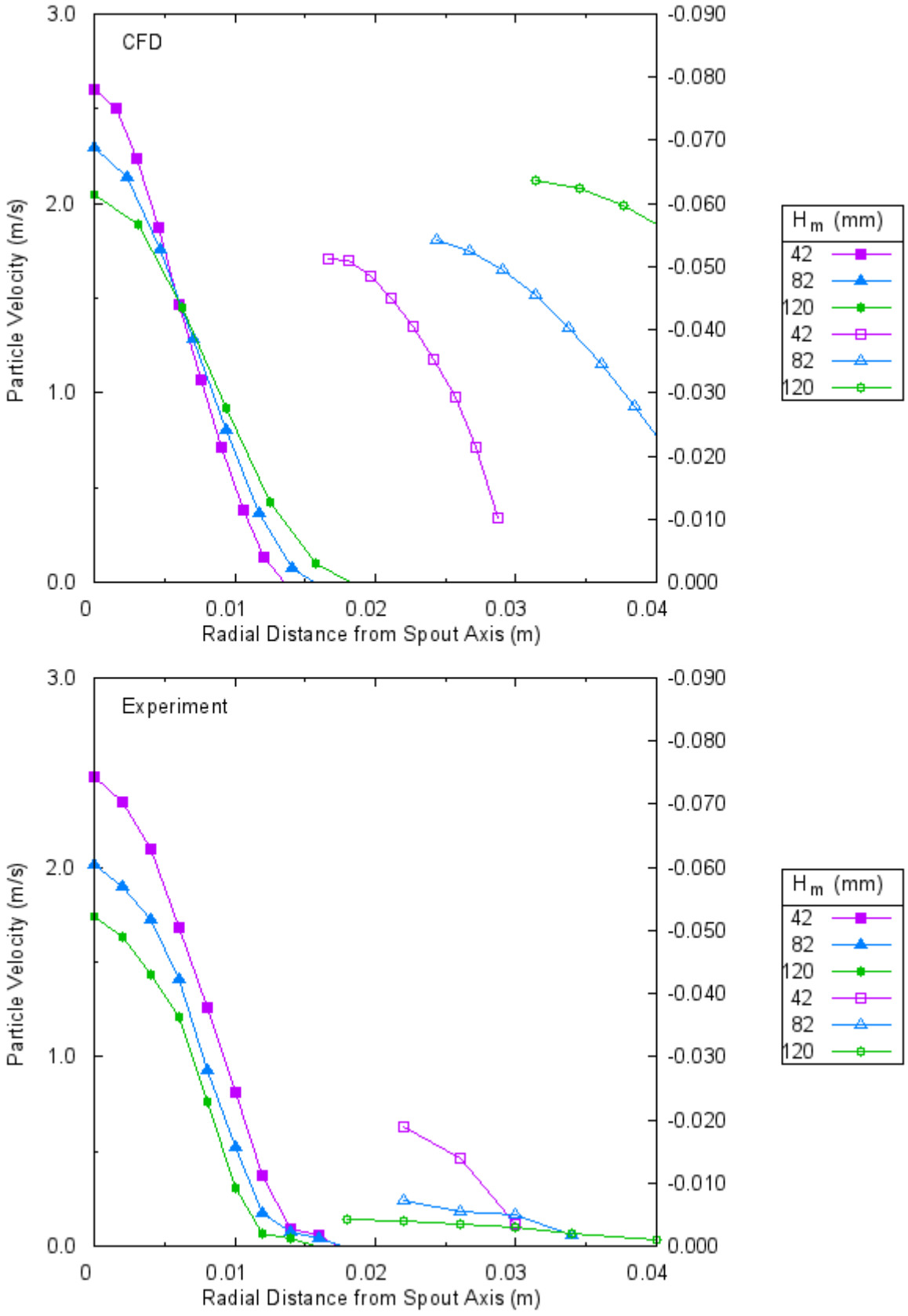

Figure 7.78 Change in particle velocity distribution with measurement height.

8 CONCLUSION

A comprehensive hydrodynamic study on conical cylindrical spouted beds filled with light and heavy particles has been carried out with computational fluid dynamics simulations. Different models were used to examine the effect of various parameters such as maximum packing limit, restitution coefficient, drag model, magnitude of drag coefficient, and inclusion of solid frictional stress into simulations on simulation results. After determination of an appropriate model, flow hydrodynamics of conical cylindrical spouted beds filled with heavy particles were analyzed in order to determine the effect of cone angle, static bed height, and particle diameter. The commercial CFD package FLUENT was used for simulations.

Two different experimental setups were used for simulations. First one is known as He et al. experimental setup which was established in 1994 in Mechanical Engineering Department of University of British Columbia, Canada. The second one was established in Department of Mechanical Engineering in Hacettepe University, Turkey and completed in 2011 and referred as Sari et al. He's experimental set contains 60 degree conic angle bed with glass beads of 1.41 mm diameter and 2500 kg/m^3 density. Sari's setup contains three beds with 60 or 45 or 30 degree conic angle. Spherical Zirconia particles of 1.0 and 0.5 mm diameter and 6050 kg/m^3 density are used. Air as spouting gas is used for both experimental sets. Gas inlet diameter and bed diameter of both sets are similar. The main difference in bed geometry is that Sari's setup's gas inlet diameter is smaller than bed base diameter therefore there are dead zones at both ends of the entrance where particles can stay. However, gas inlet diameter and bed base diameter are the same for He's experimental setup. The main difference about experimental conditions is that static bed height in He's experiment is higher than conic height which means particles filled above the conical section of the bed. Whereas in Sari's experimental sets particles stay inside the conical section of the bed.

When flow hydrodynamics of conical cylindrical spouted beds filled with light and heavy particles are examined, proper external spouting was observed for both experimental sets which satisfies expectations because the inlet gas velocity is 1.3

and 1.25 times the minimum spouting velocity for He's and Sari's experiments. Well defined spout, annulus, and fountain zones were observed during simulations. In spout zone, particles move upwards, particle velocity decreases axially away from the gas inlet and radially away from the spout center and voidage follows the same pattern. In annulus, particles move slowly downwards, particle velocity decreases towards the wall of the bed, and solid volume fraction has a constant value close to maximum packing. In fountain, particles move upwards near the core of the fountain and downwards near the sides of the fountain. This behavior is consistent with typical conical cylindrical spouted bed behavior defined in literature. Therefore it can be said that Eulerian-Eulerian two-fluid model with kinetic theory of granular flows approach is capable of simulating flow in the conical cylindrical spouted beds filled with both light and heavy particles.

The summary of effects of maximum packing limit, restitution coefficient, drag model, inclusion of frictional stress into simulations, and magnitude of drag coefficient on hydrodynamics of spouted beds filled with light and heavy particles and resulting concurrency with experiments can be summarized as follows.

Findings from CFD simulations of light particle filled conical cylindrical spouted beds:

1. The effect of maximum packing limit

   As maximum packing limit decreases, particle velocity and voidage distributions decrease. This outcome is consistent with the findings of Du et al. (2006b). Its effect on bed pressure drop cannot be determined since there wasn't any particular pattern. Its decrease causes high deviations from the experimental results for particle velocity and voidage distributions but there is not any specific pattern for bed pressure drop predictions.
2. The effect of restitution coefficient

   As restitution coefficient decreases, particle velocity and voidage distributions increase. This effect of restitution coefficient on particle velocity and voidage is also observed in Du et al. (2006b) and Wang (2006). Bed pressure drop also decreases when restitution coefficient decreases. When

restitution coefficient decreases all results agrees better with experimental results.

3. The effect of drag model

   Syamlal-O'Brien drag model cases have higher particle velocity and voidage distributions (the opposite is reported in Du et al. (2006b)) but smaller bed pressure drop results. Syamlal-O'Brien drag model case predictions for particle velocity and voidage are closer to experimental results than the Gidaspow drag model predictions but the opposite is observed for bed pressure drop predictions.

4. The effect of solid frictional stress

   Its effect changes with drag model used. For Gidaspow drag model it seems to have no effect on particle velocity and voidage distributions. But for Syamlal-O'Brien drag model case, its inclusion increases both particle velocity and voidage distributions. Shuyan et al. (2009) findings show the opposite behavior. For both drag model cases, bed pressure drop decreases dramatically when solid frictional stress included into simulations. Its inclusion into simulations results in better estimations of particle velocity and pressure drop.

5. The effect of magnitude of drag coefficient

   The increase in magnitude of drag coefficient increases both particle velocity and voidage distributions (agrees well with Wang et al. (2006)) and slightly increases bed pressure drop.

Syamlal-O'Brien drag model case with inclusion of frictional stress into simulation results, in general, agree well with the experimental results of particle velocity, solid volume fraction, and bed pressure drop for light particle simulations.

Findings from CFD simulations of heavy particle filled conical cylindrical spouted beds:

1. The effect of restitution coefficient

   As restitution coefficient decreases, particle velocity and voidage increases. On the other hand, the bed pressure drop decreases for all cases expect Gidaspow drag model with no frictional stress cases. When restitution coefficient decreases particle velocity and voidage distributions deviates

from experimental results. But, error in bed pressure drop predictions decreases as restitution coefficient decreases.

2. The effect of drag model

   Syamlal-O'Brien drag model predictions of particle velocity and voidage are higher than Gidaspow drag model predictions as well as bed pressure drop predictions. Gidaspow model results for particle velocity and voidage are closer to experimental results than Syamlal-O'Brien drag model results. The pattern on error in bed pressure drop predictions is not clear.

3. The effect of solid frictional stress

   Inclusion of solid frictional stress into simulations decreases particle velocity and voidage predictions. The bed pressure drop predictions drop dramatically (30-50 %) when solid frictional stress is included into simulations. Its inclusion increases error in bed pressure drop. But, concurrency with experimental results in particle velocity and voidage does not have specific pattern.

4. The effect of magnitude of drag coefficient

   As magnitude of drag coefficient increases, particle velocity and voidage increase however no specific pattern is determined about its effect on bed pressure drop.

It should be noted that maximum packing limit value of 0.63 was used for simulation of Sari's experiment because this is the loosely packed solid volume fraction. Therefore, its effect was not assessed for heavy particles. Gidaspow drag model case without inclusion of frictional stress into simulation results, in general, agree well with the experimental results of particle velocity, solid volume fraction, and bed pressure drop for heavy particle simulations.

As a result it was observed that effect of restitution coefficient on simulations of both light and heavy particle filled conical cylindrical spouted beds are the same for particle velocity, voidage, and bed pressure drop. The effect of drag model on particle velocity and voidage is the same for both particle weights but differs on bed pressure drop. The effect of inclusion of frictional stress into simulations on particle velocity and voidage depends on drag model used for light particle simulations on the other hand the effect is the same for both drag models for

heavy particle simulations. But, for both particle weights, the effect of inclusion of frictional stress into simulations on pressure drop is the same.

From above findings, it can be concluded that maximum packing limit and magnitude of drag coefficient therefore drag model have vital importance for CFD simulations of conical cylindrical spouted beds. Because both can cause unrealistic simulation results such as not generating external spouting as expected (e.g. when maximum packing limit set to 0.59 there wasn't any external spouting although the inlet velocity was 1.3 times the minimum spouting velocity) or generating particle outflow as not expected (e.g. when magnitude of drag coefficient was increased 4 times the original value, the particles escaped from the bed which wasn't reported in original experiment).

Other parameters; restitution coefficient and inclusion of frictional stress into simulations; have secondary effect on conical cylindrical spouted bed CFD simulations. If they are not properly assigned, they may cause overestimation or underestimation of results but they do not change the physics of the system.

The effect of bed geometry and operation conditions on flow hydrodynamics of heavy particle filled conical cylindrical spouted beds is also examined. Findings from simulations and their concurrency with findings of Sari's experiments and with findings of limited number of studies in literature are given below.

- As static bed height increases, particle velocity in spout and annulus regions increases as well as voidage. These results agree well with Sari's findings. The bed pressure drop also increases with increase in static bed height. These results agree well with Sari's results and results of Rojas (2010).
- As particle size increases, particle velocity and voidage decreases in spout and annulus regions. Neither the results of the spout region nor the annulus region agree with experimental results. Bed pressure drop decreases as particle size increases as in Sari's experiments and in Rojas (2010) and Zhou (2008).
- As conic angle increases, particle velocity and voidage increase in spout and annulus regions. Similar behavior is observed in Sari's experiments.

Bed pressure drop decreases with increase in conic angle. This outcome of simulations agrees well with experimental results and results of Zhou (2008).

Since studies in the literature on hydrodynamics of conical cylindrical spouted beds are mainly focused on particles with densities around 2500 kg/m^3, there is a gap in the literature about hydrodynamics of these beds when filled with particles having higher densities. Sari's experiments were performed to fill this gap. Indeed, literature search showed that it is the first comprehensive experimental study measuring minimum fluidization velocity, bed pressure drop, particle velocity, solid volume fraction, and gas mixing for conical cylindrical spouted beds filled with high density particles. This study is also the first comprehensive CFD study about the effects of simulation and operation parameters on hydrodynamics of conical cylindrical spouted beds having high density particles. Findings from this study that are confirmed by experiments can guide other researchers about the effects of CFD simulation parameters on hydrodynamics of conical cylindrical spouted beds, what they should expect from changing the parameter values, and the effect of geometric and operation parameters of the bed on the hydrodynamics of conical cylindrical spouted beds.

It is also known that proper scaling is critical in relating laboratory studies to full-scale production. This work could be used to identify the most important non-dimensional hydrodynamic scaling groups and possible spouted bed design correlations based on these groups.

Since coating process of nuclear fuel kernels is performed in conical cylindrical spouted beds operating at high temperature, it is important to perform simulations at high temperature. The findings from this thesis could be used to facilitate further CFD studies about hydrodynamics of conical cylindrical spouted beds operating at high temperatures, particularly by leveraging the models analyzed in this thesis for ambient temperature conditions.

BIBLIOGRAPHY

Benyahia, S., Syamlal, M., and O'Brien, T.J., 2006, Extension of Hill-Koch-Ladd drag correlation over all ranges of Reynolds number and solid volume fraciton, Powder Technology, 162, 166-174.

Bettega, R., Almeida, A. R., Correa, R. G., and Freire, J. T., 2009a, CFD modeling of a semi-cylindrical spouted bed: numerical simulation and experimental verification, Canadian Journal of Chemical Engineering, 87, 177-184.

Bettega, R., Guimares, C., and Teixeria, F., 2009b, Scale-up study of spouted beds using computational fluid dynamics, Canadian Journal of Chemical Engineering, 87, 193-203.

Bi, H., 2004, A discussion on minimum spouting velocity and jet penetration length, Canadian Journal of Chemical Engineering, 82, 4-10.

Bi, H., Macchi, A., Chaouki, J., and Legros, R., 1997, Minimum spouting velocity of conical spouted beds, Canadian Journal of Chemical Engineering, 75, 460-465.

Boulos, M.I.; Waldie, B., 1986, High Resolution Merasurement of Particle Velocities in a Spouted Bed Using Laser-Doppler Anemometry, Canadian Journal of Chemical Engineering, 64, 939-943.

Charollais, F., Fonquernie, S., Perrais, C., Perez, M., Cellier, F., and Harbonnier, G., 2004, CEA and AREVA R&D on HTR fuel fabrication & presentation of the GAIA experimental manufacturing line, 2nd International Topical Meeting on High Temperature Reactor Technology, Paper B04.

Chiesa, M., Mathiesen, V., Melheim, J. A., and Halvorsen, B., 2005, Numerical simulation of particulate flow by eulerian-Lagrangian and the Eulerian-Eulerian approach with application to a fluidized bed, Computers and Chemical Engineering, 29, 291-304.

Cooper, S., and Coronella, C. J., 2005, CFD simulations of particle mixing in a binary fluidized bed, Powder Technology, 151, 27-36.

Dan, S., Shuyan, W., Gougdong, L., Shuai, W., Yongjian, L., and Lixin, W., 2010, Simulations of flow behavior of gas and particles in a spouted bed using a second-order moment method-frictional stress model, Chemical Engineering Science, 65, 2635-2648.

Day, J. Y., Morgan, M. H., and Littman, H., 1987, Measurements of spout voidage distributions, particle velocities and particle circulation rates in spouted beds of coarse particles, Chemical Engineering Science, 42, 1461-1470.

Djeridane, T., Larachi, F., Roy, D., Chaouki, J., and Legros, R., 1998, Investigation of the mean and turbulent particle velocity fields in a spouted bed using radioactive particle tracking, Canadian Journal of Chemical Engineering, 76, 190-195.

Du, W., Bao, X., Xu, J., and Wei, W., 2006a. Computational fluid dynamics (CFD) modeling of spouted bed: Assesment of drag coefficient correlations, Chemical engineering Science, 61, 1401-1420.

Du, W., Bao, X., Xu, J., and Wei, W., 2006b. Computational fluid dynamics (CFD) modeling of spouted bed: Influence of frictional stress, maximum packing limit and coefficient of restitution of particles, Chemical Engineering Science, 61, 4558-4570.

Duarte, C., Olazar, M., Murata, V., and Barrozo, M., 2009, Numerical simulation and experimental study of fluid-particle flows in a spouted bed, Powder Technology, 188, 195-205.

Epstein, N. and Grace, J.R., 2011, Spouted Bed and Spout Fluid Beds, Cambridge University Press, Cambridge, 364p.

Ferziger, J., and Peric, M., 2002, Computational Methods for Fluid Dynamics, Springer, Berlin, 431p.

Fluent., 2006, Fluent 6.3.2 Users Guide.

Gibliaro, L., 2001, Fluidization-dynamics, Butterworth-Heinemann, Oxford, 256p.

Gidaspow, D., 1994, Multiphase Flow and Fluidization, Academic Press, San Diego, 467p.

Goethem, G. V., 2008, Generation IV reactor systems and fuel cycles (horizon 2003): technological breakthroughs in nuclear fission (int'l RDandDD), Brussels, European Commission Research Directorate-General.

Goldschmidt, M.J.V., Beetstra, R., and Kuipers, J.A.M., 2004, Hydrodynamics modelling of dense gas-fluidised beds: comparison and validation of 3D discrete particle and continuum models, Powder Technology, 142, 23-47.

Gorshtein, A.E. and Mukhlenov, I.P., 1967, Movement of solid material in a spouting layer, Zh. Prikl. Khim., 40, 2469-2475.

Grace, J. and Mathur, K., 1978, Height and structure of the fountain region above spouted beds, Canadian Journal of Chemical Engineering, 56, 533-537.

Grace, J. and Sun, G., 1991, Influence of particle size distribution on the performance of fluidized bed reactors, Canadian Journal of Chemical Engineering, 69, 1126-1134.

Gryczka, O., Heinrich, S., Deen, N.G., Annaland, M. van Sint, J., Kuipers, J.A.M., Jacob, M., and Mörl, L., 2009, Characterization and CFD-modeling od the hydrodynamics of a prismatic spouted bed, Chemical Engineering Science, 64, 3352-3375.

Gupta, C. and Sathiyamoorthy, D., 1999, Fluidized Bed Technology in Materials Processing, , CRC Press LLC, Florida, 512p.

He, Y., Lim, C., Grace, J., Zhu, J., and Qin, S., 1994a. Measurement of voidage profiles in spouted beds, Canadian Journal of Chemical Engineering, 72, 229-234.

He, Y., Lim, C., Grace, J., and Zhu, J., 1994b. Particle velocity profiles and solid flow patterns in spouted beds, Canadian Journal of Chemical Engineering, 72, 561-568.

He, Y., Guangbo, Z., Bouillard, J., and Huilin, L., 2004, Numerical simulations of the effect of conical dimensions onthe hydrodynamic behaviour in spouted beds, Canadian Journal of Chemical Engineering, 82, 20-28.

Hockey, R.L., 2004, Nuclear Energy Research Initiative Annual Report, Pacific North National Laboratory, Washington, 51p.

Hoef, M., Annaland, M., and Kuipers, J., 2004, Computational fluid dynamics for dense gas-solid fluidized beds: a multiscale modeling strategy, Chemical Engineering Science, 59, 5151-5165.

Huilin, L., Yongli, L., Yurong, H., and Bouillard, J., 2001, Numerical simulations of hydrodynamic behaviour in spouted beds, Trans IChemE, 79, 593-599.

IAEA-TECDOC-987., 1997, Fuel performance and fission product behaviour in gas cooled reactors, Wien.

Jing, S., Hu, Q., Wang, J., and Jin, Y., 2000, Fluidization of coarese particles in gas-solid conical beds, Chemical Engineering and Processing, 39, 379-387.

Kawaguchi, T., Sakamoto, M., Tanaka, T., and Tsuji, Y., 2000, Quasi-three dimensional numerical simulation of spouted beds in cylinder, Powder Technology, 109, 3-12.

Kim, H., and Arastoopour, H., 1995, Simulation of FCC particles flow behavior in a CFB using modified kinetic theory, Canadian Journal of Chemical Engineering, 73, 603-611.

Krzywanski, R., Epstein, N., and Bowen, B., 1992, Multi-dimensional model of a spouted bed, Canadian Journal of Chemical Engineering, 70, 858-872.

Kunii, D., and Levenspiel, O., 1991, Fluidization Engineering, Butterworth-Heinemann, Newton, 491p.

Lan, X., Xu, C., Gao, J., and Al-Dahhan, M., 2012, Inflence of solid-phase wall boundary condition on CFD simulation of spouted beds, Chemical Engineering Science, 69, 419-430.

Lefroy, G., and Davidson, J., 1969, The mechanism of spouted beds, Trans. Inst. Chem. Eng., 47, 120-128.

Littman, H., Morgan, M. H., Narayanan, P. V., Kim, S. J., Day, J. Y., and Lazarek, G. M., 1985, An axisymmetric model of flow in the annulus of a spouted

bed of coarse particles, Canadian Journal of Chemical Engineering, 63, 188–199.

Liu, G.-Q., Li, S.-Q., Zhao, X.-L., and Yao, Q., 2008, Experimental studies of particle flow dynamics in a two-dimensional spouted bed, Chemical Engineering Science, 63, 1131-1141.

Liu, M., Liu, B., and Shao, Y., 2011, Optimization of the UO_2 kernel coating process by 2D simulation of spouted bed dynamics in the coater, Nuclear Engineering Design, xxx, xxx-xxx.

Lu, H., Yuronga, H., Wentie, L., Ding, J., Gidaspow, D., and Bouillard, J., 2004, Computer simulations of gas-solid flow in spouted beds using kinetic-frictional stress model of granular flow, Chemical Engineering Science, 59, 865-878.

Lun, C. K. K., 1991, Kinetic theory for granular flow of dense, slightly, Journal of Fluid Mechanics, 539-599.

Mathur, K.B. and Gishler, P.E., 1955, A technique for contacting gases with coarse solid particles, A.I.Ch.E. Journal, 1, 157–164.

Nickel, H., Nabielek, H., Pott, G., and Mehner, A., 2002, Long time experience with the development of HTR fuel elements in Germany, Nuclear Engineering Science and Design, 217, 141-151.

Olazar, M., San Jose, M. J., Aguayo, A. T., Arandes, J. M., and Bilbao, J., 1992, Stable operation conditions for gas-solid contact regimes in conical spouted beds, Industrial and Engineering Chemistry Research, 31, 1784-1972.

Olazar, M., SAn Jose, M., Penas, F. J., Aguayo, A. T., and Bilbao, J., 1993, Stability anh hydrodynamics of conical spouted beds with binary mixtures, Industrial and Engineering Chemistry Research, 32, 2826-2834.

Olazar, M., San Jose, M. J., LLamosas, R., Alvarez, S., and Bilbao, J., 1995, Study of local porosities in conical spouted beds using an optical fiber probe, Industrial and Engineering Chemistry Research, 34, 4033-4039.

Olazar, M., San Jose, M. J., Izquierdo, M. A., Sonia, A., and Bilbao, J., 2004, Fountain geometry in shallow spouted beds, Industrial and Engineering Chemistry Research, 43, 1163-1168.

Pannala, S., Daw, C., Finney, C. E., Boyalakuntla, D., Syamlal, M., and O'Brien, T., 2007, Simulating the dynamics of spouted bed nuclear fuel coaters, Chemical Vapor Deposition, 13, 481-490.

Phelip, M., 2004, European Programme on HTR Fuel Technology,. 2nd International Topical Meeting on High Temperature Reactor Technology, Paper B06.

Ranade, V., 2002, Computational Flow Modeling for Chemical Reactor Engineering, Academic Press, San Diego, 474p.

Rojas, I., 2010, Preliminary results for the investigation of hydrodynamic scaling relationships in shallow spouted beds, Separation Science and Technology, 45, 1928-1934.

Roy, D., L. F., Legros, R., and Chaouki, J., 1994, A study of solid behavior in spouted bedsusing 3-D particle tracking, Canadian Journal of Chemical Engineering, 72, 945-952.

Salam, P. A., and Bhattacharya, S., 2006, A comperative hydrodynamic study of two types of spouted bed reactor designs, Chemical Engineering Science, 61, 1946-1957.

San Jose, M., Olazar, M., Alvarez, S., Izquierdo, M., and Bilbao, J., 1998, Solid cross-flow into the spout and particle trajectories in conical spouted beds, Chemical Engineering Science, 53, 3561-3570.

San Jose, M. J., Olazar, M., Izquierdo, M. A., Sonia, a., and Bilbao, J., 2001, Spout geometry in shallow spouted beds, Industrial and Engineering Chemistry Research, 40, 420-426.

Sari S., Cangal P., Kulah G., and Koksal M., 2011, Investigation of Hydrodynamic Characterictisc of Spouted Bed Nuclear Fuel Coaters, TUBITAK Report 108M432, Ankara, 163p.

Seiler, C., Fryer, P., and Seville, P., 2008, Statictial modelling of the spout bed coating process using positron emission particle tracking (PEPT) data, Canadian Journal of Chemical Engineering, 86, 571-581.

Sinclair, J., and Jackson, R., 1989, Gas–particle flow in a vertical pipe with particle–particle interactions, AIChE J., 35, 1473– 1486.

Shuyan, W., Xiang, L., Huilin, L., Long, Y., Dan, S., Yurong, H., and Yonglong, D., 2009, Numerical simulatoins of flow behavior of gas and particles in spouted beds using frictional-kinetic stress model, Powder Technology, 196, 184-193.

Taghipour, F., Ellis, N., and Clayton, W., 2005, Experimental and computational study of gas-solid fluidized bed hydrodynamics, Chemical Engineering and Science, 60, 6857-6867.

Venkatachalam, S., Sridhar, R., and Immanuel, V. P., 2009, Prediction of minimum spouting velocity in spouted bed, Asia-Pacific Journal of Chemical Engineering .

Wachem, B., Schouten, J., Krishna, R., and Bleek, C., 2000, Overview of CFD models for laminar gas-solid systems, AMIF-ESF Workshop "Computing methods for two phase flow".

Wachem, B. G., Schouten, J. C., Bleek, C. M., Krishna, R., and Sinclair, J. L., 2001, Comparative analysis of CFD models of dense gas-solid systems, AIChE Journal, 47, 1035-1051.

Waldie, B. and Wilkinson, D., 1986, Measurement of particle movement in a spouted bed using a new microprocessor based technique, Canadian Journal of Chemical Engineering, 64, 944-949.

Wang, Z., Hsiaoto, T., Lim, C. J., and Su, P., 2004, Determination of minimum spouting velocity in conical spouted beds, Canadian Journal of Chemical Engineering, 82, 11-19.

Wang, Z., 2006, Experimental studies and CFD simulations of conical spouted bed hydrodynamics, PhD thesis, University of British Columbia, Vancouver, 369p.

Wu, C.L. and Berrouk, A.S., 2009, Comments on:"Solid cross-flow into the spout and particle trajectories in conical spouted beds" bye San Jose Maria, J., et al., Chemical Engineering Science 53 (1998) 3561-3570, Chemical Engineering and Science, 64, 4457-4459.

Zhou, J., 2008, Characterizing and modeling the hydrodynamics of shallow spouted beds, PhD thesis, The University of Tennessee, Knoxville, 155p.

Zhonghua, W. and Mujumdar, A. S., 2008, CFD modeling of the gas-particle flow behavior in spouted beds, Powder Technology, 183, 260-272.

APPENDIX A SUMMARY OF A SAMPLE FLUENT INPUT

FLUENT
Version: axi, pbns, eulerian, lam, unsteady (axi, pressure-based, Eulerian, laminar, unsteady)
Release: 6.3.26
Title:

1. Models

Model	Settings
Space	Axisymmetric
Time	Unsteady, 1st-Order Implicit
Viscous	Laminar
Heat Transfer	Enabled
Solidification and Melting	Disabled
Radiation	None
Species Transport	Disabled
Coupled Dispersed Phase	Disabled
Pollutants	Disabled
Pollutants	Disabled
Soot	Disabled

2. Boundary Conditions

- Zones

name	id	type
fluid	2	fluid
center	3	axis
walls	4	wall
gas_outlet	5	outflow
gas_inlet	6	velocity-inlet
default-interior	8	interior

- Boundary Conditions

fluid

Condition	Value
Material Name	particles
Specify source terms?	no
Source Terms	()
Specify fixed values?	no
Fixed Values	()

Motion Type	0
X-Velocity Of Zone (m/s)	0
Y-Velocity Of Zone (m/s)	0
Rotation speed (rad/s)	0
Deactivated Thread	no
Porous zone?	no
Porosity	1
Solid Material Name	aluminum

center

Condition	Value

walls

Condition	Value
Wall Thickness (m)	0
Heat Generation Rate (w/m3)	0
Material Name	aluminum
Thermal BC Type	1
Temperature (k)	300
Heat Flux (w/m2)	0
Convective Heat Transfer Coefficient (w/m2-k)	0
Free Stream Temperature (k)	300
Wall Motion	0
Shear Boundary Condition	0
Define wall motion relative to adjacent cell zone?	yes
Apply a rotational velocity to this wall?	no
Velocity Magnitude (m/s)	0
X-Component of Wall Translation	1
Y-Component of Wall Translation	0
Define wall velocity components?	no
X-Component of Wall Translation (m/s)	0
Y-Component of Wall Translation (m/s)	0
External Emissivity	1
External Radiation Temperature (k)	300
Rotation Speed (rad/s)	0
X-component of shear stress (pascal)	0
Y-component of shear stress (pascal)	0
Surface tension gradient (n/m-k)	0
Specularity Coefficient	0

gas_outlet

Condition	Value
Flow rate weighting	1

gas_inlet

Condition	Value
is zone used in mixing-plane model?	no

default-interior

Condition	Value

3. Solver Controls

- *Equations*

Equation	Solved
Flow	yes
Volume Fraction	yes
Energy	yes

- *Numerics*

Numeric	Enabled
Absolute Velocity Formulation	yes

- *Unsteady Calculation Parameters*

Time Step (s)	0.00050000002
Max. Iterations Per Time Step	1000

- *Relaxation*

Variable	Relaxation Factor
Pressure	0.2
Density	0.2
Body Forces	0.2
Momentum	0.2
Volume Fraction	0.2
Granular Temperature	0.2
Energy	0.2

- *Linear Solver*

Variable	Solver Type	Termination Criterion	Residual Reduction Tolerance
Pressure	V-Cycle	0.1	
X-Momentum	Flexible	0.1	0.7
Y-Momentum	Flexible	0.1	0.7
Volume Fraction	Flexible	0.1	0.7
Energy	Flexible	0.1	0.7

- *Pressure-Velocity Coupling*

Parameter	Value
Type	Phase Coupled SIMPLE

- *Discretization Scheme*

Variable	Scheme
Momentum	First Order Upwind
Volume Fraction	First Order Upwind
Energy	First Order Upwind

- *Solution Limits*

Quantity	Limit
Minimum Absolute Pressure	1
Maximum Absolute Pressure	5e+10
Minimum Temperature	1
Maximum Temperature	5000

4. Material Properties

- *Material: particles (fluid)*

Property	Units	Method	Value(s)
Density	kg/m3	constant	2503
Cp (Specific Heat)	j/kg-k	constant	540
Thermal Conductivity	w/m-k	constant	0.96
Viscosity	kg/m-s	kinetic-theory	#f
Molecular Weight	kg/kgmol	constant	60
Standard State Enthalpy	j/kgmol	constant	-2.85841e+08
Reference Temperature	k	constant	298
L-J Characteristic Length	angstrom	constant	0
L-J Energy Parameter	k	constant	0

Thermal Expansion Coefficient	1/k	constant	0
Degrees of Freedom		constant	0
Speed of Sound	m/s	none	#f

- *Material: air (fluid)*

Property	Units	Method	Value(s)
Density	kg/m3	constant	1.225
Cp (Specific Heat)	j/kg-k	constant	1006.43
Thermal Conductivity	w/m-k	constant	0.0242
Viscosity	kg/m-s	constant	1.7894e-05
Molecular Weight	kg/kgmol	constant	28.966
Standard State Enthalpy	j/kgmol	constant	0
Reference Temperature	k	constant	298.15
L-J Characteristic Length	angstrom	constant	3.711
L-J Energy Parameter	k	constant	78.6
Thermal Expansion Coefficient	1/k	constant	0
Degrees of Freedom	constant	0	
Speed of Sound	m/s	none	#f

RESUME

Name Surname	:	Senem Şentürk Lüle
Place of Birth	:	Çorum
Date of Birth	:	1977
Marital Status	:	Married
Children	:	2
Education	:	

1990-1993	Trabzon Affan Kitapçıoğlu High School
1994-1999	Hacettepe University Nuclear Engineering Department
1999-2001	Hacettepe University Nuclear Engineering Department
2003-2004	Birmingham University Physics and Astronomy Department, United Kingdom

Language	:	English
Work Experience	:	

1999-2005	Hacettepe University Nuclear Engineering Department, Research Assistant
2005-2005	Serco Assurance United Kingdom, Radiation Shielding Modeler/Analyst
2006-today	Turkish Atomic Energy Authority, Nuclear Engineer